Title
Quasi-isentropic and shock compression of FCC and BCC metals : effects of grain size and stacking-fault energy

Author
Jarmakani, Hussam N.

Publication Date
2008

UNIVERSITY OF CALIFORNIA, SAN DIEGO

QUASI-ISENTROPIC AND SHOCK COMPRESSION OF FCC AND BCC METALS: EFFECTS OF GRAIN-SIZE AND STACKING-FAULT ENERGY

A dissertation submitted in partial satisfaction of the requirements

for the degree of Doctor of Philosophy

in

Materials Science and Engineering

by

Hussam N. Jarmakani

Committee in charge:

Professor Marc A. Meyers, Chair
Professor D. Benson
Professor V. A. Lubarda
Professor V. Nesterenko
Professor L. Rudee

2008

The Dissertation of Hussam N. Jarmakani is approved, and it is acceptable in quality and form for publication on microfilm:

Chair

University of California, San Diego

2008

DEDICATION

I would like to dedicate this piece of work to the two most important groups of people in my life: my parents and my aunt and uncle, Sam and Sue. Mother and father, this achievement is ultimately a product of your upbringing, sacrifice, perseverance, and determination throughout the years to make me the best that I can be. I hope I have made you proud. Sam and Sue, you have welcomed me into your home, treated me as one of your own, and shown me unconditional love throughout the past 11 years. Without you, none of this would have been possible. I thank you all for the support and guidance that you have given me throughout my life.

TABLE OF CONTENTS

LIST OF FIGURES

LIST OF TABLES

ACKNOWLEDGMENTS

This work was performed under the auspices of the UCOP (ILSA contract No. W-7405-Eng-48) in collaboration with Lawrence Livermore National Laboratory, through the Institute for Laser Science and Applications. TEM work on monocrystalline copper was performed under the SHaRE program at Oak Ridge National Labs. I am very thankful to Dr. Jim McNaney for his help, insight and guidance throughout my early work on copper. I also thank Dr. Bimal Kad for his tremendous help with TEM imaging and analysis. I am very thankful to Dr. Eduardo Bringa for insipiring, guiding, and motivating me to pursue research in the field of Molecular Dynamics. He was a key factor in helping us with establishing our LAMMPS molecular dynamics capabilities here at the MAE department. I would also like to thank Dr. Morris Wang for his helpful insight on my modeling efforts, as well as his TEM work that has been central to my research on nanocrystalline nickel. The help provided by Vo Nhon and in MD defect analysis is appreciated.

I would like to thank Drs. Bruce Remington, Dan Kalantar, Alice Koniges, and Dave Eder for their support throughout my work on vanadium. Dr. B. Maddox is also thanked for his discussions and help with experiments. The grateful support provided by Dr. D. Correll is also acknowledged. I would like to thank Evelyn York at the Scripps Institute of Oceanography for her tremendous help with SEM imaging throughout my thesis work. I am also very grateful to Dr. Norm Olson at NCMIR, UCSD for spending the time to train me on TEM imaging.

I am very thankful to my thesis advisor, Prof. Marc A. Meyers for the opportunity he has given me to work with him and the guidance he has provided me

throughout my thesis work. I have learned so much from him over the years and have grown as a person through interacting with him. His exceptional work ethic, motivation, and desire for knowledge are all characteristics that have positively influenced me, and I will definitely be taking these traits with me as I move on with life. I would also like to thank my committee members, Drs. Vitali Nesterenko, Vlado Lubarda, David Benson, and Lea Rudee, for the time they have taken to provide me with valuable insight on my thesis work. I also thank my friends in the Meyers group for their valuable support and friendship throughout the years. I am glad that I have met you all. I have definitely made life-long friends through their camaraderie.

Chapter 3, in full, is a reprint of the material as it appears in Materials Science and Engineering (A), 2007, Vol. 463, pp. 249-262 (authors and co-authors: H. Jarmakani, J.M. McNaney, B. Kad, D. Orlikowski, J.H. Nguyen, M.A. Meyers). Chapter 4, in part, has been submitted for publication in Acta Materialia, 2008, and, in part, has been published in Applied Physics Letters, 2006, Vol. 88, pp. 061917 (authors and co-authors: Y. M. Wang, E. M. Bringa, J. M. McNaney, M. Victoria, A. Caro, A. M. Hodge, R. Smith, B. Torralva, B. A. Remington, C. A. Schuh, H. Jarmakani, and M. A. Meyers) and the Proceedings of the Conference of the American Physical Society Topical Group on Shock Compression of Condensed Matter, 2007, AIP Press 955, pp. 239-242 (Authors and co-authors: H. Jarmakani, Y. M. Wang, E. Bringa and M. A. Meyers). Chapter 5, in full, has been submitted for publication in Acta Materialia, 2008 (authors and co-authors: H. Jarmakani, D. Kalantar, A. Koniges, D. Eder, and M. A. Meyers).

VITA

2003	Bachelor of Science, University of California, San Diego
2004	Master of Science, University of California, San Diego
2004-2008	Research Assistant, University of California, San Diego.
2008	Doctor of Philosophy, University of California, San Diego

PUBLICATIONS

- H. Jarmakani, E. Bringa, P. Erhart, B. A. Remington, Y. M. Wang, N. Q. Vo, and M. A. Meyers, Molecular Dynamics Simulations of Shock Compression of Nickel: From Mono to Nano-crystals (submitted to Acta Materialia, 2008).
- H. Jarmakani, D. Kalantar, A. Koniges, D. Eder, and M. A. Meyers, Laser-shock induced spalling and fragmentation in polycrystalline vanadium (submitted to Acta Materialia, 2008).
- E.M. Bringa, P. Erhart, H. Jarmakani, B.D. Wirth , Y. Nagai , A. Caro , J. McNaney, R. Smith, M.A. Meyers and M. Victoria, Shock wave interactions with porous nanocrystals (in progress).
- A. E. Koniges, J. Andrew, D. Eder, D. Kalantar, N. Masters, A. Fisher, R. Anderson, B. Gunney, B. Brown, K. Sain, A. M.Tobin, C. Debonnel, A. Gielle, P. Combis, J. P. Jadaud, M. A. .Meyers, H. Jarmakani, Experiments for the Validation of Debris and Shrapnel Calculations, Proc. IFSA Conference, Kobe, Japan, 2007.
- H. Jarmakani, Y. M. Wang, E. Bringa, and M. A. Meyers, Modeling of the Slip-Twinning Transition in Nanocrystalline Nickel and Nickel-Tungsten under Shock

Compression, Proceedings of the Conference of the American Physical Society Topical Group on Shock Compression of Condensed Matter, 2007, Edited by M. Elert, M. D. Furnish, R. Chau, N. C. Holmes, and J. Nguyen, AIP Press 955, pp. 239-242.

- M. A. Meyers, M. S. Schneider, H. Jarmakani, B. Kad, B. A. Remington, D. H. Kalantar, J. McNaney, B. Cao, and J. Wark, Deformation Substructures and Their Transitions in Laser-Shock-Compressed Copper-Aluminum Alloys, Met. Mat. Trans, 2007, Vol. 39 A, pp. 304.
- Y. M. Wang, E. M. Bringa, J. M. McNaney, M. Victoria, A. Caro, A. M. Hodge, R. Smith, B. Torralva, B. A. Remington, C. A. Schuh, H. Jarmakani, and M. A. Meyers, Deforming Nanocrystalline Nickel at Ultra-High Strain-Rates, Appl. Phys. Lett., 2006, Vol. 88, pp. 061917.
- M. Meyers, H. Jarmakani, J. M. McNaney, M. Schneider, J. H. Nguyen, B. Kad, Dynamic Response of Single-Crystalline Copper Subjected to Quasi-Isentropic Laser and Gas-Gun Driven Loading, J. Phys. IV, 2006, Vol. 134, pp. 37-42.
- H. Jarmakani, J.M. McNaney, B. Kad, D. Orlikowski, J.H. Nguyen, M.A. Meyers, Dynamic Response of Single Crystalline Copper Subjected to Quasi-Isentropic, Gas-Gun Driven Loading, Mat Sci and Eng A, 2007, Vol. 463, pp. 249-262.
- H. Jarmakani, J. M. McNaney, M. S. Schneider, D. Orlikowski, J. H. Nguyen, B. Kad, M. A. Meyers, Dynamic Response of Copper Subjected to Quasi-Isentropic, Gas-Gun Driven Loading, Proceedings of the Conference of the American Physical Society Topical Group on Shock Compression of Condensed Matter, 2005, edited by M. D. Furnish, M. Elert, T. P. Russell, and C. T. White, AIP Press 845, pp. 1319-1321.

- M. S. Schneider, B. Kad, D. H. Kalantar, B. A. Remington, E. Kenik, H. Jarmakani and M. A. Meyers, Laser Shock Compression of Copper and Copper-Aluminum Alloys, International Journal of Impact Engineering, 2005, Vol. 32, pp. 473-507.

FIELD OF STUDY

Major Field: Engineering (Materials Science)

ABSTRACT OF THE DISSERTATION

Quasi-Isentropic and Shock Compression of FCC and BCC Metals: Effects of Grain-Size and Stacking-Fault Energy

by

Hussam N. Jarmakani

Doctor of Philosophy in Materials Science and Engineering

University of California, San Diego, 2008

Professor Marc A. Meyers, Chair

Quasi-isentropic compression experiments (ICE) of monocrystalline copper and nanocrystalline nickel and nickel-tungsten were carried out. The ICE process allows higher pressures to be accessed while minimizing the associated temperature rise. Monocrystalline copper was subjected to pressures between 18 GPa and 52 GPa, and the deformation substructure was studies via transmission electron microscopy (TEM). Current experimental evidence suggests a deformation substructure that transitions from slip to twinning, where twinning occurs at the higher pressures (~52 GPa), and heavily dislocated laths and dislocation cells take place at the intermediate and lower pressures. Evidence of stacking faults at the intermediate pressures was also found. The Preston-Tonks-Wallace constitutive description was used to model both quasi-isentropic and shock compression experiments and predict the pressure at which the slip-twinning transition occurs in both cases.

Nanocrystalline nickel and nickel-tungsten, 13 at. % (G S between 10 and 50nm), subjected to pressures between 20 and 70 GPa, were also analyzed. Shock compression of mono and nanocrystalline nickel is simulated over a range of pressures (10-80 GPa) and compared with experimental results. Contributions to the net strain from the various mechanisms of plastic deformation such as partial dislocations, perfect dislocations, and twins are quantified in the nanocrystalline samples. The effect of stress unloading, a phenomenon often neglected in MD simulations, on dislocation behavior is computed. It is shown that a large fraction of the dislocations generated during compression is annihilated upon unloading. The present analysis resolves a disagreement consistently observed between MD computations and experimental results. Analytical models are applied to predict the critical pressures for the cell-to-stacking-fault transition and the onset of twinning as a function of grain-size and stacking-fault energy (through the addition of tungsten). These predictions are successfully compared with experimental results.

Polycrystalline vanadium was subjected to shock compression followed by tensile wave release to study spall and fragmentation behavior. These experiments are part of an effort to help predict and minimize damage to diagnostic tools and protective shields of high-powered laser facilities such as the National Ignition Facility, NIF. The shock pulse was generated by a direct laser drive at energy levels ranging between 160 J and 440 J. Glass shields placed at a specific distance behind the Va targets were used to collect and analyze the ejected fragments in order to evaluate and quantify the extent of damage. The effects of target thickness, laser energy, and pulse duration were studied. Calculations show melting at a pressure threshold of ~150 GPa, which corresponds to a laser energy level of ~ 200 J. The recovered specimens and fragments show evidence of melting at the higher energy levels, consistent with the analytical predictions. Spalling occurred by a ductile tearing mechanism that favored grain boundaries. Experimentally obtained fragment sizes were compared with predictions from the Grady-Kipp model, and a good agreement was obtained. The spall strength of vanadium under laser loading conditions was calculated from the spall thickness and found to be in the 9-18 GPa range.

CHAPTER 1

INTRODUCTION

Throughout history, humans have constantly attempted to harvest energy from different sources in nature and convert it to forms they can use. Draft animals were first used in Mesopotamia before 3000 BC for farm work and hauling wheeled vehicles [1]. Our ancestors burned wood to keep themselves warm and tapped into the flow of wind and water by means of wind and water mills as early as 4000 BC [2] to create power to drive their machinery. The modern industrialized world we live in today is a direct consequence of the inconceivable amounts of energy we have been able to unlock from fossil fuels such as coal, oil and natural gases. Figure 1.1 shows the energy consumed by the U.S. between 1650 and 2000. It is clear that at approximately 1885, fossil fuels began to dramatically multiply the rate at which energy could be poured into the economy [3].

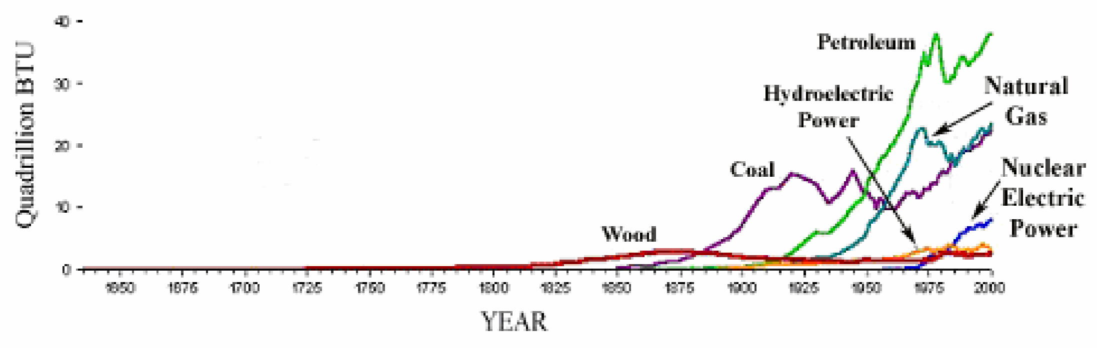

Figure 1.1: Energy consumption in the United States of America [3].

Despite the tremendous benefits and advantages of fossil fuels, serious harmful energy-related environmental and health effects have become evident due to their production and consumption. The emission of fossil fuel byproducts, namely green house gases, over the years has increased pollution and raised global average temperatures on earth. Driven by the need to minimize irreversible environmental damage and the fact that the earth's fuel deposits are finite, nuclear energy has become a good candidate for replacing current energy sources on earth.

Of all the known nuclear reactions, fission is currently of most practical significance. It is the process in which a heavy nucleus splits into two smaller nuclei. All nuclear power plants in the United States operate on the principle of fission. In 2004, the electricity produced in nuclear fission power stations had the energy equivalent of more than 12 million barrels of oil per day, and none of those stations produced any air pollution as the result of their operation [3]. A very important fission reaction that takes place in nuclear reactors as a result of neutron absorption in U-235 is as follows:

$$ {}^{235}_{92}U + {}^{1}_{0}n \rightarrow {}^{A1}_{Z1}P_1 + {}^{A2}_{Z2}P_2 + \chi \; {}^{1}_{0}n + ENERGY \qquad (1.1)$$

The products of the reaction are indicated as P_1 and P_2 signifying the various possible ways U-235 can split into as long as the sum of the neutrons and protons in the products equal that of the initial fissioning nucleus [4]. Unfortunately, the sources of radioactive waste generated during fission are numerous, and the problem of their safe disposal is an even more serious matter that has not been fully resolved. This is where fusion, another promising nuclear reaction, aims at eliminating this problem while providing an even more efficient energy source.

Fusion is the process in which two small nuclei combine or "fuse" to form a heavier nucleus. The energy released by fusion is three to four times greater than that released by fission. This is because the fraction of mass transformed into energy is that much higher in fusion. Since the reactants in fusion are much smaller than those in fission, the energy density of the fusion fuel is also much higher. A practical method of carrying out fusion in a controlled manner has not yet been realized because an incredible amount of energy needs to be put into the system before a reaction can take place [4]. This research contribution is tied with the effort to successfully carry out controlled fusion on Earth.

The minimum temperature at which a fusion reaction can take place is 100 million degrees Kelvin (~10^4eV). The reaction requiring this minimum temperature to be activated is very important in future fusion reactors and involves two isotopes of hydrogen, deuterium-D ($^{2}_{1}\mathrm{H}$) and tritium-T ($^{3}_{1}\mathrm{H}$) [4]:

$$^{2}_{1}H + ^{3}_{1}H \rightarrow ^{4}_{2}He + ^{1}_{0}n + 17.6MeV \tag{1.2}$$

Deuterium is found in sea water and tritium can be produced onsite by a reaction involving lithium. Thus, environmental effects involved with mining of products are not an issue. The waste product, helium, is a noble gas, which is also not harmful to the environment. The danger of a nuclear accident during fusion is minimized since fuel is introduced as needed. An uncontrollable reaction would most likely only lead to rapid burn up of the fuel followed by power loss. Other fusion reactions involve temperatures that are up to ten times higher than that of fusing D and T (D-T). At these temperatures, ionization takes place and plasma confinement becomes problematic.

A major effort, led by the Lawrence Livermore National Laboratory (LLNL), is currently underway to tackle and solve the problems surrounding fusion. The $1.2 billion National Ignition Facility (NIF), Figure 1.2 (a), currently under construction at LLNL is the largest laser facility in the world. It covers the length of two football fields and houses 192 laser beams. All 192 lasers are expected to be functioning by 2009, although experiments on only four of the beams are currently being run on NIF. The laser beams are designed to converge onto the inside wall of a gold cylinder, called a hohlraum, having a diameter of 5.5 mm and height of 9.5 mm. X-rays are produced due to the interaction of the lasers with the inside wall of the cylinder. They in turn converge onto and compress a 2 mm diameter capsule placed at the center of the hohlraum. The capsule contains D-T fuel. The beams are designed to produce 1.8 MJ of energy and 500 terawatts of power, more than sufficient to fuse the nuclei of deuterium and tritium and produce 600 to 1,000 times the energy initially input into the system [5]. This highly desired phenomenon, illustrated in Figure 1.2 (b), is called ignition.

The NIF target capsule is comprised of 3 main layers: the outer ablator layer, the inner frozen D-T fuel and the central D-T gas core. Polyamide is the ablator of choice at higher x-ray temperatures (350 eV). It is mechanically tough and thermally stable at a wide range of temperatures. Beryllium ablators are used at lower x-ray temperatures (250 eV). They demonstrate higher energy absorption and produce higher pressures than polyamides. Beryllium ablator capsules, illustrated in Figure 1.3, are additionally doped with copper for better x-ray absorption. The frozen solid D-T layer, just beneath

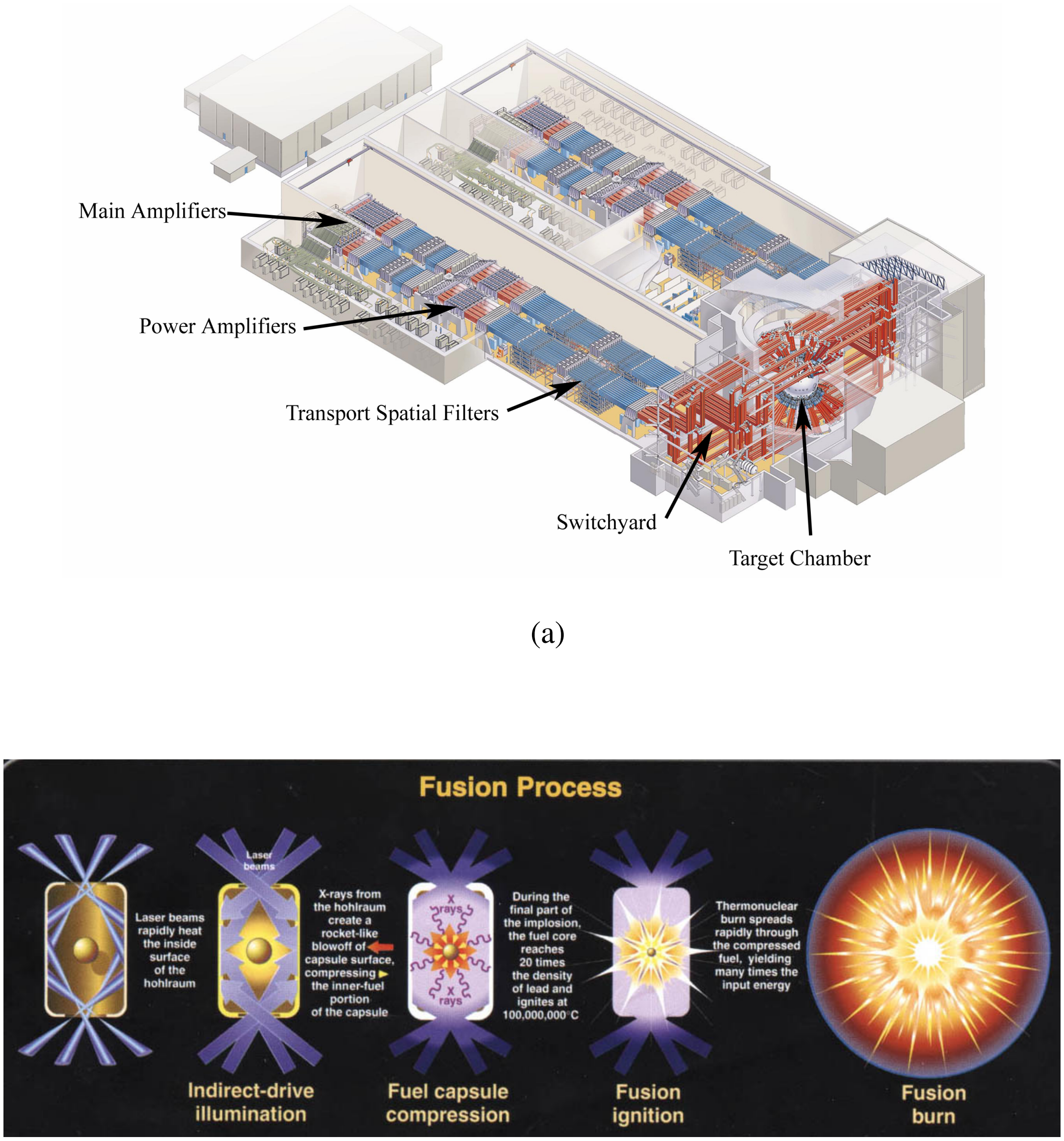

(a)

(b)

Figure 1.2: (a) Schematic of the NIF facility at LLNL (courtesy of: www.llnl.gov/nif); (b) Schematic of the inertial fusion confinement process that takes place within the target chamber (from LLNL NIF brochure).

the ablator layer, serves as the main fuel for ignition and encloses a central D-T gas core [5].

The high-intensity x-rays that converge onto the outer surface of the capsule generate shock waves due to the ablator pressure. These shock waves are of modest strength within the solid D-T region allowing for the implosion to be nearly isentropic, or quasi-isentropic. The shock waves strengthen as they travel past the high density ice layer into the lower density gas core. These shock waves, together with the compressive work, heat up the D-T gas to temperatures sufficient for ignition to occur [6]. The burn from the "hot spot" at the core spreads to the denser D-T ice region, which feeds and helps sustain the reaction. The hohlraum holding the capsule is filled with helium and hydrogen to minimize laser scattering and suppress gold ionization, and the temperature is maintained at 18 K, necessary to keep the solid D-T layer in equilibrium with the gas core.

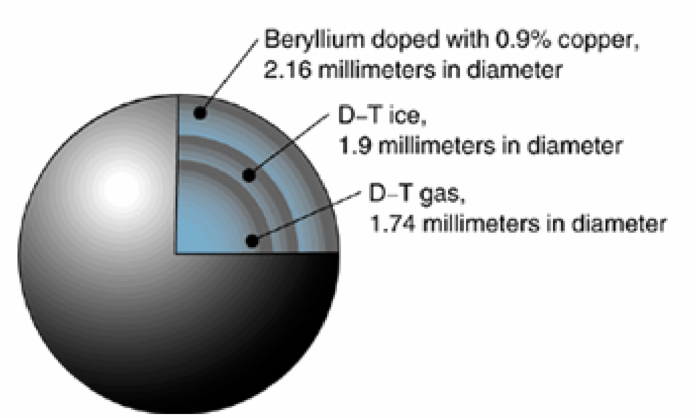

Figure 1.3: Three layers of Be ablator capsule doped with 0.9% copper [5].

In recent years, nanocrystalline (nc) metals have become good candidates for replacing the outer layer of the NIF capsules, and a major research effort is currently in place to determine the feasibility of using nc materials in NIF targets. This is due to their superior mechanical properties and ability to minimize instabilities during implosion as a result of their small grain-size [7]. Nanocrystalline materials may also produce smaller fragments during failure and can essentially cause much less damage to the expensive laser optics in the NIF target chamber. Research in this area is usually conducted on popular and well-understood metals (such as copper, nickel, tantalum, tungsten, vanadium) to allow different research teams to collaborate and compare results.

Chapter 2 provides a background to this current research. It summarizes the various quasi-isentropic compression methods carried out in labs to study materials response, reviews the dynamic behavior of nanocrystalline metals subjected to low and high strain-rate deformation, and provides a brief background to dynamic failure and spall. Chapter 3 discusses the research carried out on the quasi-isentropic compression of monocrystalline copper. Chapter 4 presents both experimental work and molecular dynamics simulations on the shock-compression of mono and nanocrystalline nickel. Chapter 5 discusses the work carried out on laser-shock induced spalling and fragmentation in polycrystalline vanadium.

CHAPTER 2

BACKGROUND

2.1 Quasi-Isentropic Compression

As an NIF target capsule implodes due to the extreme pressures created by high intensity x-rays bombarding its surface, a relatively weak shock is first generated followed by an almost isentropic compression state, a cooler state well away from the Hugoniot. Ideally, isentropic loading states are shockless thermodynamic states, where entropy, the measure of randomness in a system, remains constant. Entropy (symbolized by S) can be represented as the following differential quantity:

$$dS = dQ / T \tag{2.1}$$

where dS is the change in entropy, dQ is the amount of heat absorbed or released in a system and T is the absolute temperature. The deformation of solids in the real world, however, inevitably results in the dissipation of heat due to plastic deformation [8]. Conditions where the loading is a smooth ramp or consists of repeated smaller shocks are generally referred to as quasi-isentropic loading. Higher states of stress accompanied by relatively lower temperatures can be achieved by loading a material quasi-isentropically. This delays thermal softening and enables the understanding and characterization of the solid-state response of a material at much higher pressures.

Isentropic Compression Experiments (ICE) today are providing precise data in the isentropic compression regime to help design better targets for NIF. Quasi-isentropic compression conditions have been achieved using multi-staged gas-guns, lasers, and magnetic/pulsed loading. The Equation of State (EOS), which is the relationship between pressure, temperature and density, of various materials of interest to NIF are being determined through these experiments. Figure 2.1 shows the different Equations of State (EOS) of a "real" material subjected to various compression states. The Hugoniot describes the states achieved in a material behind a shock. Note that the isentrope, resulting from adiabatic compression, lies below the Hugoniot and very close to the implosion curve, a region of interest in inertial fusion confinement. In fact, quasi-isentropic experiments come very close to simulating conditions that occur in the depths of planets [9]. Entropy does not change with depth in planets. Only temperature and pressure changes are experienced. ICE experiments in the early seventies were aimed at mimicking these conditions.

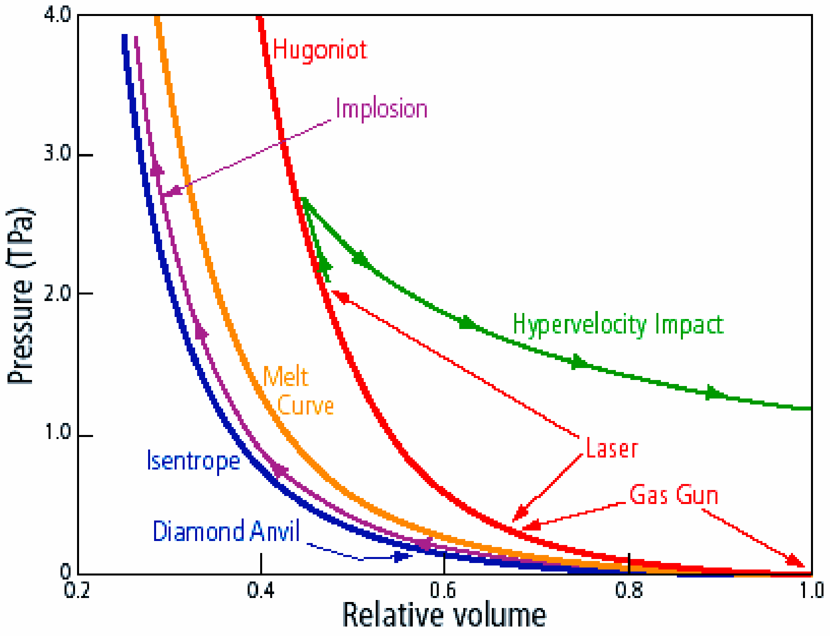

Figure 2.1: Equation of State of a "real" material in the P-V plane [9].

In addition to determining EOS of materials, experiments probing the microstructural response during quasi-isentropic compression are essential. Computational models and computer simulations need to accurately reflect the material's internal structure during deformation. Current computational models are "primitive" and do not account for this [10]. Traditional codes typically provide a simple characterization of dynamic fracture and provide a minimum pressure at which the metal fails. Results from such experiments incorporating characterization tools such as transmission and scanning electron microscopes are currently being incorporated into evolving models that describe how materials behave under extreme conditions [10]. Experiments on metals such as copper, whose behavior has been extensively studied over the years, are helping scientists compare simulations with experiments.

2.1.1 Gas-gun quasi-isentropic compression

Early work on ICE with gas-gun by Lyzenga et al. [11] used a composite flyer plate to generate a nearly isentropic pressure-density state in water. Their work was motivated by developing inter-atomic and molecular potential functions for molecular media. A series of materials of increasing shock impedance (Lexan, Al, Fe, W) were placed behind the target and impacted with a composite flyer plate comprised of the same series of materials, Figure 2.2 (a). A relatively smooth build up of pressure in the H_2O target arises after impact with the flyer plate. Figure 2.2 (b) shows the results of the pressure and specific volume (dots) within the H_2O layer at the indicated times after impact compared with the theoretical Hugoniot and isentrope.

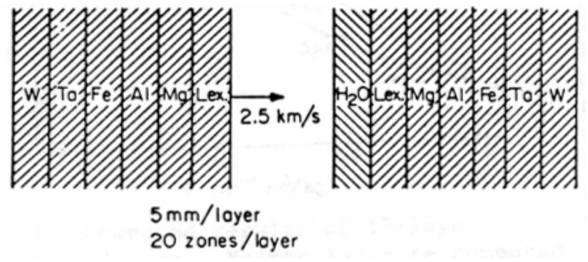

(a)

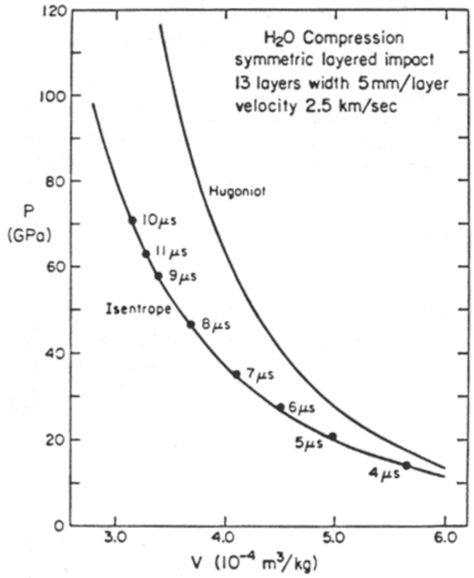

(b)

Figure 2.2: (a) Layered composite flyer-plate impactor; (b) Comparison of P-V results to the theoretical isentrope and Hugoniot [11].

Barker [12] used a flat-nosed projectile where a thin layer of material was simply placed on the nose-piece to cushion the impact and produce a gently rising input wave, Figure 2.3 (a). The layers have increasing shock impedance (equal to the product of density and sound velocity, ρc). This layer is referred to as a “pillow”. The pillow had a smoothly rising shock impedance in its thickness direction away from the target and was fabricated using powder technology. The concentrations of various powders were smoothly varied through the thickness of a powder blanket which was then pressed to produce the desired impedance profile. The shock impedance at the impact surface was kept as low as possible, and the impedance at the back surface matched that of the projectile nose-piece, as illustrated in Figure 2.3 (b). The thickness of the pillow (2mm in Barker's work [12]) determines the rise time of the input wave. When the desired peak stress is high, the rise time of the input wave is usually decreased in order to minimize edge effects that can destroy the uniaxial-strain conditions.

It is typical of this impact method to generate an undesirable small shock followed by a gently rising compressive wave in the specimen. An ICE wave tends to gradually steepen and develop into one or more shock waves. Pillow impactors are designed to delay this shocking up process to maximize the time that the target specimen is under a quasi-isentropic compression state. Figure 2.4 shows the gently rising particle velocities in a 6061-T6 aluminum sample measured at two different locations along the thickness of the sample. The maximum pressure obtained was 9 GPa, and the accompanying strain-rate was 10^5 s^{-1}. The sample had a "stepped" geometry to enable a dual-VISAR system to measure the free surface motion at two different locations. Note how the particle velocity profile at 10.09 mm is steeper than that at 3.65 mm.

The stress-strain loading curve, Figure 2.5, was also obtained by using the average wave velocity between the two locations, known as the Lagrangian wave speed, and integrating the following conservation of mass, momentum and energy equations for plane wave propagation:

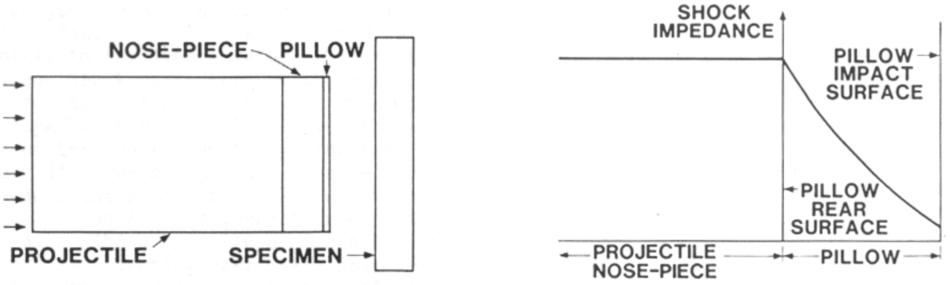

(a) (b)

Figure 2.3: (a): Projectile with a nose-piece and pillow; (b) Shock impedance profile of nose- piece and pillow [12].

$$d\sigma = \rho_0 U_w dU_p \tag{2.2}$$

$$dV = -V_0\ dU_p / U_w \tag{2.3}$$

$$dE = -\ P\ dv \tag{2.4}$$

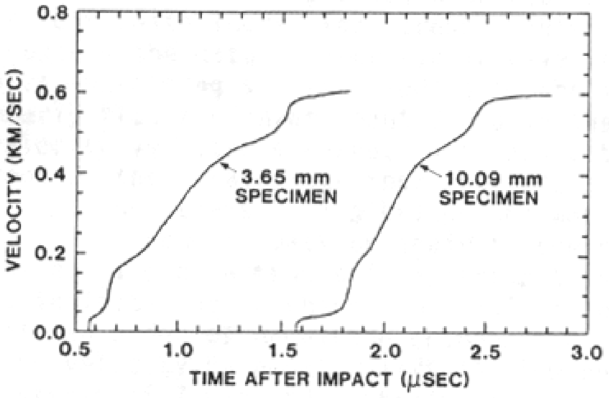

Figure 2.4: Particle velocity profiles at two different locations in a 6061-T6 Al sample [12].

The quasi-isentropic loading from the pillow impact results in stresses that are higher than the Hugoniot at any given strain which seems to be the opposite of what is expected because of the higher temperatures along the Hugoniot. This apparent higher stress state during quasi-isentropic loading can be attributed to the fact that the specimen undergoes localized heating on its shear planes during deformation which can cause a temporary reduction in yield strength in Hugoniot experiments. However, in the quasi-isentropic case, the stress rise in the material is more gradual giving more time for heat to dissipate away from the shear planes. This keeps the temperature lower during deformation and keeps the yield strength high, and the quasi-isentrope, thus, rises above the Hugoniot.

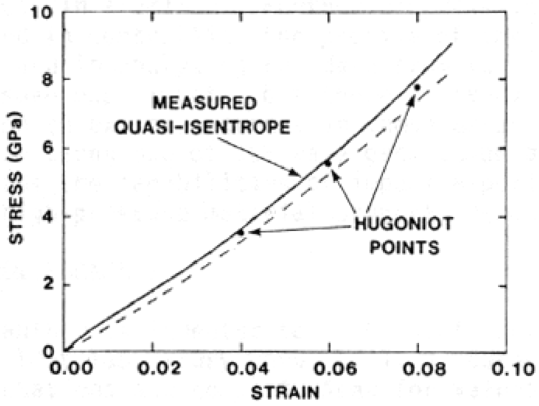

Figure 2.5: Stress-strain loading path in 6061-T6 Al along with three Hugoniot points and the dashed shock hydrostat [12].

Mogilevskii et al. [13] and Adadurov et al. [14, 15] both used controlled explosive experiments to launch a projectile onto their target to produce the ICE waves. Their work is mentioned here since they use unique methods to produce the desired ICE waves, and their procedures can also easily be replicated in a gas-gun environment. Mogilevskii et al. [13] attempted to study the effect of quasi-isentropic compression on the hardening of [112] copper. They used a layer of liquid hydrogen between the projectile (made of aluminum alloy D16T) and the sample to weaken the primary shock.

Projectile velocities of 2.4 and 3.6 km/s resulted in primary shock waves having intensities of 35 and 70 Kbar, respectively. A brass plate was also used to further weaken the primary shock to 20 Kbar at an impact velocity of 2.9 km/s. The whole assembly was cooled to 20.5 K using liquid hydrogen. At the highest projectile velocity investigated (3.6km/s), the calculated residual temperatures in the copper sample were 170 K in the quasi-isentropically compressed region after the primary shock and 375 K in the final shocked region after "shock-up". Annealing effects in the samples were, therefore, minimal making it possible for metallographic investigations.

Vickers microhardness measurements were carried out along the thickness of the impacted samples. The initial average microhardness of the samples was 93.8 kgf/mm^2. Figure 2.6 shows the results of three experiments. Measurements 1 and 3 are the results from the samples loaded through the layer of hydrogen, and measurement 2 is the result of the direct collision of the projectile with the sample. The sample homogenously hardens throughout its thickness when directly impacted by the projectile since the same shock wave travels throughout. When isentropically compressed, the microhardness is lower near the face of the impacted surface than the shock compression zone (~6mm into the sample). This is a direct consequence of the decrease in the rate of deformation in the quasi-isentropic compression zone, which yields a lower dislocation density and in turn gives a lower hardness reading. The mean rate of plastic deformation is related to the dislocation density and dislocation velocity by the Orowan equation:

$$\dot{\gamma} = k\rho b\bar{v} \tag{2.5}$$

where k is a correction parameter, ρ is the density of dislocations, b is the Burgers vector, and $\bar{v}$ is the mean velocity of dislocations [16]. If a limiting velocity for $\bar{v}$ is set as v_s, the shear wave velocity, then the total dislocation density, ρ is directly proportional to $\dot{\gamma}$. Thus, the hardness ($=k\rho^{1/2}$) also increases with $\dot{\gamma}$.

Cross-sections in the $(\bar{1}\,\bar{1}\,1)$ plane were cut and etched for defect analysis. The samples loaded quasi-isentorpically showed two distinct deformation features in the region closer to the surface or upper zone (< 6mm) and away from the surface (> 6mm) or lower zone. The upper zone, Figure 2.7 (a) showed little traces of shear with respect to the $(\bar{1}1\bar{1})$ and $(1\bar{1}\,\bar{1})$ and very actively developed twins with respect to the (111) plane. These twinning traces are with respect to the (111) $[\bar{2}11]$ and (111) $[1\bar{2}1]$ systems. The lower zone, Figure 2.7 (b) showed evidence of well-developed twinning with respect to the $(\bar{1}\,\bar{1}\,\bar{1})$ $[1\bar{1}2]$ and $(\bar{1}1\bar{1})[\bar{1}12]$ systems, with no shear with respect to the (111) plane.

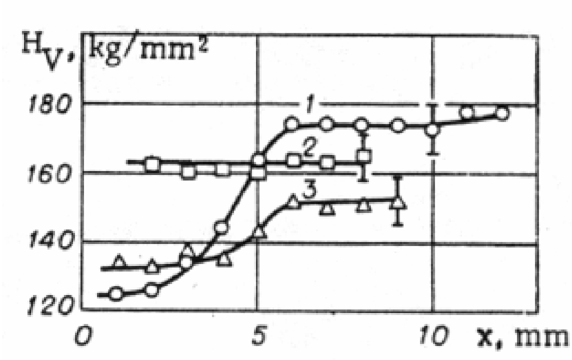

Figure 2.6: Vickers hardness vs. depth along the $(\bar{1}\bar{1}1)$ plane: 1) quasi-isentropic loading, $P_{primary}$=20 kbar and P_{shock}=400 kbar; 2) shock loading, P_{shock}=300 kbar; 3) quasi-isentropic loading, $P_{primary}$=35 kbar, P_{shock}=300 kbar [13].

Adadurov et al. [14, 15] used a layered system of plates to produce multiple small magnitude single shocks acting in sequence to quasi-isentropically compress organic targets, namely monomer acrylic acid amides and polypropylene polymers. Each repeating shock is weak, and the resultant change in entropy is small. Thus, by compressing the material with a series of small shocks rather than one strong shock, the total change in entropy is smaller and, hence, quasi-isentropic. Compression waves with different profiles could be tailored by varying the relative dynamic stiffness of the plates, their thicknesses, and their initial distance from the target. The pressure could be made to increase monotonically with time or gradually increase in a stepwise manner.

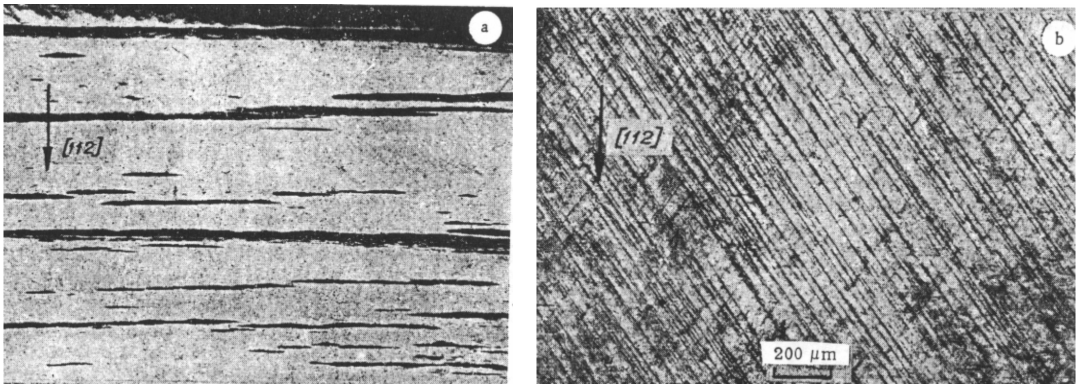

(a) (b)

Figure 2.7: (a) Deformation structure obtained by Mogilevski et al. [13] in $(\bar{1}\,\bar{1}\,1)$ plane at the upper zone of the sample; (b) Deformation structure in $(\bar{1}\,\bar{1}\,1)$ plane at the lower zone of the sample, $P_{primary}$=20 kbar and P_{shock}=400 kbar.

The three multiple single shock experimental setups used by Adadurov [15] are illustrated in Figure 2.8. Method (a) simply involves embedding the sample into a stiffer metallic enclosure or a "bulb" and directly impacting it with a projectile. Multiple shock waves are generated due to the reflection of the main shock wave from the denser metallic walls of the bulb. The sample was typically cooled to 4.2 K, and this condition was well maintained at the end of the experiment due to the rapid heat transfer from the experimental region towards the walls of the bulb. The bulb was sometimes cooled again after the experiment to 77 K. Method (b) consists of transmitting a shock wave through a system of screens having different dynamic stiffnesses, usually increasing away from the sample (4-copper, 5-perspex). Method (c) involves compressing the target by successive impacts from an assembly of striker plates made from high dynamic stiffness materials (1-perspex, 2-aluminum, 3-copper) moving towards the target at different times. Loading by this method produces complicated compression processes (e.g. spallation) due to interactions between the striker plates after they reflect from the target.

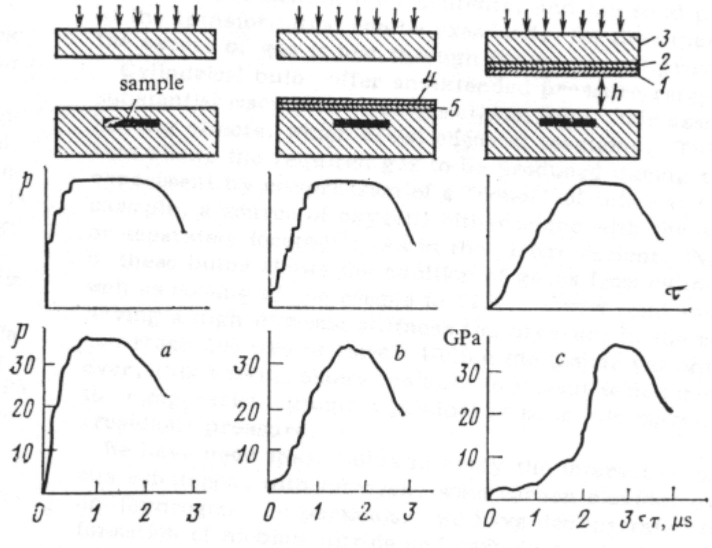

Figure 2.8: (a) Multiple Shock Compression; (b) Shock Compression through a system of plates; (c) Shock Compression by successive impacts from striker plates [15].

The first single shock in early layered systems posed a problem. Its amplitude was usually relatively large (a considerable fraction of the maximum pressure) compared to the ones that followed and significantly contributed to the final temperature rise [15]. In an earlier study by Adadurov et al. [14], to reduce the magnitude of the primary shock, a 10 mm brass projectile was launched onto a system of plates consisting of Plexiglas-steel-Plexiglas-steel placed in front of the sample. The thicknesses of the plates, essential in determining the loading path, were 3, 1, 2 and 1.5 mm, respectively. The primary shock was significantly decreased when the plate thicknesses were successively decreased towards the direction of the target. Figure 2.9 shows how the buffer layer significantly reduced the amplitude of the primary shock while still reaching the same maximum pressure of 500 kbar in the target.

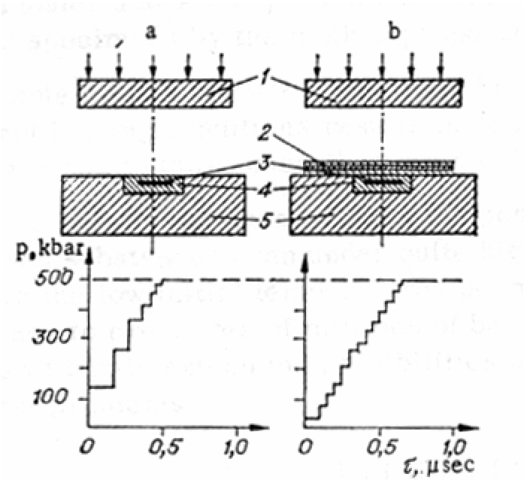

Figure 2.9: Comparison of pressure profiles with and without plate system [14].

Chhabildas and Barker [17] performed quasi-isentropic compression experiments on tungsten using both a powder gun and a two-stage light gas-gun setup to attain pressures up to 78 and 250 GPa, respectively. Density graded and layered materials were both used to produce the quasi-isentropic loading conditions. The density graded material or “pillow” was fabricated using powder techniques giving rise to a smooth and finite loading rate, and the layered impactor consisted of PMMA/aluminum/copper giving rise to a series of small multiple shocks. The PMMA layer was used as a buffer to further reduce the amplitude of the repeat shocks. A VISAR setup similar to that in [12] was used to measure particle velocities and obtain the stress-strain loading path in these experiments.

The constitutive response, Figure 2.10, from the powder gun experiments up to 78 GPa reveal an initial shock path up to 12 GPa followed by an isentropic loading path up to 78 GPa, with a corresponding strain rate of 10^5 s^{-1}. Interestingly, the shock Hugoniot states [18, 19] lie below the experimentally determined isentrope, suggesting that the shear strength of tungsten is dependent on the loading rate. Its strength is, thus, higher for the lower strain rates experienced during quasi-isentropic compression. The results of previous studies in both quasi-isentropic and Hugoniot states were in good agreement with their results [18, 19].

The quasi-isentrope from the initial shocked state of 47 GPa to 170 GPa from pillow experiments is represented by the solid line in Figure 2.10. The ICE stress-strain curve from an initial shocked state of 67 GPa up to 250 GPa obtained from the layered quasi-ICE drive is indicated by the dashed line. Both sets of data are in good agreement where they overlap. The loading rates in these higher pressure experiments were on the order of 10^6 s^{-1}, 3-4 orders of magnitude lower than shock experiments. The data shows that the quasi-isentrope lies above the Hugoniot up to 140 GPa, where it crosses over and lies below it. The authors suggest that the strength of tungsten increases more rapidly with pressure under quasi-isentropic loading than in shock loading. Bat'kov et al. [20-22] have also confirmed this behavior in copper and aluminum.

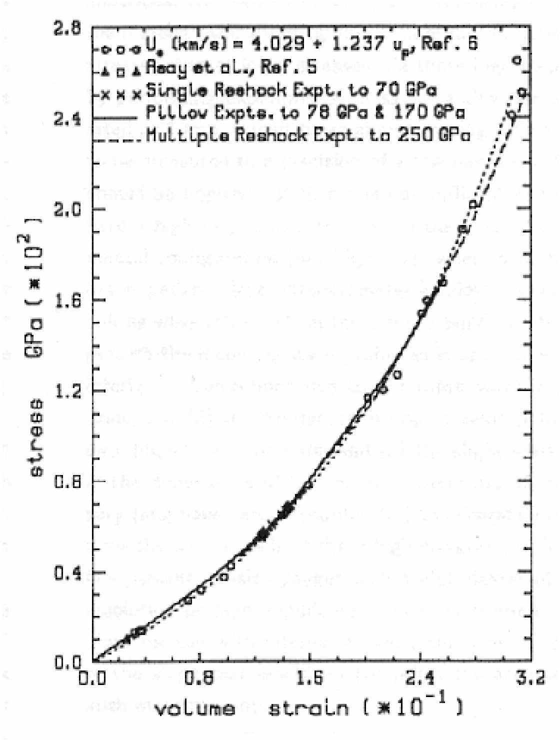

Figure 2.10: Quasi-isentropic stress-strain loading path for tungsten compared with Hugoniot measurements [17].

Recent work by Rosenberg et al. [23] utilizes the "ring-up" method, where the stress rises in steps, to measure the shear strength of copper, iron and mild steel. The experimental set-up involved a single-stage gas-gun where a lower impedance plate was placed on the impact face of the targets to force the ring-up of the stress pulse. The longitudinal and lateral stresses were monitored using strain gauges, and the shear strength was evaluated using equation the following equation:

$$2\tau = \sigma_x - \sigma_y \qquad (2.6)$$

Figure 2.11 shows the results of the lateral and longitudinal stresses of a copper sample during the “ring-up” process and the measured shear strengths of all three materials. The data is also compared to that of shock experiments conducted by the authors (open symbols). The plot suggests that the shock shear strength remains constant (or even drops in the case of Fe) for the pure metals and increases in mild steel. The quasi-isentropic data (filled in symbols), on the other hand, suggest that the shear strengths of Fe and steel increase at a faster rate than the steel in the single shock, and the strength of copper remains constant. A microstructural study by Gray et al. [24] on copper subjected to “pillow-ramp”, step, and prompt shock loading revealed that the post-shock yield strength increased with decreased loading rate. This was attributed to the increased amount of defect storage in the material since lower temperatures during quasi-isentropic conditions prevent annealing effects from taking place. It should be noted that this is in contrast with the results by Mogilevskii et al. [13].

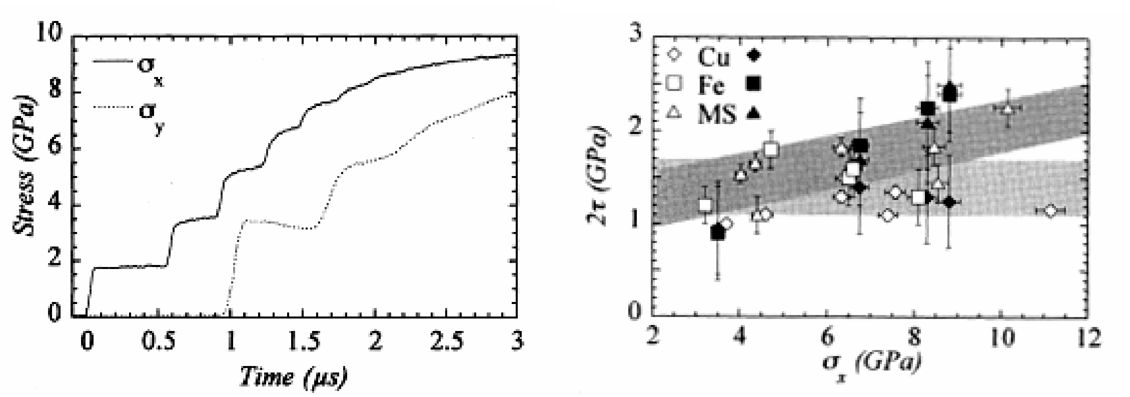

(a) (b)

Figure 2.11: (a) Longitudinal and lateral stresses in copper; (b) Shear strength vs. longitudinal stress for Cu, Fe and mild steel [23].

2.1.2 Laser quasi-isentropic compression

An advancement in the study of material behavior under extreme conditions (*dε/dt* $>>10^5$ s^{-1} and P>> 10^{10} GPa) has recently taken place due to breakthroughs in high-powered laser technologies. Shockless laser drives have been developed at the Lawrence Livermore National Laboratory (NOVA) and the University of Rochester, New York (OMEGA) that generate a gently rising pressure pulse that keeps the temperature of samples investigated well below their melting temperature. The laser-sample interaction allows diagnostic tools to determine solid-state strength, peak pressures and strain-rates applied. A recovery tube filled with aerogel usually captures the samples allowing post shock deformation analysis to be carried out

A description of the OMEGA shockless drive is given by Remington et al. [25]. The drive consists of a low-Z, low-density reservoir (typically carbon foam or plastic) having a thickness of 0.2 to 0.4 mm that is placed in front of a sample (Al, 10-30 μm) and separated by a vacuum gap that is 0.2-0.4 mm wide. Figure 2.12 (a) provides a schematic of the setup. A square pulse with energy of 0.5 to 2.0 KJ and duration of 4-11 ns is used to drive a shock through the low-Z reservoir. Once the shock reaches the back side of the reservoir (i.e. the side opposite from the Al sample), the reservoir unloads into the vacuum as a gas of “ejecta” until the reservoir material is exhausted and gently loads onto the sample. The pressure applied to the sample, which increases smoothly and monotonically in time, is given by the following equation:

$$P_{ram} = \rho_{ejecta} v^2{}_{ejecta} \tag{2.7}$$

The pressure wave is measured with a line-velocity interferometer incident on the back side of the 10-30 μm flat Al sample. There are no traces of shock discontinuities observable in the free surface profile, $U_{FS}(t)$, meaning that the rising pressure pulse is shockless, Figure 2.12 (b). The applied pressure at the front face of the Al sample can be determined by back integrating the free-surface velocity profile using standard hydrodynamic equations and the known EOS for Al. Clearly, the peak pressure in the sample is directly proportional to the shock pressure in the reservoir. Based on numerical simulations, it is expressed as follows:

$$P_{sample} \; \alpha \; P_{res} \frac{\omega_L^{0.5} I_L^{0.76}}{t_L^{0.13}} \tag{2.8}$$

where ω_L is the laser frequency, I_L is the intensity, and t_L is the laser pulse length. The pressure in the sample is expressed in terms of laser energy by noting that $I_L \alpha \frac{E_L}{\phi_L^2 t_L}$,

where $\phi_L \; \alpha \; L_{res} \; \alpha \; V_{shk} \; t_L \; \alpha \left(\frac{P_{res}}{\rho_o} \right) t_L$ for an optimized system and ϕ_L, L_{res}, V_{shk} and ρ_o are laser spot size, reservoir thickness, shock velocity, and initial density in the reservoir, respectively. Substituting these relations into Equation (2.8) results in the following:

$$P_{sample} \; \alpha \; \frac{(\rho_o E_L)^{0.43}}{t_L^{1.37}} \left(\frac{\omega_L}{3} \right)^{0.28} \tag{2.9}$$

The above expression reveals that increasing the total laser energy or decreasing the pulse length would result in an increase in peak pressure in the reservoir. The disadvantage of decreasing the pulse length, however, is that the pressure pulse would steepen more rapidly into a shock wave at higher pressures, thus, melting or vaporizing the target and increasing the strain rates. The strain rate in the sample depends on three factors: (1) the sound speed in the reservoir at shock break-out which determines how fast the reservoir unloads; (2) the thickness of the vacuum gap, which determines how spread out or diffuse the unloading ejecta becomes; (3) the compressibility of the sample, which determines its strain in compression. The applied strain rate is expressed given by the following relation:

$$\dot{\varepsilon} \;\alpha\; \frac{1}{nL}\left(\frac{P_{shk}}{\rho_{res}}\right)^{1/2} \tag{2.10}$$

where n represents compressibility of the sample and ρ_{res}. By modifying laser intensity, reservoir density, and vacuum gap size of the setup, the peak pressures and strain rates can be made to vary from 10 to 200 GPa and $5\text{x}10^6$ to $1 \text{ x } 10^8 \text{ s}^{-1}$.

The shockless OMEGA drive was used in a recent study to analyze the response of aluminum (6061-T6) [26]. Samples were subjected to pressures of 18 and 40 GPa and strain rates of 10^7 s^{-1} and $5\text{x}10^7 \text{ s}^{-1}$, respectively. The experiment was also simulated using an arbitrary Langrangian-Eulerian hydrodynamics code, CALE [27]. The code included a laser deposition model that determined the laser-reservoir interactions and a realistic equation of state that determined the crater formation process. The model also assumed that the samples were isotropic and followed a Steinberg-Guinan constitutive response [28]. The simulations provided detailed information on the loading pulse as it traveled though the sample and eventually steepened into a shock. At 150 μm into the 18 GPa sample, the loading transitions into a shock as is indicated by the temperature rise (from ~380K to 400K). Figure 2.13 (a) shows the temperature rise in the 40 GPa sample, and the nearly isentropic to shock loading transition that occurs at about 50μm into the sample, where the temperature rises from 500K to 900K.

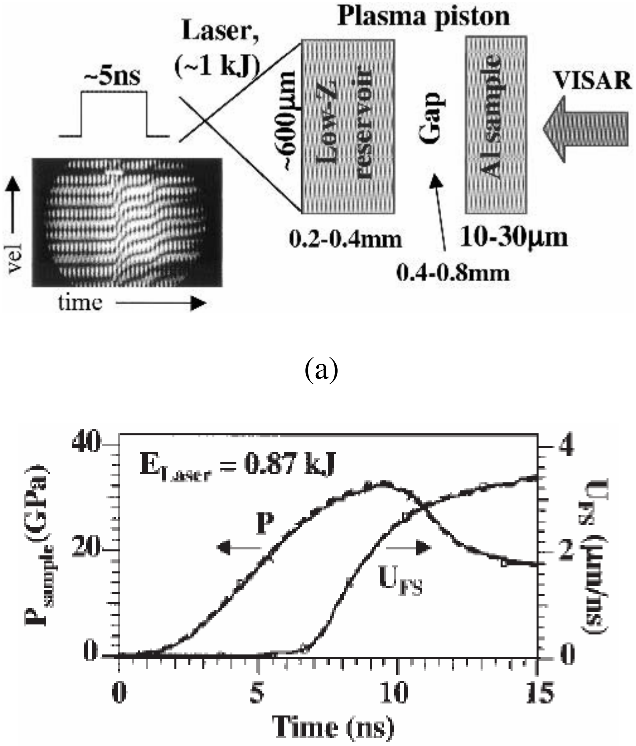

(a)

(b)

Figure 2.12: (a) Laser ICE setup in the OMEGA facility; (b) Free surface velocity of the back surface and applied pressure on the front surface of the Al sample [26].

The recovered samples analyzed showed interesting features, namely the cratered region facing the drive and crack-like features that followed the grain boundaries, Figure 2.13 (b). The crater depth is ~300μm, in agreement with depths calculated by CALE. It was found that the crater depth varies with peak pressure as follows:

$$h_{crater} = (9\mu m / GPa) P_{max} (GPa) \qquad (2.11)$$

Interestingly, no shear bands within the specimen or melt features due to the plasma interaction on the surface were evident. The authors note that since the thickness of the layer where shockless loading occurs is relatively small, the use of the Steinberg-Guinan constitutive response (which is based on shock-loaded tests) is appropriate and captures the basic deformation behavior of their experiment.

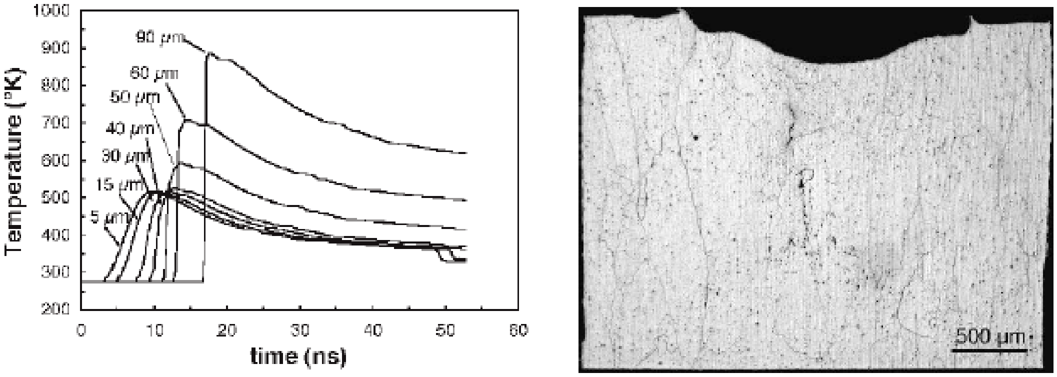

(a) (b)

Figure 2.13: (a) Temperature vs. time profiles indicating the nearly isentropic to shock loading transition in the 40 GPa sample [26].

2.1.3 Magnetic quasi-isentropic compression

High intensity magnetic fields obtained by magnetic flux compression have successfully been used to quasi-isentropically load targets. Early work on magnetic loading incorporated explosives that increased the magnetic field intensity experienced by the samples investigated [29]. The rate of change of pressure was low enough to prevent shocks from developing and maintain a quasi-isentropic compression state at elevated pressures. The EOS of materials under isentropic conditions was better described by this method, and the temperature rise at a given pressure was much lower than that reached on the shock Hugoniot at comparable conditions.

Figure 2.14 (a) is an illustration of the magnetically driven compression apparatus that incorporates explosives to load samples [29]. An initial magnetic field is produced by a pair of coils and a capacitor bank. The field diffuses through a stainless-steel liner that is surrounded by an explosive. When the field reaches its peak value, the explosive is detonated causing the liner to cylindrically implode. The implosion compresses the magnetic flux and increases the magnetic field intensity. Due to the interaction of the magnetic field with eddy currents generated in the sample tube and liner an outward pressure is exerted on the liner and an inward pressure is applied on the sample tube.

Figure 2.14 (b) shows the magnetic field strength (B) inside the sample tube and between it and the liner, the magnetic flux (Φ) between the sample and tube and the liner, and the pressure (P) on the sample tube, as a function of time. The sample in this case was Lucite, and parameters were calculated using a magnetohdrodynamics (MHD) code [30, 31]. Pulsed x-rays were used to determine the pressure and specific volume relationship of the Lucite sample, and P-V curve lied below Lucite Hugoniot data (i.e. to the left of the Hugoniot curve) indicating that the compression was nearly isentropic.

The Z accelerator in Sandia National Laboratories has been able to successfully produce quasi-isentropic loading conditions in samples by means of only high current densities and magnetic fields [32-34]. The principle used to generate fast pulsed power to drive the samples is illustrated in Figure 2.15 (a). A short circuit is produced between the anode and cathode in the Z accelerator causing a current flow in the inner surface of both components. The interaction between the current density and magnetic field in the insulating gap region produces a pressure that is exerted on the inside surface of the sample. Since magnetic pressure scales with the magnetic field strength, B, as B^2, and $B = \mu_o J$, where J is the current density, the pressure exerted on the sample can be expressed as:

$$P = \left(\frac{I^2 \mu_o}{2W^2} \right) \tag{2.12}$$

where I is the applied current, W is the width of the conductor at the sample location upon which current flows, and μ_o is the magnetic permeability of free space. Equation (2.12) shows that the applied pressure will follow the same trend as the input current profile, and the magnitude of the loading depends on the magnitude of the input current and on the width of the conductor at the sample location.

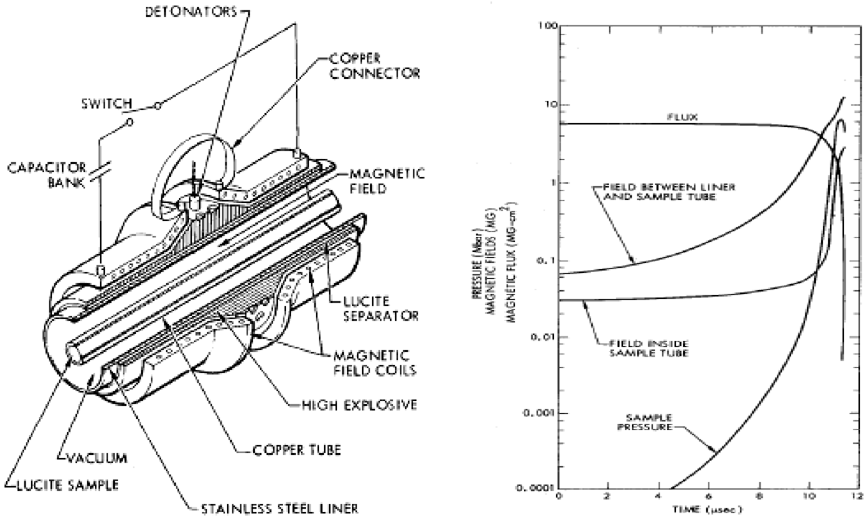

(a) (b)

Figure 2.14: (a) Schematic of magnetic loading apparatus; (b) Pressure, magnetic field, and flux vs. time [29].

The Z accelerator is capable of storing ~12 MJ of electrical energy and creating 22 MA of current [32]. When fired, the machine can produce powers up to 50 TW. The anode and cathode of the Z-accelerator, Figure 2.15 (b), are made of flat panels that maintain a symmetric current density, and consequently symmetric pressure, over the samples during loading. As opposed to other quasi-isentropic compression techniques, experiments on the Z-machine are repeatable, and precise control over loading pressures and the rise times are possible to meet experimental requirements. Unfavorable initial small-magnitude shocks present in many isentropic compression techniques also do not occur on Z. Nevertheless, the loading is not perfectly isentropic due to the presence of irreversible processes such as elastic to plastic transitions, dissipative effects, and possible non-equilibrium phase transitions. As opposed to Hugoniot experiments that define only one point on the P-V curve, one isentropic loading experiment on Z can provide experimental data over a wide P-V range.

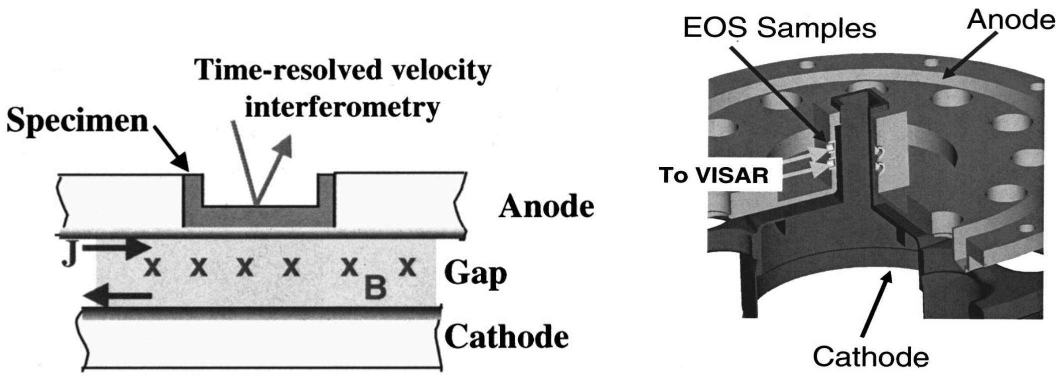

(a) (b)

Figure 2.15: (a) Illustration of the current path and resultant magnetic field created between the anode and cathode of the Z accelerator; (b) Experimental configuration used to gather isentropic data on the Z accelerator [32, 33].

A method utilizing velocity interferometry (VISAR) similar to that in [12], [17] and [35] was used to measure the velocity from the rear surface of two copper samples. The Lagrangian wave speed was calculated by measuring the rise time of the velocity profile at two different depths. Knowing this wave speed and utilizing the differential equations for conservation of mass, momentum, and energy in Lagrangian coordinates (Equations 2.2, 2.3, and 2.4) the path dependent stress and specific volume relationship was calculated from its initial conditions to its final compressed state. Figure 2.16 (a) shows the free surface velocity profile at two depths and the input current profile for one such experiment. As expected, the rise time of the velocity profile decreased as the wave propagated through the 0.5 mm and 0.8 mm thick copper samples, almost developing into a shock in the latter. Calculations at LLNL indicated only a 0.7 % difference in pressure between the two samples suggesting that experiments on Z are repeatable and reliable. The stress-specific volume relationship calculated from the quasi-isentropic loading is shown in Figure 2.16 (b) and compared to Hugoniot experiments. Reisman et al. [34] have also used the Z accelerator to obtain EOS data on tantalum, molybdenum and beryllium. They observed that their ICE measurements deviated very slightly from previous Hugoniot measurements by gas-gun. They concluded that such an observation was expected since the Hugoniot and compression isentrope differ by less than 1% in the pressure regime they considered (up to 40 GPa).

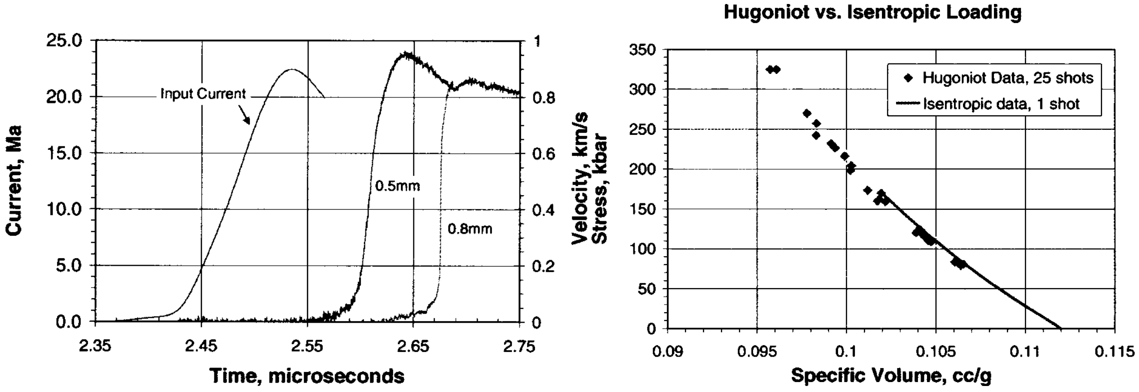

(a) (b)

Figure 2.16: (a) Input current and free surface velocity from the rear surface of two copper samples, 0.5 and 0.8 mm thick; (b) Stress-specific volume relationship of copper under quasi-ICE and Hugoniot states [32].

2.2 Nanocrystalline Materials

Materials having grain sizes of approximately 100 nm or less are typically referred to as nanocrystalline. These materials are characterized by a large volume fraction of grain boundaries which significantly alters their mechanical behavior as compared to their coarse-grained counterparts (grain sizes 10-300 μm) [7, 36, 37]. The strength of these materials is dramatically increased as grain size is reduced into the nanometer regime since the increased density of grain boundaries impedes the movement of defects (i.e. dislocations) making the material more resistant to deformation. There is, however, some controversy as to whether this relationship between the grain size and strength, known as the Hall-Petch relationship, holds beyond a grain size of ~ 20 nm [7, 36, 37]. Various studies on Cu have shown an increase, decrease or plateau in yield strength when the grain size was reduced beyond this limit.

Many efforts worldwide have attempted to study the mechanical properties of nanocrystalline materials at low strain rates below 1 s^{-1}. The review article by Meyers et al. [7] discusses the most significant findings in detail.

2.2.1 Deformation mechanisms at low strain rates (< 1 s^{-1})

Nanocrystalline materials tend to exhibit much reduced ductility, due in part to a low work hardening rate leading to early strain localization and failure. The introduction of processing flaws (i.e. porosity, impurities, etc) is also a key reason behind reduced ductility in early nanocrystalline materials. The deformation mechanisms occurring under conventional strain rates are only now beginning to be quantitatively understood and five different mechanisms are emerging that describe the physical processes during plastic deformation:

2.2.1.1 Breakup of dislocation pile-ups

As the grain size is decreased, the number of dislocations piled up against grain boundaries decreases. This number is a function of the applied stress and of the distance to the source. At a critical grain size, we can no longer use the concept of a pile up to explain the plastic flow. Figure 2.17 (a) shows pile-ups for a grain size in the micrometer regime. The sources are assumed to be in the center of the grain, leading to positive and negative pile ups generated by the activation of a Franck-Read source. As the grain size is reduced to the nanocrystalline regime, the number of dislocations at the pile-up is reduced to one. Thus, the multiplying effect on the stress field is lost. This is shown in Figure 2.17 (b). This effectively nullifies the Hall-Petch $\left(\sigma_y \propto d^{-1/2}\right)$ relationship.

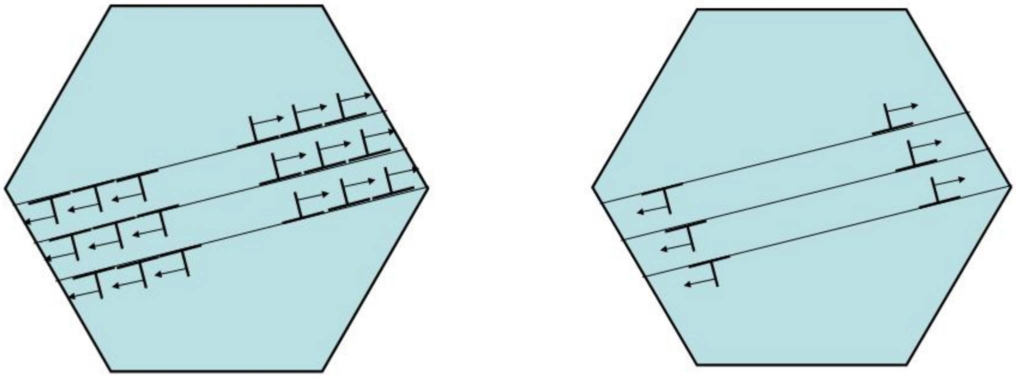
(a) (b)

Figure 2.17: Breakup of dislocation pile-up; (a) micrometer sized grain; (b) nanometer sized grain [7].

2.2.1.2 Core and mantle models

These models are extensions of the Ashby concept of geometrically and statistically stored dislocations as applied to polycrystalline aggregates. Meyers and Ashworth [38] extended this treatment. Although these models have taken several forms, the basic idea, illustrated in Figure 2.18, is that the deformation within a grain is composed of two parts: the core, or grain interior, which is subjected to a more homogeneous state of stress; and the mantle, or grain boundary region, in which several factors contribute to increased resistance to plastic flow and work hardening: grain-boundary sources, change in orientation in the plane of maximum shear, and elastic and plastic incompatibility. This leads to enhanced cross-slip. Thus, the grain can be divided into two regions: core and mantle. Figure 2.18 shows how the relative fractions of these two regions vary with grain size. As the grain size is decreased into the nanocrystalline region, the mantle dominates the plastic flow process. This mechanical deformation process has been recently modeled by Fu, Benson, and Meyers [39, 40].

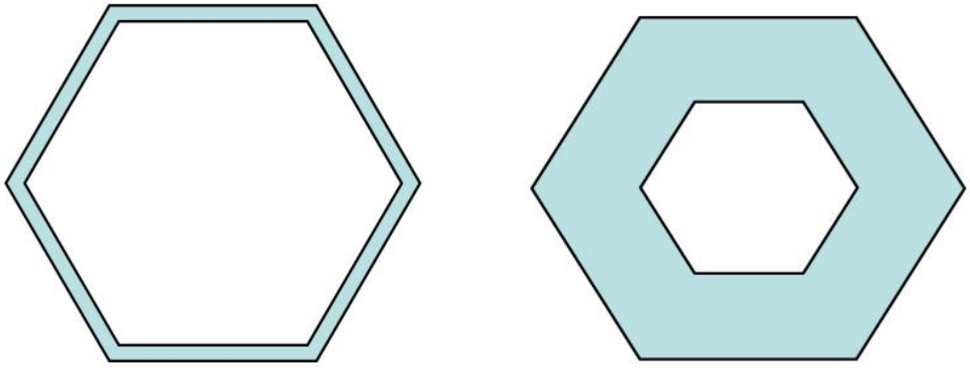

(a) (b)

Figure 2.18: Core and Mantle Model; (a) Micrometer-sized grain; (b) nanometer-sized grain [7].

2.2.1.3 Grain-boundary sliding models

These models use the Coble creep equation, as a basis, which expresses the strain rate as proportional to a d^{-3} term. As d is decreased, the contribution to plastic flow coming from grain-boundary sliding increases. Chokshi et al. [41] were the first to point out this mechanism. However, the simple Coble equation ignores the necessity of plastic flow to accompany sliding in order to accommodate the grains. It was subsequently developed by Conrad [42], among others. Figure 2.19 shows a polycrystalline aggregate in which the top layer has been translated to the right with respect to the bottom layer, creating a shear strain. It is clear that sliding alone cannot accomplish this. Ashby and Verall [43] addressed this problem successfully for superplastic deformation and proposed a neighbor exchange mechanism capable of effecting plastic strain. Fu et al. [39] have shown that the incorporation of the plastic accommodation term into the diffusion leads to grain boundary sliding at strain rates on the order of 10^{-4} s^{-1}, for sizes of 20 nm.

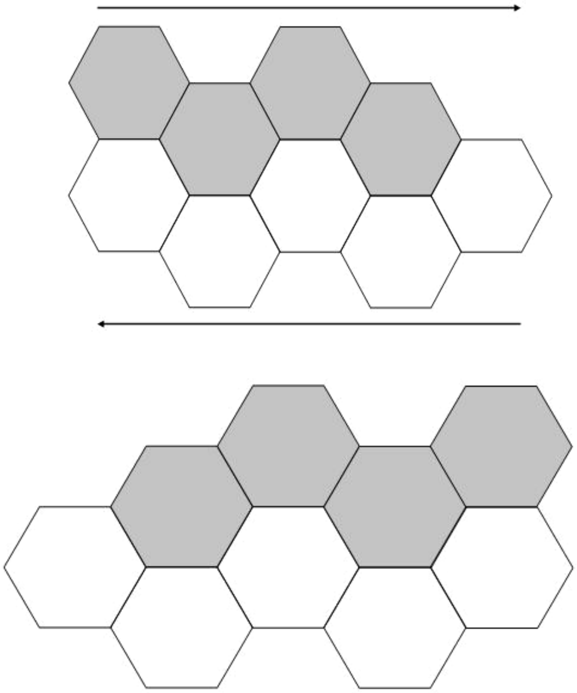

Figure 2.19: Sliding of four grains (upper dark) with respect to bottom grains [7].

2.2.1.4 Grain-boundary source-sink models

Prompted by molecular dynamics simulations carried out primarily by van Swygenhoven and coworkers (e. g., Weertman et al. [44]) and by TEM observations showing a low dislocation density after appreciable plastic deformation (e.g., Kumar et al. [37]), a combined grain-boundary source-sink model is evolving. When the grain size is reduced to the nanocrystalline regime, the mean free path of dislocations generated at grain-boundary sources is severely limited. Rather than cross slipping and the associated generating work hardening, these dislocations can run freely until they meet the adjacent grain boundary, which acts as a sink. Thus, the dislocation density remains low throughout the plastic deformation process, and work hardening is not significant. Figure 2.20 shows this model in a schematic fashion.

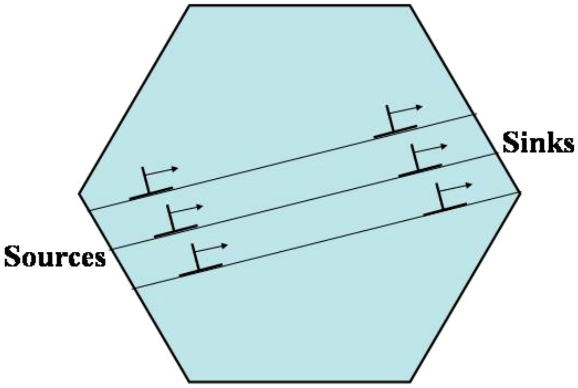

Figure 2.20: Grain-boundary source-sink model [7].

The extensive review carried out by Meyers et al. [7] recently concludes that the dislocation emission and annihilation at grain boundaries is the prominent mechanism in the nanocrystalline regime. The generation of a dislocation from a grain boundary and its movement through the grain (segment BC in Figure 2.21 (a)) entails the production of segments AB and CD that are left behind. The analysis carried out by Zhu et al. [45] leads to the calculation of stacking-fault separation, which is considerably larger than in the conventional grain size regime. Figure 2.21 (b) shows, in a schematic fashion, how dislocations emitted on parallel planes can deform the grain and produce plastic strain.

2.2.1.5 Grain coalescence model

Recent observations by Shan et al. [46] and Ma et al. [47] point out an interesting possibility: that nanometer-sized grains rotate during plastic deformation and coalesce along directions of shear, creating larger paths for dislocation movement. Figure 2.22 shows this in schematic fashion. The orientations of the slip systems with highest Schmid factors are represented by a short line in each grain. As plastic deformation takes place, two neighboring grains might rotate in a fashion that brings their orientation closer together. This is shown by the arrows in Figure 2.22 (a). In Figure 2.22 (b) the orientation of the three grains is essentially identical, leading to possible long paths for slip, shown in Figure 2.22 (c). This mechanism actually can lead to softening and localization and is consistent with the limited ductility often exhibited by nanocrystalline metals.

2.2.2 Deformation mechanisms at intermediate strain rates (up to ~10^3 s^{-1})

There are a recent handful of studies of nc materials at “high” strain rates (up to 10^3/s). Despite all these efforts, there are still many open questions regarding the mechanisms of plastic deformation in nanocrystals. In addition, there are no experiments on nanocrystals at ultra high strain rates (above 10^6/s). Recent results demonstrate a unique advantage of laser-produced shock compression over flyer-plate produced shocks: the rapid post-shock cooling is responsible for the retention (for subsequent characterization) of the shock substructure at much higher pressures [48].

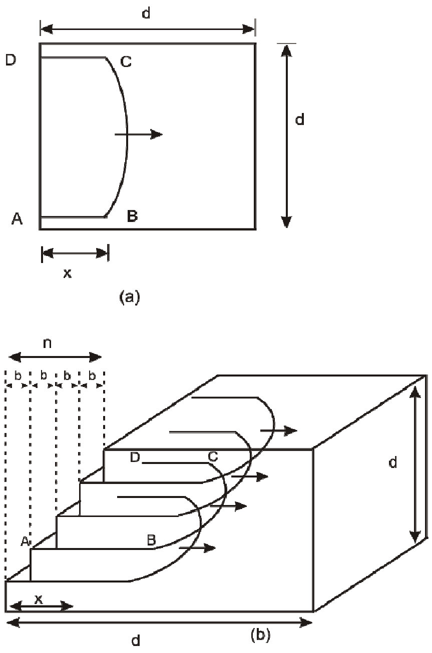

Figure 2.21:: (a) Dislocation traveling through nanograin and leaving behind two segments AB and CD; (b) Dislocations traveling through nanograin in parallel planes and creating a shear strain γ (from Meyers et al. [7]).

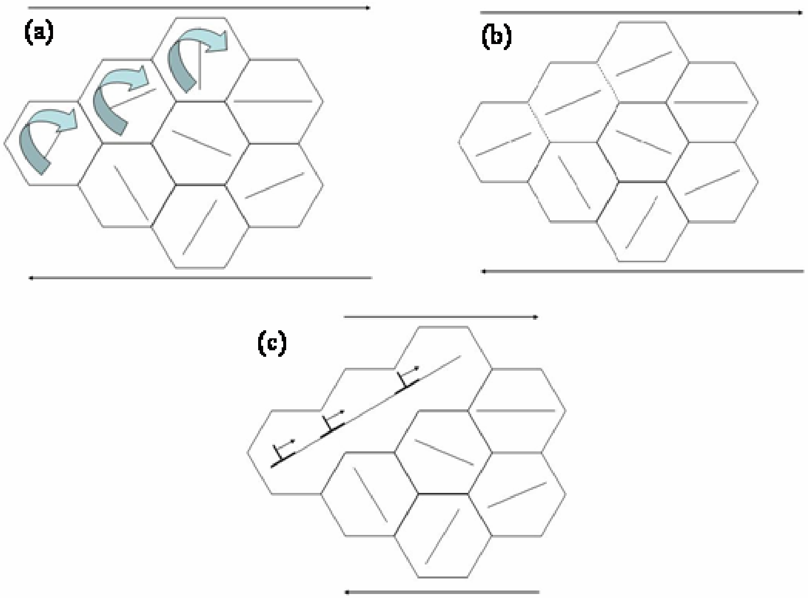

Figure 2.22: Grain coalescence model.

Dalla Torre et al. [49] studied the mechanical response of nanocrystalline electrodeposited nickel (grain size ~20 nm) subjected to strain rates between 10^{-5} s^{-1} and 10^{3} s^{-1}. The increase in ultimate tensile stress (UTS) was up to 75% (2.5 GPa) at the high strain rates, Figure 2.23 (a). The strain hardening rate also increased with increasing strain rate. A change in fracture mode was observed in the nc samples as compared to the lower strain-rate experiments, where the fracture surfaces showed minor or no signs of plasticity and little or no necking.. The angle of the fracture surface with respect to the tensile direction changed from 90º to ~ 65º - 55º, corresponding to the plane of maximum shear, and a smaller neck area formed. Shear bands with a width of 200-300 μm, also formed along the fracture surface, Figure 2.23 (b). Larger grains close in the vicinity of the shear band region were revealed by TEM and attributed to localized heating caused by the high-speed deformation process. Dislocations were not detected inside the larger grains.

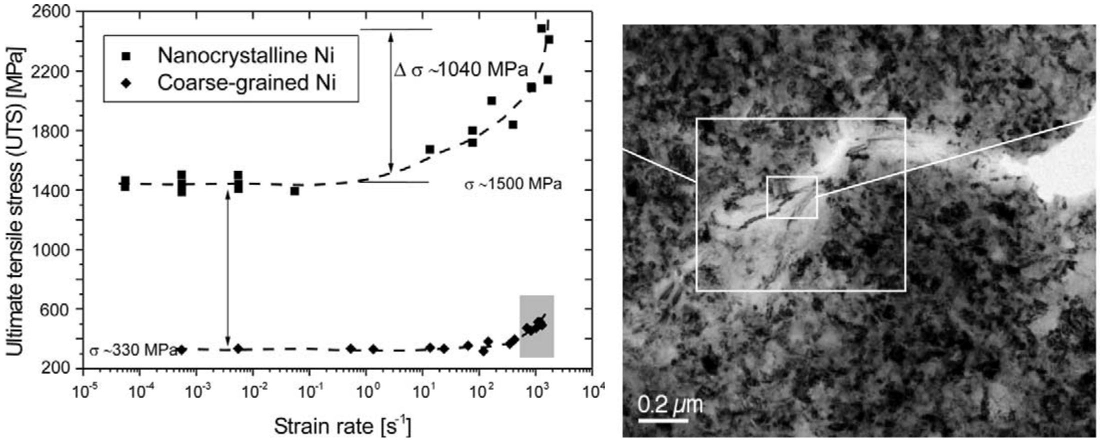

(a) (b)

Figure 2.23: (a) UTS vs. strain rate for nc and coarse-grained Ni; (b) Shear band formation at strain rate of $1.7\text{x}10^{3}$ s^{-1} [49].

Jia et al. [50] conducted dynamic compression tests on electrodeposited nanocrystalline copper up to strain rates of ~10^4 s^{-1}. The grain size of their samples was ~ 28 nm. It should be noted that their samples contained small angle grain boundaries, and the authors did not consider possible effects of grain size distribution, as deformation tends to concentrate in larger grains, hence, decreasing the strength but increasing ductility. As a result, their samples were not as strong as other nc samples prepared by severe plastic deformation (SPD), consolidation, inert-gas consolidation, and compaction (all processes that tend to produce high angled grain boundaries). Figure 2.24 illustrates the dynamic stress-strain behavior of nc copper at strain rate of $1.4x10^4$ s^{-1} as compared to its coarse grained counter part (30 μm). A significant enhancement in yield stress is observed in the nc sample, and strain hardening is also apparent at all strain rates investigated. The influence of strain rate on strain hardening was more apparent than that on the yield stress.

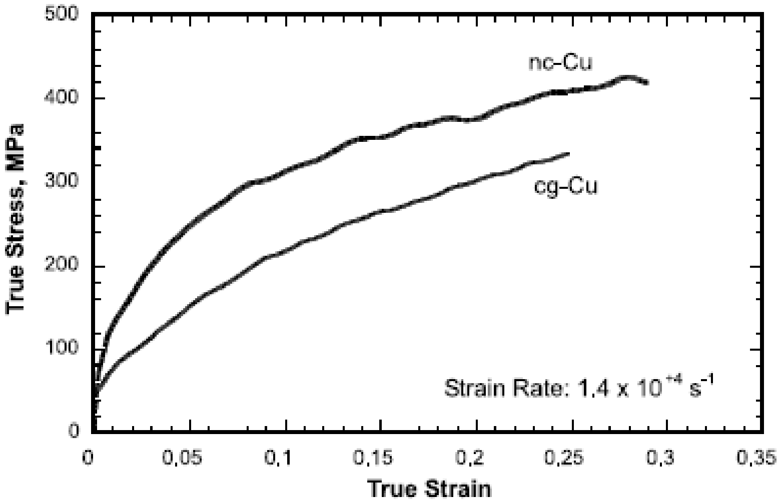

Figure 2.24: Compressive stress-strain curves: nc-Cu and cg-Cu at a strain rate of $1.4x10^4s^{-1}$ [50].

The dependence of flow stress on strain rate appeared to be weak for both coarse-grained and nanocrystalline copper at strain rates below ~ 4x10^3 s^{-1}. At strain rates above 4x10^3 s^{-1}, the flow stress increased rapidly in both cases. The slope of the rate sensitivity curve was, however, slightly higher for the coarse-grained copper, suggesting that there is a microstructural effect on the strain rate dependence at such high strain rates. The conventional rate sensitivity plot, Figure 2.25, of flow stress versus the logarithm of strain rate summarizes the aforementioned observations.

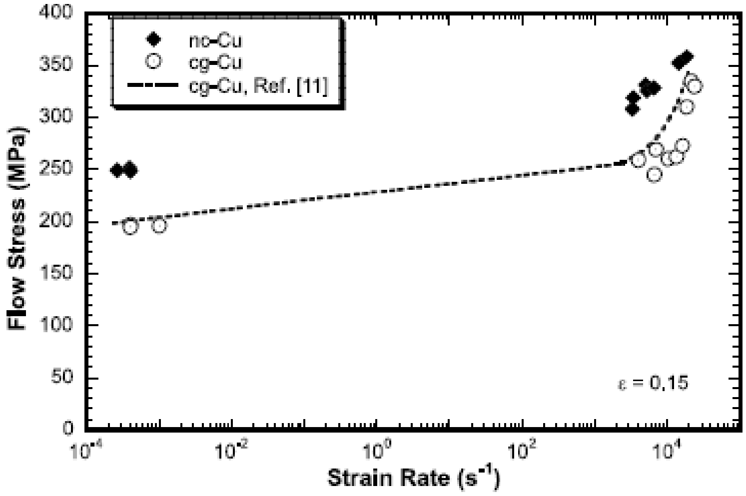

Figure 2.25: Flow stress dependence on strain rate of nc and cg Cu [50].

Another significant high-strain rate study was done on nanocrystalline iron by Jia et al [51]. A two-step compaction and consolidation process was used to produce samples with grain sizes ranging between 20 μm and 80 nm. A drastic effect of grain size on flow stress was revealed (Figure 2.26 (a)), as the flow stress increased from 200 MPa at a grain size of 20 μm to 2.6 GPa at a grain size of 80 nm, a 13-fold increase. Strain hardening was evident for all grain sizes investigated, and very little influence of strain rate on the strain hardening was observed. An interesting transition from strain hardening to strain softening was observed between 1 μm and 300 nm. The specimens with the smallest grain sizes also failed much earlier in the experiments.

The influence of the strain rate on the flow stress is plotted in Figure 2.26 (b). As the grain size decreases into the nanometer regime, the strain rate sensitivity is reduced. There is a two-fold increase in flow stress in the 20 μm sample as the strain rate increases from 10^{-4} s^{-1} to 10^{4} s^{-1}, where as the flow stress increases by only 100 MPa in the 80 nm sample within that range. The smaller grain size samples also show less strain-rate sensitivity at the higher strain rates as compared to the coarse grained samples. The mode of deformation of the samples dramatically changed as grain size was decreased. In the 20 μm to 980 nm range, the deformation features were uniform at all strain rates and no shear bands developed. For grain sizes below 300 nm, shear bands were found to develop right at the onset of plastic deformation, providing an explanation to the change in strain hardening behavior at that grain size. Both quasi-static and high strain-rate compression experiments revealed shear bands. Figure 2.27 (a) is an optical micrograph of the uniform deformation features in a 980 nm sample deformed at a low strain rate, whereas Figure 2.27 (b) is a micrograph of the non-uniform shear banding phenomenon in a 268 nm sample deformed at high strain rates. TEM revealed elongated grains within the shear band and equiaxed ones outside the bands.

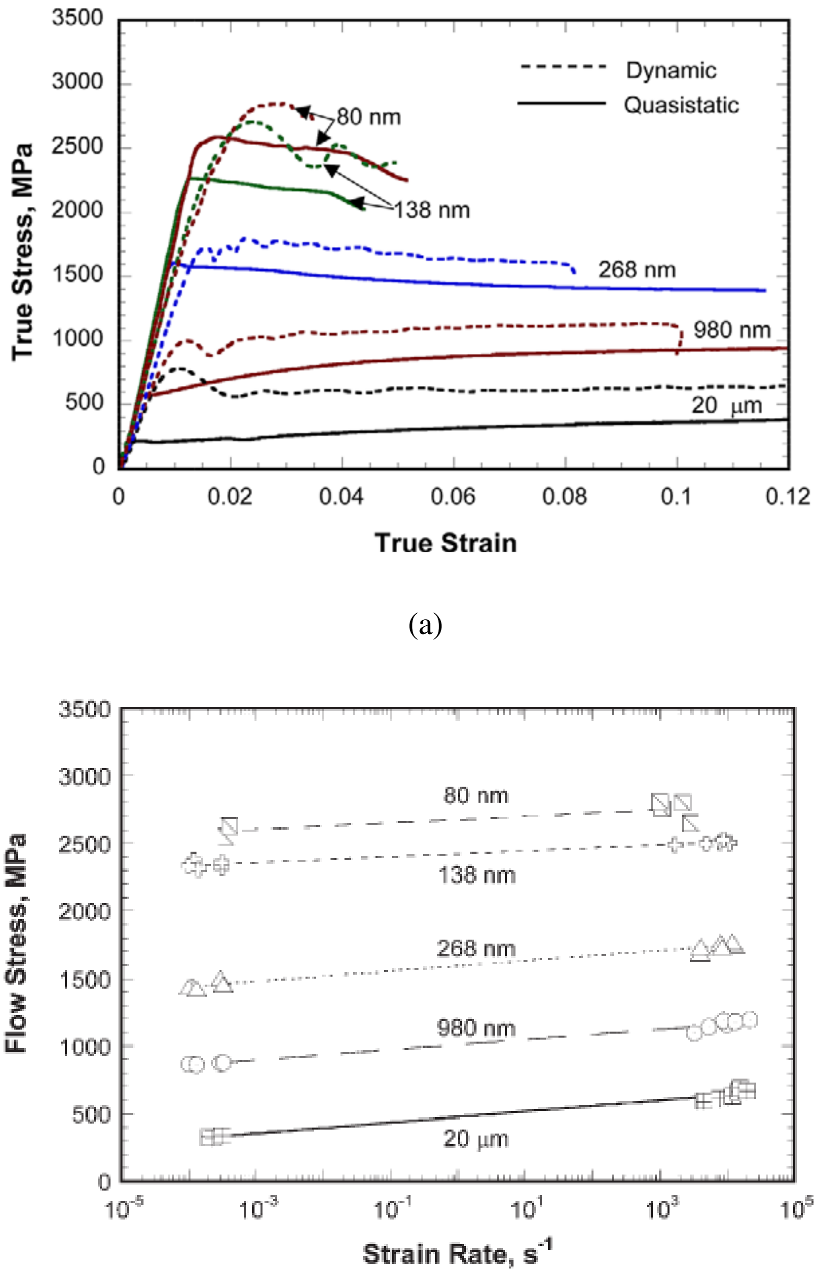

(a)

(b)

Figure 2.26: (a) Stress-strain curves of cg and nc Cu at quasi-static and dynamic strain rates; (b) Flow stress vs. strain rate of different grain size samples [51].

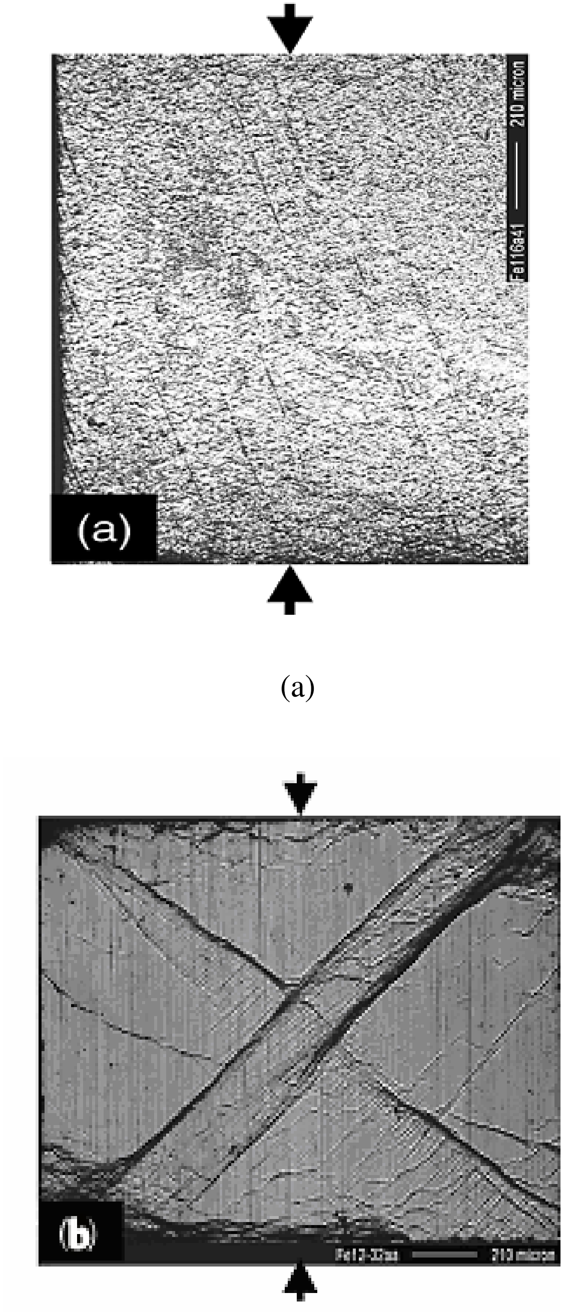

(a)

(b)

Figure 2.27: (a) Uniform deformation features at low strain rate in 980 nm Fe; (b) Non-uniform deformation/shear bands at high strain rates in 268 nm Fe [51].

2.3 Dynamic Failure and Spall

The dynamic failure and spall of metals induced by laser irradiation is a concern of great significance to the successful operation of the National Ignition Facility (NIF). Protection from spalling and fragmentation is necessary to preserve the functionality of the laser optics systems and diagnostic tools of the main target chamber. However, studies on the extent of damage to metal targets and their surrounding caused by laser impingement of the surface are scarce. Spall is the dynamic fracture taking place inside a solid body as a result of tensile stresses that develop due to the interaction of waves propagating in the body. Figure 2.28 (a) is an illustration showing this phenomenon during plate impact. Compressive waves traveling from the energy deposition surface of a body intersect those reflecting from the rear surface, causing internal ruptures, or spallation, if the tensile stresses are sufficiently high. Damage accumulation takes place in four stages: (a) nucleation of voids or cracks at existing damage sites, (b) growth of individual voids or cracks, (c) coalescence of voids or cracks, and (d) fragmentation [52-54]. The growth and coalescence of cracks during dynamic failure is illustrated in Figure 2.28 (b) at different times. Much of the research on dynamic fracture has been carried out under planar flyer-plate impact [55-59] and high explosive detonation [60-64]. These typical methods of generating shock waves produce pressures below 100 GPa and pulse durations with a minimum of 50 ns.

As mentioned previously, only recently have laser-driven shock experiments begun to gain momentum [25, 26, 65-76]. The advantages of using high-intensity lasers

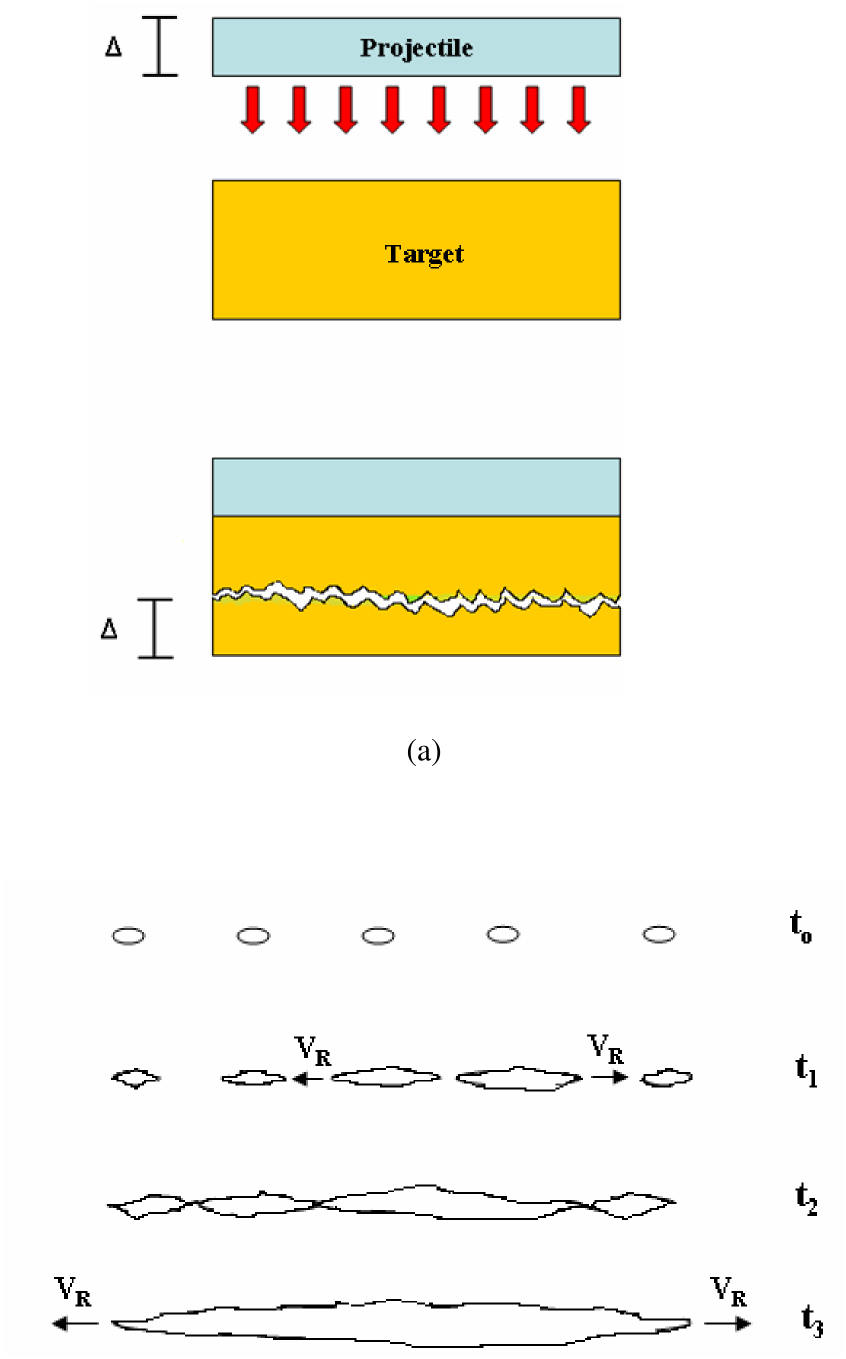

(a)

(b)

Figure 2.28: (a) Dynamic failure due to plate impact; (b) Crack growth and coalescence during dynamic failure (Adapted from Meyers and Aimone [52].

to produce shocks in metals lie in the fact that extremely high pressures (in the TPa range) and strain rates (~ 10^9 s^{-1}) can be achieved with pulse durations of only a few nanoseconds. More accurate microstructural characterization is also possible due to the self- quenching mechanism associated with laser shock (discussed in detail by Meyers et al. [76] and Cao et al. [77]). Interestingly, almost no research has been carried out on the dynamic behavior of materials shocked above their melting pressures. A notable exception is the study by Rességuier et al. [78] on the liquid spall in laser shock-loaded tin. Lubarda et al. [79] looked at the void growth in copper induced by laser compression. Little is known about the process of material ejection from the spalled surface of laser-shocked samples, and the fragmentation, spreading of debris, and extent of damage to surrounding objects are all issues that still need to be addressed. This obviates the need for the investigation whose results are reported in Chapter 5: the fragmentation and spall of vanadium induced by laser irradiation.

CHAPTER 3

QUASI-ISENTROPIC COMPRESSION OF MONOCRYSTALLINE COPPER

The NIF target capsule wall is doped with copper to enhance energy absorption, and being able to simulate its implosion under NIF's laser beams requires the understanding of the response of its constituents: beryllium and copper. Our work focuses on copper since it is being incorporated into current designs. Copper is also a preferred FCC model material to work on. Figure 3.1 is an SEM image of the final Cu-doped Be capsule wall. The image shows various layers with the brighter regions corresponding to higher concentrations of Cu and the darkest regions corresponding to pure Be Layers. The bright lines at ~9 μm correspond to increased oxidation signifying the end of a sputtering run. In this section, results on the microstructural response of copper quasi-isentropically compressed by gas-gun and laser techniques will be introduced.

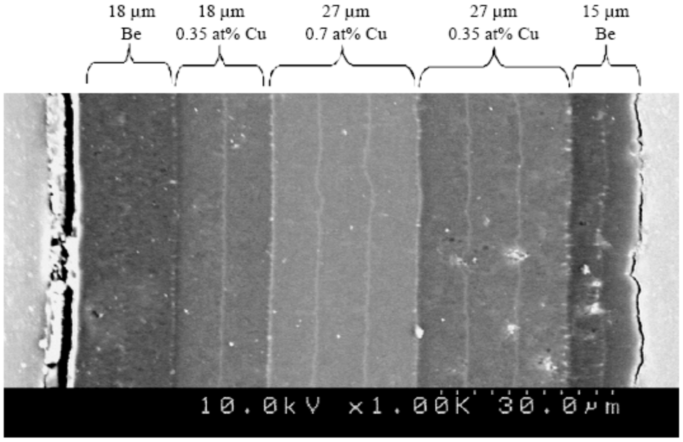

Figure 3.1: Target capsule wall consisting of Be doped with various concentrations of Cu [80].

The response of copper to very high strain-rate deformation is reasonably well understood. In particular, shock experiments on copper have been carried out for over 50 years. Techniques using explosives and flyer plates were first employed to create the compressive pulse in the material, and pressures attained were on the order of tens of GPa with accompanying strain rates on the order of 10^4/s with durations on the order of microseconds or fractions thereof. Early experiments by Johari and Thomas [81] investigated defect substructures generated in explosively deformed copper and copper-aluminum alloys. More recently, laser pulses have been used to study shock compression in copper. The rapid heating and thermal expansion of the surface layers causes a shock to propagate through the material. Shock pressures higher than planar impact set-ups can be achieved (up to 75,000 GPa), and the strain rates attained are as high as 10^9-10^{11} s^{-1}. A basic difference is that the duration of the pulse in laser-shock is on the order of nanoseconds rather than microseconds. In this work, however, quasi-isentropic compression experiments via gas-gun and laser are carried out on [001] copper, and the recovered deformation substructure is analyzed.

3.1 Experimental Techniques

3.1.1 Gas-gun ICE setup

The two-stage gas gun and experimental set up for this work are located at Lawrence Livermore National Labs (LLNL). Functionally-graded material (FGM) impactors designed with increasing density profile (or shock impedance), as depicted in Figure 3.2, were used to produce the smoothly rising pressure profiles 82. Three different FGMs were used, each providing a certain density range. The first FGMs providing densities between 1.2 g/cc to 8 g/cc consisted of aluminum and tungsten powders in a resin matrix. The second FGMs allowing for lower densities between 0.1 g/cc to 2.7 g/cc incorporated a foam matrix, and the third allowing for a higher density range between 2.7 g/cc and 15 g/cc consisted of sintered aluminum and tungsten powders. The density is varied by simply adding these pre-mixed layers, each having a thickness of 200 ±20 μm. The FGMs are usually made of 10-25 layers, allowing for the tailoring of specific thermodynamic paths during experimentation [82].

The copper samples were cylindrical, and their height and diameter were both 5 mm. The samples were press-fitted into a copper plate and lapped as one piece to ensure both sides were flat. The copper plate held seven samples that were simultaneously impacted during each experiment. A backing plate was placed on the back surface to transfer the shock and prevent reverberation. An illustration of the copper plate is presented in Figure 3.3.

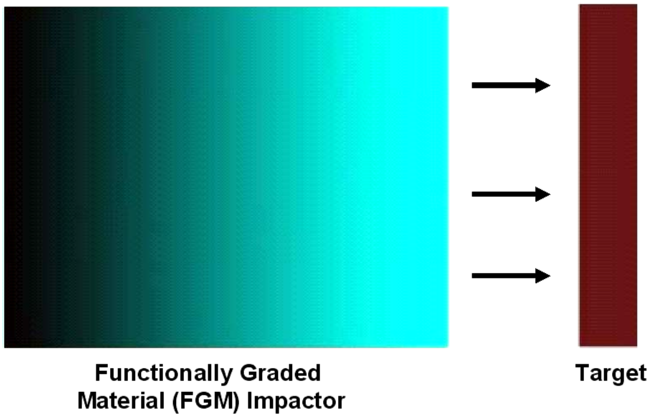

Figure 3.2: Illustration of FGM impactor hitting target (darkness proportional to density).

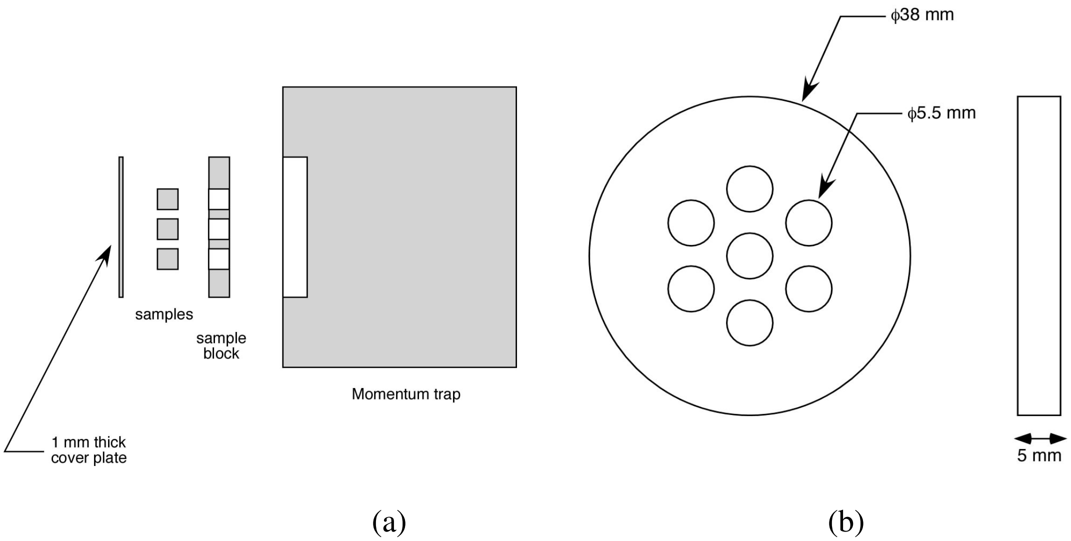

Figure 3.3: (a) Overview of the setup; (b) Sample mount.

3.1.2 Laser ICE setup

The Omega Laser System at the University of Rochester, NY, was used to generate a smoothly rising pressure pulse in the material. This pulse is created by focusing a laser beam on a reservoir material (carbon foam) facing the sample and separated from it by a necessary vacuum gap (~ 250 μm). The beam creates a plasma that "stretches out" through the vacuum and discharges onto the sample. The strain-rates achieved with this set up were on the order of 10^7 s^{-1}, three orders of magnitude higher than that of the gas-gun experiments. McNaney et al. 26, 83 use the same shockless laser drive setup to compress and recover polycrystalline aluminum and [001] copper, and a more detailed description of the setup can be found in their publications. An illustration of the setup is provided in Figure 3.4. This setup was also used to compress our nanocrystalline nickel and nickel-tungsten samples.

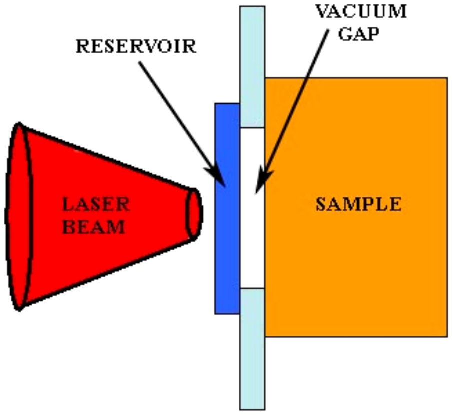

Figure 3.4: Schematic of the laser ICE setup

3.1.3 TEM

Copper TEM analysis was carried out at the Oak Ridge National Laboratory on a Philips CM-30 operating at 300 kV. Thin TEM foils were prepared using a twin-jet Struers Tenupol-3 polisher with an electropolishing solution composed of 7% H_2SO_4 in methanol. Cylindrical cuts having a diameter of 3 mm were made through the center of each specimen by EDM (Electron Discharge Machined). Figure 3.5 shows a typical as-recovered sample. TEM specimens were then sliced from each cylinder. An average of four TEM foils was extracted from each sample. The specimens were further polished down using 1200, 2400, and 4000 grit paper, respectively, to approximately 100 μm. In the case of the laser ICE samples, more care had to be given to sample preparation since quasi-isentropic loading was only limited to the area near the bottom of the crater (~120 μm). The near isentropic wave eventually steepens into a shockwave as it traverses the material, and both regimes have very different operative deformation mechanisms. Discs having a diameter of 3 mm were cut through the center of the impacted sample and further mechanically ground to approximately 100 μm with extreme care such that the deepest part of the crater was not polished away. A 30 % nitric acid in methanol solution was used for electropolishing. A dummy copper sample was used to cover the front end (cratered surface) of the loaded specimen for the initial polishing which lasted 45 seconds and corresponded to 50 μm of material being polished away from the back surface. The dummy specimen was then removed and a final polishing occurred such that the hole formed at a distance less than 25 μm from the loaded surface.

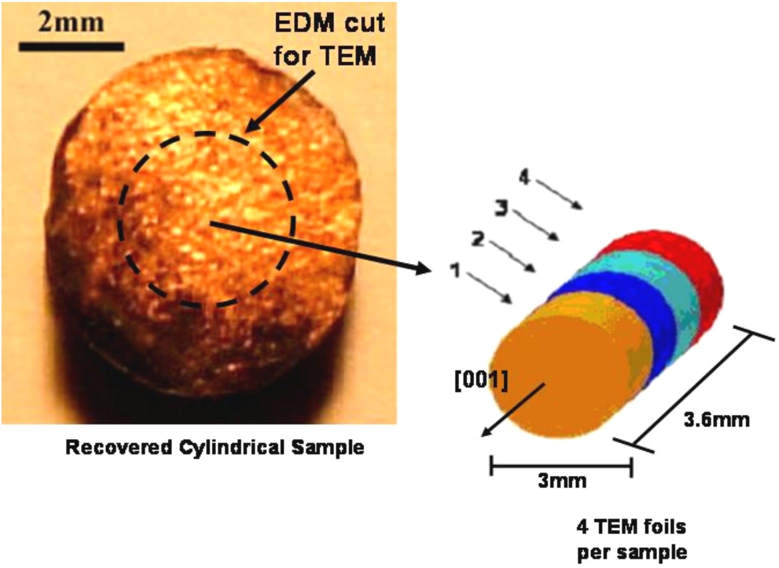

Figure 3.5: As-recovered cylindrical sample showing EDM cut and schematic of the TEM foils extracted from recovered sample.

3.1.4 SEM

SEM imagining in this work was carried out on an FEI Quanta 600. Surface features on laser impacted single-crystalline copper and nanocrystalline nickel samples were analyzed by SEM.

3.1.5 Micro-hardness measurements

Microhardness measurements were performed on all monocrystalline samples. After polishing to eliminate the heat affected zone (~ 50 μm on each side) and provide a smooth surface, the impacted surface was indented using a Vickers tip attached to a Leco: M-400-H1 microhardness machine. Ten indents were taken on each polished surface, and the load applied was 200 gF, with a hold time of 15 s.

3.2 Pressure Profiles

The pressure profiles in Figure 3.6 were obtained from simulations (CALE, hydrodynamics code) carried out at LLNL that were benchmarked to data matched to experiments which had a velocimetry diagnostic. Five experiments, 52-L (1700 m/s), 34-L (1260 m/s), 18-L (730 m/s), 44-S (1760 m/s) and 26-S (1260 m/s), were carried out, with 52-L experiencing the highest pressure of 52 GPa and 18-L experiencing the lowest pressure of 18 GPa. Table 3.1 shows the pressures, strains and strain rates achieved in the different experiments. Two distinct pressure profiles were attained, one having a hold-time of approximately 10 μs (“long pulse’ - L) and one having relatively no hold time (or a “short pulse” - S). The long-pulse samples belong to experiments 52-L, 34-L and 18-L, and the short-pulse samples belong to 44-S and 26-S. It should be noted that the “long-pulse” samples 52-L and 34-L exhibited a slight spike or shock at the onset of the pulse duration due to the experimental setup causing a deviation from the desired quasi-isentropic conditions. The likely effect on the microstructural deformation process is discussed in the results section. In the case of experiments 44-S, 26-S and 18-L that were closest to the desired isentropic ideal, “shocking-up”, which is the steepening of the isentropic wave into a shockwave as it propagates through the sample, did not occur in the CALE simulations. This was concluded by studying the temperature profiles generated by CALE, and a “jump” in temperature was not observed.

The as-recovered samples belonging to each batch were in the form of cylindrical specimens having an average diameter of 6mm and average thickness of 3.6 mm. Analysis of these samples enabled the comparison of the deformation mechanisms activated at this broad range of pressures. The strain rate versus pressure plot for these ICE experiments is given in Figure 3.7. Strain rates achieved were on the order of 10^4/s. A comparison of the current data with shock experiments is provided in Section 3.5

Table 3.1: Pressure Profile data: strain, strain-rate, peak pressure.

Set No.	**Velocity (Km/s)**	**Equivalent Plastic Strain (ε)**	**Strain Rate (1/s)**	**Peak Pressure (GPa)**
52-L	1.7	-0.3	6.49×10^4	52
44-S	1.76	-0.23	5.67×10^4	44
34-L	1.26	-0.21	3.69×10^4	34
26-S	1.26	-0.15	4.44×10^4	26
18-L	0.73	-0.11	1.80×10^4	18

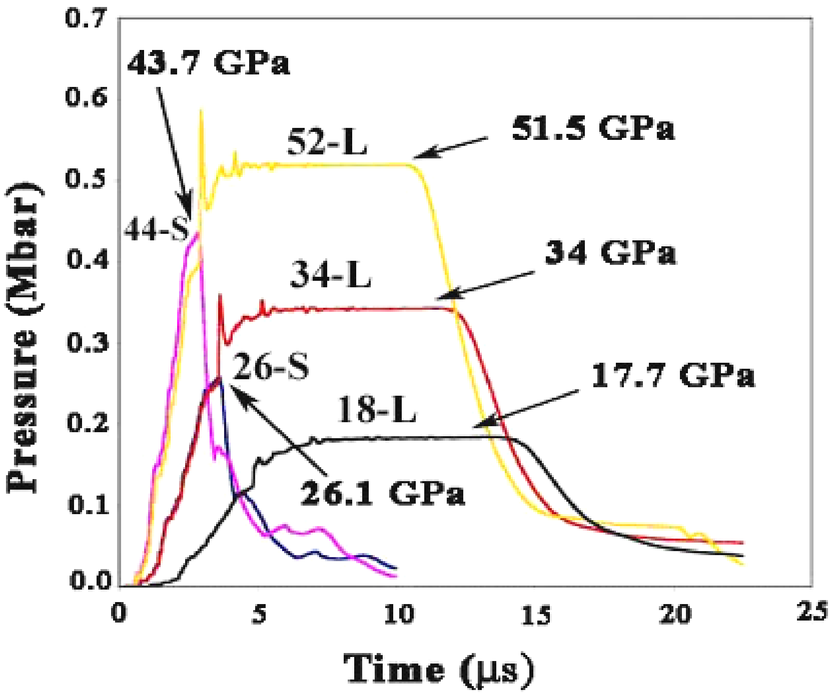

Figure 3.6: Pressure profiles of gas-gun ICE experiments; S and L are short and long pule experiments, respectively.

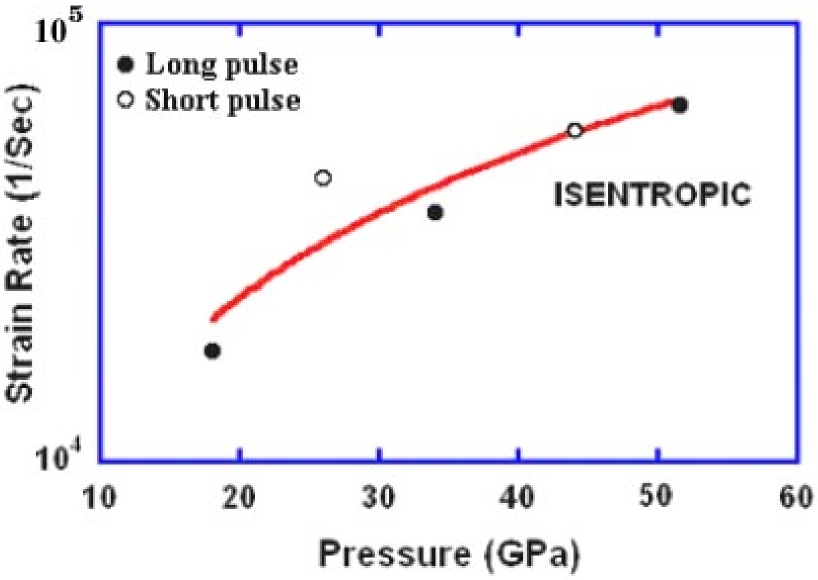

Figure 3.7: Strain Rate vs. Pressure for gas-gun ICE.

3.3 Microhardness Results

An interesting trend in hardness was observed. The value increases with peak pressure until approximately 45 GPa, as illustrated in Figure 3.8. It then saturates and begins to drop off dramatically. It can be seen that the hardness value at 52 GPa is almost two-thirds that of the intermediate pressure samples. It is hypothesized that the drop in hardness may be due to recovery processes taking place at the impact surface. This may be caused by the elevated temperature rise occurring at the higher peak-pressure conditions. Figure 3.8 also shows this rise in temperature as the peak pressure increases.

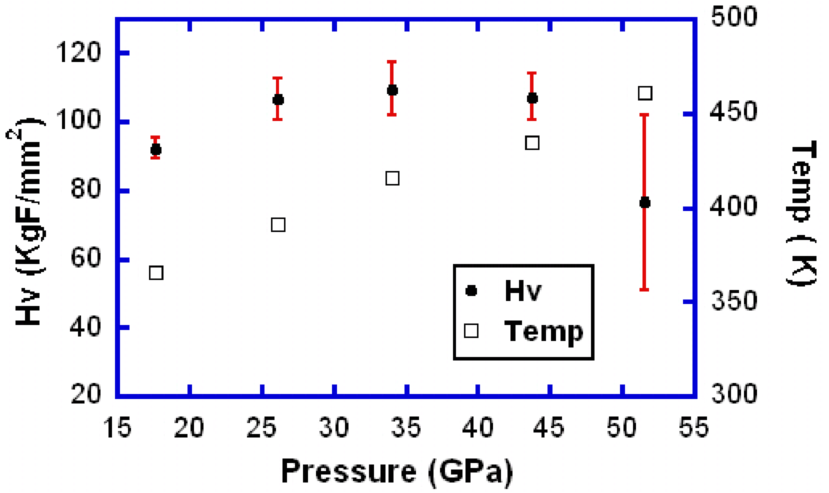

Figure 3.8: Hardness and Temperature Vs. Peak Pressure for gas-gun ICE experiments.

3.4 TEM Results

TEM results are presented next with an emphasis on the experiments closest to the intended quasi-isentropic ideal: 44-S, 26-S and 18-L. Although other deformation microstructures were observed, it should be noted that dislocation substructures such as cells and laths were most abundant in our TEM study. Twins and stacking faults were observed at the higher pressure experiments (52 and 44 GPa, respectively). These features can sometimes be indistinguishable without the use of HRTEM. Our operative definition of twinning is strictly based on the formation of a twin diffraction pattern. If we do not see a twin diffraction pattern, but rather "fringes" in our images, then we conclude the defect is a stacking fault. Diffraction patterns taken from all samples investigated revealed a [001] crystal orientation, as seen in Figure 3.9, confirming that sample orientation is not a variable in this study. This is to be expected as all impacted samples (from all 5 experiments) were cut out from the same [001] copper crystal.

(a) (b)

Figure 3.9: (a) [001] orientation of all samples. (b) Typical diffraction pattern of samples indicating the [001] orientation.

3.4.1 Experiment 44-S

Dislocation cells were the predominant deformation substructure in the samples belonging to this group. Diffraction patterns with beam direction B=[001] confirmed the [001] crystal orientation of all samples investigated. At 0.15 mm (the closest distance from the impact surface investigated) within the specimen, dislocation cells with an average cell size of 0.36 μm, seen in Figure 3.10 (a), were evident. At approximately 2mm (the farthest from the impact surface investigated) within the specimen, dislocation cells with an average cell size of 0.43 μm were evident. Table 3.2 summarizes the cell sizes measured at the various depths. Besides dislocation cells, elongated dislocation features (not as dense as those in 52-L) running along the $[\bar{2}\bar{2}0]$ direction were present, Figure 3.10 (b). The features had a thickness of ~ 0.1 μm with an average spacing between them of 0.44 μm.

At 0.77 mm from the impact surface, dislocation cells were predominant. Long dense laths/bands of dislocation walls were also observed, as seen in Figure 3.11 (a). Consistent with previous observations, the bands run along the [220] direction. The band thickness and spacing measured at this depth were 0.44 μm and 0.71 μm (summarized in Table 3.2). One interesting observation comprised of two dislocated lath variants intersecting at a point, Figure 3.11 (b).

Table 3.2: 44-S - Features at various depths

Depth (mm)	**Lath thickness (μm)**	**Lath spacing (μm)**	**Cell size (μm)**
0.15	0.1	0.44	0.36
0.77	0.44	0.71	0.46
1.34	-	-	0.38
1.85	-	-	0.43

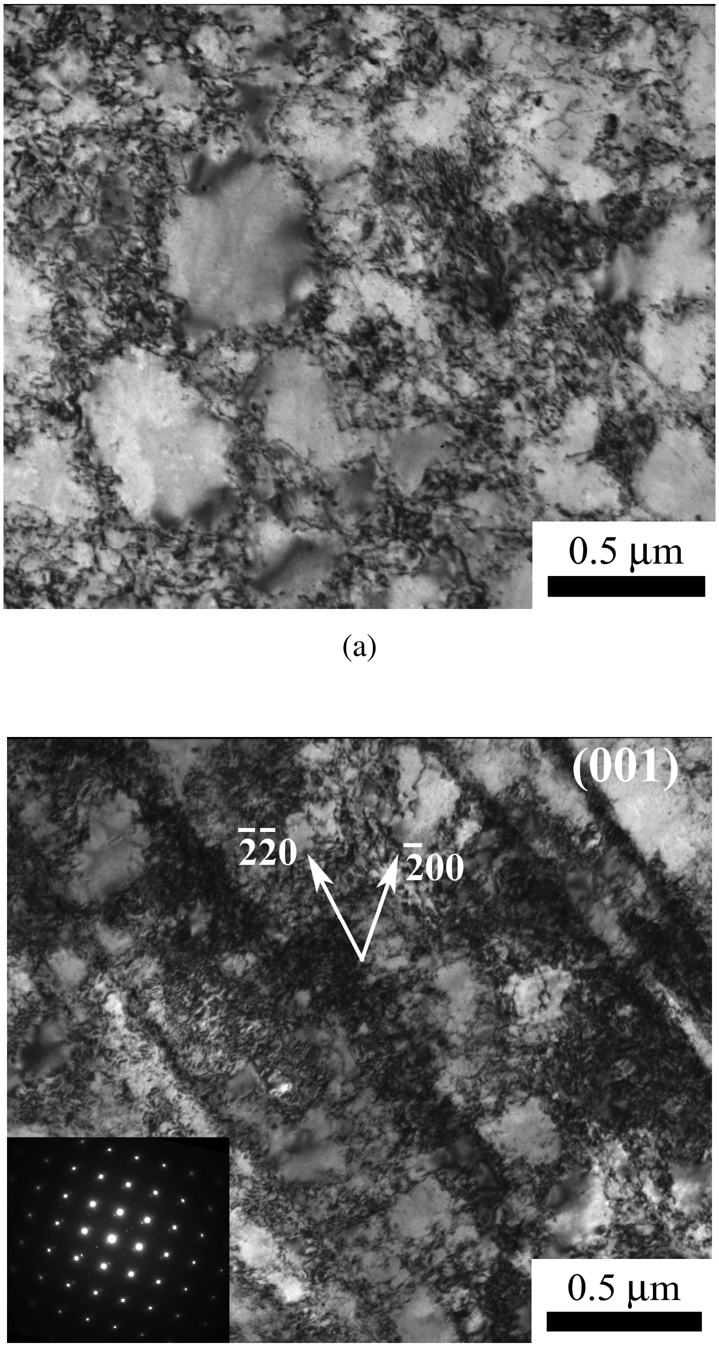

(a)

(b)

Figure 3.10: Quasi-isentropic gas-gun experiments, 44 GPa (short pulse), depth of 0.15 mm: (a) dislocation cells, average cell size: 0.36 μm; (b) dislocated laths and cells.

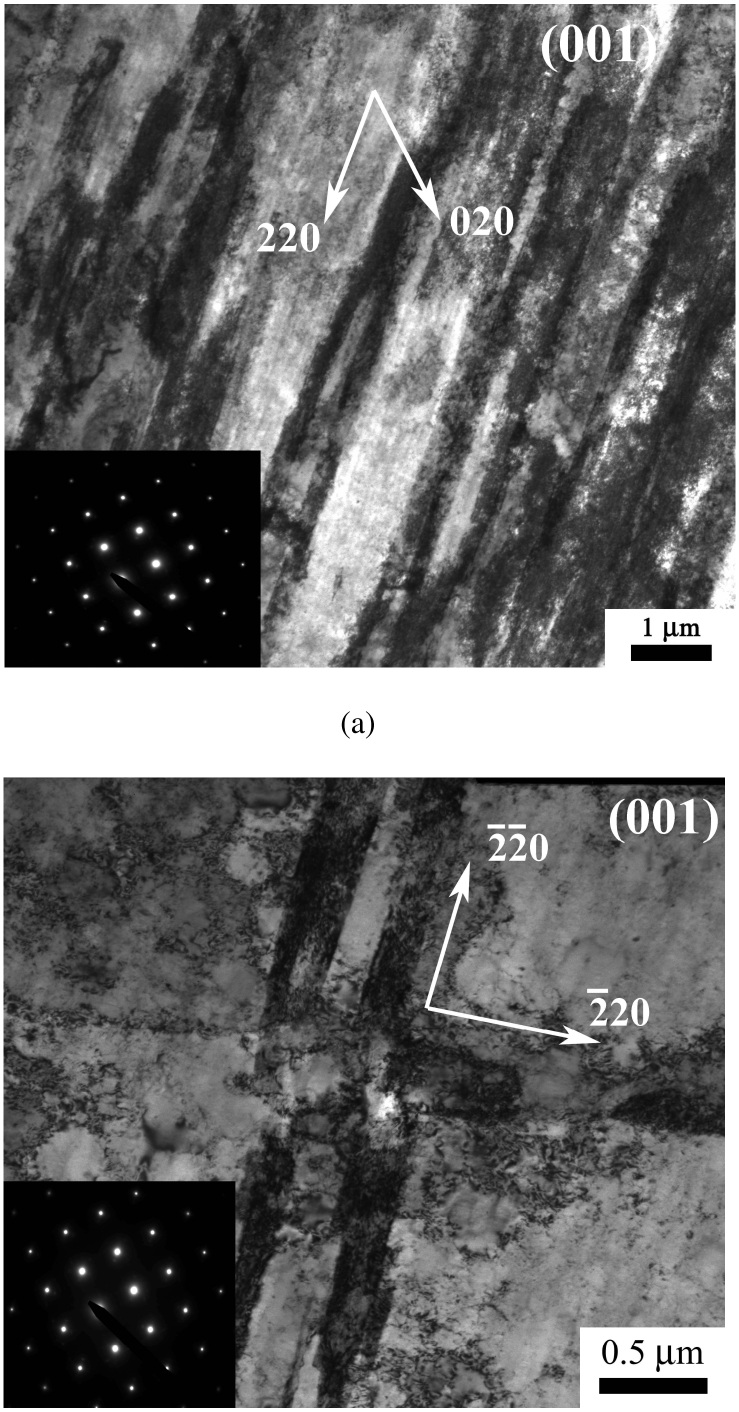

(a)

(b)

Figure 3.11: Quasi-isentropic gas-gun experiments, 44 GPa (short pulse), depth of 0.77 mm: (a) dislocated laths; (b) Intersecting laths.

3.4.2 Experiment 26-S

Dislocation cells were the most abundant deformation features unveiled in this pressure condition. The average dislocation cell size increased from 0.4 µm at 0.25 mm within the sample to 0.5 µm at 2.7 mm (summarized in Table 3.3). Features such as stacking faults, dislocated laths and elongated cells were revealed in a few of the specimens explored, but they were not as abundant and occupied a much smaller area than the cells. At 0.9 mm from the surface, stacking faults were evident in a few isolated regions. Figure 3.12 (a) shows an example of such a region. The thickness of the stacking faults is approximately 80 nm, and the spacing between the bands is approximately 0.1 µm. One stacking fault variant stretches along the $[\bar{2}20]$ direction. Further evidence of the same stacking fault variant was seen at 1.3 mm from the impact surface, Figure 3.12 (b). The thickness of the features was larger (~ 0.3 µm), however, due to the pressure decay with distance. The average stacking-fault spacing was 0.13 µm.

Table 3.3: 26-S - Features at various depths

Depth (mm)	**Staking fault thickness (µm)**	**Stacking fault spacing (µm)**	**Cell size (µm)**
0.25	-	-	0.4
0.9	0.08	0.1	0.42
1.3	0.3	0.13	0.4
1.8	0.28	1.21	0.49
2.7	0.291	0.73	0.5

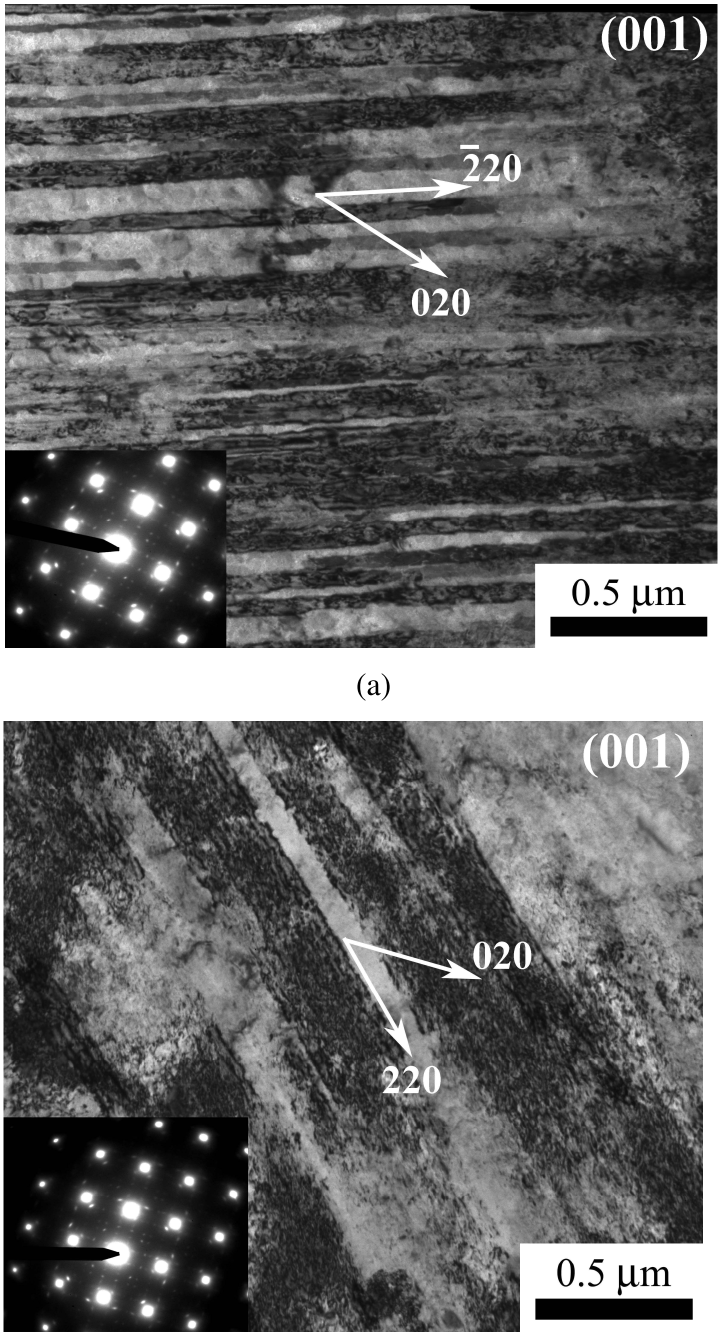

(a)

(b)

Figure 3.12: Quasi-isentropic gas-gun experiments, 26 GPa (short pulse): (a) depth of 0.9 mm - region of stacking faults along [$\bar{2}20$]; (b) depth of 1.3 mm - stacking faults along [220].

At the same depth, narrow and heavily dislocated laths were observed, as seen in Figure 3.13 (a). The two lath variants perpendicular to each other can be seen running along the [220] and $[\bar{2}20]$ directions, consistent with previous observations. An interesting area (not shown) within the sample at roughly 1.8 mm consisted of small slip-like features (along [220] direction) surrounded by a sea of dislocation cells. At 2.3 mm from the impact surface, dislocated laths and elongated dislocation cells, Figure 3.13 (b), were revealed. A summary of the thickness and spacing between the laths is provided in Table 3. The elongated cells are stretched along the same [220] orientation as that of the laths. This detail leads to the hypothesis that the laths at higher pressures closer to the impact surface relax into these elongated cells (and successively into regular dislocation cells) at lower pressures further away from the impact surface.

3.4.3 Experiment 18-L

Relatively large dislocation cells were the most abundant deformation feature for this lowest pressure condition. The average dislocation cell size varied from approximately 0.44 μm at 0.13 mm within the specimen to 0.6 μm at 2 mm. Table 3.4 provides a summary of the cell sizes with distance. Elongated cells and some lath-like activity were noticed in some regions, in particular closest to the impact surface at approximately 0.1 mm within the sample. Figure 3.14 perfectly exemplifies the findings in this pressure group. Both cells and dislocated lath-like features relaxing into elongated cells can be seen. The orientation of the laths/elongated cells is along the [220] direction. This orientation is the same as that of the laths observed in the previous experiments.

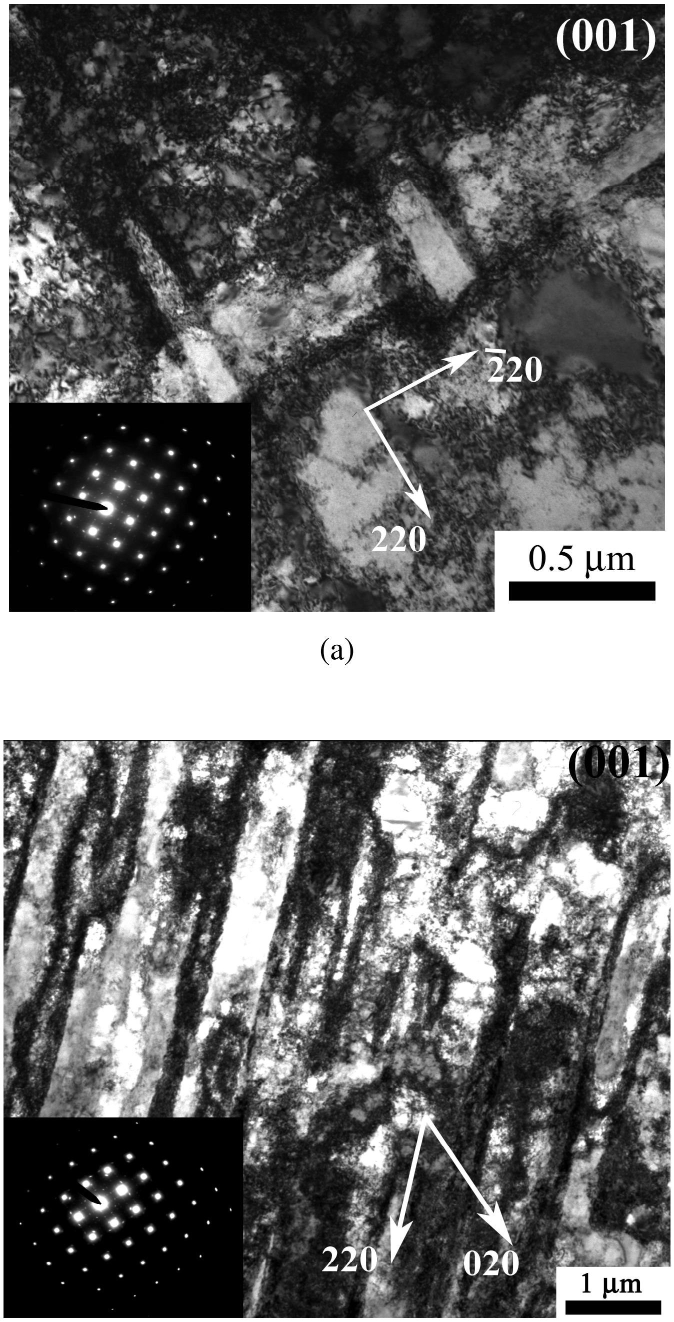

(a)

(b)

Figure 3.13: Quasi-isentropic gas-gun experiments, 26 GPa (short pulse): (a) depth of 1.3 mm - intersecting laths at 1.3 mm from impact surface; (b) depth of 2.3 mm - dislocated laths and some elongated cells.

Table 3.4: 18-L - Features at various depths

Depth (mm)	**Cell size (μm)**
0.13	0.44
0.15	0.55
0.67	0.62
0.72	0.64
1.3	0.41
1.9	0.63

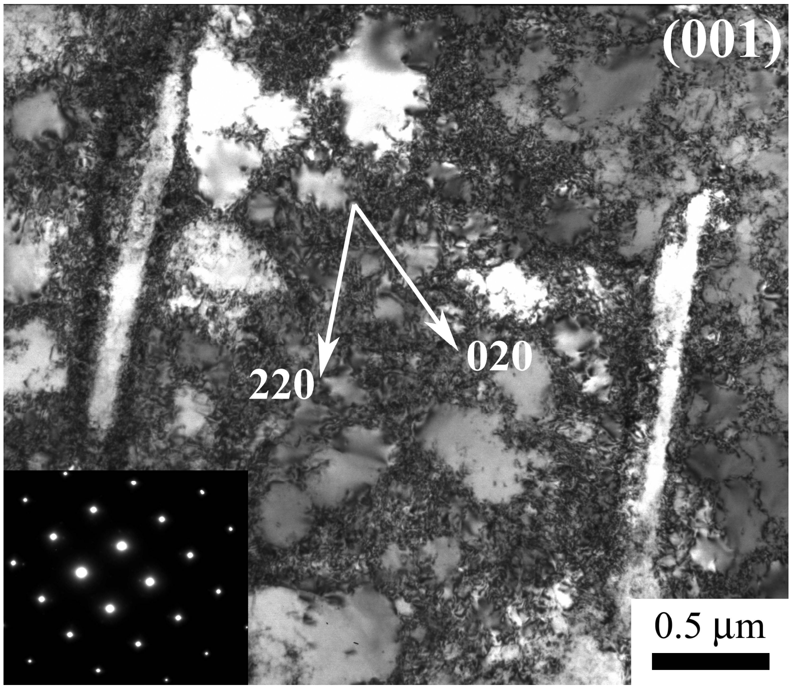

Figure 3.14: Quasi-isentropic gas-gun experiments, 18 GPa (long pulse), depth of 0.13 mm - dislocation cells and laths/elongated cells.

3.4.4 Experiment 52-L

TEM samples analyzed from 52-L revealed various deformation substructures. Dense dislocation substructures were most abundant. The size of dislocation cells close to the impact surface was too small to be discernable. At approximately 0.1mm from the impact surface, the microstructure predominantly consisted of dislocation activity with some limited evidence of twining. The deformation features were rather inhomogeneous. Figure 3.15 (a) shows very clear twinned regions. The extra spots in the diffraction pattern confirmed the existence of these twins. At a beam direction B=[011], both small and large twins were observed having $(\bar{1}\bar{1}1)$ twin habit planes. These micro-twins are embedded within dislocated laths running along the same direction as the twins (labeled in Figure 3.15 (a)). The smallest twins measured had a length of approximately 80 nm, and the longest twins were on the order of 1.5 μm. Longer twins existed in the TEM images, but they ran across the entire image and their full length was not captured. More TEM images at 0.1mm from the surface taken with B=[001] showed stacking faults running along the [220] direction, Figure 3.15 (b). Their thickness and spacing are summarized in Table 4.5. In certain areas, dislocated laths were captured intersecting each other (not shown) at 90º.

Heavily dislocated laths were observed at 0.7 mm and 1.2 mm deep. Lath thickness and spacing are tabulated in Table 4.5. Figure 3.16 shows laths 1.2 mm deep at a beam direction B=[001] running along the [220] direction. These features are in agreement with the "wavy sub-grains" observed after high-pressure shock compression of copper by Murr [84]. They are also analogous to the ones observed by Gray [85] in

Table 3-5: 52-L – Features at various depths in gas-gun ICE experiments

Depth (mm)	Twin Thickness (μm)	Twin spacing (μm)	Twin length (μm)	Lath thickness (μm)	Lath Spacing (μm)	Cell size (μm)	Staking fault thickness (μm)	Stacking fault spacing (μm)
0.1	0.02	0.1	0.08-1.5	0.48	0.45	-	0.053	0.13
0.7	-	-	-	0.6	0.45	-	-	-
1.2	-	-	-	0.7	0.4	0.15	-	-
1.8	-	-	-	-	-	0.2	-	-

specimens where the residual strain was high. It is suggested that the substructures are due to thermal recovery of the microstructure. Additionally, twinning, confirmed by a diffraction pattern, was evident at this depth. Dislocation cells were distinguishable at 1.2 mm deep (tabulated in Table 3.5).

3.4.5 Experiment 34-L

Dislocation cells were predominant at 0.14 mm from the impact surface of the specimens investigated in this group. The average cell sizes at the various depths investigated are tabulated in Table 6. Dislocation bands were observed at 0.6μm, seen in Figure 3.17 (a), running in the [220] direction. Two lath variants elongated in the [220] and $[2\bar{2}0]$ were also seen intersecting, Figure 3.17 (b). This is consistent with previous observations in 52-L and 44-S. The laths seem to act as either barriers to dislocation motion, thus, locking them in or as nucleation sites for dislocation activity. In addition to dislocation cells, heavily dislocated lath-like features were still evident at 0.7mm and 1mm running along [220]. Interesting features consisting of long laths/slip-like features with trapped in dislocations, identical to Figure 3.17, were observed in a small region 1.5mm deep (thickness and spacing tabulated). They were also stretched along the [220] direction.

The plot shown in Figure 3.18 (a) summarizes the change in cell size with distance into the sample for the various pressure conditions considered. It can be seen that the cell size gradually increases with distance away from the impact surface for each pressure condition. This is consistent with previous investigations by [48, 84, 85].

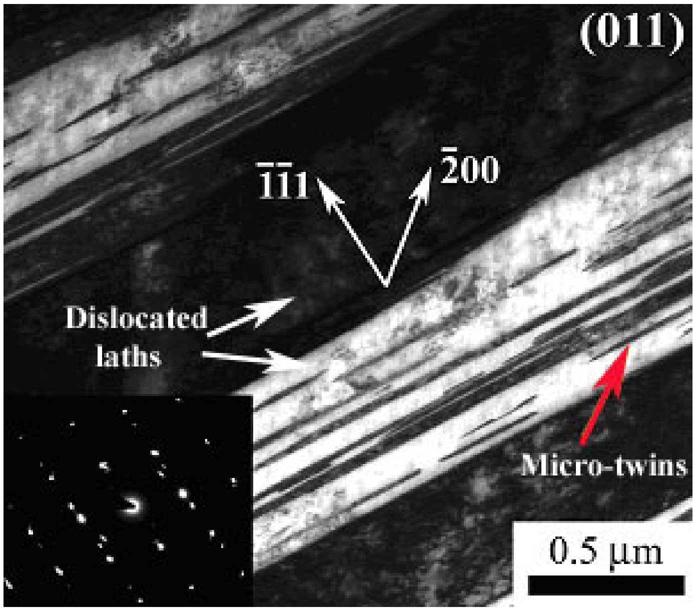

(a)

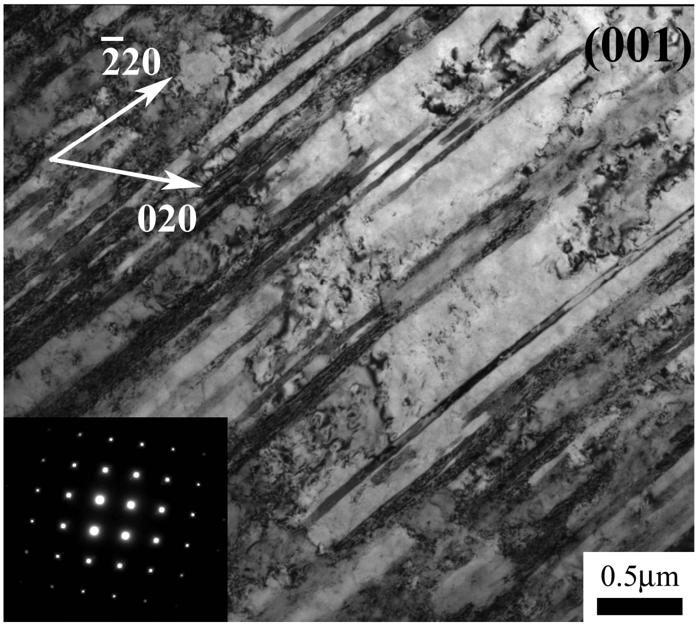

(b)

Figure 3.15: Quasi-isentropic gas-gun ICE experiments, 52 GPa (long pulse), depth of 0.1 mm: (a) Twinned regions showing dislocated laths and microtwins , B=[011]; (b) Stacking faults running along $[\bar{2}20]$, b=[001].

Table 3.6: 34-L – Features at various depths.

Depth (mm)	**Lath thickness (µm)**	**Lath spacing (µm)**	**Cell size (µm)**
0.14	-	-	0.28
0.6	0.25	1.16	0.25
0.7	-	-	0.29
1	-	-	0.26
1.5	0.23	2.65	0.3

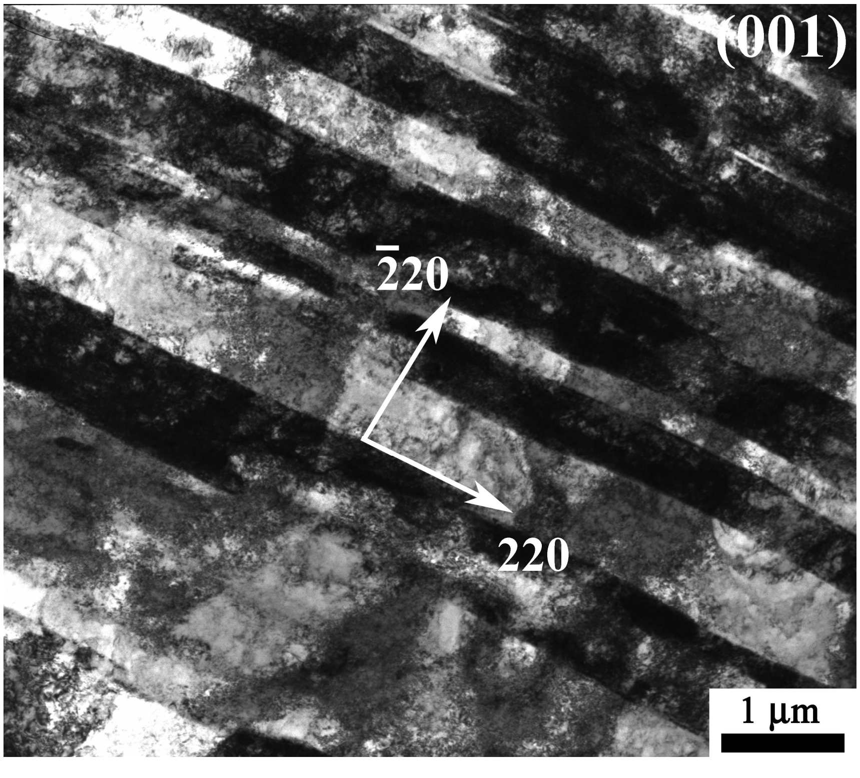

Figure 3.16: Quasi-Isentropic gas-gun experiments, 52 GPa (long pulse), depth of 1.2 mm, heavily dislocated laths running along [220].

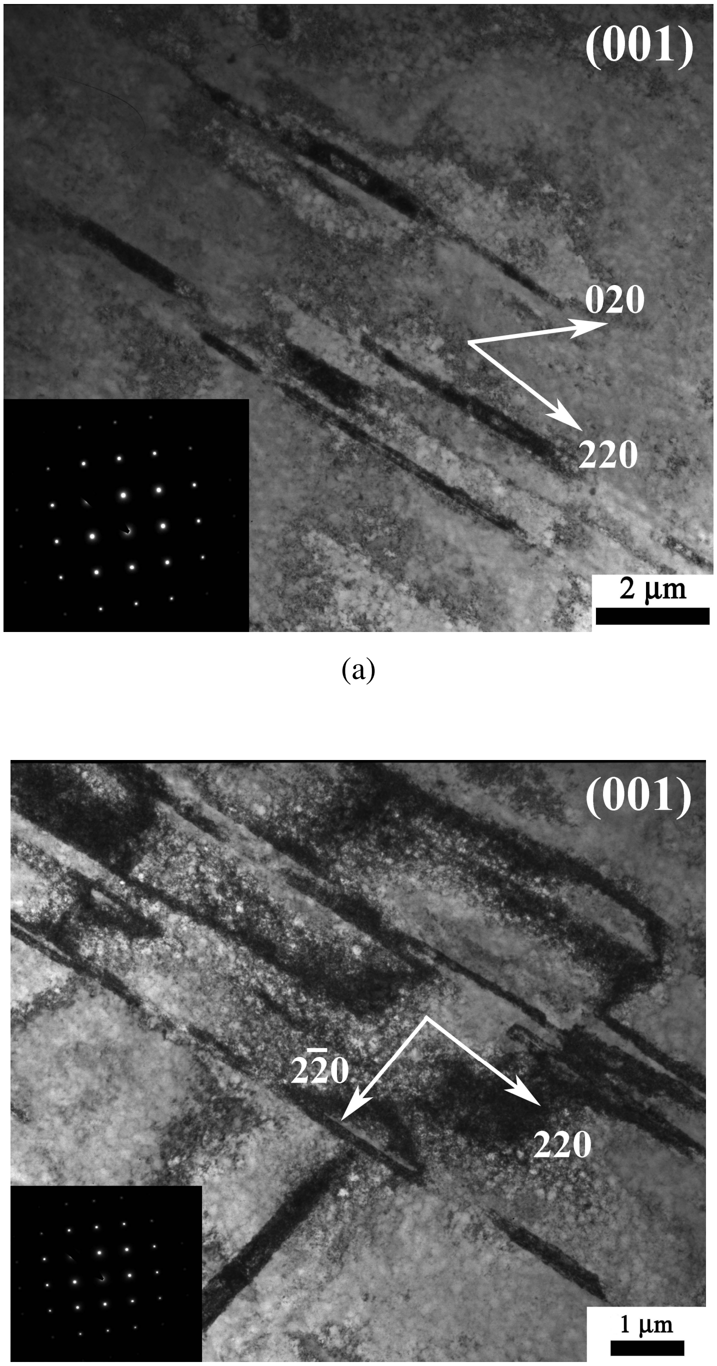

(a)

(b)

Figure 3.17: Quasi-isentorpic gas-gun experiments, 34 GPa (long pulse), depth of 0.6 mm deep: (a) Dislocated laths; (b) Intersecting laths.

In comparing the relative cell sizes of all the pressure conditions, two specifics that interfere with ideal experimental conditions need to be noted. First, experiments 52-L, 34-L and 18-L were subjected to a much longer pulse duration than that of 44-S and 26-S. The pulse duration was approximately 10 μs for 52-L, 34-L and 18-L as compared to less than 1 μs for 44-S and 26-S. Second, the CALE simulations reveal that 52-L and 34-L exhibit an unfavorable phenomenon; a slight shock at the onset of the pulse duration (due to the experimental setup). Experiments 44-S and 26-S are, therefore, much closer to the desired isentropic ideal that was intended.

The average cell size measured for 44-S is not consistent with measurements from the other experiments. Note that although 44-S experiences a higher peak pressure (44 GPa) than 34-L, it has larger cells. The cells in 44-S are also very close in size to those of 26-S, the other “short-pulse” experiment. Figure 3.18 (b) shows the change in cell size as a function of strain. The cell-sizes clearly decrease with increasing strain as is expected (with the exception of 44-S). Bassim and coworkers [86-89] have performed studies on the decrease in dislocation cell size with strain on copper and steel, and their work is consistent with our observations.

The “long-pulse” experiments, 52-L, 34-L, and 18-L**,** show a clear decrease in the average dislocation cell size with increasing peak pressure, consistent with prior work on high strain rate deformation of metals [48, 84, 85]. Sencer et al. [90] subjected copper samples to both a triangular and square-top shock wave to study the effect of pulse duration on the deformation microstructure (peak pressures were the same). They observed little variation in cell size in either case but noted that the dislocations were more irregular in shape in the triangle-top than in the square-top wave. In their work,

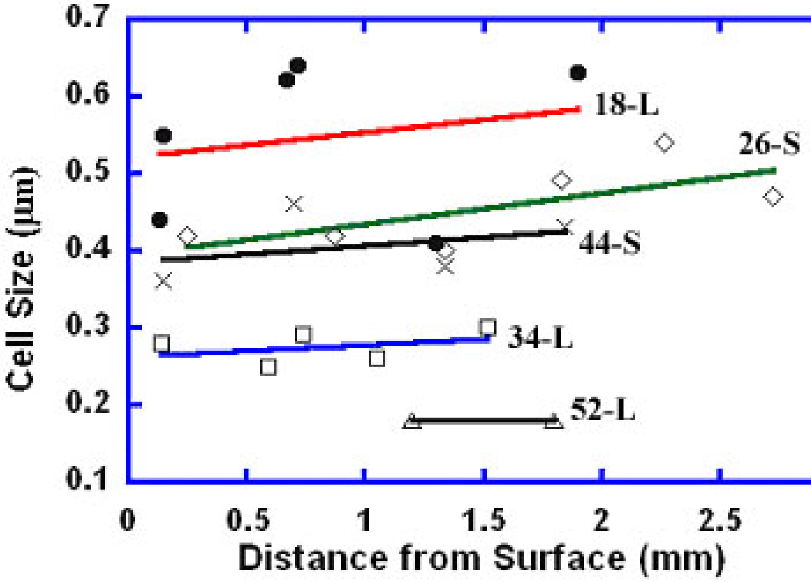

(a)

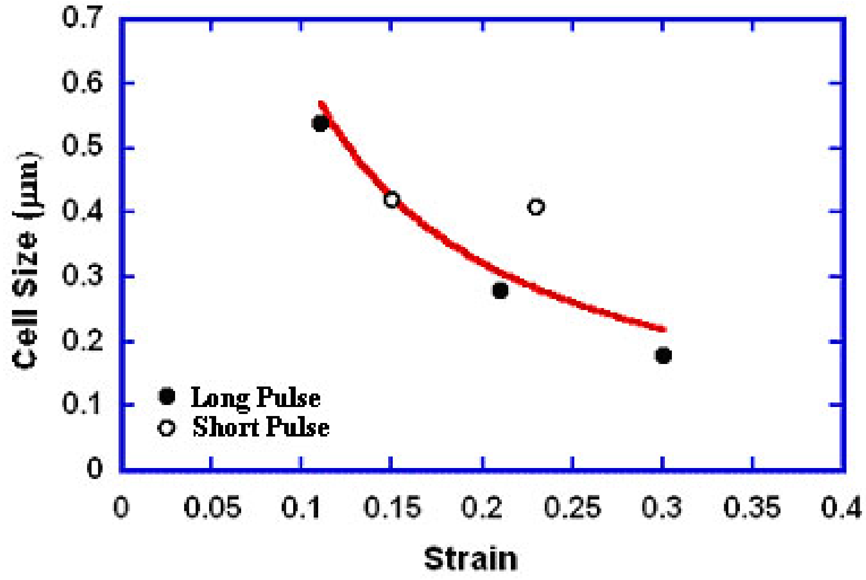

(b)

Figure 3.18: (a) Cell size vs. distance from surface for all pressure conditions; (b) Cell-size vs. strain for all pressure conditions.

Meyers and Murr [84, 91] note that dislocation cell structures are mostly dependent upon peak pressure and the time available to move these dislocations into arrays characterized by cell dimensions and wall size and structure. The dislocation cell size is, therefore, determined by the peak pressure whereas the wall structure and recognition of the cell structure are determined to a degree by the pulse duration which relates to the available time for dislocations to reorganize into more stable energy configurations.

3.5 Comparison: ICE VS. Shock

A comparison of the recovered microstructure revealed in the quasi-isentropic compression experiments is made with that of shock compressed copper achieved via both explosively driven flyer plates and direct laser drives. The work of B. Cao et al. [92] on flyer-plate shock and Schneider et al [48] on laser-shock of [001] copper is drawn upon. The peak pressures investigated in both cases are within the range of that studied in the ICE experiments (approximately 20 GPa to 60 GPa) and are suitable for comparison purposes. In the case of flyer plate impact, an explosion drives a plate that impacts a target at a known velocity. The strain rates typically achieved and reported in literature are on the order of 10^6 1/s, and pulse durations are on the order of 0.1 to 0.2 μs. This long pulse duration (also experienced in experiments 52-L, 34-L, and 18-L of the ICE experiments) allows shock generated defects to reorganize into lower energy configurations and allows more time for annealing and recrystallization to take place. Laser shock, on the other hand, is achieved by the rapid heating created by laser pulses illuminated on the material's surface. Strain rates reported in these experiments are on the order of 10^9 1/s**,** and the pulse durations are on the order of 5 ns. Due to the very short pulse duration, the pressure decay in the sample is very rapid and post-shock heating is minimized.

Shock experiments are dictated by the following Swegle-Grady [93] expression:

$$\dot{\varepsilon} = 7.84 \times 10^{-33} \times P^{4} \ \mathrm{s}^{-1} \tag{3.1}$$

where as the isentropic experiments have the following relationship derived from results of CALE simulations:

$$\dot{\varepsilon} = 1.17 \times 10^{-7} \times P^{1.1} \, \mathrm{s}^{-1} \tag{3.2}$$

Figure 3.19 (a) compares the different strain rate regimes attained in shock and ICE. It is clear that strain rates achieved in shock are on the order of 10^9 /s, 10^4 to 10^5 orders of magnitude higher than ICE experiments. Figure 3.19 (b) shows the temperature rise in both cases. Clearly, the temperature rise is more severe in shock at higher peak pressures as compared to ICE. The temperature rise for the ICE experiments was obtained from CALE simulation, and the rise for shock was calculated from thermodynamic relations and known equation of state parameters for copper.

3.5.1 Comparison of deformation substructures: 18-30 GPa

As discussed previously, dislocation activity was the main deformation behavior in the quasi-ICE experiments at 18 GPa. At 20 GPa, laser shock experiments exclusively contain well-defined cellular dislocations (not shown here) with an average cell size diameter between 0.2 and 0.3 μm [48]. This result is in accordance with previous investigations on shock by Murr [84]. The pulse duration was, however, 10 to 100 times higher in Murr’s work. The plot in Figure 3.20 shows that the dislocation cell-size in laser shock is significantly lower than in quasi-isentropic compression (0.25 μm versus 0.5 μm). This is attributed to the much higher strain-rates achieved during laser-shock. The pulse duration is much longer in the ICE experiments, allowing for the defect substructures to relax and form a more stable energy configuration, and hence, larger dislocation cells. Some evidence of staking faults (Figure 3.12), as previously reported, was observed at 26 GPa in the ICE experiments. Stacking faults were seen at the higher pressure regimes in both flyer plate and laser shock (discussed next), but not between 18 and 30GPa. In their work, B. Cao et al. [92] carry out experiments at 30 GPa and above. A comparison of the defect substructure for this pressure group with flyer-plate experiments is not made because of the lack of published data.

3.5.2 Comparison of deformation substructures: 30-40 GPa

Some similarity between all three cases was found in this range. In laser shock, this pressure regime produced dense dislocation tangles, stacking faults, and micro twins. Figure 3.21 (a) shows staking faults and dislocation tangles marked as DT and SF. There are no readily discernable dislocation cells, a clear indication of the pressure dependence of the deformation mechanisms. All four stacking fault variants *viz* the partial dislocations $(1\,1\,\bar{1})1/6[112]$, $(111)1/6[\bar{1}\,\bar{1}\,2]$, $(\bar{1}\,1\,1)1/6[1\,\bar{1}\,2]$, and $(1\,\bar{1}\,1)1/6[\bar{1}\,1\,2]$ are observed. The stacking fault variants are along the same orientation in all three cases. Given the incident energy input as parallel to [001], it is not surprising that all four stacking fault variants are activated in laser shock since they have the same critical resolved shear stress.

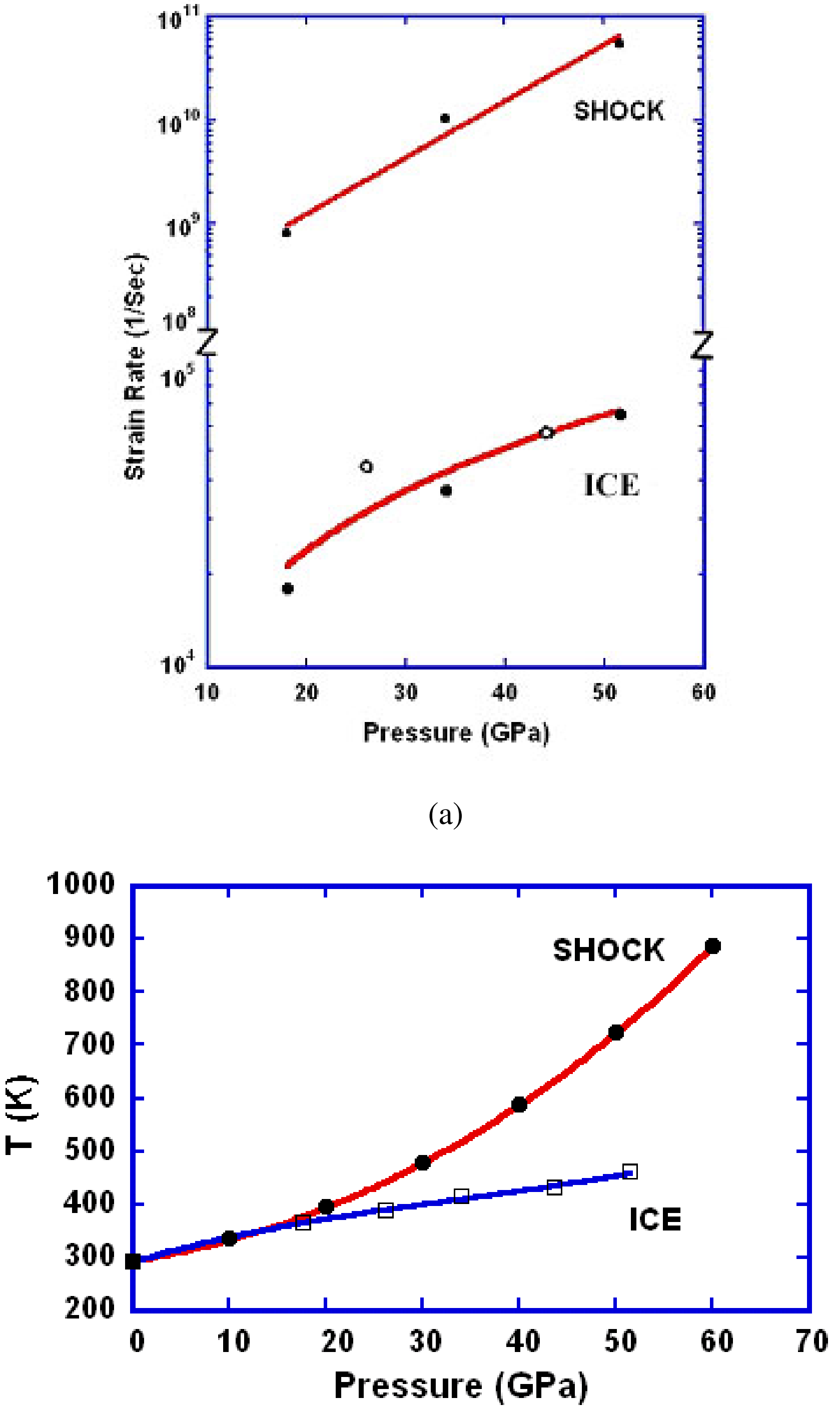

(a)

(b)

Figure 3.19: (a) Comparison of the strain rate regimes attained in shock and gas-gun ICE; (b) Comparison of the temperature rise in shock and ICE.

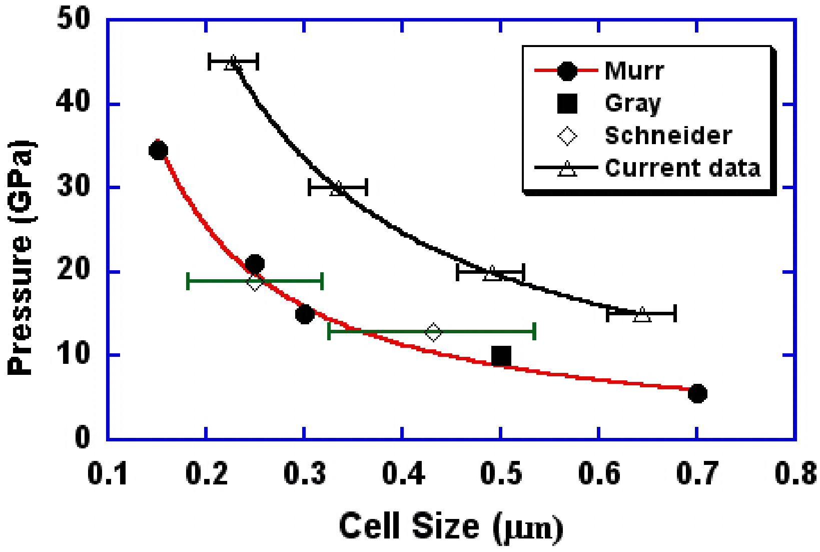

Figure 3.20: Comparison of cell sizes at different pressures: ICE, laser-shock and flyer-plate impact.

The density of occurrence of the stacking faults along the $[\bar{2}20]$ is, however, greater than along $[220]$ in laser shock. In ICE, the stacking faults and laths that are most abundant run along the [220] direction. However, their occurrence is less frequent and not as abundant as in laser shock and flyer plate experiments. This is attributed to the difference in the strain rate regime in ICE (less by a factor of 10 to 100).

For the flyer plate experiments, staking fault patterns similar to shock are observed at 30 GPa. Two sets of stacking faults along $[\bar{2}20]$ and $[220]$ in the (001) plane are shown in Figure 3.21 (b), where the TEM electron beam direction is [001]. These orientations are consistent with ICE experiments, since the same partial dislocations are active in both cases. The average spacing between the stacking faults is

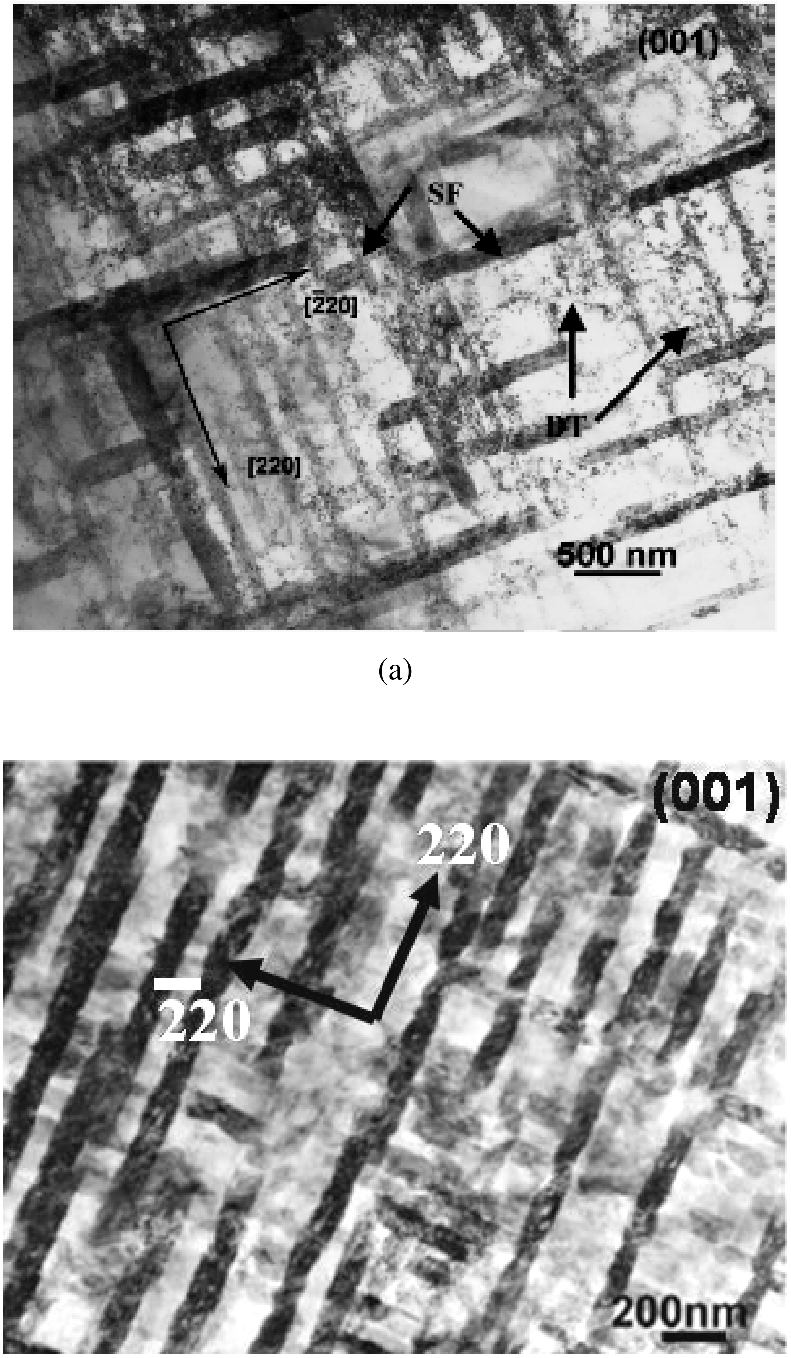

(a)

(b)

Figure 3.21: (a) Stacking faults at 40 GPa in laser-shocked sample (from Schneider et al. [48]); (b) Staking faults at 30 GPa in flyer-plate impacted sample (from Cao et al. [92]).

between 230 and 450 nm for laser shock and between 180 and 220 nm for flyer-plate impact. The spacing in the ice experiments ranges between 100 and 500nm.

3.5.3 Comparison of deformation substructures: 40-60 GPa

In laser shock, the deformation microstructure at 55 GPa consists of a high density of micro-twins (Figure 3.22 (a)) and laths (Figure 3.22 (b)). Two sets of micro-twins are observed when imaged at B = [0 0 1]. They appear at exactly 90 degrees from one another aligned along $[2\,2\,0]$ (set A) and $[\bar{2}\,2\,0]$ (set B) directions, respectively, and they are present roughly in same proportion (not shown here). When imaged in the edge orientation at B close to $[\bar{1}\,0\,1]$, Figure 3.22 (a), the micro-twins from set A have the (111) habit plane and are elongated along $[1\,\bar{2}\,1]$. This set of micro-twins exhibits a wide range of lengths, from as small as 70 nm to as large as 1μm; In contrast, the set B micro-twins have a near uniform length of 70 nm. Correspondingly, these two same twin variants running along [220] $[\bar{2}\,2\,0]$ were also captured in the ICE experiments at 52 GPa.

Unlike the micro-twins, the laths in laser-shock are elongated close to $<2\,2\,0>$. In some regions they are aligned along $[\bar{2}\,2\,0]$ and in others along $[2\,2\,0]$. Given the curvature of the laths it is unlikely that they conform to any single habit plane. The lath interface plane is parallel to [001] and therefore uniquely different from micro-twins. This microstructure represents the recovered state of a heavily twinned and dislocated structure. These laths are similar to those observed in the ICE experiments at 52GPa, 0.7mm and 1.2mm from the impact surface. A striking similarity can be seen between

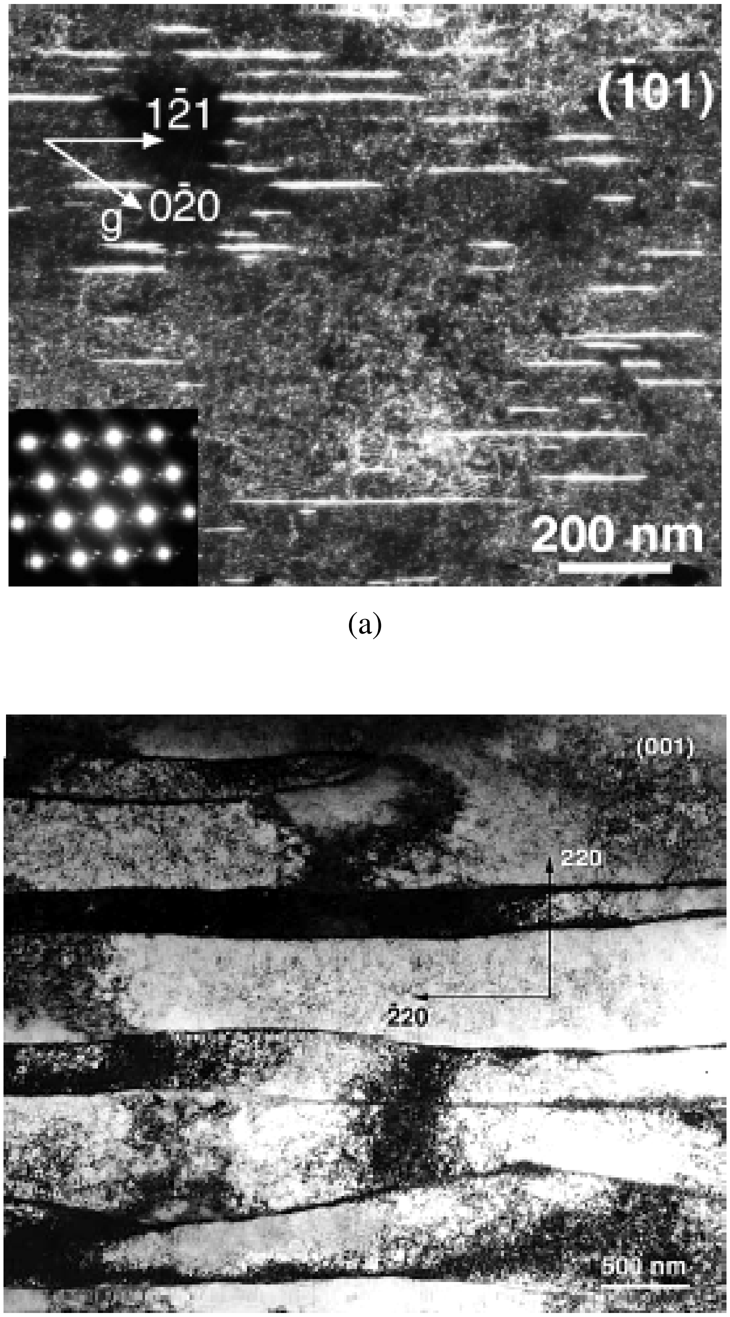

(a)

(b)

Figure 3.22: (a) Micro twins observed in laser shock at 55 GPa; (b) Laths observed in laser shock at 55 GPa [48].

the laths shown in Figure 3.22 (b) and those in Figure 3.16. The laths are oriented along the [220] direction in both cases.

The flyer-plate samples shocked at 57 GPa revealed deformation bands, slip bands, recrystallized regions, dislocation tangles and some micro-twins. Only one set of micro-twins was observed having a $(\bar{1}\,\bar{1}\,1)$ habit plane, as seen in Figure 3.23 (a). The size of the micro-twins varies from 80 nm to 180 nm. Interestingly, the same micro-twin variant was observed in the ICE experiment at 52 GPa, elongated along the $[\bar{2}\,2\,0]$ direction. In one of the flyer-plate samples, a deformation band having a width of 1.8 μm is seen running diagonally along the sample, Figure 3.23 (b), intersecting smaller neighboring slip/stacking faults. Selected area diffraction identifies the vertical slip as $(1\,\bar{1}\,1)$.

The average width of the stacking faults observed was approximately 500nm. Further into the sample, regular dislocation cell arrays running across the sample were observed. Dislocation tangles between these arrays were also evident. The distance between the dislocation arrays were approximately 500 nm as well leading to the hypothesis that the arrays are due to the recovery or relaxation of the stacking-fault arrays. Similar to all three experiments, a decrease in dislocation density with depth into the sample is evident. Unlike the features seen in laser shock and ICE, fully recrystallized regions were seen in the flyer-plate experiments.

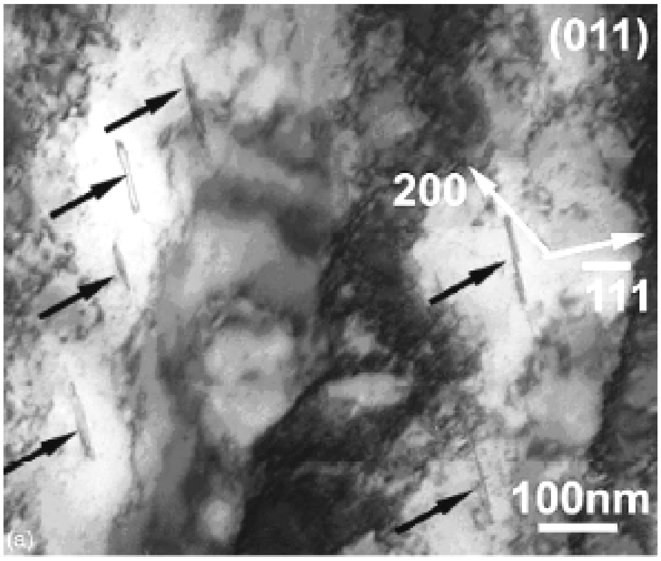

(a)

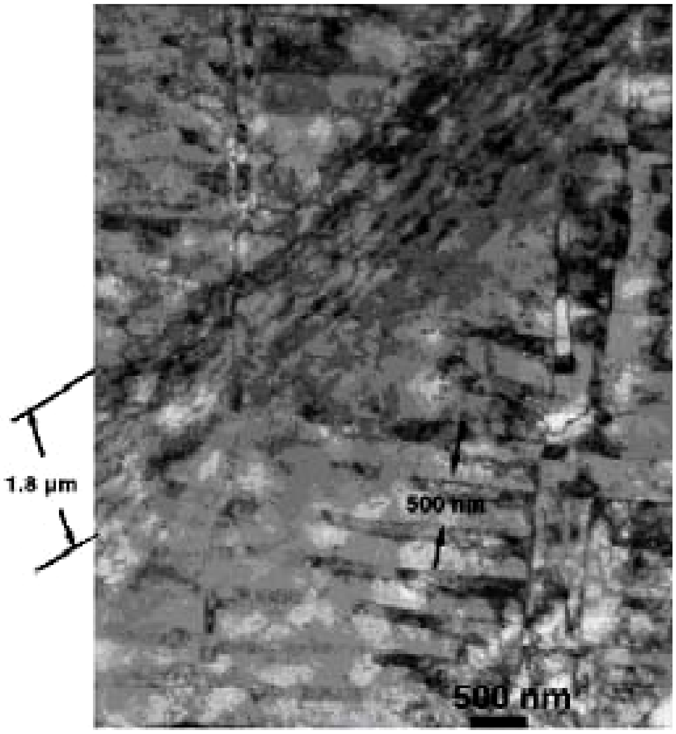

(b)

Figure 3.23: (a) Micro-twins observed in plate impact at 57 GPa; (b) Slip bands and stacking faults observed in plate impact at 57 GPa [92].

3.6 Laser ICE: Copper

McNaney et al. [83] used a shockless laser drive setup to compress and recover [001] copper. The strain rate achieved in our laser quasi-isentorpic compression experiments was further extended from 10^4 s^{-1} (gas-gun range) to ~10^7 s^{-1}. Of all the experiments carried out, the three peak pressures reported for the laser ICE experiments are 18 GPa, 24 GPa, and ~56 GPa. These pressures are very reasonably close to the pressures achieved in three of the gas-gun experiments (18 GPa, 26 GPa, 52 GPa) allowing for a comparative study. The pressure estimate of 56 GPa is more uncertain than the others because of the lack of benchmarking the data for the reservoir material used in the experiment. An extrapolation from higher pressure data was done instead.

3.6.1 Crater width and depth

The front face of each sample had a crater as a result of the damage induced by isentropic loading. The diameter and depth of the craters correspond to the magnitude of the loading pressures. Figure 3.24 (a) shows an SEM image of a single crystal copper specimen loaded to 240 kbars. The measured width of the crater was ~1.5 mm. The depth of the crater was ~1.8 mm. Plots of the crater widths and depths are given in Figure 3.24 (b) and (c). The widths of the crater vary from about 1mm for 10 GPa to 2.1 mm at the highest pressure, 56 GPa.

The data fit well to a power law curve. The differences in crater depth are more apparent: at low pressures, the depth is about 0.05 mm growing to 0.2 mm at the highest pressure. These results are a stark contrast to laser shocked specimens. Laser shock specimens show very limited surface damage and no discernable crater as a result of

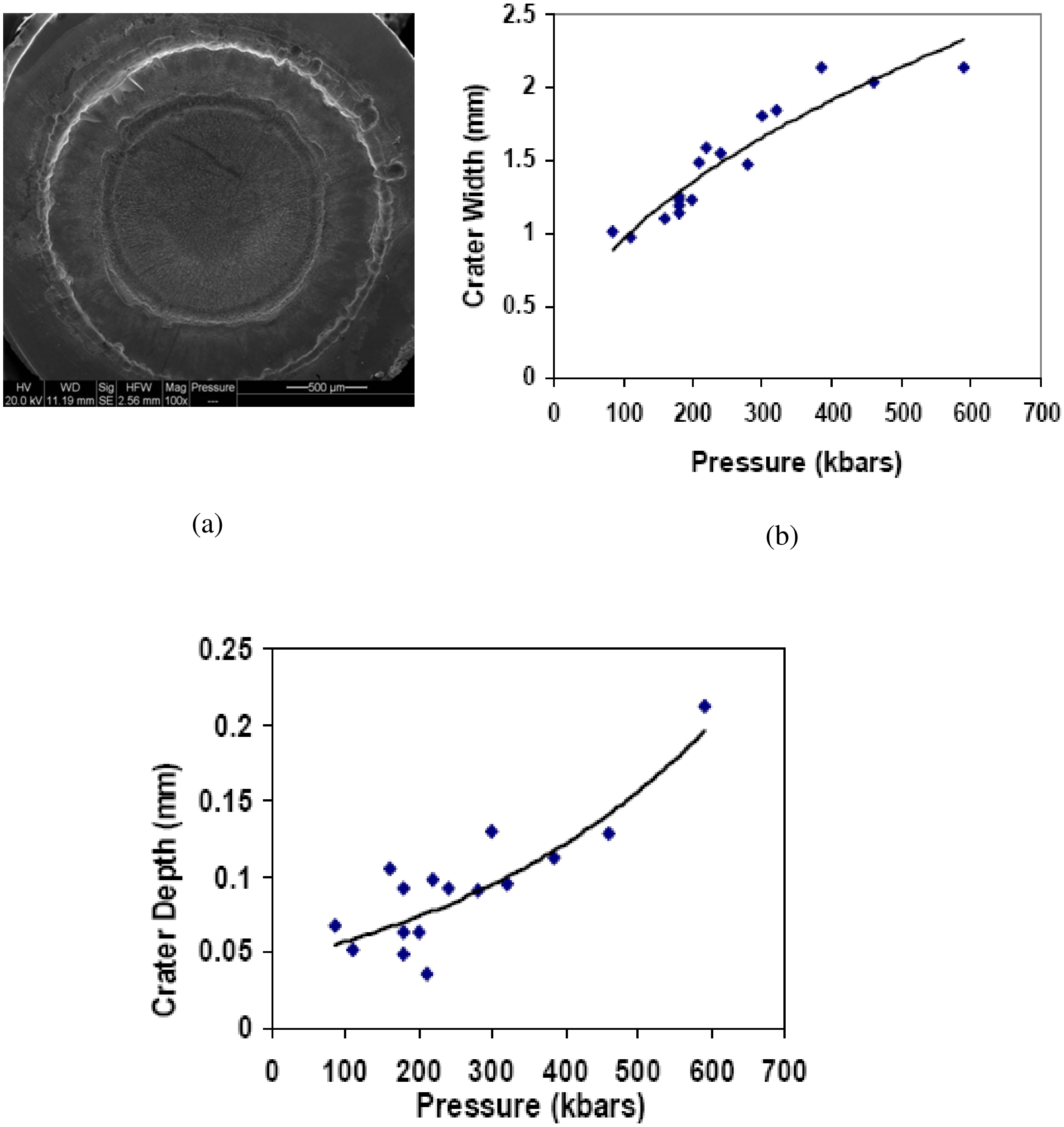

(a)

(b)

(c)

Figure 3.25: (a) SEM of surface of sample quasi-isentorpically loaded to 24 GPa; (b) Crater width vs. pressure; (c) Crater depth vs. pressure.

loading. However, it is important to note that spot size and loading times are different for the two techniques and influence the amount of surface damage.

3.6.2 Pressure profiles

Typical pressure profile modeled by CALE are presented in Figure 3.26 (a) and (b). The 24 GPa experiment is illustrated in this case. As can be seen, the peak pressure gradually decays as it traverses the sample. At approximately 100 μm, the pressure pulse becomes perfectly vertical, hence, transitioning into a shock. This can also be inferred from the temperature profile. There is a temperature rise at that depth from ~370 ºK to 400 ºK indicating that the loading path is no longer quasi-isentropic. The quasi-isentropic region is, hence, limited to a distance within the material that is 100 microns away from the loaded surface. Figure 3.26 (c) provides a comparison between the strain-rate regimes achieved during shock, gas-gun ICE and laser ICE conditions.

3.6.3 TEM: Laser ICE

At the highest pressure of approximately 59 GPa, a large number of faults/twins was observed, Figure 3.27 (a). They were preferentially oriented along the [022], identical to what has been reported in laser shocked copper [48] and the gas-gun ICE experiments. They were found near regions of extremely high dislocation densities. Laths spaced at regular intervals of 500 nm (also their average width) were also observed with heavily dislocated regions in between. At a lower pressure of 24 GPa, stacking faults were dominant. An interesting image, Figure 3.27 (b), was taken of a transitional substructure showing dislocation cells to the right and stacking faults to the left. The average

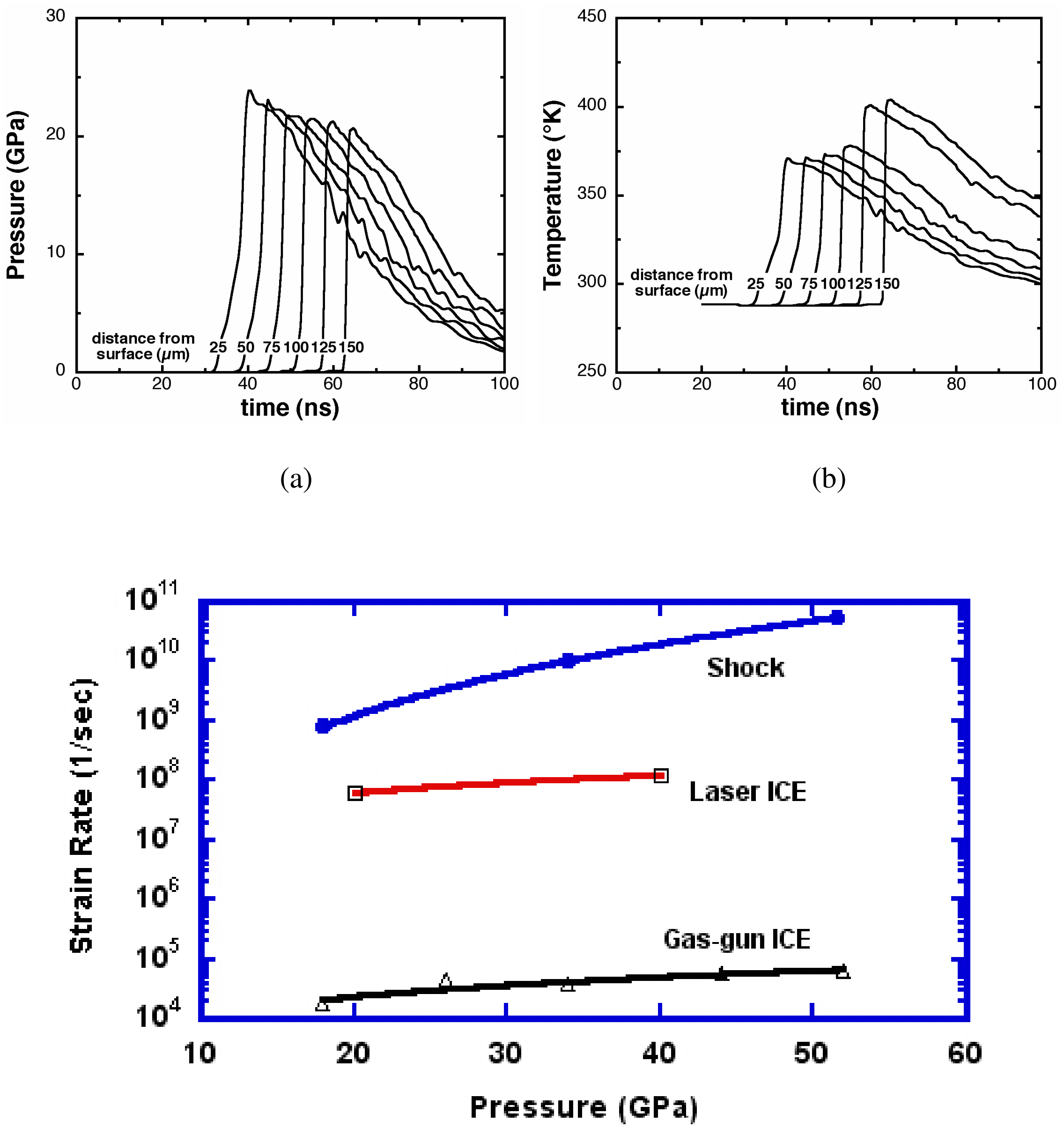

(a) (b)

(c)

Figure 3.26: (a) Pressure vs. time; (b) Temperature vs. time; (c) comparison of strain-rate regimes in shock, laser ICE, and gas-gun ICE conditions.

dislocation cell size was 0.2 μm and the cells were comprised of <110> type dislocations. The stacking faults were identical to the four variants observed in laser shock compression having a {111}1/6<112> nature. The average spacing was 650 nm with a width of nearly 150 nm. There was no visible difference in the material that contained cells and the area that contained stacking faults. The imaged area was taken from near the center of the sample and deepest part of the crater.

Dislocation cells, Figure 3.27 (c), similar to those observed in shock loading were the predominant mode of deformation for the samples loaded to 18 GPa. The defects were primarily ½ <110> type dislocations which have relaxed into cells. The cell sizes measured in the isentropic specimens at this pressure were approximately 0.3 μm,. It is interesting to note that one unique characteristic of the isentropic compression was the uniformity of the cell sizes at the given pressure. Unlike shock loading where there was substantial variance between cell sizes, the quasi-isentropically loaded specimens were very similar in size and shape. Also, the dislocation cells were more clearly defined as compared to laser shocked samples previously studied. This is likely a result of the isentropic loading conditions.

3.6.4 Constitutive modeling

Two separate models to predict the twinning threshold using the Preston-Tonks-Wallace and Zerilli-Armstrong constitutive equations are presented, respectively. These models determine the critical pressure for twinning in both shock and ICE regimes. It is well-known that different metals have different threshold twinning pressures. In the case of FCC metals, this pressure is a function of stacking-fault energy. Slip and twinning are

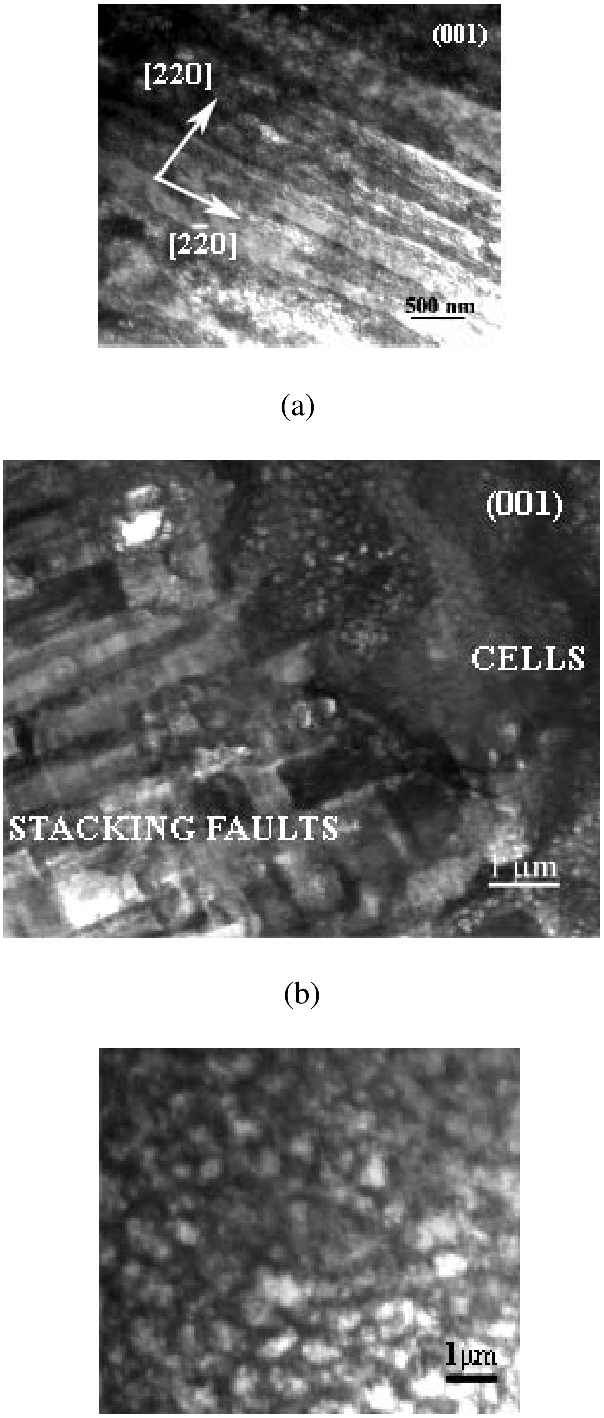

(a)

(b)

(c)

Figure 3.27: (a) Twins/laths at 59 GPa; (b) Dislocation cells and stacking faults at 24 GPa; (c) Dislocation cells at 18 GPa.

visualized as competing mechanisms, where slip is a temperature and strain-rate dependent phenomenon and twinning is much less sensitive to these variables.

3.6.4.1 Preston-Tonks-Wallace model

The Preston-Tonks-Wallace constitutive equation is used to determine the critical pressure for twinning in both shock and ICE regimes [94]. It is well-known that different metals have different threshold twinning pressures. In the case of FCC metals, this pressure is a function of stacking-fault energy [72]. Slip and twinning are visualized as competing mechanisms, where slip is a temperature and strain-rate dependent phenomenon and twinning is much less sensitive to these variables.

Using the general approach of Murr et al. [95] and Meyers et al. [96], we estimate the twinning threshold pressure for quasi-isentropic and shocked regions by considering the constitutive response of copper for the two regimes, shockless and shocked. The twinning threshold is taken to be the point at which the tensile flow stress (e.g., 2τ) is equal to the tensile twinning stress, taken to be 490 MPa [96] in this work, and is assumed to be temperature and strain rate independent.

A number of models have been developed to estimate the flow stress as a function of strain rate and temperature [97, 98] and additionally pressure [94, 99, 100]. With the exception of the Preston-Tonks-Wallace (PTW) constitutive description [94], none that allow for a pressure dependence are applicable over the range including both the thermal activation regime and the dislocation drag regime. Thus, in estimating the flow stress we will employ the model developed by PTW [94] as it is well suited for the very high strain rates in the experiments considered. If we restrict our analysis to constant strain rate paths, the instantaneous flow stress can be calculated from:

$$\tau = \hat{\tau}_s + \frac{1}{p}\left(s_0 - \hat{\tau}_y\right)\ln\left\{1 - \left[1 - \exp\left(-p\frac{\hat{\tau}_s - \hat{\tau}_y}{s_0 - \hat{\tau}_y}\right)\right]\exp\left[\frac{-p\theta\psi}{\left(s_0 - \hat{\tau}_y\right)\left[\exp\left(p\frac{\hat{\tau}_s - \hat{\tau}_y}{s_0 - \hat{\tau}_y}\right) - 1\right]}\right]\right\} \tag{3.3}$$

where we have preserved the notation used in [94] for simplicity. The work hardening saturation stress and yield stress in the *thermal activation* regime are given by:

$$\hat{\tau}_s = s_0 - \left(s_0 - s_\infty\right) erf\left[\kappa\hat{T}\ln\left(\gamma\,\dot{\varepsilon}/\dot{\psi}\right)\right] \tag{3.4}$$

$$\hat{\tau}_y = y_0 - \left(y_0 - y_\infty\right) erf\left[\kappa\hat{T}\ln\left(\gamma\,\dot{\varepsilon}/\dot{\psi}\right)\right] \tag{3.5}$$

where s_0, s_∞, y_0, and y_∞, are the values $\hat{\tau}_s$ and $\hat{\tau}_y$ take at zero and very high temperature respectively, $\dot{\psi}$ is the plastic strain rate, $\hat{T}$ is the homologous temperature and *erf* is the error function. The flow stress is normalized to the shear modulus, *G*. e.g., $\hat{\tau}_y = \tau_y/G$. The parameters κ, γ are dimensionless material constants and $\dot{\varepsilon}$ is given by:

$$\dot{\varepsilon} = \frac{1}{2}\left(\frac{4\pi\rho}{3M}\right)^{1/3}\sqrt{G/\rho} \tag{3.6}$$

where M is the atomic mass and ρ is the density. The temperature dependence of the shear modulus was approximated as $G(\rho,T) = G_0(\rho)\left(1 - \alpha\hat{T}\right)$, where $G_0(\rho)$ is the zero temperature modulus as a function of density and α is a material constant. The pressure dependence of the model is due to the pressure dependence of the shear modulus.

In the strong shock regime the behavior is given by:

$$\hat{\tau}_s = s_0 \left(\dot{\psi} \big/ \gamma \dot{\varepsilon} \right)^{\beta} \tag{3.7}$$

$$\hat{\tau}_y = s_0 \left(\dot{\psi} \big/ \gamma \dot{\varepsilon} \right)^{\beta} \tag{3.8}$$

where β is a material constant and s_0 and γ are employed for continuity. In order to accommodate the observed increase in strain rate sensitivity at moderate strain rates an additional dependency is included as:

$$\hat{\tau}_y = y_1 \left(\dot{\psi} \big/ \gamma \dot{\varepsilon} \right)^{y_2} \tag{3.9}$$

where y_1 and y_2 are material constants.

The complete model is:

$$\hat{\tau}_s = \max \left\{ s_0 - \left(s_0 - s_\infty \right) erf \left[\kappa \hat{T} \ln \left(\gamma \dot{\varepsilon} / \dot{\psi} \right) \right], s_0 \left(\dot{\psi} \big/ \gamma \dot{\varepsilon} \right)^{\beta} \right\} \tag{3.10}$$

$$\hat{\tau}_y = \max \left\{ y_0 - \left(y_0 - y_\infty \right) erf \left[\kappa \hat{T} \ln \left(\gamma \dot{\varepsilon} / \dot{\psi} \right) \right], \min \left[y_1 \left(\dot{\psi} \big/ \gamma \dot{\varepsilon} \right)^{y_2}, s_0 \left(\dot{\psi} \big/ \gamma \dot{\varepsilon} \right)^{\beta} \right] \right\} \tag{3.11}$$

The model provides a smooth transition between the thermal activation regime and the strong shock regime.

In using the model to describe the <100> single crystal used in this investigation the model parameters were slightly modified to match the low strain rate work hardening behavior for <100> copper displayed in [72]. In particular the work hardening rate, θ, was adjusted to a value of 0.01 and saturation stress, s_0, to a value of 0.0045. All other parameters are as given in [94]. Although the flow behavior is a function of strain, strain rate, and temperature, at very high strain rates the flow stress is essentially at the saturation value for all values of strain. In the shockless region, the temperature, strain, and strain rate from the hydrodynamic solution previously presented were used. In the shocked region, the temperature and strain were taken from the simulations while the strain rates were determined as outlined above (Equation 3.1). It has also been assumed that the flow stress and twinning stress, being dependent on the atomic energy barrier, scale with the shear modulus, as is typical in high pressure constitutive models.

Results of these calculations are presented in Figure 3.28 where the flow stress, as a function of peak drive pressure, for the shockless and shocked region are plotted. The twinning threshold was assumed to vary with pressure (or equivalently density) through the density dependence of *G*:

$$\sigma_T(P) = \sigma_T^0 \frac{G(T,P)}{G_0} \tag{3.12}$$

where σ_T^0 and G_0 are the twinning threshold stress and shear modulus at ambient pressure respectively. It can be seen from the figure that the slip-twinning transition in shock loading is approximately 18 GPa, in agreement with literature [48]. The steep shock loading curve arises due to the high strain-rate dependence on both the shock pressure and flow stress [26]. On the other hand, the isentropic gas-gun condition does not transition into the twinning regime and a critical twinning stress is, therefore, not reached. This is inconsistent with experimental observations, since twinning was observed at ~52GPa. The presence of the shock at the start of the shock pulse (Figure 3.6) for this pressure condition creates a deviation from quasi-isentropic conditions and may account for the presence of the observed twins.

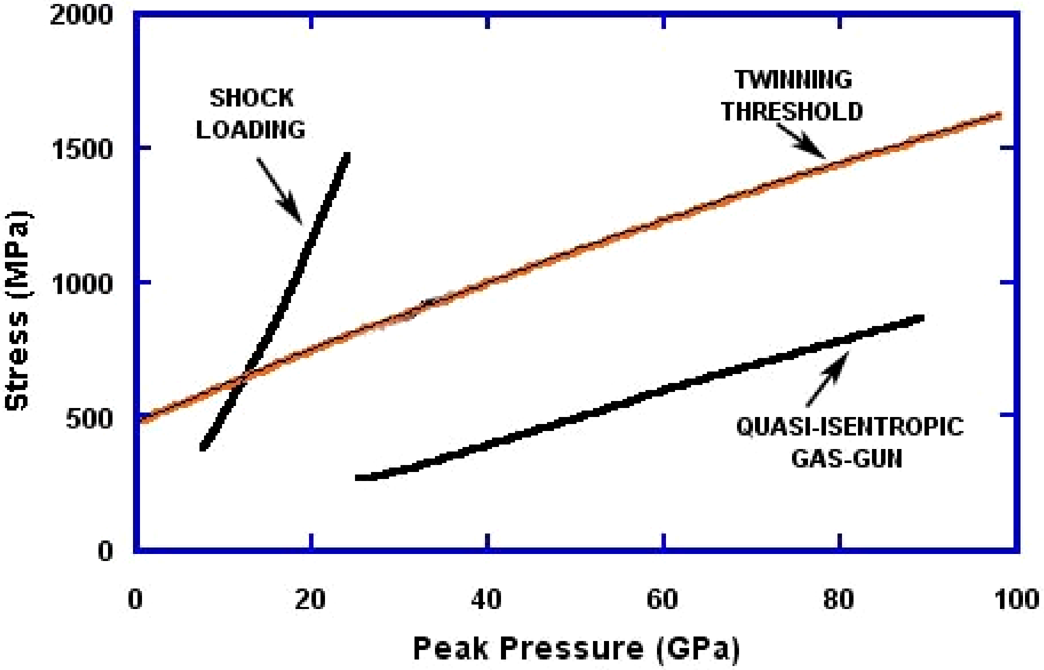

Figure 3.28: Flow stress of [100] oriented copper vs. peak pressure in shock and ICE.

3.6.4.2 Zerilli-Armstrong model

In this model, 300 MPa is the value adopted as the twinning threshold in monocrystalline copper [101], and for simplicity, it is assumed that this value is constant at all imposed pressures (i.e. independent of temperature and strain-rate effects). The dependence of strain-rate on pressure in both shock and ice is given by Equations 3.1 and 3.2, respectively, and the strain (ε) can be calculated from the following momentum balance equation 72:

$$P = \frac{C_0^{\,2}(1-e^{3})}{V_o[1-S(1-e^{\varepsilon})]^2} \tag{3.13}$$

A work-hardening function *f* (ε), however, is incorporated that represents the behavior of the stress-strain curve for monocrystalline copper with the closest orientation to [001]. This polynomial is taken from Diehl [102]:

$$\begin{aligned}\sigma_o f(\varepsilon) = 45510\varepsilon^6 - 86899\varepsilon^5 + 63406\varepsilon^4 \\ - 21834\varepsilon^3 + 2901.8\varepsilon^2 + 464.8\varepsilon - 1.92\end{aligned} \quad \text{MPa} \tag{3.14}$$

The temperature rise associated with shock compression and ICE conditions are established by the following two equations (plots in Figure 3.19 (b)):

$$T_{shock} = 10^{-19} P^2 + 2 \times 10^{-9} P + 295.55 \tag{3.15}$$

$$T_{ICE} = 318.03 + 2.75 \times 10^{-9} \times P \tag{3.16}$$

The constitutive response of copper is given by the Z-A expression below. The values of σ_G, C_3, and C_4 are adopted from [97], and a slight modification to incorporate the strain function, *f* (ε), is made:

$$\sigma = \sigma_G + \sigma_o f(\varepsilon) exp(-C_3 T + C_4 T \ln \dot{\varepsilon}) \tag{3.17}$$

The results of this model are given in Figure 3.28. The Z-A model predicts, just as in the PTW model, that twinning will not occur in the quasi-isentropic experiments, given the range of pressures considered in the experiments. The slip stress never exceeds 300 MPa but is closest at a pressure of 60 GPa (~250 MPa). The evidence of twinning at 52 GPa in the ICE experiments can therefore be attributed to the presence of the initial shock at the onset of the pulse duration. In the case of shock, the twinning threshold is approximately at 30 GPa. This result is in agreement with experimental results obtained by Schneider et al. [48].

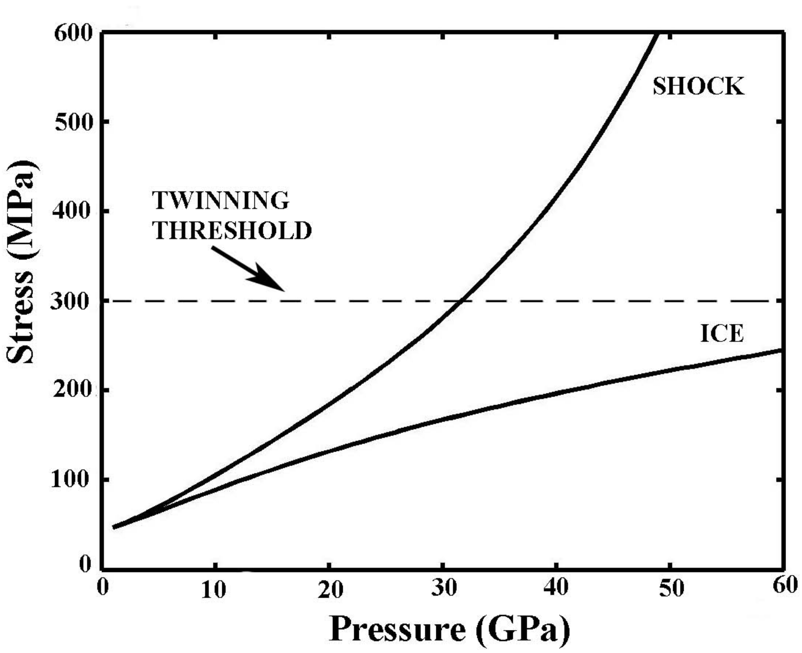

Figure 3.29: Z-A model showing pressure vs. flow stress of [001] copper in ICE and Shock.

3.7 Conclusions

- The deformation features seen in the quasi-isentropic compression experiments of monocrystalline copper are consistent with those seen in laser and flyer-plate shock [73, 92], but the pressures where the features dominate the response are quite different. For instance, the formation of stacking faults and twins occurs at lower pressures in shock as compared to ICE.
- The cell sizes in ICE are also uniformly larger than those left behind from shock (laser and flyer plate) even where the hold times are commensurate.

- The trend in cell size measurements obtained from the gas-gun ICE samples undergoing the long and short pulses reinforces previous observations that pulse duration may not be playing a key role in determining cell-size.
- Our observations on cell-size lead to the proposition that the loading path during ICE, through the lower strain rates and temperatures attained, are having a real effect on the material response and causing production of fewer dislocations.
- The slight shock in experiments 52-L and 34-L caused a deviation from ideal quasi-isentropic conditions and may have been the reason there was a slight inconsistency in the peak pressure-cell size relationship.
- Experiments 44-S and 26-S that were closest to the quasi-isentropic ideal did not exhibit twins, but rather stacking faults, dislocated laths and cells.
- Modeling of the quasi-isentropic compression condition, using the Preston-Tonks-Wallace constitutive equation, revealed that twinning should not occur under the pressure regime investigated in these experiments.
- The presence of twinning in the experiments is attributed to the occurrence of an undesirable shock at the onset of the pulse duration due to the experimental set-up. This shock imparts larger strains and strain-rates, hence, causing twinning.

Chapter 3, in full, is a reprint of the material as it appears in Materials Science and Engineering (A), 2007, Vol. 463, pp. 249-262 (authors and co-authors: H. Jarmakani, J.M. McNaney, B. Kad, D. Orlikowski, J.H. Nguyen, M.A. Meyers).

CHAPTER 4

MOLECULAR DYNAMICS SIMULATIONS AND EXPERIMENTS ON THE SHOCK-COMPRESSION OF NICKEL: FROM MONO TO NANO-CRYSTALS

The main motivation behind studying the behavior of nanocrystalline materials under extreme pressure and strain-rate regimes is to determine their feasibility as target capsules for NIF. They exhibit superior mechanical properties (in some cases a tenfold increase in strength as compared to their coarse grained counterparts) and are less susceptible to hydrodynamic instabilities during implosion. It has been shown that the thickness of the shock front is a function of grain size and pressure; its thickness decreases with decreasing grain size and increasing pressure [103-106]. The enhanced sharpness of the front in nc materials would allow much less oscillations to occur in the front, hence, decreasing the likelihood of forming undesirable instabilities. Nanocrystalline materials also produce smaller fragments during failure, making them very favorable for use as target capsules since they would potentially cause much less damage to the surrounding expensive optics.

In Molecular Dynamics (MD), each atom is treated as a point mass where force rules describe the inter-atomic interactions. Newton’s equations are integrated to advance the atomic positions and velocities, and thermodynamic statistics are extracted from the motion of these atoms. MD simulations of nanocrystalline metals are ideally suited for comparison with laser-shock compression experiments because of similar time and length scales; thus, the combination of experiments and simulations provides valuable insight on the deformation processes involved. It should be pointed out that the difference between mono and polycrystals in MD resides in the absence and presence of grain boundaries, respectively. The box sizes of the largest simulations being run today are approaching ~ 300 nm^3, which is at the upper range of the nanocrystalline range.

4.1 Single Crystals

Molecular Dynamics (MD) simulations of shock phenomena in perfect fcc single crystals have been carried out for just over 25 years [107-109]. Most of the simulations to date have used the Lennard-Jones 6-12 spline pair-potential [110-113] and the more realistic embedded atom method (EAM) many-body potentials for copper [114-118]. Holian and Lomdahl [110] and Germann and co-workers [111, 113] showed, using L-J potentials that, at shock strengths above the Hugoniot Elastic Limit (HEL), shock waves traveling along the [001] orientation resulted in the emission of intersecting Shockley partial dislocations that slipped along all the {111} close-packed planes. Stacking faults were formed since the trailing partial was never released. The large mobility of the partials at the shock front was such that the plastic wave was always overdriven (i.e no elastic precursor observed). This dislocation behavior is very similar to the model proposed by Smith [119], except that partial dislocation loops are emitted in MD simulations rather than perfect dislocations as outlined by the Smith model.

Germann and co-workers [111, 113] further studied shock propagation in the other [110] and [111] low index directions, where they observed rather different behavior. An elastic precursor separated the shock front from the plastic region in the

[111] case, and solitary wave trains were generated followed by an elastic precursor and a complex plastic zone in the [011] case. In both orientations, trailing partials were emitted leading to full dislocation loops bounded by thin stacking fault ribbons. These loops were periodically nucleated at the shock front, as proposed by Meyers [120], since they grew at a slower rate than the plastic shock velocity.

Bringa et al. [117] also studied the effect of crystal orientation on the shock Hugoniot along the low index directions ([001], [011], and [111]) using two EAM potentials for copper [121, 122]. The plasticity in the three orientations was qualitatively similar to that of Germann et al. [111, 113]. Cao et al. [118] investigated the non-symmetric [221] orientation, where a two-wave (elastic and plastic) structure was observed. The deformation features and shock Hugoniot obtained compared very well with experimental results. However, upon compareing the density of the deformation features with experimental observations in recovered samples, they found that dislocation densities in simulations were several orders of magnitude higher. Two reasons were suggested by Cao et al. [12] for the difference: (a) the much shorter rise time in molecular dynamics simulations and (b) the post-shock relaxation and recovery processes that take place in real experiments.

To the knowledge of the authors, only one paper by Kum [123] analyzes the deformation features in shock-compressed single-crystalline Ni along the three low-indexed orientations. Two Morse-type pair potentials and one EAM potential were used in that work. However, the study is limited to one piston velocity and does not calculate the Hugoniot obtained from MD.

4.2 Nanocrystals

In contrast with monocrystals, numerous investigators have carried out molecular dynamics studies of plastic deformation in nanocrystalline metals, e.g. [124-129]. In two classic papers, Swygenhoven et al. [124, 126] studied the response of nc Ni (grain size: 3-12 nm) under uniaxial loading; they observed intergranular sliding at the smaller grain sizes and dislocation emission from grain boundaries at the larger grain sizes. They used the Finnis-Sinclair Ni potential [130]. Schiøtz et al. [125, 128] studied the behavior of nc Cu (grain size: 3-7 nm) under uniaxial deformation and observed softening as the grain size decreased beyond a threshold due to grain-boundary sliding. The effective medium theory was used to describe the forces between the atoms [131, 132]. Yamakov et al. [127] studied nc Al (g.s. 20-70 nm) under tensile loading using a many-body interatomic potential [133] and observed that, contrary to its coarse-grained counterpart, mechanical twinning was a key deformation mechanism.

Studies on the response of nc metals under shock compression are limited to mostly Cu [134-136]. MD shock studies on the shock response of metals having a higher stacking-fault energy, such as Ni and Al, have not been carried out to date. Bringa et al. [134] studied shock compression of nc Cu. An increase in strength during shock loading was observed due to the suppression of grain-boundary sliding under compression, which was identified as being due to a Mohr-Coulomb-like mechanism. As pressure increased, a shift in the maximum hardness to lower grain sizes was observed. However, beyond a critical pressure, increased dislocation activity due to higher temperatures resulted in a drop in strength. Their simulations revealed both perfect and partial dislocations as well as nano-twins.

In this study, we analyze the response of mono and nanocrystalline nickel governed by an EAM potential. The shock Hugoniot in the [001] direction is first determined and compared to experimental results (Section 4.3). Upon verifying the conformity of the potential with experimental results, we then study the effect of shock compression as well as release on nano-crystalline nickel (grain-size 5 and 10 nm). Molecular dynamics results are compared to laser-shock experiments carried out on nc Ni at LLNL [137, 138] as part of the National Ignition Facility (NIF) program (Section 4.8). Analytical constitutive models are utilized to predict the critical pressures at which a stacking-fault transition occurs in single-crystalline Ni (Section 4.5) and a twinning transition occurs in nano-crystalline Ni and compared with MD simulations and experimental observations (Section 4.10).

4.3 Computational Methods

The MD simulations were carried out using the Large-scale Atomic/Molecular Massively Parallel Simulator (LAMMPS) code [139] and a nickel embedded-atom method (EAM) potential developed by Mishin et al. [140]. This potential was fitted to provide a stacking-fault energy of 125 mJ/m^2 [141]. The EAM views each atom as embedded in a host lattice consisting of all other atoms. Each atom in the system is viewed as an impurity that is part of a host of all other atoms. The “embedding energy” of the impurity is determined by the electron density of the host before the impurity is added. The energy of an atom (or impurity) *i* is represented as a function of the electron density at the atom site plus an electrostatic interaction due to the host [142, 143]:

$$E_i = F_i[[\rho_i(R_i)]] + \frac{1}{2}\sum_j \varphi(R_{ij}) \tag{4.1}$$

where ρ_i is the electron density of the host without atom *i*, φ is the short range electrostatic pair potential as a function of the distance R_{ij} between atoms *i* and *j*, and *F* is the "embedding energy", which is a function of the host electron density, ρ_i, induced at site i by all other atoms in the system. The total energy is the sum over all individual contributions:

$$E_{tot} = \sum_i E_i = \sum_i F_i[\rho_i(R_i)] + \frac{1}{2}\sum_{ij} \varphi(R_{ij}) \tag{4.2}$$

Figure 4.1 (a) shows the total energy per atom as a function of the lattice parameter determined by this potential (both in uniaxial and hydrostatic compression), with the minimum at the lattice spacing of nickel, a_o=0.352 nm. Figure 4.1 (b) shows the pressure-specific volume relationship of the potential as well as the experimental Hugoniot obtained from Rice et al. [144]. The potential (in hydrostatic compression) compares fairly well with the experimental data up to pressures of ~ 130 GPa, where it begins to significantly deviate. As a result, we have limited our study to shock pressures below this value. It should be noted that the drop in the P-V relation at V/V_o~0.58 is simply due to the fact that the potential is not defined beyond these values.

The [001] monocrystalline nickel sample consisted of 2 x 10^6 atoms and had dimensions of 17.6 nm x 17.6 nm x 70.4 nm (50 x 50 x 200 unit cells), large enough to calculate the shock Hugoniot and study the early stages of shock-induced plasticity. The

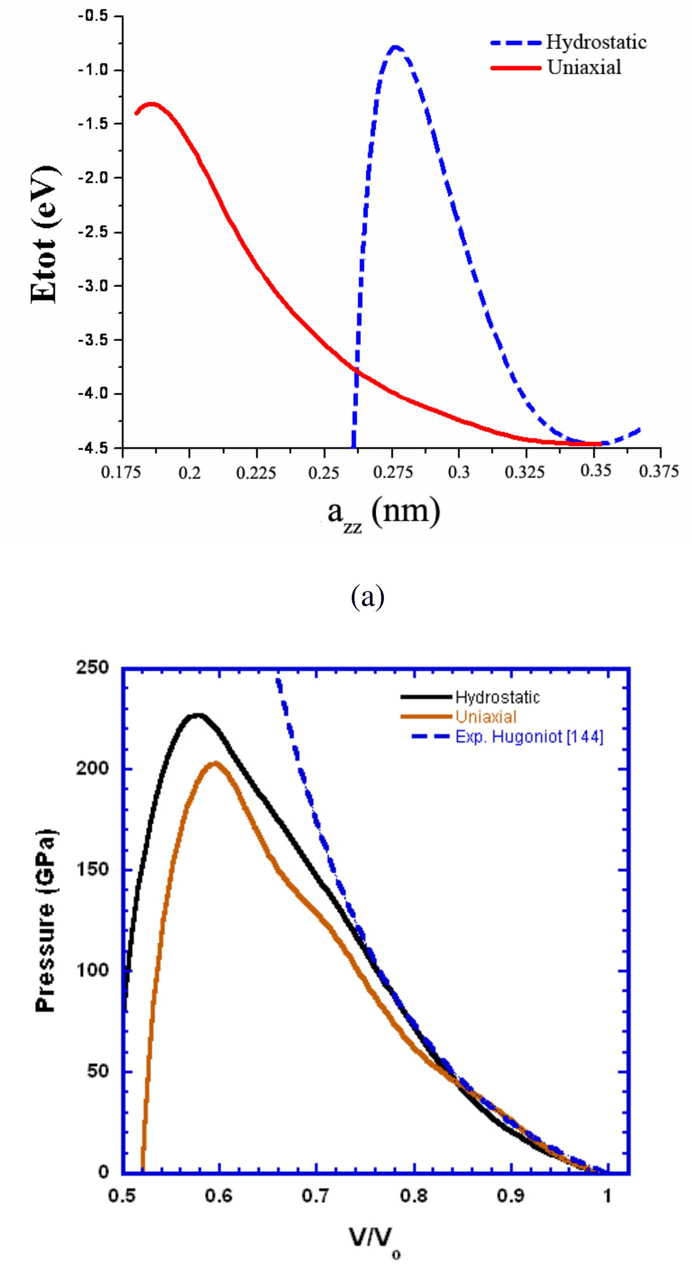

(a)

(b)

Figure 4.1: (a) Total energy per atom versus the lattice parameter defined by the Mishin-Farkas potential; (b) P-V relation of Mishin-Farkas compared with experimental Hugoniot.

three coordinate axes were oriented in the [100], [010], and [001] directions. In order to minimize edge effects, periodic boundary conditions were imposed on the lateral surfaces, and the surfaces normal to the shock-wave propagation direction were set as free surfaces. The shock waves were produced by driving a piston, defined by a few atomic planes, into the sample at a specific velocity U_p, similar to other studies [117, 118]. Two nanocrystalline samples were used in this study, one having a grain size of 5 nm and the other 10 nm. The 5 nm grain-sized sample consisted of 1,980,372 atoms (50x50x200 unit cells, 17.6 nm x 17.6 nm x 70.4 nm), and the 10 nm grain-sized sample had 7,942,605 atoms (100 x 100 x 200 unit cells, 35.2 nm x 35.2 nm x 70.4 nm). Prior to compression, the specimens were first equilibrated to achieve a minimum energy state, and the initial temperature was set as 5 K. The velocity of the shock wave, U_s, was measured by analyzing the shock front propagation in the sample at different time steps, and the shock pressure was calculated from the following Hugoniot relation [145]:

$$P_{shock} = \rho_o U_s U_p \tag{4.3}$$

4.4 Shock Propagation and Defect Generation in [001] Monocrystalline Nickel

The HEL occurs at a shock pressure of ~ 40 GPa, at which stacking faults begin to develop as the key deformation feature. Interestingly, experimental studies have observed twinning to occur in single-crystalline nickel at a comparable shock pressure of ~ 35 GPa [146-148]. Above the HEL, the shock wave splits into an elastic precursor and a plastic front. This behavior is very different from previous MD studies on [001] fcc single-crystals, where the plastic front is usually over-driven [111-113, 117, 118].

Figure 4.2 (a) shows the single front shock wave propagating through the sample at 6, 8 and 10 p, with a particle velocity, U_p, equal to 0.6 km/s, below the HEL; Figure 4.2 (b) shows the two-front wave for U_p ~ 0.9 km/s, above the HEL.

Figure 4.3 (a) compares the P-U_p relationship determined from the current MD simulations with experimental results [120]. Clearly, the P-U_p relationships in both cases are very similar allowing meaningful comparisons between the two. Figure 4.3 (b) presents both the MD and experimental U_s-U_p relations. At a piston/particle velocity of ~ 0.7 km/s (just above the HEL), the U_s for MD case splits into a faster elastic wave and a lagging plastic wave, the average of the two being closer to the experimental U_s data. As the piston velocity increases in MD, the velocity of the plastic wave increases, whereas that of the elastic wave decreases; at a piston/particle velocity of ~ 1.5 km/s, the shock wave becomes overdriven.

It was initially rationalized that this two-wave structure may be the result of the high stacking-fault energy of nickel, causing the second trailing partial to be emitted and slowing down the plastic wave, thereby allowing the elastic wave to lead. But, upon further investigation of the samples, this was found not to be the case. As with previous studies on [001] fcc single crystals, only partial dislocation loops are emitted. Figure 4.4 (a) is a cross-sectional view through a sample shocked with U_p=0.786 km/s (just above the HEL) showing stacking-fault formation behind the shock front. Note the <110> family of directions along which the stacking faults are oriented. Figure 4.4 (b) shows, from a different angle, the formation of the lagging plastic zone (also for the case U_p=0.786 km/s) whereby the elastic precursor outruns the partial dislocations

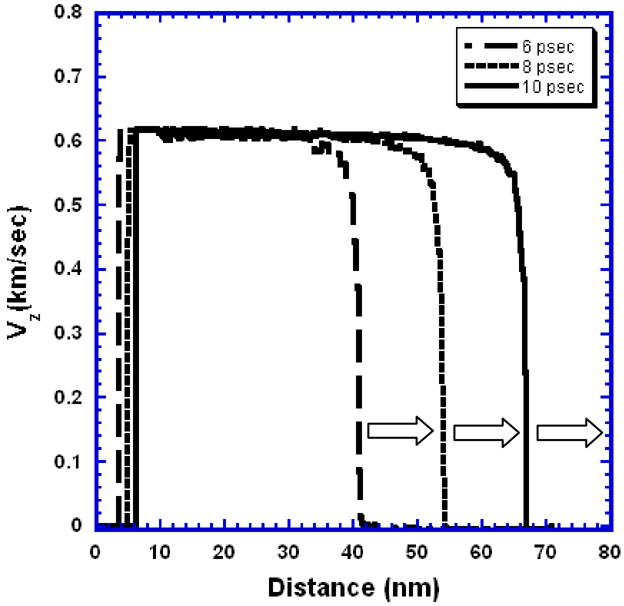

(a)

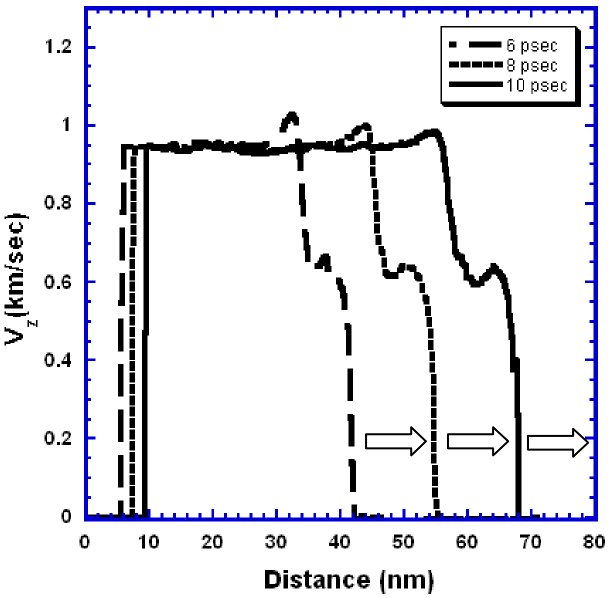

(b)

Figure 4.2: (a) Piston/particle velocity at 6, 8 and, 10 ps versus distance (below the HEL) for P~35 GPa; (b) Piston/particle velocity at 6, 8 and 10 ps versus distance (above the HEL) for P~48 GPa.

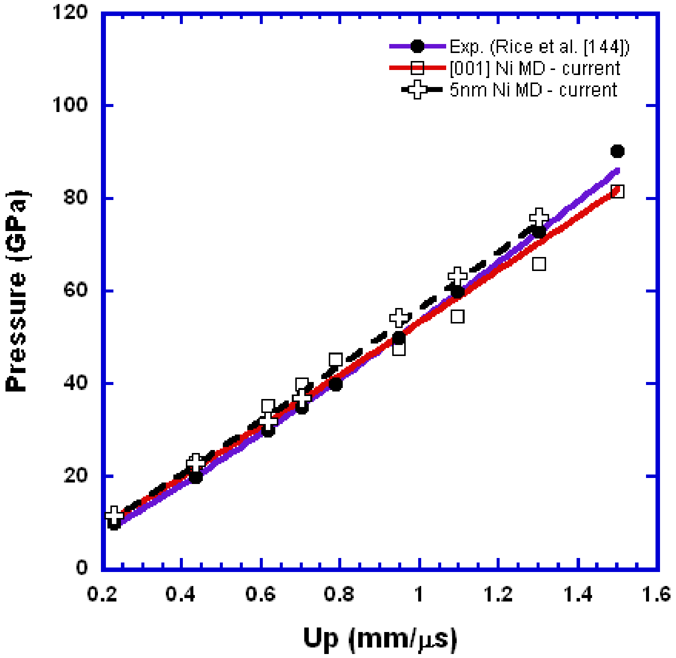

(a)

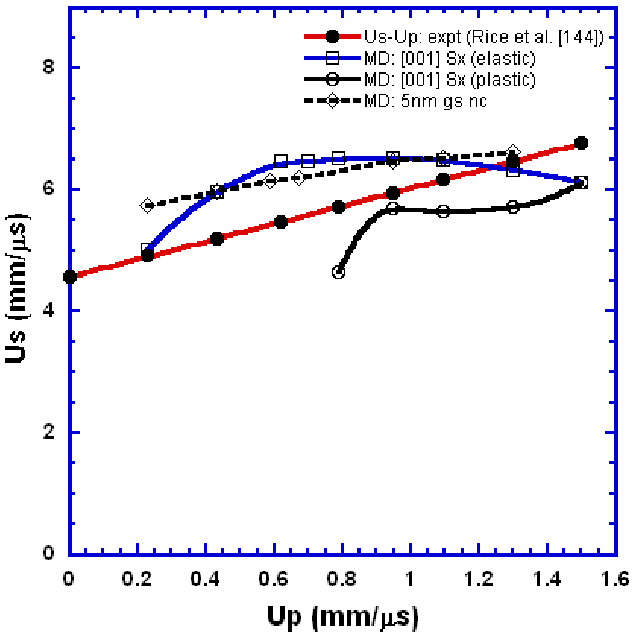

(b)

Figure 4.3: (a) P-U_p relationship for Ni, both MD and experimental data by Rice et al. [144]; (b) U_s-U_p relationship, both MD and experimental data.

and new partial dislocation loops are generated just behind the leading elastic wave front. This picture is analogous to the homogeneous dislocation model [120], reproduced in Figure 4.4 (c). It should be noted that, for better visualization, the "centrosymmetry" parameter is used, to identify defective atoms (dislocation cores and stacking faults). It is of the form [149]:

$$C = \sum_{i=1}^{6} | \vec{r}_i + \vec{r}_{i+6} |^2 \qquad (4.4)$$

where $\vec{r}_i$ and $\vec{r}_{i+6}$ are the vectors from the central atom to the opposite pair of nearest neighbors (6 pairs in fcc system, i.e. the coordination number). Atoms in perfect fcc lattice positions have a C equal to zero, whereas atoms having faulty stacking will generate a nonzero C.

The shear stresses in the sample were studied as the shock pressure was increased. The shear stress was determined by the following equation since off-diagonal terms are negligible:

$$\tau_{shear} = \frac{1}{2}\left[\sigma_{zz} - \frac{1}{2}\left(\sigma_{xx} + \sigma_{yy}\right)\right] \qquad (4.5)$$

where σ_{zz} is the normal stress in the shock propagation direction and σ_{xx} and σ_{yy} are transverse normal stresses. Figure 4.5 (a) shows the z-component of stress (σ_{zz}) and the shear stress plotted against sample depth at 10 ps into the simulation (U_p~0.945 km/s). Figure 4.5 (b) shows that the shear stress in the sample increases up to σ_{zz} ~ 70 GPa, after which it drops. The maximum value of the shear stress, τ_s~7 GPa, is consistent with the stress required to nucleate shear loops, equal to ~ G/10 (for Ni, G=76 GPa).

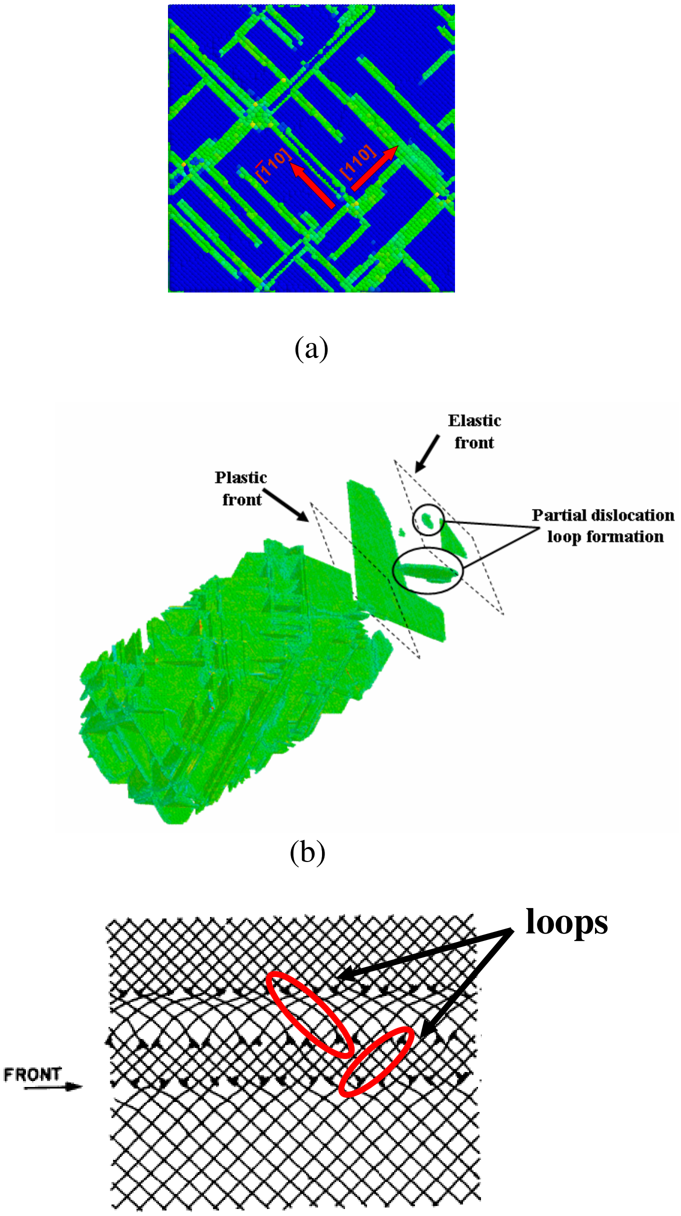

(a)

(b)

(c)

Figure 4.4: Shock compression of Ni along [001]; U_p=0.786 km/s (a) Stacking faults, view along longitudinal z direction; (b) Plastic and elastic zone formation; notice formation of dislocation loops; (c) Dislocation interface in homogeneous generation model [120].

This drop coincides with the HEL (total pressure ~ 40GPa), where plasticity sets in.

The defect spacing as a function of shock pressure was analyzed in order to quantify the induced plasticity, Figure 4.6 (a). Clearly, the stacking-fault spacing decreases as the shock pressure increases. Copper data from Cao et al. [118] are plotted as well. Holian and Lomdahl [110] introduced two fundamental deformation parameters: shock-induced plasticity and shock strength. Shock-induced plasticity is defined as a_o/l, where a_o is the lattice parameter (=0.352 nm for Ni), and l is the average lattice spacing between stacking faults. They defined shock strength as the ratio between particle velocity and speed of sound in the material, U_p/C_o (C_o=4.581 km/s for Ni). This shock-induced plasticity as a function of shock strength is plotted in Figure 4.6 (b). MD data on Cu from Cao et al. [118], predictions from the homogeneous nucleation model of Meyers [120], and experimentally measured data from Murr [84] are also shown on the plot. For the results from Meyers [120] and Murr [84], the dislocation spacing, l, was extracted from the reported dislocation densities ρ, using the equation $l = \sqrt{\rho^{-1}}$. The plasticity data from the current MD results are consistent with those of Cao et al. [118], Holian and Lomdhal [110], and analytical calculations by Meyers [120]. The experimentally-determined shock plasticity of Ni from Murr [84] is, however, lower than the theoretical and MD results by an order of magnitude. This suggests that relaxation processes are clearly at play in real experiments resulting in lower dislocation densities, as will be shown below.

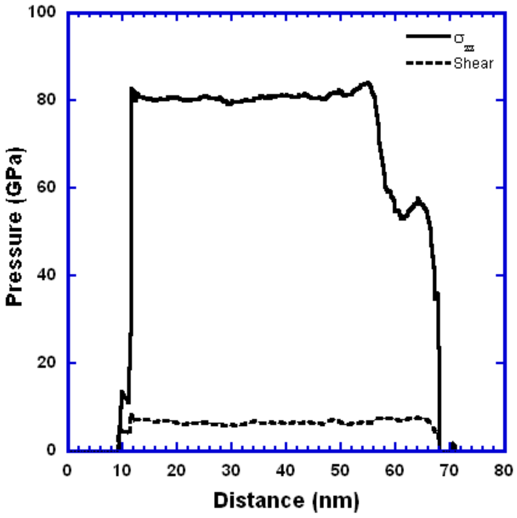

(a)

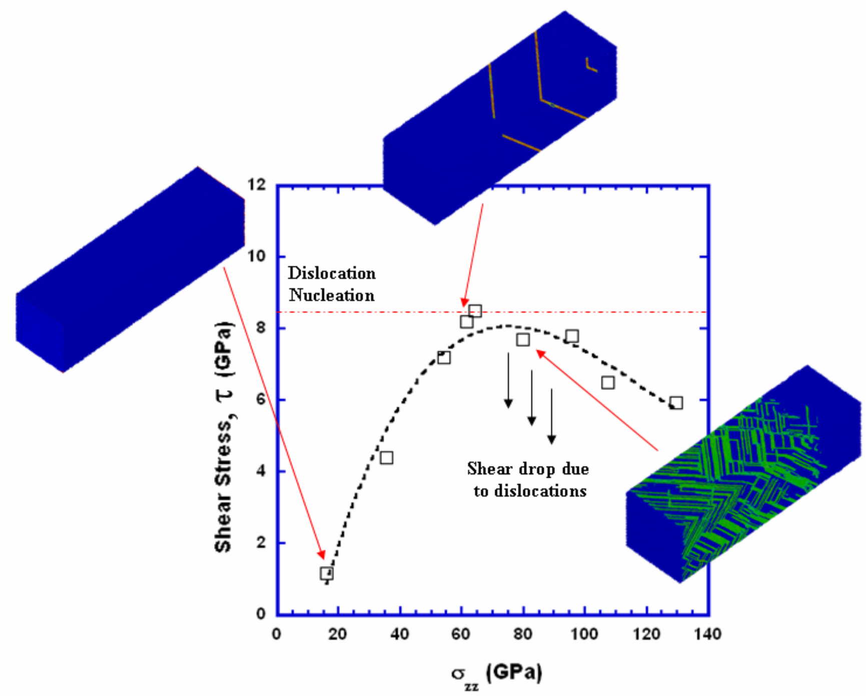

(b)

Figure 4.5: (a) Shear stress and σ_{zz} vs. sample depth, U_p~0.945km/s; (b) Shear stress vs. σ_{zz}.

The effect of release (stress unloading) in the MD simulations was studied for comparison with experiments. The piston was released after 10 ps and the pressure ($P_{tot}=f(\sigma_{xx}, \sigma_{yy}, \sigma_{zz})$)was allowed to retract back to zero. Interestingly, almost all the partial dislocation loops disappear. The spacing between the few remaining stacking faults was measured, and the resulting residual plasticity was calculated. Figure 4.6 (b) shows the MD plasticity after release; an order of magnitude drop is evident, synonymous with the experimental data by Murr [84]. The pressure rise due to compression and the accompanying drop due to release are shown in Figure 4.7 for the case of U_p=1.1 km/s. Only the defective atoms are shown.

4.5 Dislocation Loop Analysis: Stacking-Fault Transition

The nucleation of dislocation loops was first treated by Cottrell [150] and later further developed by Xu and Argon [151], Rice [152], and others. A mechanism was also proposed by Khantha and Vitek [153] for the generation of dislocations under extreme conditions. At pressures above 3 to 3.2 GPa, the activation energy for loop nucleation is lower than the thermal energy; thus, nucleation becomes thermally activated, whereas under conventional deformation at ambient temperature, it is not activated. As previously mentioned, Meyers [120] proposed in 1978 that dislocations in shock compression were homogeneously generated by loop expansion. Figure 4.8 (a) shows shear loops generated on {111} planes making an angle of 54.7º with the shock compression plane, (001). Whereas the nucleation and growth of perfect dislocation loops can lead to the formation of a cellular structure after multiple cross-slip and relaxation of the dislocation configurations, the stacking-fault packets observed in

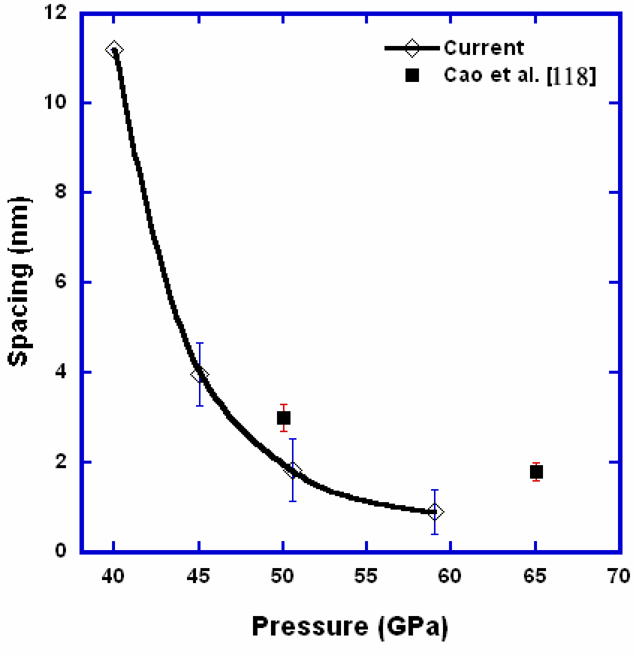

(a)

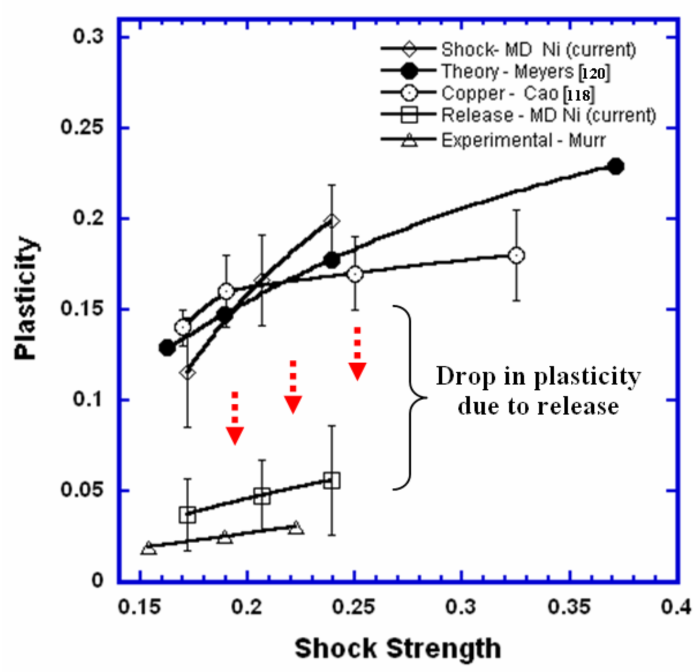

(b)

Figure 4.6: (a) Spacing of dislocations vs. shock pressure; (b) Holian-Lomdahl [110] plot showing plasticity (a_o/l) vs. shock strength (U_p/C_0).

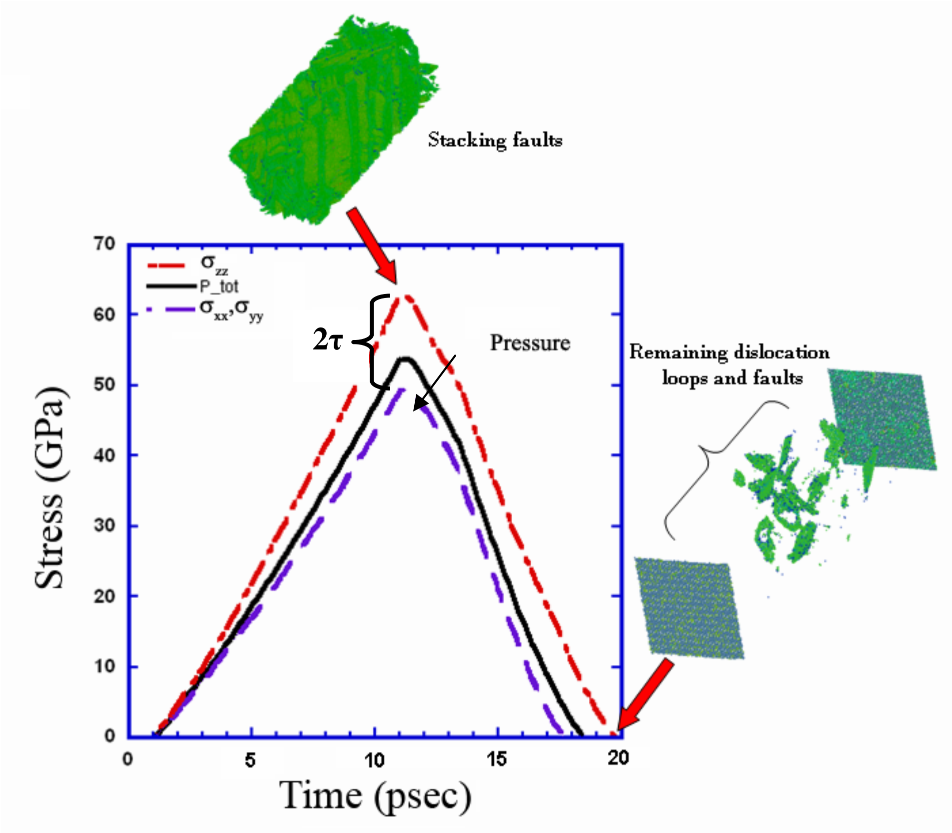

Figure 4.7: P_{tot}, σ_{xx}, σ_{yy}, σ_{zz} vs. time step, U_p=1.094 km/s.

shock-compression above 20 GPa cannot be accounted for by this mechanism. The corresponding nucleation of partial loops is shown in Figure 4.8 (b).

The calculation recently introduced by Meyers et al. [154] for the energetics of nucleation of partial dislocation loops in copper is extended here for nickel. The analytical development is reproduced for the sake of clarity and continuity. The critical radius, r_c (Figure 4.8), can be found from the maximum of the energy *vs* radius curve (Cottrell [150] and Hull and Bacon [155]):

$$\frac{dE}{dr} = 0 \tag{4.6}$$

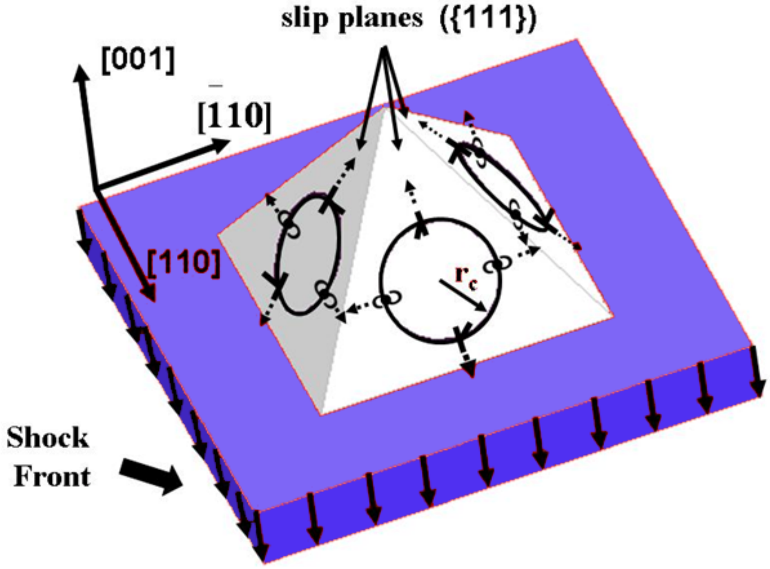

(a)

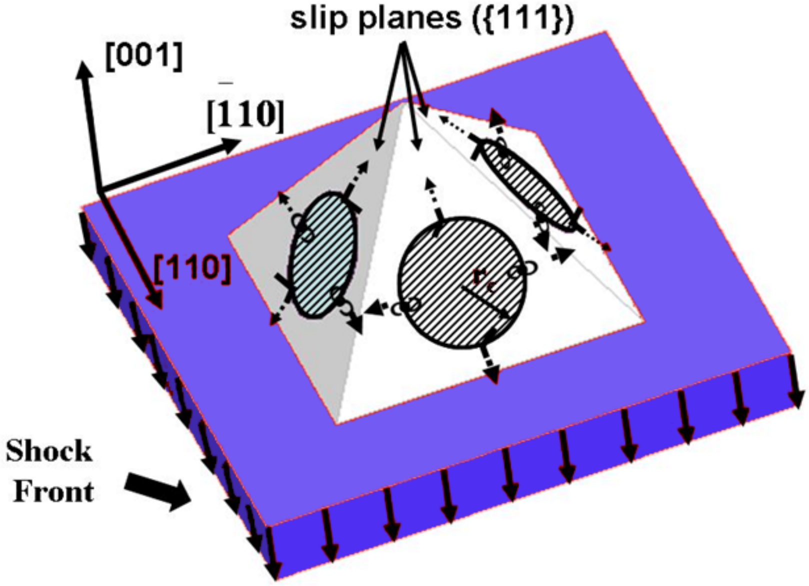

(b)

Figure 4.8: Nucleation of dislocation loops at slip planes behind the shock front, which is in red (propagation along [001]): (a) perfect dislocations and (b) partial dislocations (adapted from [118])

The total energy of a perfect dislocation loop with radius *r* is the sum of the increase of the energy E_1, due to a circular dislocation loop (assumed to be one-half edge and one-half screw), and the work *W* carried out by the applied stress τ on the loop (assumed to be circular):

$$E = E_1 - W = \frac{1}{2} G b^2 r \left(\frac{2-\nu}{1-\nu} \right) \ln \left(\frac{2r}{r_o} \right) - \pi r^2 \tau b \tag{4.7}$$

where *v* is poisson's ratio, *G* the shear modulus, *b* the Burgers vector, and τ the shear stress. The critical radius is obtained by taking the derivative of Equation (4.7) with respect to *r* and applying Equation (4.6):

$$r_c = \frac{Gb}{8\pi\tau} \left(\frac{2-\nu}{1-\nu} \right) \left(\ln \frac{2r_c}{r_o} + 1 \right) \tag{4.8}$$

To obtain the total energy of the partial dislocation loop (Figure 4.8 (b)), both the energy of the stacking fault, E_2, and the work done by the shear stress, *W,* have to be incorporated:

$$E=E_1+E_2-W \tag{4.9}$$

In this case, the energy of the stacking fault has to be accomplished by the generation and expansion of dislocation loops. The shear stresses generated by shock compression are on the order of the stresses required for the nucleation of shear loops Substituting the values of E_1, E_2, and *W* into Equation (4.9):

$$E = \frac{1}{4} G {b_p}^2 r \left(\frac{2-\nu}{1-\nu} \right) \ln \left(\frac{2r}{r_o} \right) + \pi r^2 \gamma_{sf} - \pi r^2 \tau b_p \tag{4.10}$$

where γ_{sf} is the stacking-fault energy and b_p is the Burgers vector for a partial dislocation. The critical radius is obtained by the same method:

$$r_c = \frac{G\left(\frac{b}{\sqrt{3}}\right)^2}{8\pi\left(\frac{\tau b}{\sqrt{3}} - \gamma_{sf}\right)}\left(\frac{2-\nu}{1-\nu}\right)\left(\ln\frac{2r_c}{r_o}+1\right) \tag{4.11}$$

For Ni, we have ν=0.31, γ_{sf} =130 mJ/m^2, and G=76 GPa at zero pressure. G changes with pressure as follows [156]:

$$\mathrm{G}=76+1.37P \text{ (GPa)} \tag{4.12}$$

The Burgers vector, b_o, at P=0 is equal to 0.249 nm; it changes with shock pressure as:

$$b = \left[\frac{C_o^{\ 2}}{2PS^2V_o}\left(\sqrt{1+\frac{4PSV_o}{C_o^{\ 2}}}+\frac{2S(S-1)V_oP}{C_o^{\ 2}}-1\right)\right]^{1/3} b_o \tag{4.13}$$

where C_o is 4.581 km/s, S is 1.44, and V_o is the specific volume of Ni (m^3 /kg) at zero pressure. The shear stress, τ, assuming elastic loading, can be calculated from the shock pressure through Equation (4.6):

$$\tau = -\frac{1-2\nu}{2(1-\nu)}P \tag{4.14}$$

The calculated results are shown in the normalized plot of Figure 4.9 (a) (pressure and critical radius are divided by the shear modulus and Burgers vector, respectively. It can be seen that critical radius for perfect dislocations is lower than for partial dislocations at lower pressures; with increasing of pressure, partial dislocations become more favorable. The predicted transition pressure for Ni is ~27 GPa, close to the experimentally observed twinning transition pressure, 35 GPa [84, 146-148], and about half the pressure at which stacking faults began to appear in our Ni MD study. The predicted transition pressure for Cu, ~ 5 GPa, is also significantly lower than both

MD and experimentally observed results [48, 73]. Experimental evidence for the cell-stacking-fault transition has been gradually amassing for copper, and the TEM micrograph of Figure 4.9 (b) is clear. For Ni, the transition pressure is much higher (27 GPa). This exceeds the critical pressure for twinning (P=16 GPa, calculated in Section 4.10 and is consistent with the absence of stacking-fault observations in shock compressed nickel. Thus one has the following defect regimes as P is increased:

Cu: cells→stacking-faults→twins

Ni: cells→twins

It should be noted that these results are not in complete agreement with our MD computations and previous work [109-113, 158], which predict perfect dislocations for shock along [111] and partials and stacking faults along [001]. Our release simulations do show, however, that very few perfect dislocation loops survive after the stacking faults are allowed to relax (Figure 4.7) as the pressure drops to zero.

The TEM micrograph from Figure 4.9 (b) comes from a quasi-isentropic laser compression experiment at a nominal pressure of 24 GP for a [001] copper monocrystal [157]. One sees adjacent regions of stacking faults and dislocation cells, with a well defined discrete boundary. This was a fortuitous observation and the transition can be caused by pressure or strain rate. Nevertheless, it clearly illustrates the dual nature of the microstructure induced.

4.6 MD Simulations of Shock in Nanocrystalline Nickel

The 5 nm grain-sized sample was subjected to piston velocities between 0.2 km/s and 1.3 km/s, and its Hugoniot was found to be very close to that of the monocrystalline sample. Figure 4.3 (a) shows the consistency of the P-U_p relationship for the 5 nm grain-sized samples with both experimental and single-crystal MD results. The shock velocity, U_s is slightly higher in the nano-crystalline sample, as seen in Figure 4.3 (b). Figure 4.10 (a) provides an illustration of the shock wave for U_p =0.67 km/s as it traverses the sample (average velocity vs. distance). The corresponding shock pressure within the sample is ~38 GPa, which is right at the HEL limit for the monocrystalline sample. Since grain boundaries (i.e. defects) exist in the sample, the HEL is lower than that in the single crystal. A single-wave structure is evident and not a two-wave structure as seen in the single crystalline results. This may be due to the fact that the particle velocities vary from grain to grain, introducing fluctuations in the front that do not allow the plastic and elastic components to be resolved.

In comparison with the single-crystal profiles shown in Figure 4.2 (a), the front thickness is increased from ~ 2 nm to ~ 10 nm. Figure 4.10 (b) shows the nanocrystalline sample at 0 ps after it has been relaxed to minimize its internal energy prior to shock propagation (left) and after the shock-wave has traveled for 10 ps (right). Grain boundaries act as sources and sinks for partial dislocations, leaving stacking faults behind as they travel through the grains. Two of these are marked for clarity. This defect configuration is similar to the one observed by Van Swygenhoven et al. [126, 129] and Bringa et al. [134]. Leading partials are mainly emitted from the grain

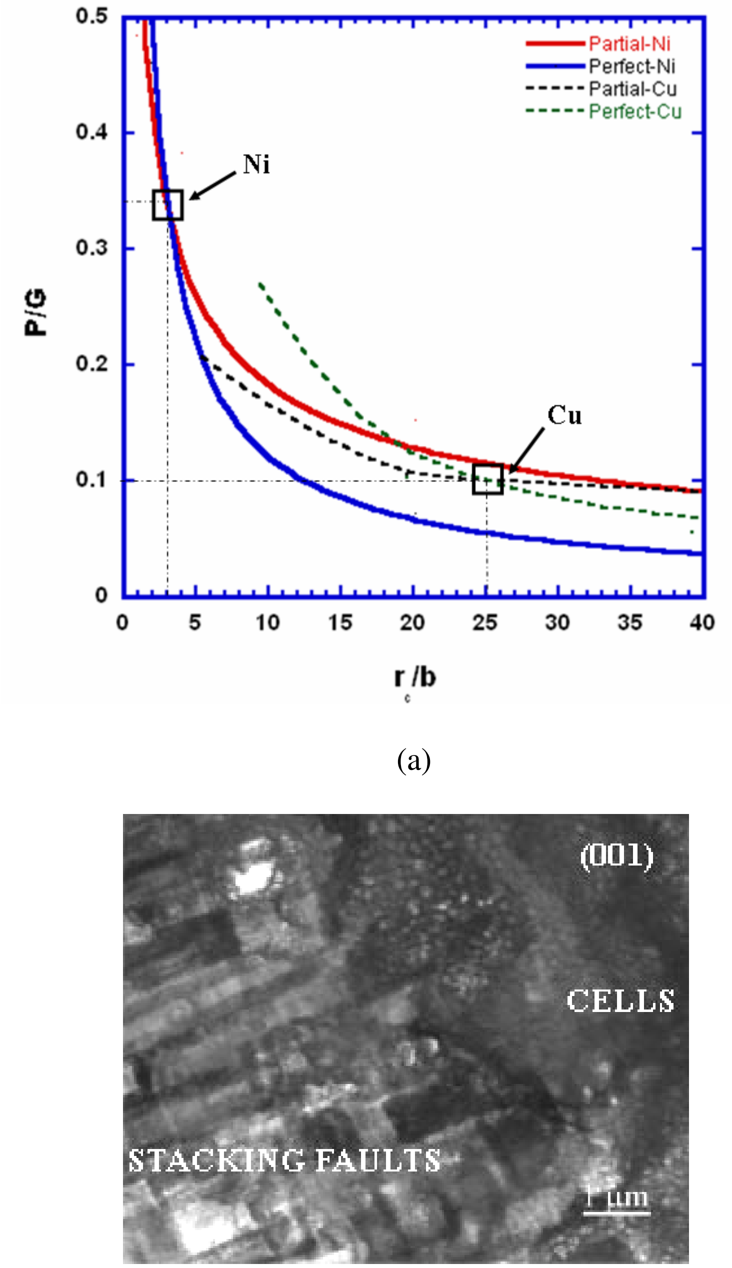

(a)

(b)

Figure 4.9: (a) Critical radius of perfect and partial dislocations for Ni and Cu decreases with shock pressure; (b) Stacking faults and cells in the same TEM micrograph of laser-shocked copper demonstrating that there is a critical value for transition.

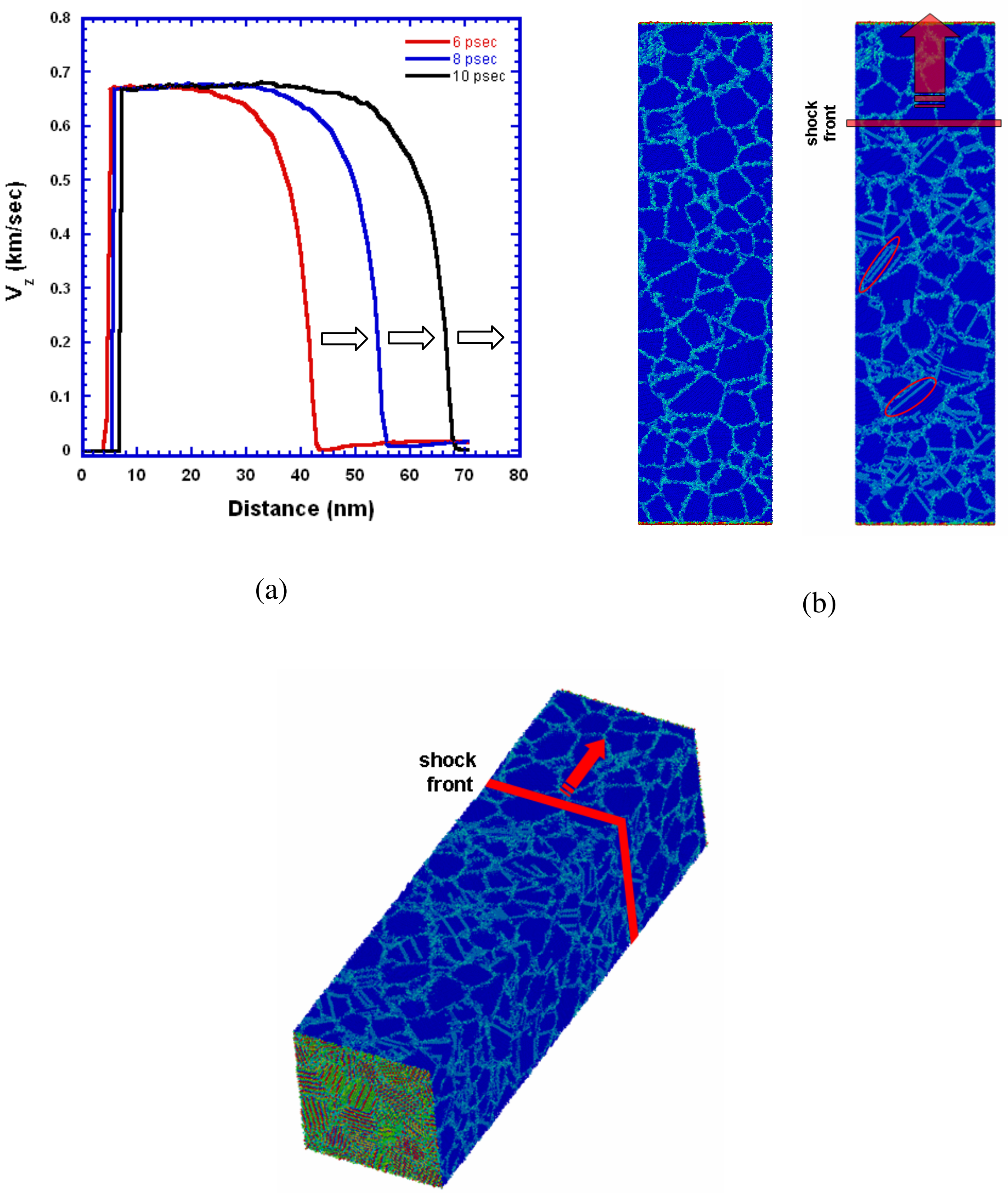

(a)

(b)

(c)

Figure 4.10: Shock compression of nanocrystalline specimen, g. s. = 5 nm, $U_p = 0.67$ km/s; (a) Z-component of velocity vs. distance; (b) 5nm grain-sized sample at 0 ps and 10 ps; (c) 3-D view of sample at 10 ps.

boundaries, and trailing partials are seldom released. Limited evidence of twinning was also observed. Figure 4.10 (c) is a three-dimensional view of the sample.

A quantitative analysis of the deformation mechanisms was carried out on three samples that were shocked using the same piston/particle velocity of 0.67 km/s (~ 38 GPa): 5 nm Ni, 10 nm Ni and 10 nm Cu (Cu Mishin potential [159]). The three samples provide the means to study the effect of grain size and a different potential on the deformation behavior. Contributions to the effective strain introduced by shock compression from the various mechanisms of plastic deformation were calculated by determining the relative motion between nearest neighbor pairs of atoms, and resolving this motion along the strain axis. The procedure to quantify the dislocation contributions to the total plastic strain consists of three steps. The first step locates nearest neighbor atom pairs that have been sheared on glide planes and assigns local Burgers vectors responsible for the shearing. This step requires correction for the strain caused by atom pairs that are cut by multiple dislocations with different Burgers vectors. The second step distinguishes atoms in grain interiors that are cut by lattice dislocations from those that are involved in GB mechanisms. The third step evaluates the strain caused by the motion of the identified dislocations. Detailed procedures can be found in references [160, 161]. Using this method, the contributions from partial dislocations, perfect dislocations, multiple dislocations on the same slip plane, and twinning can be identified. The difference between the total plastic deformation and these other contributions can then be attributed to grain-boundary sliding.

Figure 4.11 shows the three shocked samples. The color code is as follows: the blue atoms are not displaced and are in their original minimum energy state, the green

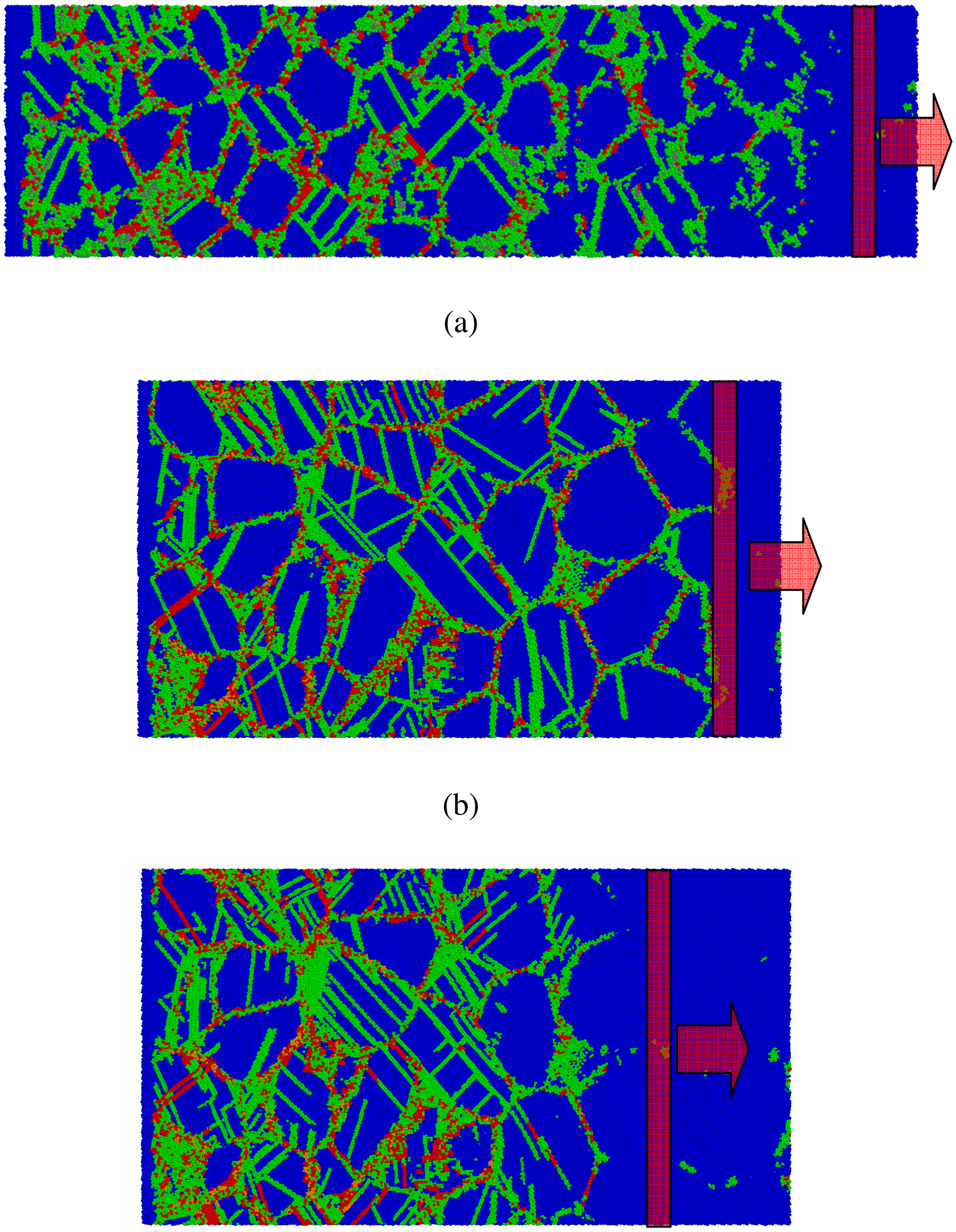

(a)

(b)

(c)

Figure 4.11: Comparison of deformation stucture for same particle velocity of U_p=0.67 mm/μs (a) 5 nm Ni; (b) 10 nm Ni; (c) 10 nm Cu (position of shock front marked for the three samples).

atoms are displaced by the Burgers vector of a Shockley partial, the red atoms are displaced by a burgers vector of a perfect dislocation, and the orange atoms are displaced by a Burgers vector larger than that of a perfect dislocation. Table 4.1 lists the strains due to the different types of dislocations in three samples: 5 nm Ni, 10 nm Ni, and 10 nm Cu. Column (1) gives the strain contribution of twinning; the second and third columns, (2) and (3), provide the contribution due to one partial and one perfect dislocation in a slip plane, respectively. Column (4) provides the contribution of more than one dislocation per slip plane. Column (5) is the total strain due to dislocations (= (2) + (3) + (4) + (5)). The last column (6) gives the strain due to grain-boundary shear. For the 5 nm Ni, the total shock strain in the sample was calculated to be ~ 0.13. Figure 4.12 shows the shock strain as a function of U_p in the mono and nanocrystalline samples as well as the applied strain-rates. Tthe total strain contribution due to dislocations (0.014) is dominated by partials. Partials make up ~ 60 % of the total strain due to dislocations; perfect dislocations account for ~ 10 %. The contribution due to twinning is 26 %. By subtracting the strain due to dislocations from the total strain, one obtains the strain due to grain-boundary sliding, 0.116; this represents approximately 90 % of the total.

In the case of the 10 nm samples, the strain contribution due to partials is 63 % for Ni and 56 % for Cu. Perfect dislocations account for 17 % of the dislocation strain in Ni and 21 % in Cu. The twinning contribution is greater in Cu, 19 % as compared to 16 % in Ni. This is to be expected since the stacking fault energy of Cu is significantly lower. Grain boundary sliding accounts for approximately 58 % of the total strain in both 10 nm Ni and Cu in comparison with ~ 90 % for 5 nm Ni, signifying that it becomes more difficult for larger grains to slide past one another under compression. Note that the front portions of the 10 nm Cu and Ni samples do not show the grain boundaries highlighted in green. This is due to the fact that no grain boundary sliding is taking place because the shock front has not yet traveled through that region. The contribution due to partials is comparable in the 5 and 10 nm grain-sized samples, but that from perfect dislocations is greater in the 10 nm samples. Interestingly, the twinning contribution is greater in the 5nm grain-sized sample (5nm Ni: 25.7 %, 10 nm Ni: 15.7 %). This result is in agreement with the models proposed by Chen et al. [162] and Zhu et al. [45], where they show that propensity for twinning increases with decreasing grain-size.

4.7 Experiments on the Quasi-Isentropic Compression of Nanocrystalline Nickel and Nickel-Tungsten

4.7.1 Experimental techniques

4.7.1.1 Gas-gun quasi-isentropic compression set-up

The two-stage gas-gun set-up described in section 3.1.1 was used for quasi-isentropically compressing nanocrystalline Ni and Ni-W (13 at %) at strain-rates of ~ 10^{4}-10^{5} s^{-1} [82].

4.7.1.2 Laser quasi-isentropic compression set-up

The Omega Laser System at the University of Rochester, NY, was used to generate a smoothly rising pressure pulse in the material (Figure 3.4) as described in section 3.1.2.

Table 4.1: Strain contributions due to various mechanisms in MD specimens shocked at a piston/particle velocity of U_p=0.67 km/s (total strain of 0.13).

	(1) twins (x 10^{-2})	**(2) partials (x 10^{-2})**	**(3) perfect (x 10^{-2})**	**(4) > 1 dis. in slip plane (x 10^{-2})**	**(5) correction factor**	**(6) Total strain due to dislocations (x 10^{-2})**	**(7) Grain-boundary shear (x 10^{-2})**
Ni 5nm (shock)	0.00355	0.0118	0.00142	0.000101	0.00053	0.0138	0.116
Ni 5nm (shock-release)	0.0029	0.0073	0.00182	0.000533	0.00045	0.01	-
Ni 10 nm (shock)	0.0032	0.0159	0.0035	0.000319	0.00059	0.0203	0.075
Cu 10 nm (shock)	0.0042	0.0164	0.0045	0.000352	0.00058	0.0218	0.075

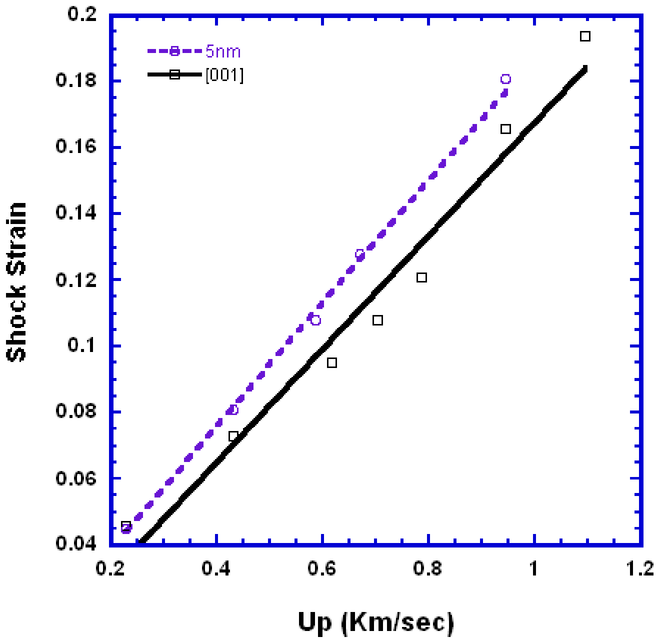

(a)

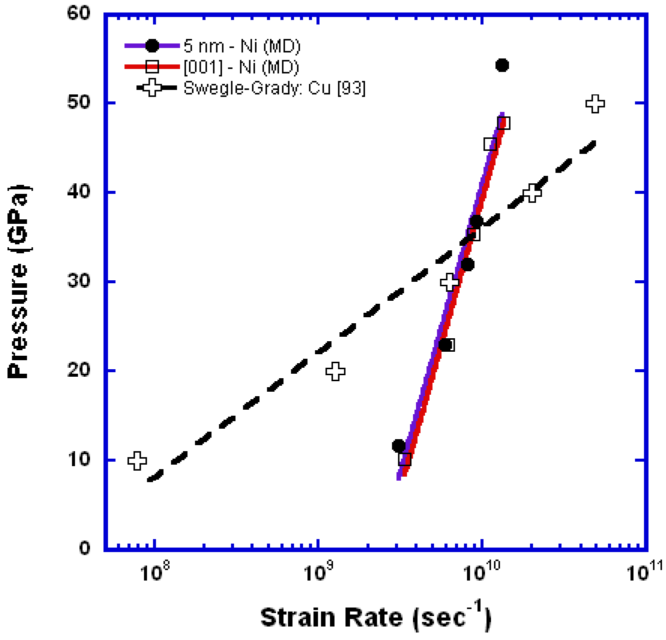

(b)

Figure 4.12: (a) Shock strain vs. piston velocity; (b) Pressure vs. strain rate: comparison between Swegle-Grady relation [93] and MD simulations.

4.7.1.3 Focused Ion Beam (FIB)

An FIB (FEI NOVA 600 Dual-Beam) technique was used to prepare TEM specimens from laser-compressed nc Ni and Ni-W samples. The FIB enables the operator the ability to precisely cut out samples from specified locations beneath the cratered surface. The possibility of introducing artifacts into the specimens was eliminated by also preparing specimens using an electropolishing technique for comparison.

4.7.1.4 TEM

TEM on nanocrystalline nickel and nickel-tungsten was carried out on a Philips CM-300 FEG microscope operating at 300 kV located at Lawrence Berkley National Laboratory.

4.7.1.5 Micro-hardness measurements

Microhardness measurements were performed on all nanocrystalline samples. The samples were sectioned by EDM. After polishing to eliminate the heat affected zone (~ 50 μm on each side) and provide a smooth surface, the cross-section was indented using a Vickers tip attached to a Leco: M-400-H1 microhardness machine.

4.7.2 Experimental results

Nanocrystalline nickel samples having grain sizes between 30 and 100 nm were compressed via the laser ICE [137, 138] and gas-gun ICE drives and subjected to pressures between 20 and 70 GPa. The samples were both purchased from Goodfellow Inc. and made by electrodeposition at LLNL. The technique involved depositing a relatively thick 300 μm nc layer on top of a copper substrate. The Goodfellow samples were also glued to a copper substrate to facilitate shock loading experiments. To further reduce the grain size of the samples to ~ 10 nm, nanocrystalline nickel-tungsten samples were also prepared by Schuh and coworkers [163, 164]. Tungsten (5, 10 and 13 wt. %) was added to the nickel electrolyte during electrodeposition to stabilize the grain boundaries. The Ni-W samples were also quasi-isentropically compressed [138]. Microhardness measurements and transmission electron microscopy analysis on the samples are reported next.

4.7.2.1 Microhardness results

The samples and loading conditions are tabulated in Table 4.2. The as-received samples consisted of a 300 μm nanocrystalline layer that was electrodeposited over a copper substrate. They were in the form of cylindrical specimens having a height of ~7mm and diameter of 3-5 mm. All laser compressed samples exhibited craters at the center of their top surface (~1 mm^2, the size of the laser spot) due to the unloading of the plasma from the reservoir material, Figure 4.13 (a). The depth of the craters varied between 20 and 100 μm depending on the pressure. Microhardness measurements were taken from five locations on the top surface. The samples were then sectioned in half, and 10 measurements were taken from the cross-section, Figure 4.13 (b). The samples that were compressed by gas-gun were not cylindrical. Rather, a rectangular 300μm nanocrystalline layer was detached from the copper substrate and embedded flush in a copper sample 'holder'.

Table 4.2: The various sample types subjected to different loading conditions.

Sample	**Laser ICE Pressure (GPa)**	**Gas-gun ICE Pressure (GPa)**
70 nm NiW	20, 40	-
50 nm Ni	20, 30, 40, 70	20
15 nm NiW	20	-
9 nm NiW	20, 70	20

It was extremely difficult to take hardness readings inside the craters from the top surface because these regions were dimly lit, charred, and highly irregular due to the violent deformation that had taken place. Some regions inside the craters were found, however, where the molten had solidified and created smooth surfaces allowing for accurate measurements to be taken. A 5-40% decrease in hardness was found inside the craters (region E) as compared to the outer regions (A, B, C, D). At ~70 GPa, several samples displayed a 40 % decrease in hardness.

To ensure that cross-sectional measurements were not affected by any surface effects, such as melting/softening, amorphization, due to laser bombardment, readings were taken 50 μm below the top surface. In all cases, a 5-30 % relative increase in hardness was observed underneath the crater as compared to the unshocked regions. The increase in hardness is a strong indicator that dislocations were stored during the high-strain rate deformation process, thus strengthening the nc samples. This is in contrast to quasi-static loading experiments on nanocrystalline materials where this work hardening phenomenon does not occur.

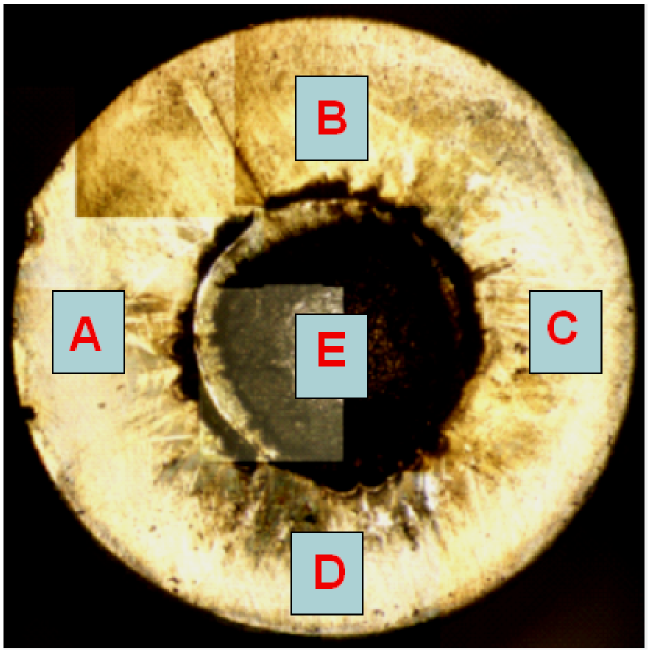

(a)

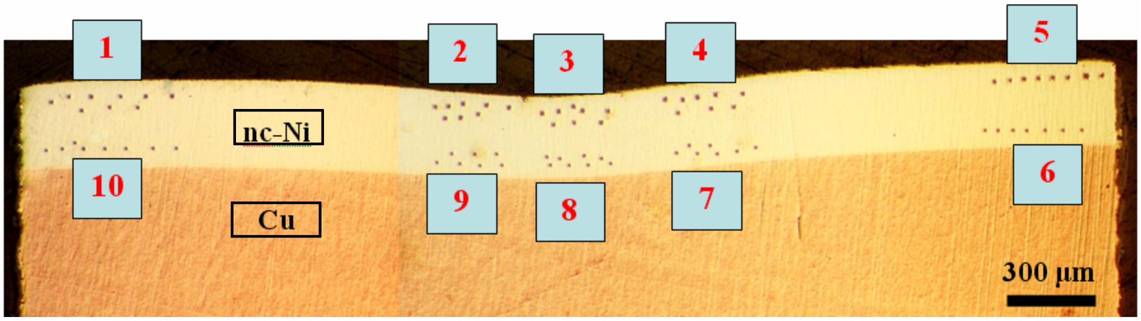

(b)

Figure 4.13: (a) Microhardness measurements from 5 locations on top surface; (b) Microhardness measurements from 10 positions on cross-section.

Figure 4.14 (a) presents the cross-sectional hardness measurements taken from positions 1, 2, 3, 4 and 5 (Figure 4.13 (b)) for the various samples investigated. The increase in hardness at position 3 (underneath the crater) is apparent. It can also be seen that the two 70 nm samples exhibited the highest hardness values followed by the 9 nm, 15 nm and 50 nm samples, respectively. Figure 4.14 (b) summarizes the hardness increase in the laser experiments as a function of pressure for the four grain sizes investigated. There seems to be no grain size effect on the hardening rate.

Two experiments were carried out on an ICE gas-gun setup [82] to study the response of the nano-crystals subjected to the same pressure of 20 GPa at a much lower applied strain rate (~10^4 s^{-1}) (TEM images are not available). Preliminary results show that 50 nm nickel strengthens considerably (~30 %), whereas 9 nm Ni-W exhibits a very slight increase in hardness (~ 2 %). This behavior may be due to the fact that the 9nm Ni-W grains are so small that they are unable to allow for much plasticity to take place. Hence, grain boundary sliding may be the predominant deformation mechanism. Another possibility may be that the grain boundaries are acting as sources and sinks to dislocations and not allowing dislocations to be stored after unloading.

4.7.2.2 TEM: nanocrystalline nickel

As previously mentioned, a dual-beam focused ion beam (FIB) was used to prepare cross-sectional TEM samples. The FIB made it possible to precisely locate and remove samples from regions of greatest interest, 50 μm - 150 μm beneath the center of the crater. The applied pressure pulse is expected to slightly decay and transition into a shock within this depth range. However, TEM images in this range did not show any

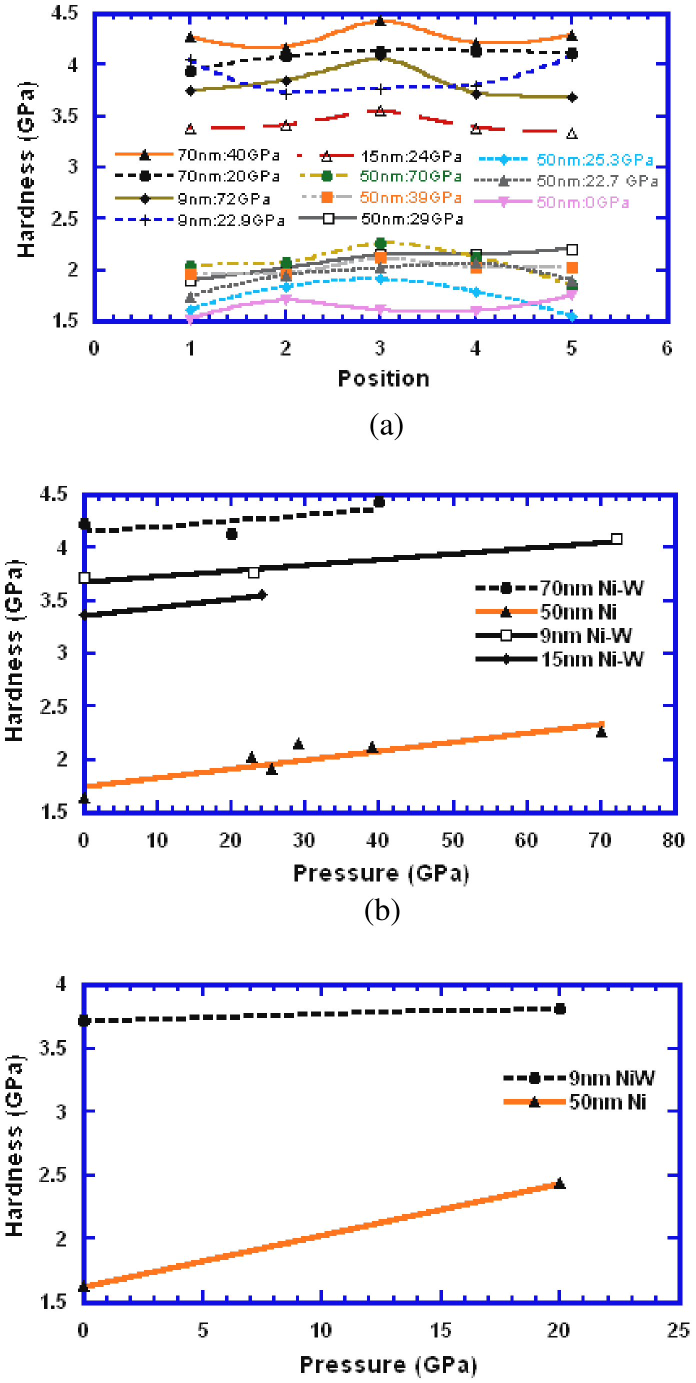

(a)

(b)

(c)

Figure 4.14: (a) Hardness vs. position: cross-section; (b) Hardness vs pressure: Laser ICE; (c) Hardness vs pressure gas-gun ICE.

considerable microstructural differences. The as-prepared samples revealed slightly elongated grains with an average aspect ratio of 2.5, Figure 4.15. This grain structure is typical of the electrodeposition method given the relatively thick nc layer.

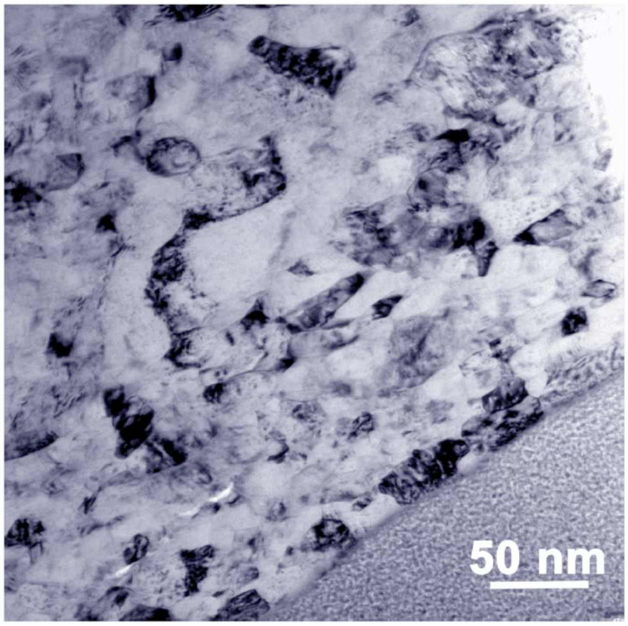

Figure 4.15: As-prepared 30-50 nm nickel showing elongated grains (and an amorphous platinum coating on the lower right to protect the surface during FIB) [137].

TEM images of nickel samples with grain sizes between 30-70 nm laser-compressed to 20 GPa (Figure 4.16 (a)), 40 GPa (Figure 4.16 (b)), and 70 GPa are provided. The samples were taken from 150 μm beneath the crater surface. Heavy dislocation activity was prevalent in all the samples, indicating that dislocations are a carrier of plasticity at these extreme conditions and small grain sizes. Deformation twins were not observed in any of the samples, even at pressures and grain sizes up to 70 GPa and 70 nm, respectively. Twinning will be further discussed and modeled in section 4.10. The 30-50 nm samples shocked at 40 GPa (13 % strain) exhibited a higher dislocation density than that shocked at 20 GPa (8 % strain), consistent with previous studies on pressure effects on dislocation density [48, 84, 91].

The dislocation density estimated for the 40 GPa sample through dark-field images, was ~10^{16} m^2. This is in stark contrast to quasi-static experiments where dislocations are not stored in the material. Dislocations are only observed during in-situ testing [165, 166]. Minor grain growth was observed in the samples, and a thin 10-20 nm amorphous layer was found on one of the samples shocked at 20 GPa, possibly due to melting and the very high cooling rates associated with laser compression.

4.7.2.3 TEM: nanocrystalline nickel-tungsten

TEM images verified that tungsten forms a solid solution with nc Ni and does not precipitate. Again, an FIB was used to remove TEM specimens from specified locations beneath the crater, ~100 μm. Since the pressure decays as the wave propagates through the material, the FIB method allowed for precise pressures from hydrocode simulations to be assigned to the specimen locations. Figure 4.17 is a TEM image of an electrodeposited 15 nm Ni-W sample.

A shift in deformation mechanisms was observed at this much smaller grain size regime of 10-15 nm [138]. Samples shocked at ~ 40 GPa revealed deformation twins as the predominant defect structures, Figure 4.18. A very low density of pre-existing annealing twins was observed in the as-prepared samples. The annealing twin lamellae run parallel to one another whereas deformation twin lamellae are lenticular in shape. The twin density of shock loaded samples increased dramatically after shock loading, verifying that twinning is a key deformation process that takes place at these grain sizes.

However, the addition of tungsten lowers the stacking-fault energy, and the increased twinning cannot be attributed to the decreased grain size alone. The squares in Figure 4.18 identify growth twins, whereas the circles indicate deformation twins. The addition of tungsten decreases the stacking fault energy of nickel, hence, increasing its propensity to twin. This will be further discussed in the modeling section, 4.10.

TEM results on 70 nm Ni-W shocked at 20 and 40 GPa showed deformation twinning as an active deformation substructure. This implies that the change in stacking fault energy due to the addition of tungsten must be playing a key role in determining the modes of deformation in these materials under these extreme conditions. TEM work on the 9 nm Ni-W and 50 nm Ni samples compressed by gas-gun are still not available and are the focus of future work.

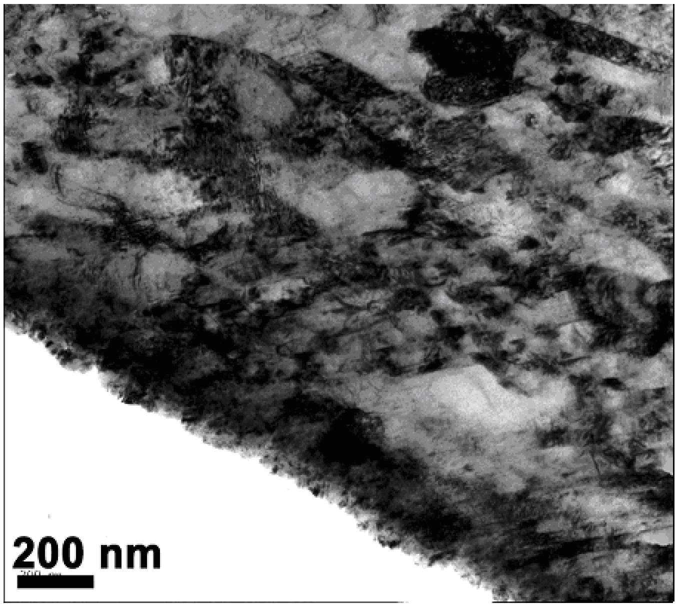

Figure 4.16: TEM of Ni with G. S. of 30-50 nm shocked at ~ 40 GPa showing dislocations.

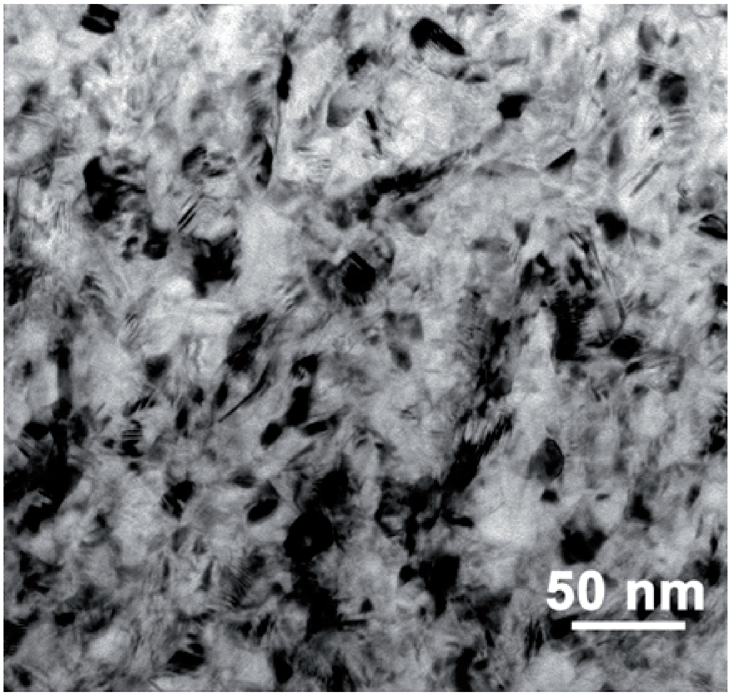

Figure 4.17: Electrodeposited Ni-W sample with grain size of ~10-15nm [138].

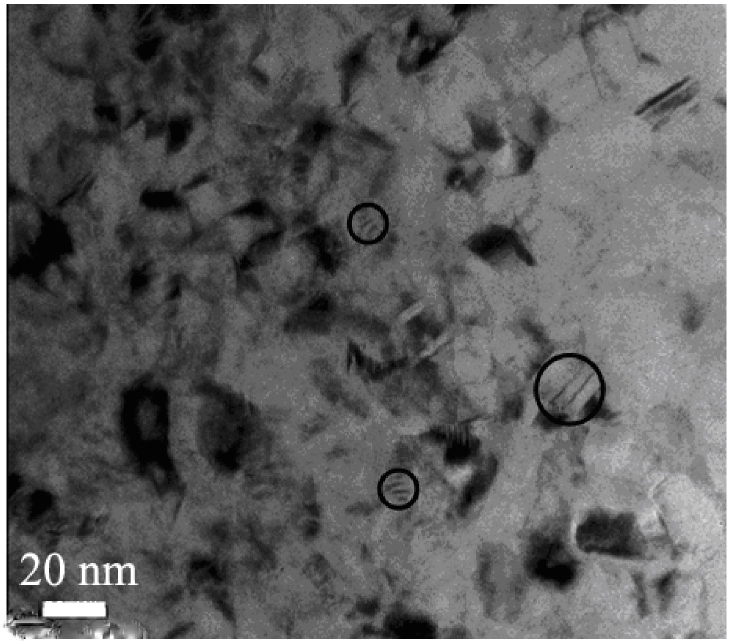

Figure 4.18: TEM of Ni-W (13 at %) with G. S. of 10-15 nm shocked at ~ 40 GPa; deformation twins are evident (circles).

4.8 Comparison of MD with Experimental Results

The dislocation behavior in MD does not give the same trend as in laser-shock experiments. This discrepancy in dislocation behavior between simulations and actual experiments could be due to several factors. The samples in the experiments go through release, which leads to the annihilation and reabsorption of partials. There may be a grain size effect at play. Smaller grains favor partial dislocations, and one may have to go to larger grain sizes for full dislocations to be energetically favorable. The MD potentials may not be very accurate in describing the stacking-fault and twinning energy surfaces, and the value of these surfaces under stress could change considerably. Another possibility may be that the time needed for the emission of perfect dislocation is much longer than the time scales simulated in MD. Loading and unloading in the laser shock experiments take place within ~ 6 and 10 ns, whereas the simulations are in the picosecond range only capturing initial stages of deformation. Warner et al. [167] recently showed that a full dislocation takes much longer than partials and twins to be emitted from a crack tip.

4.9 MD Simulations of Unloading in Nanocrystalline Nickel

In an analogous manner to the unloading MD simulations carried out on monocrystals (Figure 4.7), the effect of unloading on the deformation structure of nc Ni was studied to provide a more realistic comparison with the experiments. The sample shocked at 38 GPa, U_p=0.67 km/s, was allowed to unload and the dislocation behavior within the grains was analyzed. Figure 4.19 (a) shows the average pressure within the sample as a function of time as it is loaded and unloaded. Figure 4.19 (b) shows the sample at 0 ps (before shock), at 11 ps (first ps consisted of equilibration) before it is unloaded, and 18 ps after it has been unloaded to zero pressure. The principal features are stacking faults, which are mostly emitted from grain boundaries during compression. After unloading, ~ 38 % of the partials are reabsorbed. The red circles show regions where partials are reabsorbed and the black circles indicate the partial dislocations that survive after unloading. The reabsorbtion of partials causes the contribution due to perfect dislocations to increase from 10.3 % before unloading to 18.2 % after unloading. This phenomenon would explain the fact that partial dislocations are not observed in the experiments, only full dislocations.

For comparison, a smaller sample having ~ 500,000 atoms and dimensions of 17.6 x 17.6 x 17.6 nm was compressed uniformly in uniaxial strain to a pressure of ~ 38 GPa and then allowed to unload. The final strain and strain-rate applied were the same as that experienced by the shocked sample, the principal difference being that there is no wave propagation in the latter simulations. Figure 4.20 (a) shows the average pressure within the sample as a function of time. The sample was compressed uniaxially for 4 ps to a strain of 0.13, held there for 10 ps, and released back to 0 strain within 4 ps. Figure 4.20 (b) shows the various stages of deformation. Partials are emitted and reabsorbed during this process. Table 4-3 lists the strain contributions due to the various plastic deformation mechanisms in the sample. There are no major differences in defect distribution between uniform and shock compression. The percentage of strain corresponding to grain-boundary sliding is slightly decreased, as can be seen by comparing Table 4-1 and Table 4-3. Interestingly, approximately 39 % of the partials

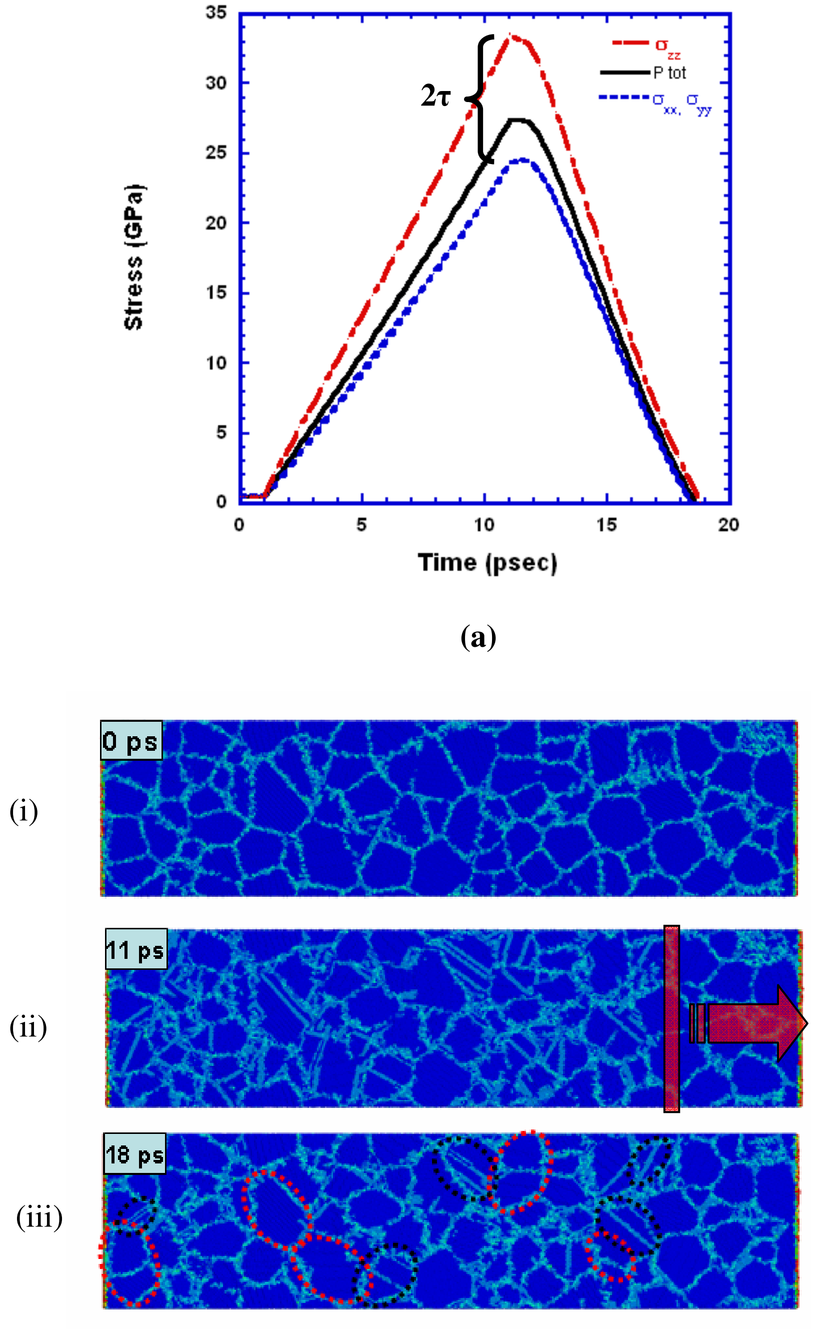

(a)

(b)

Figure 4.19: (a) Average pressure rise and release in sample for U_p=0.67 km/s; (b) Deformation features (i) before compression, (ii) at maximum compression, and (iii) release back to zero pressure.

Table 4.3: Strain contribution due to various mechanisms in MD specimen uniformly and uniaxially compressed to a total strain of 0.13.

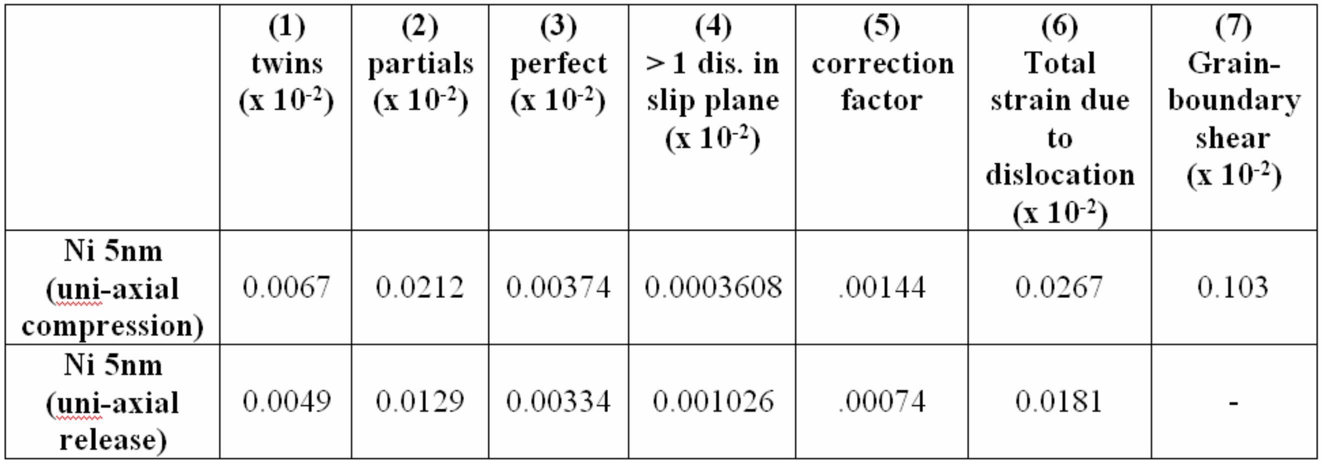

	(1) twins (x 10^{-2})	**(2) partials (x 10^{-2})**	**(3) perfect (x 10^{-2})**	**(4) > 1 dis. in slip plane (x 10^{-2})**	**(5) correction factor**	**(6) Total strain due to dislocation (x 10^{-2})**	**(7) Grain-boundary shear (x 10^{-2})**
Ni 5nm (uni-axial compression)	0.0067	0.0212	0.00374	0.0003608	.00144	0.0267	0.103
Ni 5nm (uni-axial release)	0.0049	0.0129	0.00334	0.001026	.00074	0.0181	-

disappear after unloading. Before unloading, grain-boundary sliding accounts for ~ 79 % of the total uniaxial strain, in comparison with shock compression (~ 90%).

4.10 The Slip-Twinning Transition in Shock Compression

The two most common mechanisms of plastic deformation in metals are slip (or dislocation motion) and deformation twinning; slip is by far more frequent than twinning. Slip simply involves the sliding of atomic planes past each other when a mechanical stress is applied, whereas twinning is a process where a region of the crystal undergoes a homogeneous shear such that the original crystal structure is reestablished in a new orientation. This results in the twinned region becoming a mirror image of the parent crystal by a reflection through a “twin composition plane” [155]. During deformation twinning, twinning dislocations actually play a role as atoms in planes parallel to the composition plane are sheared. Twinning generally occurs at low temperatures, high rates of shear loading, and in conditions where there are few slip systems available to accommodate plastic deformation [16].

Mechanical twins introduce two opposing effects on the response of materials to plastic deformation. They further subdivide the grains and increase the number of dislocation barriers, hence, increasing the work-hardening rate [168]. Conversely, they allow a means for the material to plastically deform via twinning shear, reducing the work hardening rate [169].

The primary aim of this section is to provide a constitutive description of the onset of twinning in nickel and nickel-tungsten subjected to shock compression. The parameters affecting slip and twinning will be discussed first, followed by modeling of

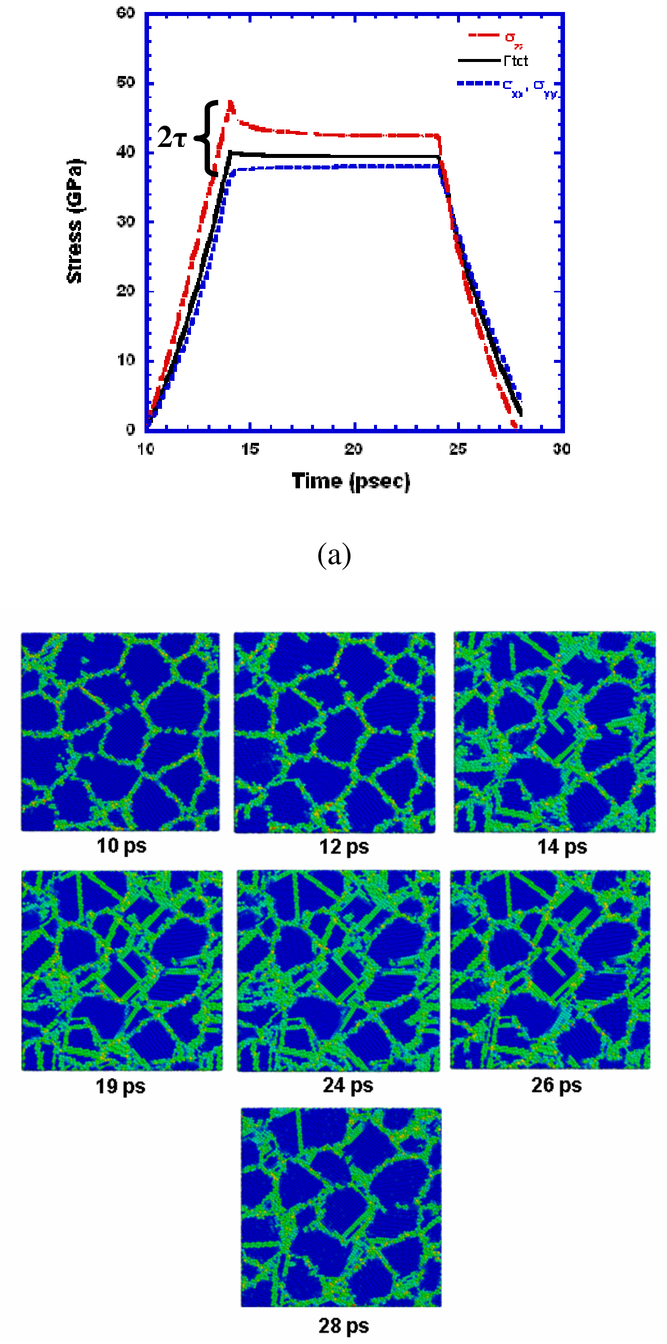

(a)

(b)

Figure 4.20: (a) Uniaxial compression and relaxation of 5nm grain sized Ni sample; (b) Frames at different times showing emission and annihilation by reabsorption of partial dislocations into grain boundaries.

the onset of twinning in both materials. Predictions of the model are compared to experimental work carried out on nanocrystalline nickel and nickel-tungsten at LLNL [137, 138].

4.10.1 Modeling of slip in nickel

The constitutive response for slip of FCC metals is well modeled by the Zerilli-Armstrong constitutive description [97], which captures the essential physical phenomena:

$$\sigma_{slip} = \sigma_G + C_2 \varepsilon^n \, exp(-C_3 T + C_4 T \, ln \, \dot{\varepsilon}) + k_s d^{-1/2} \qquad (4.15)$$

Where σ_G is the athermal component of stress, ε the strain, n the work hardening exponent, d the grain size, T the temperature, k_s the Hall-Petch slope, and C_2, C_3 and C_4 are constants. For Ni, σ_G=48.4 MPa, C_2=2.4 GPa, C_3=0.0028 K^{-1}, C_4=0.000115 K^{-1}, and k_S=0.2 MN/$m^{3/2}$. The strain-hardening exponent n of the nc Ni samples was simply equated to 0 as determined by measurements carried out on the same material by Choi et al. [170]. The values of C_3 and C_4 used are those for copper [97] since data on Ni was not available. The nickel Hall-Petch slope for slip, k_S, has been established by several researchers [171-173]. Asaro and Suresh [174] compiled hardness data for nickel spanning both the micrometer and nanometer regimes. A k_S value of ~0.2 MN/$m^{3/2}$ was calculated from that set of data. Stress-strain plots of nickel with micrometer sized grains from Andrade [175] were utilized to establish C_2. The current model predicts a yield strength of ~ 1.9 GPa for Ni having a grain size of 30 nm, which is in good agreement with the literature [176, 177].

4.10.2 Modeling of slip in Ni-W, 13 at. %

Roth et al. [178] obtained the increase in yield stress in Ni as a result of alloying with different elements. They estimate that the flow stress of Ni increases from 100 MPa to approximately 450 MPa due to the addition of 13 at. % W. A plot of the increase in flow stress of Ni with tungsten content is shown in Figure 4.21 (a). The data was extracted from work carried out on Ni having a grain size between 100 µm and 300 µm. The effect of solid solution addition on the yield stress increment is:

$$\Delta\sigma_{SS} = \Big(\sum_i K_i^{1/m} C_i\Big)^m \tag{4.16}$$

where m is ~ 1/2 , K_i is the strengthening constant for solute *i,* and C_i is the concentration of solute *i* (for W, K_i=977 MPa at. fraction $^{-1/2}$). The Zerilli-Armstrong equation as a function of tungsten content is obtained by adding the solid-solution term into the athermal component of stress:

$$\sigma_{slip} = \sigma_G + \Big(\sum_i K_i^{1/m} C_i\Big)^m + C_2\varepsilon^n \exp(-C_3 T + C_4 T \ln\dot{\varepsilon}) + k_s d^{-1/2} \tag{4.17}$$

The strain hardening exponent, *n*, for the nanocrystalline Ni-W samples was again equated to 0 [170]. The Z-A model predicts a yield strength of ~2.2 GPa for Ni-W with a grain size of 10 nm, very close to the 2.38 GPa value reported by Choi et al. [170]. The Hall-Petch slope for Ni-W was estimated using yield strength data on Ni-W samples having grain sizes in the micrometer regime and micro-hardness measurements carried out on the nc Ni-W samples. A k_S value of 0.1 MPa/m$^{3/2}$ was estimated.

4.10.3 Modeling of Twinning

Despite the fact that dislocation activity is directly associated with twinning, slip by dislocation motion is much more sensitive to strain rate and temperature [179-182], whereas twinning is much less sensitive to these parameters [183]. Figure 4.21 (b) shows the twinning shear stresses as a function of temperature for a number of metals. It clearly indicates that the twinning stress is temperature insensitive over the range considered. This trend is actually still subject to debate, as results have been conflicting. In their review article on mechanical twinning, Christian and Mahajan [184] proposed that BCC metals have a negative dependence of twinning stress on temperature, whereas FCC metals have a weakly positive dependence. In the analysis on the onset of twinning that follows, it is assumed that the twinning shear stress is insensitive to temperature, pressure and strain rate.

4.10.4 Grain-size and stacking-fault effects on twinning

The effect of grain size on the twinning stress has been found to be greater than that on the slip stress for many metals and alloys [185]. A Hall-Petch relationship can, thus, be ascribed to the twinning stress:

$$\sigma_T = \sigma_{To} + k_T d^{-1/2} \tag{4.18}$$

where k_T is the twinning Hall-Petch slope (higher than the k_S slope for slip), σ_{To} is the initial twinning stress assumed for a monocrystal $\left(\lim_{d \Rightarrow \infty} (d^{-1/2}) = 0 \right)$, and d is grain size. Haasen [186] carried out low-temperature tensile tests on mono-crystalline Ni and observed twinning at 4.2 K and 20 K at a shear stress considerably higher than that for

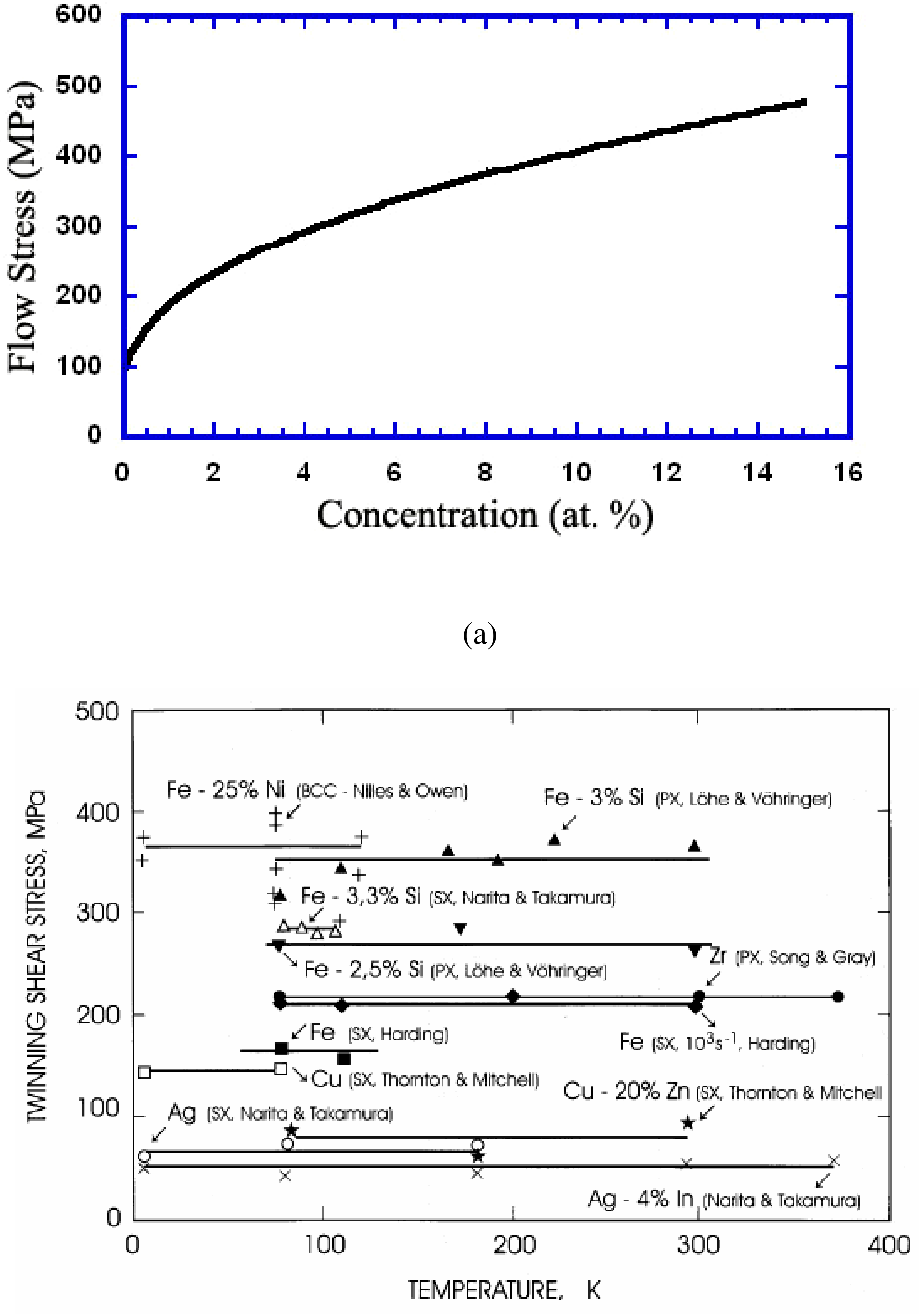

(a)

(b)

Figure 4.21: (a) Slip stress of Ni as a function of the concentration of W (at %); (b) Twinning stress as a function of temperature for a number of metals-both mono and polycrystals (from Meyers et. al. [183]).

copper. This shear stress was estimated to be equal to 250-280 MPa, which is equivalent to a normal stress, σ_{T_o}, of 500-560 MPa.

Meyers et al. [187] conducted shock compression experiments on copper up to pressures of 35 GPa. They detected an abundance of twins for grain sizes between 100 and 300 μm, but found no traces of twinning at a grain size of ~ 10 μm. Similar results were obtained by Sanchez et al. [188]. Vöhringer [189] established that the twinning Hall-Petch slope for copper, k_T, is ~0.7 MN/m$^{3/2}$, which is significantly higher than that for slip, k_S ~0.3 MN/m$^{3/2}$. In the present modeling of nickel, it is assumed that k_T for nickel is three times k_S. Thus, a k_T value of 0.6 MN/m$^{3/2}$ is used for Ni.

Solid-solution strengthening and stacking-fault energy effects are incorporated into the slip-twinning model as a result of alloying with tungsten. The addition of solute atoms hinders the movement of dislocations, hence creating a strengthening effect [190]. Alloying also significantly reduces the stacking fault energy, γ_{SF}. For instance, it has been shown that the stacking-fault energy of copper decreases by nearly 50 % by the addition of 2 wt. % aluminum [141]. This effect is related to the change in the electron to atom ratio (e/a). Partial dislocations are under elastic equilibrium, where the repulsive forces between the bounding partials are balanced by the forces needed to minimize the stacking fault area and maintain a minimum energy configuration. Thermodynamically, alloying can alter the difference in the free energy between the HCP (stacking fault ribbon) and FCC structures and, therefore, the energy of the ribbon between two partials as well as their separation.

It is well-established in the literature that the twinning stress, τ_T, varies with stacking-fault energy (Narita and Takamura [191]). Venables [192, 193] and Vöhringer [194, 195] performed extensive analysis on the twinning stress for a number of alloys and found that it varies with the square root of the stacking-fault energy:

$$\tau_T = k\left(\frac{\gamma_{sf}}{Gb_S}\right)^{1/2} \tag{4.19}$$

where, k is a proportionality constant and G is the shear modulus. Equation (4) has been incorporated into our analysis. A k value of 6.8 GPa was estimated for nickel alloys. The shear modulus and stacking-fault energy of Ni as a function of tungsten concentration can be found in work by Tiearney et al. [196]. At 13 at. % tungsten content (that present in the nc Ni-W samples), a shear modulus of 88 GPa and stacking-fault energy of 52.5 mJ/m^2 (60% drop in *SFE*) are reported.

Assuming a twinning Hall-Petch slope three times that of slip, a k_T value for Ni-W equal to 0.3 MPa/ m$^{3/2}$ is obtained. Just as in the case of pure Ni, a Hall-Petch behavior accounting for the effect of grain size on the twinning stress is adopted in predicting the critical twinning transition pressure in Ni-W (13 at. %). The following expression for the twinning stress was used:

$$\sigma_T = k\left(\frac{\gamma_{sf}}{Gb_S}\right)^{1/2} + k_{T_{NiW}} d^{-1/2} \tag{4.20}$$

For Ni-13 at. % W, k =6.8 GPa, $k_{T_{NiW}}$ =0.3 MPa, γ_{sf} = 52.5mJ/m^2, G=88 GPa, b_S =0.249 nm.

4.10.5 Critical pressure for the slip-twinning transition

In this analysis, it is assumed that the transition from slip to twinning occurs when the shear stress for twinning, τ_T, becomes equal to or less than the shear stress for slip, τ_S:

$$\tau_T \le \tau_S \tag{4.21}$$

If one uses the same conversion parameters:

$$\sigma_T \le \sigma_S \tag{4.22}$$

This is a reasonable approximation since both mechanisms are subjected to the same stress system at the shock front. It should be mentioned that the criterion described here is based on the critical shear stresses for slip and twinning; the pressure only enters insofar as it determines the shear stress and strain rate.

We assume the twinning stress, σ_T, to be pressure and temperature independent. The dependence of shock pressure on strain rate for Ni, obtained through the Swegle-Grady relationship [93], is not available in the literature. As an approximation, the strain rate versus pressure behavior of copper is adopted. The reasoning for this approximation is that Al and Cu, both FCC metals, have a strain-rate response to shock pressure that is very comparable even though the stacking fault energy of Al is much higher. One would expect that the behavior of Ni should not significantly deviate from that of Al and Cu. Thus, the Swegle-Grady relationship for Ni is given by Equation 3.1.

Two separate aspects have to be considered in the analysis: (a) plastic strain at the shock front and (b) shock heating. Both plastic strain by slip (and associated work hardening) and shock heating alter the flow stress of a material by slip processes and need to be incorporated into the computation. The total (elastic + plastic) uniaxial strain, ε, at the shock front is related to the change in specific volume by [145]:

$$\frac{V}{V_0} = e^{\varepsilon} \tag{4.23}$$

The pressure dependence on strain, determined from Rankine-Hugoniot equations, equation of state, and Equation (4.23) is expressed as follows [145]:

$$P_{shock} = \frac{C_0^{\,2}(1 - e^{\varepsilon})}{V_o[1 - S(1 - e^{\varepsilon})]^2} \tag{4.24}$$

The associated temperature rise in Ni as a function of shock pressure is represented by Equation (4.25), which is a polynomial that was generated from thermodynamically calculated data in [145]:

$$T_{shock} = 8 \times 10^{-20} \times P_{shock}^{\;\;2} + 9 \times 10^{-10} \times P_{shock} + 301.5 \;\; K \tag{4.25}$$

For Ni-W, the temperature rise and strain associated with a given shock pressure are determined just as outlined in the case for pure Ni.

Figure 4.22 (a) shows both the slip stress, σ_S (incorporating thermal softening, strain-rate hardening, and work hardening) and σ_T as a function of pressure. The point at which the horizontal line determined by σ_T, Equation (4.18), intersects the slip stress at a given shock pressure, is defined as the critical twinning transition pressure. This transition pressure for nickel having a grain size of 30nm was found to be ~ 78 GPa, This result is consistent with the fact that twins are not observed in experiments up to

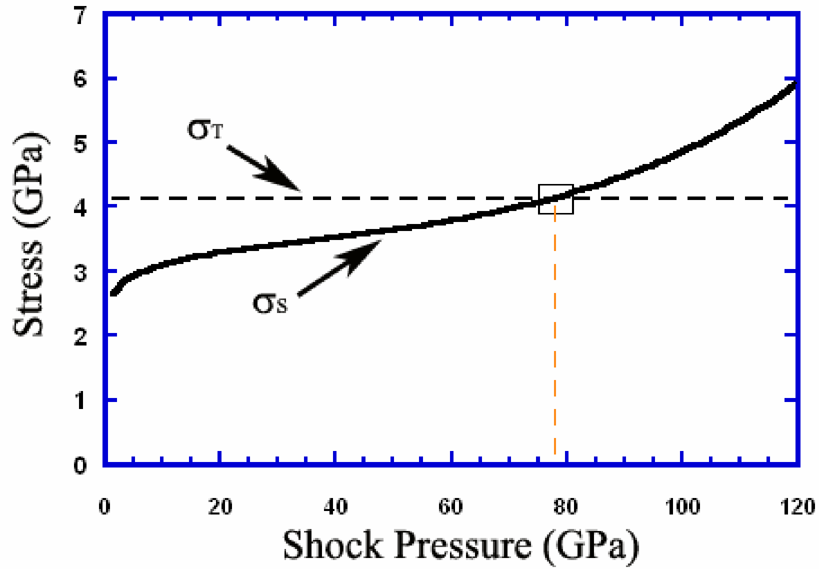

(a)

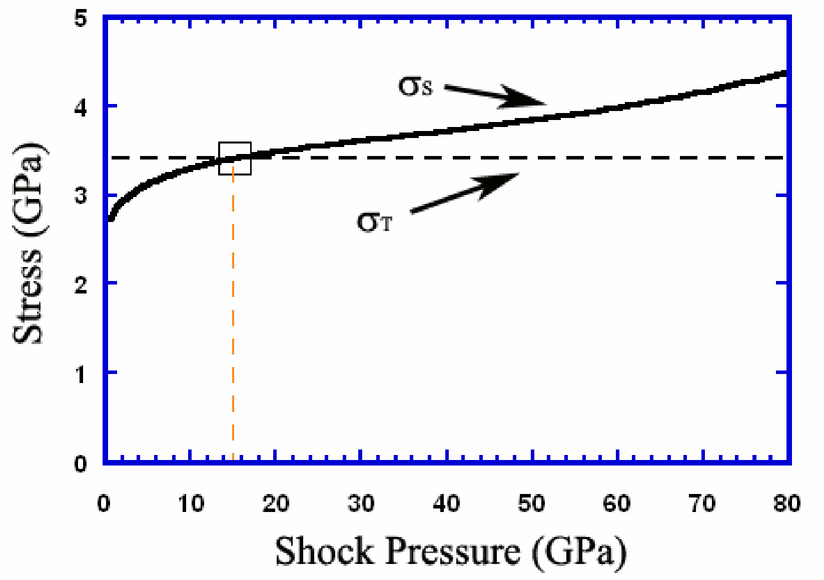

(b)

Figure 4.22: (a) Slip and twinning stress vs. shock pressure for nanocrystalline nickel (g. s. = 30nm); twinning threshold ~78 GPa; (b) Slip and twinning stress vs. shock pressure for Ni-W (13. at. %) having a grain size of 10nm; twinning transition takes place at ~ 16 GPa.

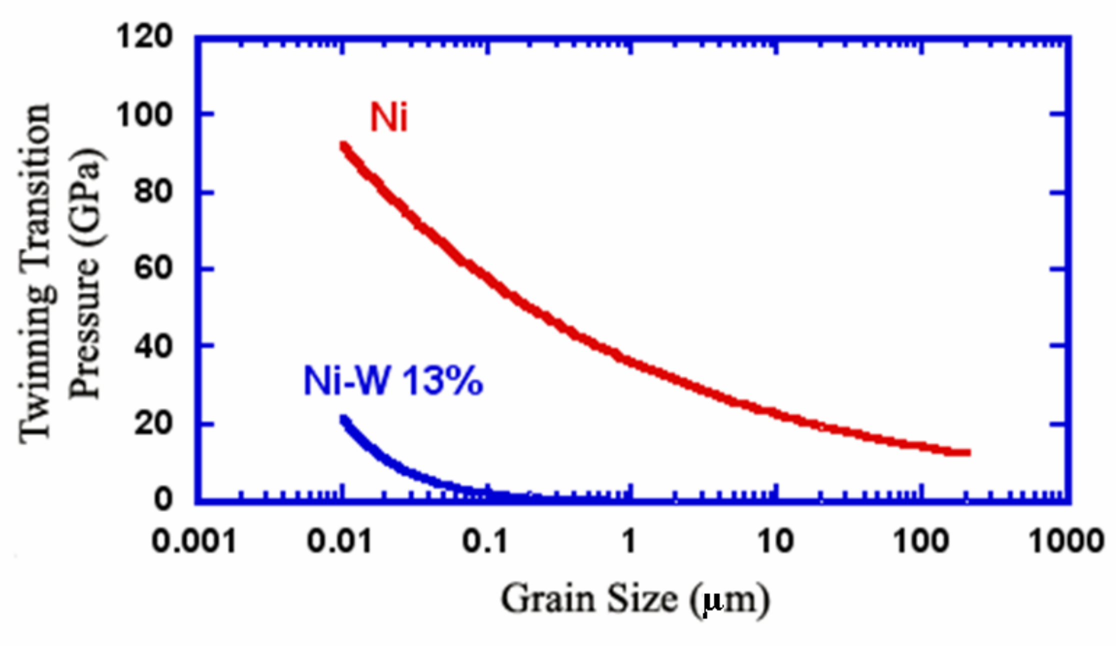

Figure 4.23: Calculated twinning-transition pressure vs. grain size for Ni and Ni-13 at. %W.

pressures of ~70 GPa. The result of the twinning transition pressure for nc Ni-W, 13 at. %, having a grain size of 10 nm is illustrated in the plot in Figure 2.22 (b). It is equal to 16 GPa, and is consistent with experiments where twins were observed at pressures of ~ 38 GPa.

The twinning-transition pressure as a function of grain-size (micro to nanometer regime) was also calculated. The strain-hardening exponent was varied between *n*=0.5 in the micrometer regime (as determined by fitting to stress-strain plots found in Andrade [175]) and *n*=0 in the nanometer regime [170]. The result is shown in Figure 4.23. It clearly shows the much higher transition pressure in Ni as compared to Ni-W as well as the effect of grain size on the slip-twinning transition.

4.11 Conclusions

4.11.1 Monocrystalline nickel

- Molecular dynamics simulations of shock compression of [001] Ni provided a constitutive response consistent with Hugoniot data from experiments by Rice et al. [144]. Partial dislocation loops were emitted at the shock front along the {111} slip systems, consistent with the early homogeneous dislocation generation model [120].
- The pressure at which a transition from dislocation cells to stacking-faults occurs in Ni was found to be 27 GPa, close to the experimentally observed twinning pressure of 35 GPa.
- The analytical calculations of the cell-stacking fault and slip-twinning transition in monocrystalline nickel are:
  - Cells → stacking-faults: P~ 27 GPa
  - Slip → twinning: P ~ 15 GPa

  In contrast, for monocrystalline copper, they are [154]:
  - Cells→ stacking-faults: P~5 GPa
  - Slip → twinning: P~50 GPa

Thus, the experimental results corroborate the analysis, which shows that nickel twins at a pressure below the stacking-fault formation; thus, individual stacking-faults are not observed [84]. On the other hand, for copper, the stacking-fault transition occurs at a lower pressure than the twin threshold, and a stacking-fault regime is predicted and is indeed observed at intermediate pressures [48, 73].

4.11.2 Nanocrystalline nickel

- The MD simulations predict dislocation densities orders of magnitude larger than the ones observed experimentally, confirming earlier comparisons in copper by Cao et al. [118]. The cause for this discrepancy is identified: upon unloading from the peak pressure, the majority of dislocations generated in shock compression is annihilated. This suggests that previous observations of residual structures bear little resemblance to the defect configuration during compression.
- The total strain due to dislocations was analyzed in the nc Ni samples, and this was mainly governed by partial dislocations, where grains acted as sources and sinks. The effects of grain-size (5 nm vs. 10 nm) and a different potential (Ni vs. Cu) were studied. Slightly more twinning was observed in Cu, as expected. Grain-boundary sliding was found to be slightly less in the 10 nm G. S. sample since it is more difficult for larger grains to shear past each other. More twinning was also favored for the smaller Ni 5 nm sample as compared to the 10 nm Ni sample.
- An analytical model of the slip-twinning transition in nanocrystalline nickel (GS ~30 nm) under shock compression predicts a critical twinning pressure of 78 GPa, consistent with TEM observations at the same grain size which show no evidence of twinning at shock pressures up to 70 GPa.
- The same model applied to nanocrystalline nickel-tungsten (G. S. ~10 nm) under shock compression predicts a critical twinning pressure of 16 GPa, consistent

with TEM observations that show twin formation in nc Ni-W (G. S. 10-15nm) at a shock pressure of 38 GPa.

Chapter 4, in part, has been submitted for publication in Acta Materialia, 2008 and, in part, has been published in Applied Physics Letters, 2006, Vol. 88, pp. 061917 (authors and co-authors: Y. M. Wang, E. M. Bringa, J. M. McNaney, M. Victoria, A. Caro, A. M. Hodge, R. Smith, B. Torralva, B. A. Remington, C. A. Schuh, H. Jarmakani, and M. A. Meyers) and the proceedings of the conference of the American Physical Society Topical Group on Shock Compression of Condensed Matter, 2007, AIP Press 955, pp. 239-242 (Authors and co-authors: H. Jarmakani, Y. M. Wang, E. Bringa and M. A. Meyers).

CHAPTER 5

LASER-SHOCK INDUCED SPALLING AND FRAGMENTATION IN POLYCRYSTALLINE VANADIUM

The prediction and mitigation of damage from shrapnel and debris is a very integral part of the design of experimental configurations for high-powered laser facilities such as NIF. If target debris issues are not resolved, it is possible that they can damage diagnostic tools and optical protection shields. LLNL is in the process of developing the tools and codes to allow evaluation of target configurations in order to better predict and mitigate the generation and impact of debris. The Janus laser is being used for a number of experiments in which thin plates representative of typical diagnostic shields are irradiated and material is spalled off of the backside of the thin plate and collected in both aerogel and on glass. Representative shield materials include Ta and V. In this chapter, a series of these controlled experiments on vanadium aimed at determining the amount of debris and shrapnel produced are discussed.

5.1 Experimental Procedure

5.1.1 Optical Microscopy

The grain-sizes of the vanadium samples studied in this work were measured with the aid of a Zeiss Axio Imager Optical Microscope. The vanadium foils were obtained from Alpha Aesar and had a purity of approximately 99.8%. Three different foil thicknesses were used: 75 μm, 127 μm, and 250 μm. Specimens from each of the three as-received foils were cut, polished, and etched to measure the grain size. The specimens were polished using 1200, 2400, and 4000 grit paper, followed by 0.3 and 0.05 µm alumina compound. The etchant used was a mixture of 1 mL HF, 30 mL HNO_3, and 30 mL lactic acid. Micrographs of the grains revealed after etching are shown in Figure 5.1 (a), and a summary of the grain sizes and aspect ratios are given in Table 5.1. All specimens exhibited grain elongation due to rolling.

Table 5.1: Grain sizes of as-received Vanadium foils

Thickness	**Grain Size (Top/Bottom Surface)**	**Aspect Ratio**	**Grain Size (Cross-Section Surface)**	**Aspect Ratio**
75 µm	100 µm	3.5:1	16 µm	6:1
127 µm	64 µm	2.4:1	20 µm	3:1
250 µm	126 µm	4:1	13 µm	8:1

5.1.2 SEM

Surface features of laser-impacted vanadium samples were studied using an FEI Quanta 600 located at the Scripps Institute of Oceanography, UCSD and a Phillips XL30 ESEM located at the nano3 facility at UCSD.

5.1.3 Janus laser experimental setup

The laser experiments were conducted at the Jupiter laser facility, Lawrence Livermore National Laboratory. Figure 2 is an illustration of the cross-sectional view of the experimental set-up. Figure 5.2 (a) shows the general set-up of the experiment and Figure 5.2 (b) – (d) are depictions qualitatively showing the damage that occurs to the

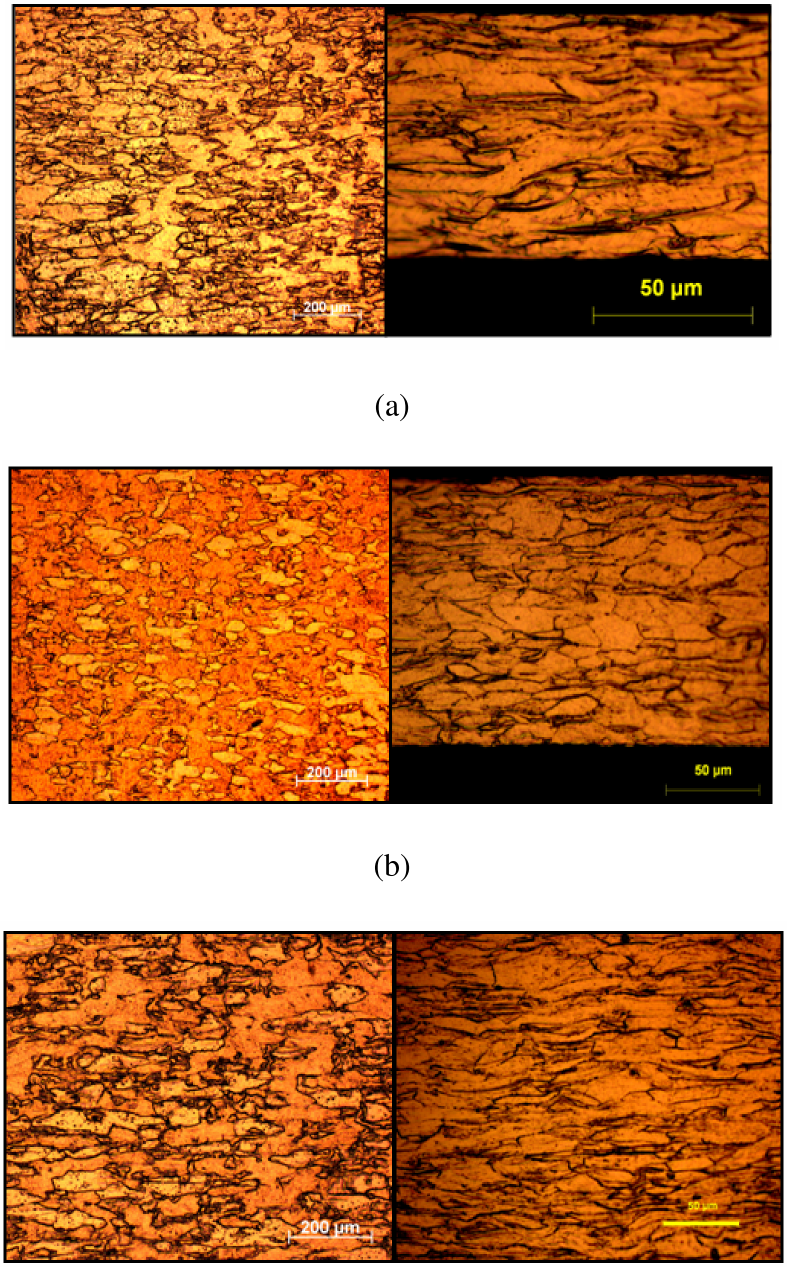

(a)

(b)

(c)

Figure 5.1: Grain structure of top/bottom surface (left) and cross-section (right) of samples: (a) 75µm thickness; (b) 127 µm thickness; (c) 250 µm thickness.

vanadium targets as the thickness changes. Figure 5.2 (b) shows complete blow-off of the thinnest vanadium samples; Figure 5.2 (c) shows blow-off surrounded by a spall surface in the intermediate thickness samples; Figure 5.2 (d) shows solely spall, which occurs in the thickest samples.

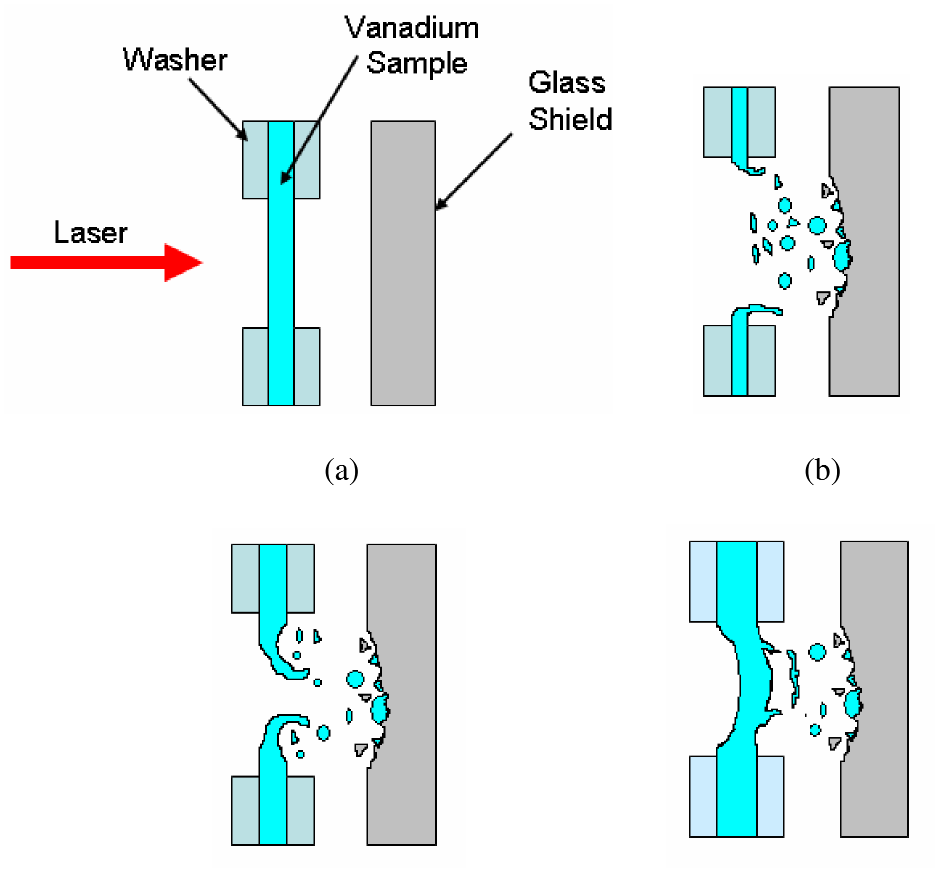

(a) (b)

(c) (d)

Figure 5.2: (a) Schematic of the cross-sectional view of the experimental set-up; (b) laser shock of thinnest target; (c) laser shock of intermediate thickness target; (d) laser shock of thickest target.

A Nd-glass laser with a 532 nm pulse width was used to generate the high-pressure laser-driven shocks in the vanadium samples. Both 3 and 8 ns square pulse lengths were used to study the effect of pulse duration on material behavior. A 1 mm kineform phase plate (KPP) was used to generate a flat intensity profile that was 1 mm square in size. The vanadium samples were cut into small 3.5 x 5 mm rectangles and glued between two steel washers having a 10 mm outer diameter and 2.5 mm inner diameter. Glass slides were placed parallel to the targets, approximately 12 cm behind, to collect vanadium fragments, and to analyze the resultant damage. The associated laser energies and pulse durations of the samples investigated are tabulated in Table 5.2.

Table 5.2: Laser energy and pulse duration of experiments

Exp. No.	**Foil Thickness (μm)**	**Energy (J)**	**Diagnostic**	**Pulse Length (ns)**
3	75	290	Glass Shield	3
4	75	167	Glass Shield	3
5	127	228	Glass Shield	3
8	250	438	Glass Shield	3
9	127	430	Glass Shield	3
11	250	251	Glass Shield	3
12	250	442	Aerogel	3
13	127	381	Aerogel	3
14	127	209	Aerogel	3
15	75	199	Aerogel	3
18	127	218	Glass Shield	8
22	127	218	Glass Shield	8

5.2 Results and Discussion

Section 5.2.1 presents the calculated pulse decay as well as a thermodynamic analysis determining the melting temperature as a function of pressure. Section 5.2.2 provides the detailed characterization of the recovered specimens in order of increasing thickness. Section 5.3 provides fragment size modeling of vanadium due to spall, and Section 5.4 discusses spall strength calculations of vanadium based on the laser-shock experiments. Section 5.5 provides the conclusions for this work.

5.2.1 Calculated pulse decay and modeling of melting of vanadium under shock compression

The pressure pulse decay profiles of the laser shock experiments on vanadium were calculated at three different energy levels around which the experiments were conducted: 100 J, 200 J, and 400 J. Since no VISAR experiments were conducted, the pressure profiles were computed based on calibrated laser shock experiments on tantalum carried out at 200 J [197]. The conversion of parameters from Ta to Va was carried out using the conservation of energy equation:

$$\Delta E = \frac{1}{2} U_p^{\ 2} \qquad (5.1)$$

where ΔE is the change in energy and U_p is the particle velocity. The internal energy inside the shock-compressed material is a function of the laser energy and, to a first approximation, we assume that this function is material independent. Differences in optical absorptivity or reflectivity between V (= 61%) and Ta (= 78%) are neglected. The experimental pressure values as a function of distance into the material obtained from the tantalum experiments [197] are listed in Table 5.3. The predicted pressure pulse decay profiles in vanadium for various input energies (100 J, 200 J, and 400 J) are presented in Figure 3.

Table 5.3: Pressure and U_p values as a function of distance obtained from laser shock experiments on tantalum by Eder et al. [197]

Distance (μm)	Pressure (GPa)	U_p (km/s)
100	150	1.664
200	60	0.819
250	40	0.584

The temperature rise due to shock and the melting temperature as a function of pressure were computed in order to determine the theoretical pressure at which vanadium will melt when subjected to shock compression. The Clausius-Clapeyron relation describes the effect of pressure on the temperatures at which phase transitions occur between two states of matter [145]. For melting, this relation is given by:

$$\frac{dP}{dT} = \frac{\Delta H_m}{T \Delta V_m} \tag{5.2}$$

where ΔH_m is the enthalpy of fusion at the melting point (422 J/g) and ΔV_m is the volume change associated with melting, assumed to be independent of pressure. ΔV_m for vanadium is expressed as:

$$\Delta V_m = \left(\frac{1}{\rho_{T_m}} - \frac{1}{\rho_{T_o}} \left(1 + \frac{\Delta V}{V_o} \right) \right) \tag{5.3}$$

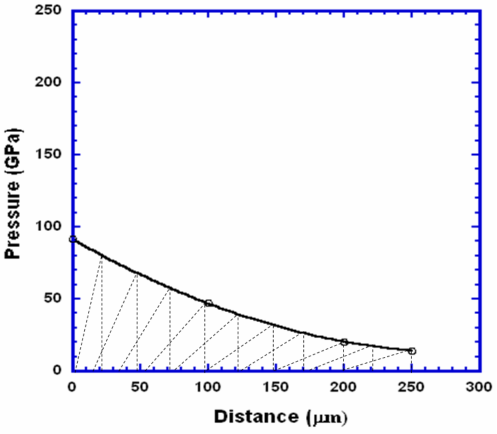

(a)

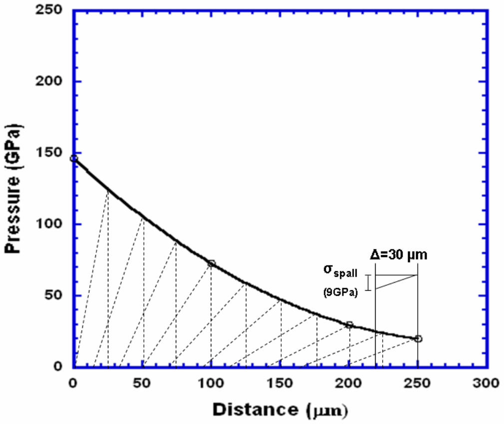

(b)

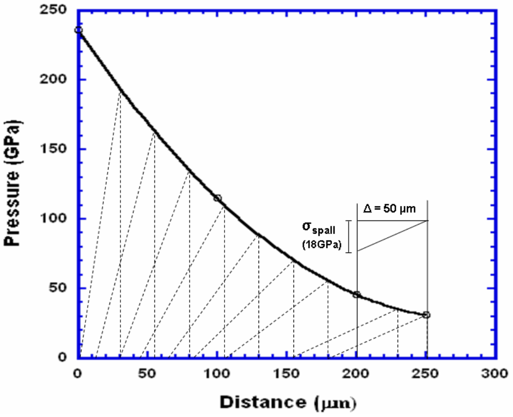

(c)

Figure 5.3: Predicted pulse decay: (a) 100 J; (b) 200 J; (c) 400 J.

where $\frac{\Delta V}{V_o}$ is the change in volume from T_o to T_m, ρ_{T_m} is the density of solid vanadium at the melting temperature, 5.76 g/cm^3 (this value was determined from Sorkin et al. [198] where they indicate that $\frac{V(Tm)}{V(To)} = 1.06$), ρ_{T_o} is the density at ambient temperature and pressure (= 6.11 g/cm^3) and $\frac{\Delta V}{V_o}$ is given by:

$$\frac{\Delta V}{V_o} = 3\gamma T_m \tag{5.4}$$

where γ is the thermal expansion coefficient, $8.4\text{x}10^{-6}$ K^{-1}, and T_m is the melting temperature of vanadium, 2,183 K. Rearranging Equation (5.2), integrating and solving for melting temperature as a function of pressure yields the following expression that relates the melting temperature to pressure:

$$\int_{(T_m)_o}^{(T_m)_P} \frac{dT}{T} = \frac{\Delta V}{\Delta H} \int_{P=o}^{P} dP \Rightarrow \ln(T_m)_p = \frac{\Delta V}{\Delta H} P + \ln(T_m)_o \tag{5.5}$$

The temperature rise induced by shock compression has been extensively analyzed and modeled in the literature [145]. The shock temperature rise can be calculated by the following equation:

$$\begin{aligned} T_s = T_o \exp\left[\frac{\gamma_o}{V_o}(V_o - V_1)\right] + \frac{P(V_o - V_1)}{2C_v} + \\ \frac{\exp\left[\frac{-\gamma_o}{V_o} V_1\right]}{2C_v} \int_{V_o}^{V_1} P \exp(\frac{\gamma_o}{V_o} V)\left[2 - \frac{\gamma_o}{V_o}(V_o - V)\right] dv \end{aligned} \tag{5.6}$$

where the pressure dependence on volume or the Hugoniot is given as:

$$P = \frac{C_o(V_o - V)}{\left[V_o - S(V_o - V)\right]^2} \tag{5.7}$$

γ_o is the Grüneisen parameter (=2 for vanadium [199]), C_v is the specific heat capacity (= 489 J/Kg K), and V_o and V_1 are the initial and current specific volumes of the material, respectively. V_1 can be calculated from the following relationship [145]:

$$V_1 = \frac{C_o^{\,2}}{2PS^2}\left[\sqrt{1 + \frac{4PSV_o}{C_o^{\,2}}} + \frac{2S(S-1)V_oP}{C_o^{\,2}} - 1\right] \tag{5.8}$$

The melting temperature (determined from the Clausius-Clapeyron relation) and the shock temperature rise as a function of pressure are given in Figure 5.4. The melt curve determined by the Clausius-Clapeyron relation (red solid line) is in agreement with experimental work carried out by Jephcoat et al. [199]. Their work was, however, confined to pressures up to 100 GPa. Interestingly, our modeling captures the surprisingly small melting slopes seen in bcc metals, which are clearly documented by extensive work by Errandonea et al. [200]. The predicted shock temperature profile (solid black line) is in agreement with data reported by McQueen et al. [201] up to a pressure of ~ 160 GPa, where it begins to deviate. The plot shows that vanadium remains solid up to a pressure of ~ 150 GPa, after which it melts. The predicted melting pressure of 150 GPa is lower than experimentally obtained results by Dai et al. [202]; they determined a melting pressure of ~ 250 GPa. The release curve for vanadium from McQueen et al. [201] is also plotted in Figure 5.4. It lies below the melt curve suggesting that any material that melts under shock will be quenched back to the solid state upon release.

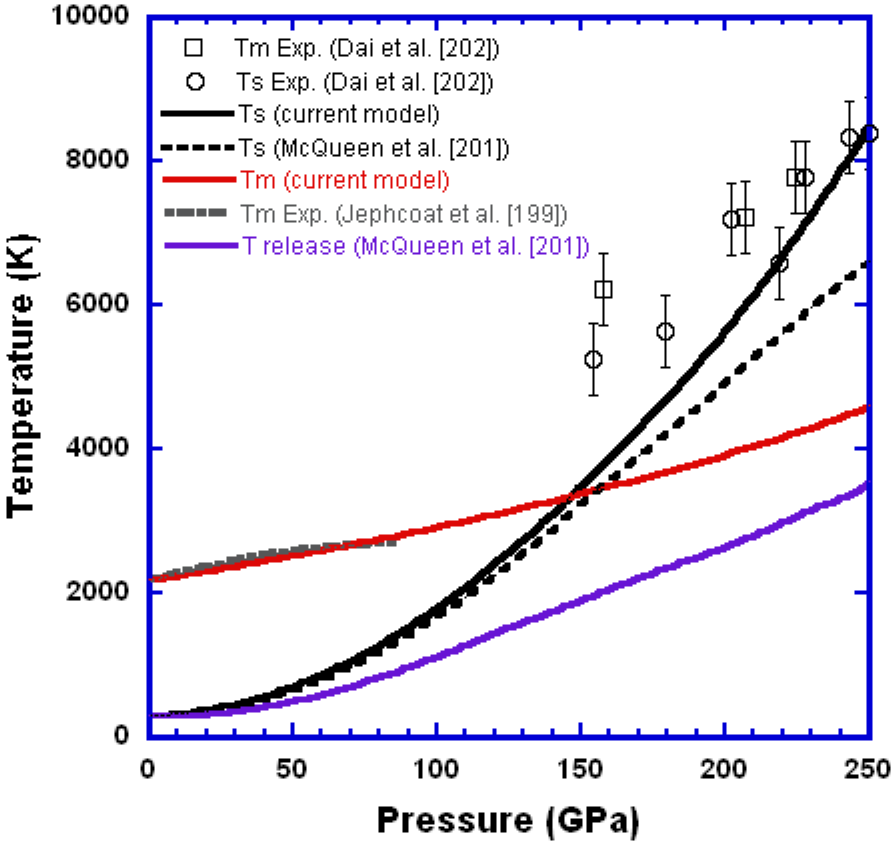

Figure 5.4: Shock temperature rise and melting temperature as a function of pressure.

5.2.2 Characterization of samples

The analysis and characterization of the samples were carried out by optical and scanning electron microscopy (SEM), and the findings are presented in three sections in the order of increasing thickness of the samples: 75 µm, 127 µm, and 250 µm.

5.2.2.1 Experiments on 75 µm thick targets

Three 75 µm thick samples were laser shocked at energy levels of 167, 199, and 290 J, and at a pulse length of 3 ns. Almost complete blow-off occurred in all the samples as shown in Figure 5.5 (a), except for small portions around the hole of the washer that remained. Figure 5.5 (b) shows an SEM image of the surface of the "lip" that remained after irradiation for the 167 J experiment. The exposed grains from the spall region show the characteristic elongated configuration. The blow-off surfaces of the samples where vanadium was ejected revealed a flaking phenomenon mostly attributed to grain boundary separation. Separation along grain boundaries can clearly be seen in Figure 5.5 (c), 199 J, which also captures the grains elongated along their rolling direction.

The samples shocked at 167 and 290 J had glass shields placed behind them whereas the sample shocked at 199 J had an aerogel setup (aerogel experiments are not discussed in this study). Because of their very small thickness, a significant amount of vanadium was ejected onto the glass shields as compared to the samples having a larger thickness. Most of the damage and rubble was collected at the center of the glass shields. Figure 6 shows micrographs of the damage on the surface of the glass shields induced by vanadium fragments for both the 167 and 290 J experiments (Figure 5.6 (a) and (b)). Clearly, the extent of damage from the ejected fragments is greater in the 290 J experiment. In order to quantify the damage induced by the vanadium fragments on the glass shields, a circular grid was superimposed on the glass shield images, as shown in Figure 5.6 (c). The imaging software, ImageJ, was used to help determine the number of fragments per area as a function of distance away from the central damaged zone. Clearly, the plot in Figure 5.6 (d) shows that the extent of damage (fragments per unit area) is more significant in the 290 J glass shield compared to the 167 J glass shield. Note the reduction in damage away from the central crater.

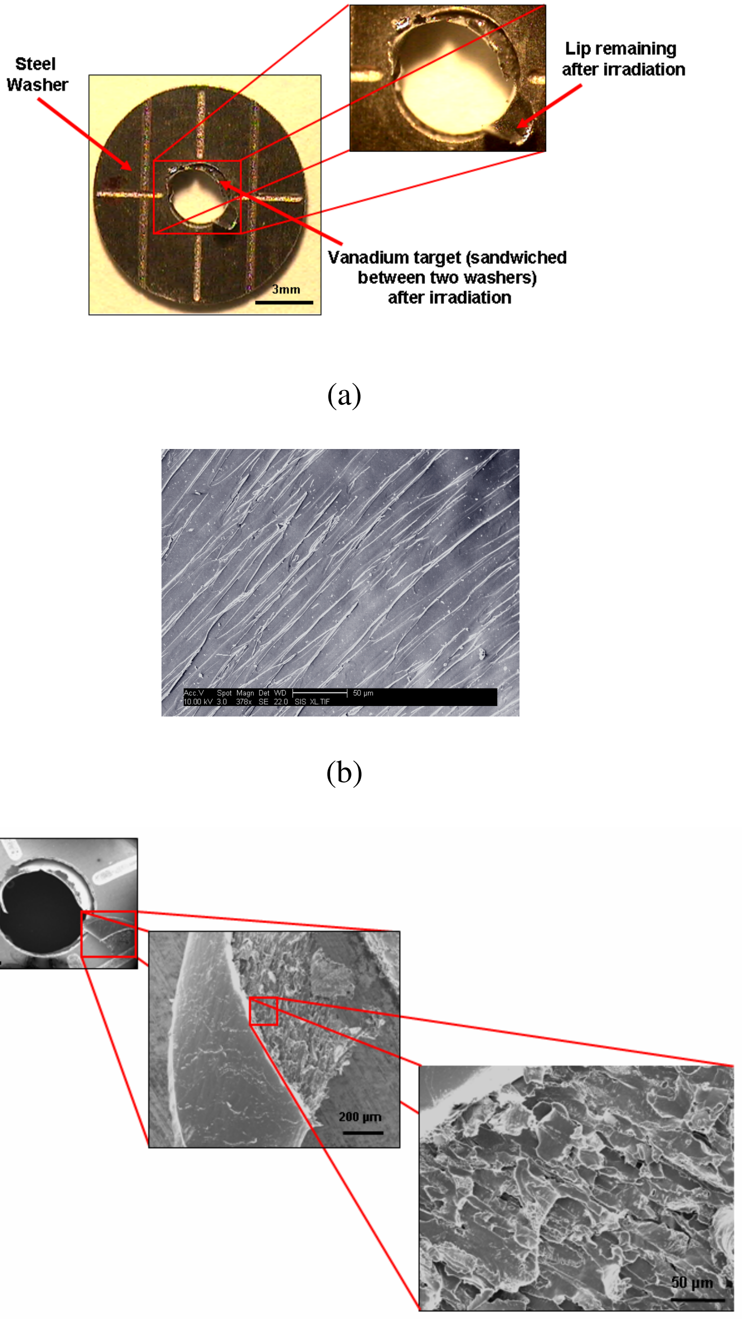

(a)

(b)

(c)

Figure 5.5: (a) 75 µm thick specimen after laser shock, 167 J; (b) surface of "lip" showing elongated grains, 167 J; (c) blow-off surface of 75µm thick samples showing flaking due separation along grains, 199 J.

SEM images of the glass shields revealed that vanadium debris collected in two forms: (a) solid fragments and resolidified molten fragments. In the case of the 167 J experiment, solid vanadium fragments and “splashes” were evident around the edges of the central crater, Figure 5.7. Figure 5.7 (a) shows the main central crater and the induced damage from the vanadium. Figure 5.7 (b) is a close-up view of an area around the crater showing mostly vanadium flakes and occasional “splashes” (circled). It should be noted that the occurrence of resolidified vanadium around the crater was less frequent than that of the 290 J experiment. Figure 5.7 (c) shows a high density of vanadium debris around the central crater. This image is a close up of the area within the box highlighted in Figure 5.7 (a). SEM analysis of the glass shield from the 290 J experiment showed more significant damage and a greater amount of melting of vanadium around the edges of the central crater, Figure 5.8(a). Note the radial and circumferential cracks on the glass surface due to the vanadium fragments. Figure 5.8 (b) shows larger vanadium fragments surrounded by vanadium “splashes”. Figure 5.8 (c) is a higher magnification SEM image of the resolidified vanadium. The image to the right suggests that the vanadium particle was ejected in liquid form from the target and formed a solid outer shell enclosing the inner liquid core as it traveled towards the glass shield. Upon impact, the outer shell was squashed releasing the inner liquid core around it.

It should be noted that the modeling of the melting and shock temperature rise, Figure 5.4, suggests that any vanadium that melts under shock compression should resolidify upon release since the release curve (blue line) lies beneath the melt curve (red line). However, melting is a homogeneous process (no nucleation and growth being

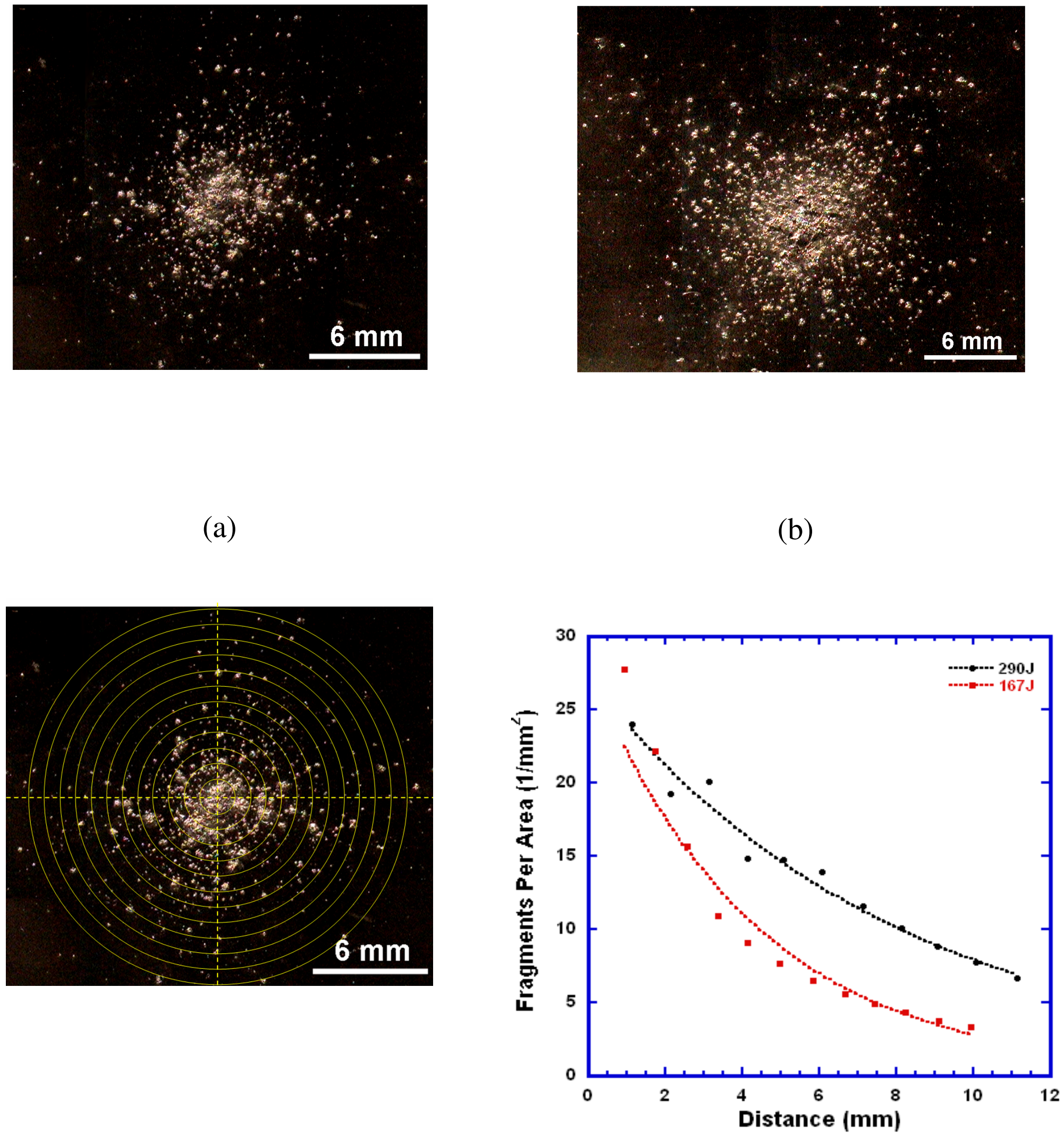

(a)

(b)

(c)

(d)

Figure 5.6: Glass shields damaged by vanadium, 75 µm; (a) 167 J; (b) 290 J; (c) circular grid placed on glass shield for fragment quantification; (d) fragments per area as a function of distance from central damage.

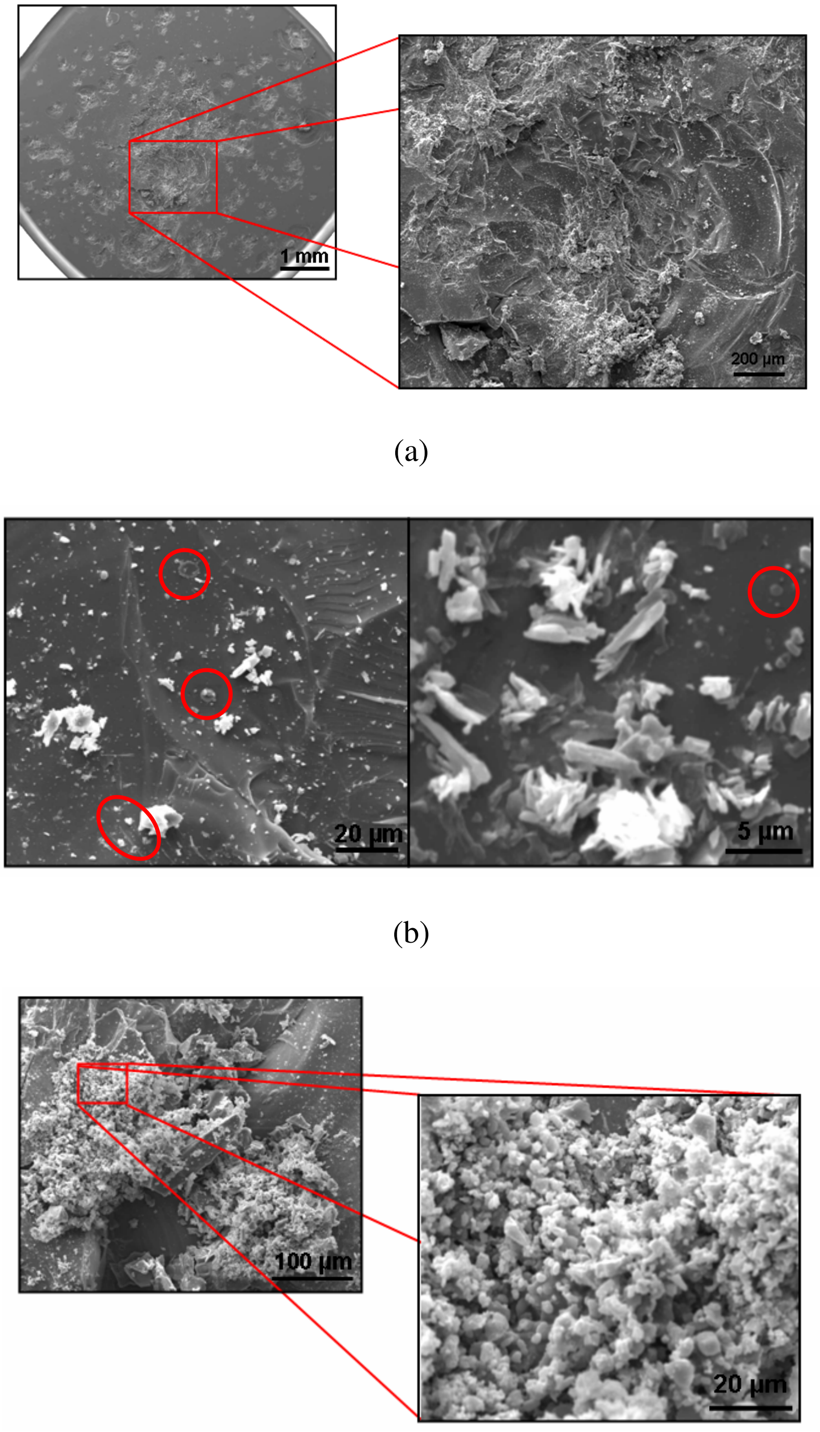

(a)

(b)

(c)

Figure 5.7: Glass shield of 75 µm specimen shocked at 167 J, 3 ns; (a) central crater; (b) vanadium particles near center crater; (c) vanadium debris near central crater.

required) whereas solidification requires nucleation and growth and is therefore time dependent. As observed from the SEM results, melting of vanadium does indeed occur in the experiments. This implies that melting must have occurred under shock and not release (known as high pressure melting). A survey of the literature suggests that this phenomenon is not very common. Furthermore, the very short pulse durations (3 ns) in the experiments provide very little time for the material to solidify upon release, and that is why we most likely observe melting on the glass shield. Melting upon impact with the glass shield may also be a possible scenario.

Energy dispersive spectroscopy (EDS) was conducted on the glass shields, and the energy spectrum was analyzed to confirm elements present. Elemental analysis on the large vanadium fragment pertaining to the dotted square in Figure 5.8 (b) and the background/glass-shield within the area of the small solid square was carried out. The energy spectrum from the vanadium fragment, Figure 5.9 (a), shows a very strong vanadium signal, ~ 65 wt. %. The Au and Pd signal is due to the coating applied on the surface of the glass-shield. Figure 5.9 (b) is the elemental analysis carried out on only the glass-shield showing predominantly Si (i.e. constituent of glass), ~ 30 wt. %.

5.2.2.2 Experiments on 127 μm thick targets

The 127 μm vanadium targets that were analyzed in this study were subjected to the following laser energies: 209, 218, 228, 381, and 430 J. The 209 J and 381 J experiments had aerogels placed behind the targets instead of glass shields (only the targets are studied in these cases), and two 218 J experiments were carried out with both glass shield and aerogel set-ups. The pulse duration in all cases was 3 ns except for the

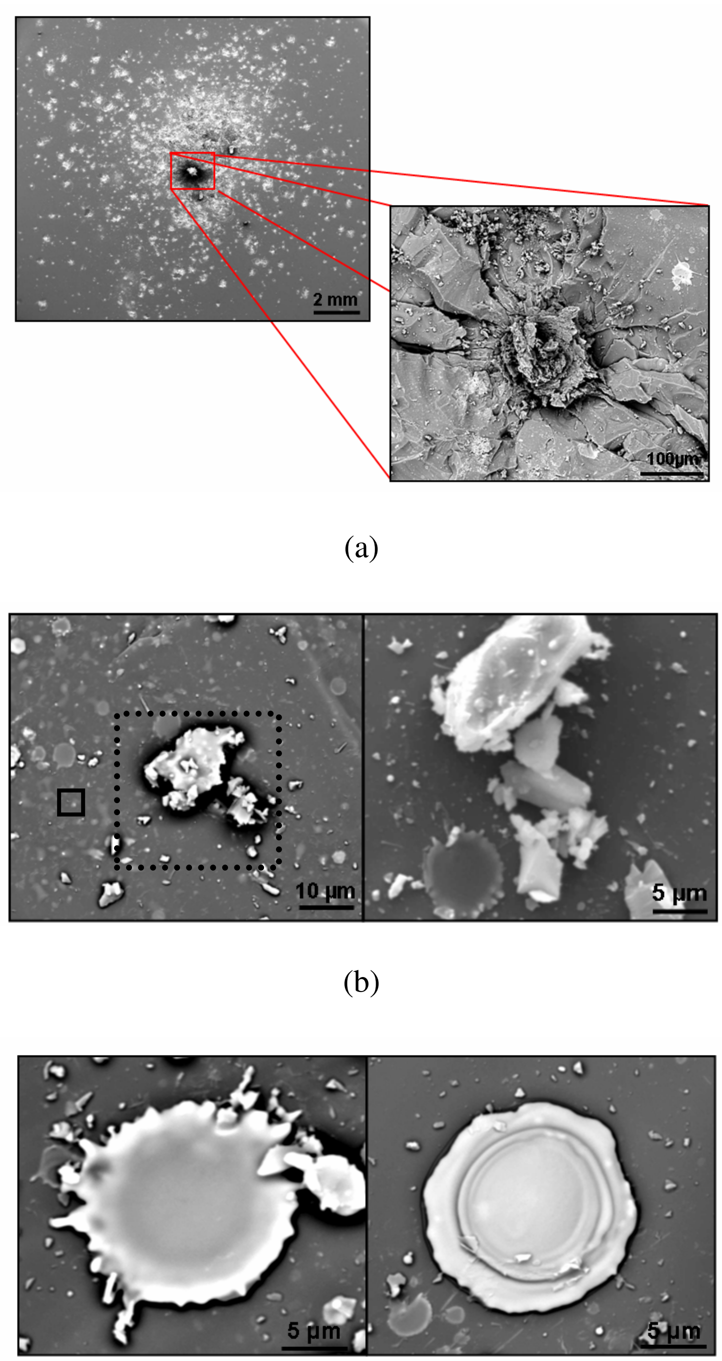

(a)

(b)

(c)

Figure 5.8: (a) Glass shield of 75 μm specimen shocked at 290 J, 3 ns: (a) central crater with radial and circumferential cracks; (b) solid particles and fragments; (c) particles that were molten upon impact, 290 J.

218 J experiment, where it was 8 ns. The 218 J and 228 J experiments provide a means to compare the effect of the change in pulse duration at comparable laser energies. In all cases, the target showed tearing away around the square laser spot, and a spall surface formed around the hole or area blown off, as shown in Figure 10 for one of the 218 J experiments. The vanadium sample pertaining to the 218 J, 8 ns experiments had a slightly larger blow-off diameter compared to the 209 J, 3 ns experiment, likely due to both the increased pulse duration and slightly higher energy level.

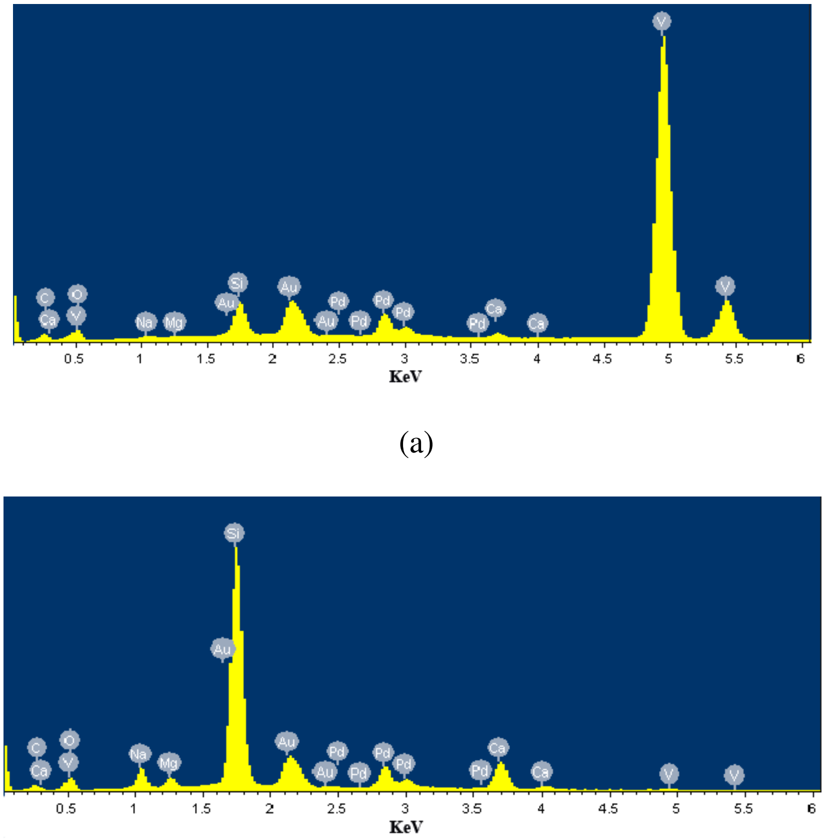

(a)

(b)

Figure 5.9: Energy Dispersion X-ray Spectroscopy from (a) vanadium fragment on glass shield (large dotted square in Figure 5.8 (b)); (b) background/glass shield (small solid square in Figure 5.8 (b)), 290 J 3 ns.

In comparison with the 75 µm thick targets, more material around the laser spot survived, Figure 5.10 (a). The direct interaction of the laser with the vanadium surface also caused melting. Flaking and peeling away along the grain boundaries can clearly be seen in Figure 5.10 (b), and dimpling and void formation on the blown-off surface was also evident, Figure 5.10 (c), which are characteristics of ductile behavior. These features typically form as a result of void nucleation, growth and coalescence. The blow-off diameter increased with pulse duration. Figure 5.11 shows the increase in the blow-off diameter as the laser energy is increased.

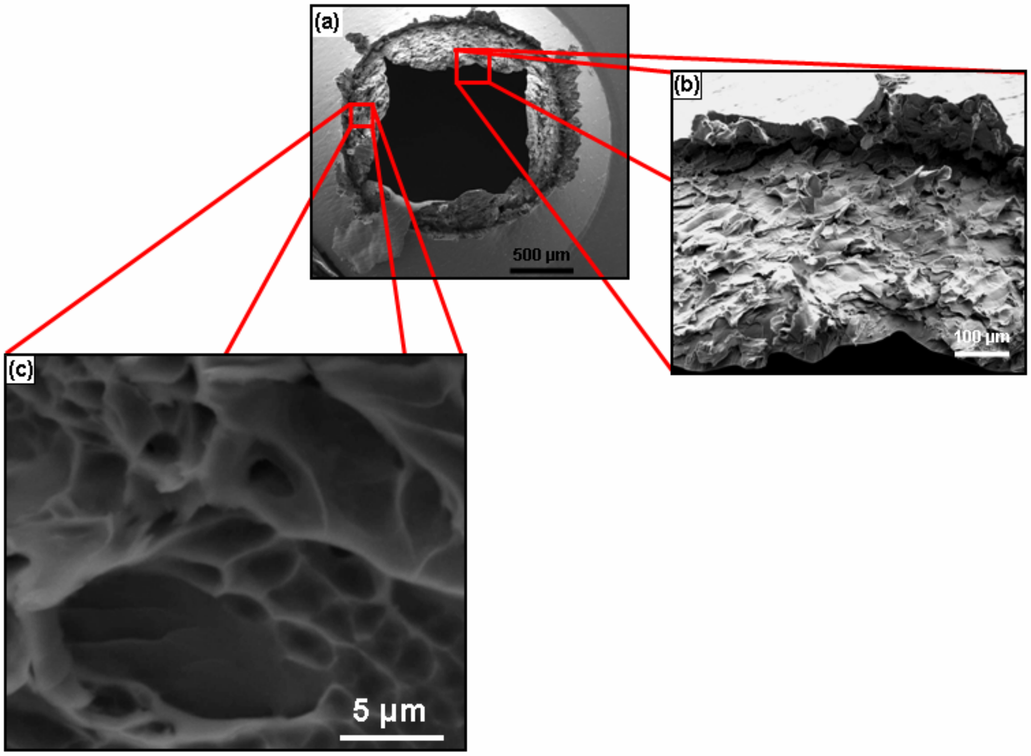

Figure 5.10: 127 µm thick specimen after laser shock, 218 J, 8 ns; (a) overall view showing blow-off and spalled region; (b) flaking due to grain boundary separation; (c) dimples and voids.

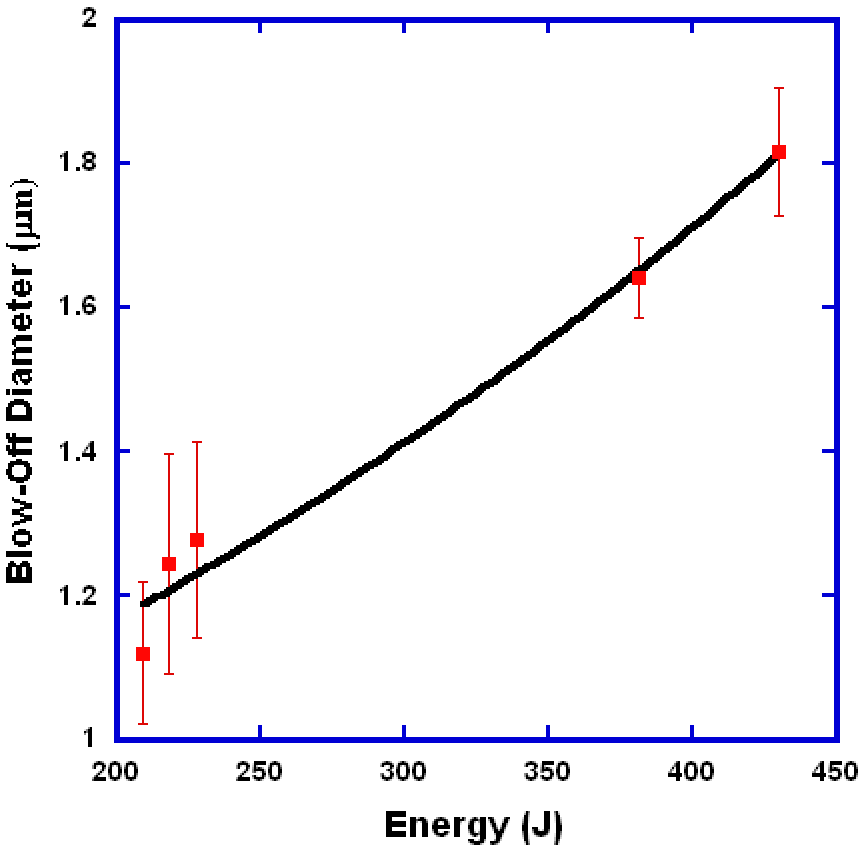

Figure 5.11: Blow-off diameter of 127 µm thick specimens.

The glass shields analyzed showed a clear effect of the increase in laser energy and pulse duration. Much more damage and debris was accumulated on the glass shields pertaining to the higher energy experiments. Figure 5.12 shows images of the cratered surfaces of the glass shields placed behind the 127 µm thick targets. The glass shield in Figure 5.12 (a) was placed behind the target subjected to a 218 J pulse having a duration of 8 ns, whereas the glass shield in Figure 5.12 (b) belonged to the 3 ns pulse at 228 J. The higher pulse duration does not seem to have increased the amount of damage on the glass shield. However, it resulted in larger fragments being ejected from the vanadium targets, as would be expected. In fact, the damage on the glass shield having the 3 ns pulse was significantly greater. Figure 5.12 (c) presents the surface of the glass shield behind the target subjected to 430 J. Clearly, a greater amount of vanadium was ejected onto the glass shield causing more damage. One can see the geometrically square nature of the central damaged zone in Figure 5.12 (c), which is due to the square geometry of the laser focal spot incident on the target. Figure 5.12 (d) is a plot showing the quantification of the fragmentation on the glass shields. Clearly, the fragments per area increase as the laser energy increases.

SEM images of the glass shields revealed that a more significant amount of vanadium melted and splashed onto the surface in the case of the 8 ns laser pulse at the lower energy level. Figure 5.13 shows the greater degree of melting that occurred in the 218 J, 8 ns experiment as compared to the 228 J, 3 ns. The glass shield placed behind the target subjected to a 3 ns pulse at 430 J revealed the most considerable amount of melting, Figure 5.14. At this highest energy level, tiny vanadium fragments in the form of whiskers (~ 3 μm in length) were evident and spread around the main cratered region.

5.2.2.3 Experiments on 250 μm thick targets

The 250 μm thick vanadium targets that were analyzed were subjected to laser beams having the following energies: 251 J, 438 J, and 442 J. The pulse duration in all cases was 3 ns (the 442 J experiment had an aerogel recovery setup). Because of the increased thickness, the targets were not punctured through. Instead, spall fracture formed on the back surface of all the 250 μm targets, Figure 5.15. Figure 5.16 is a plot

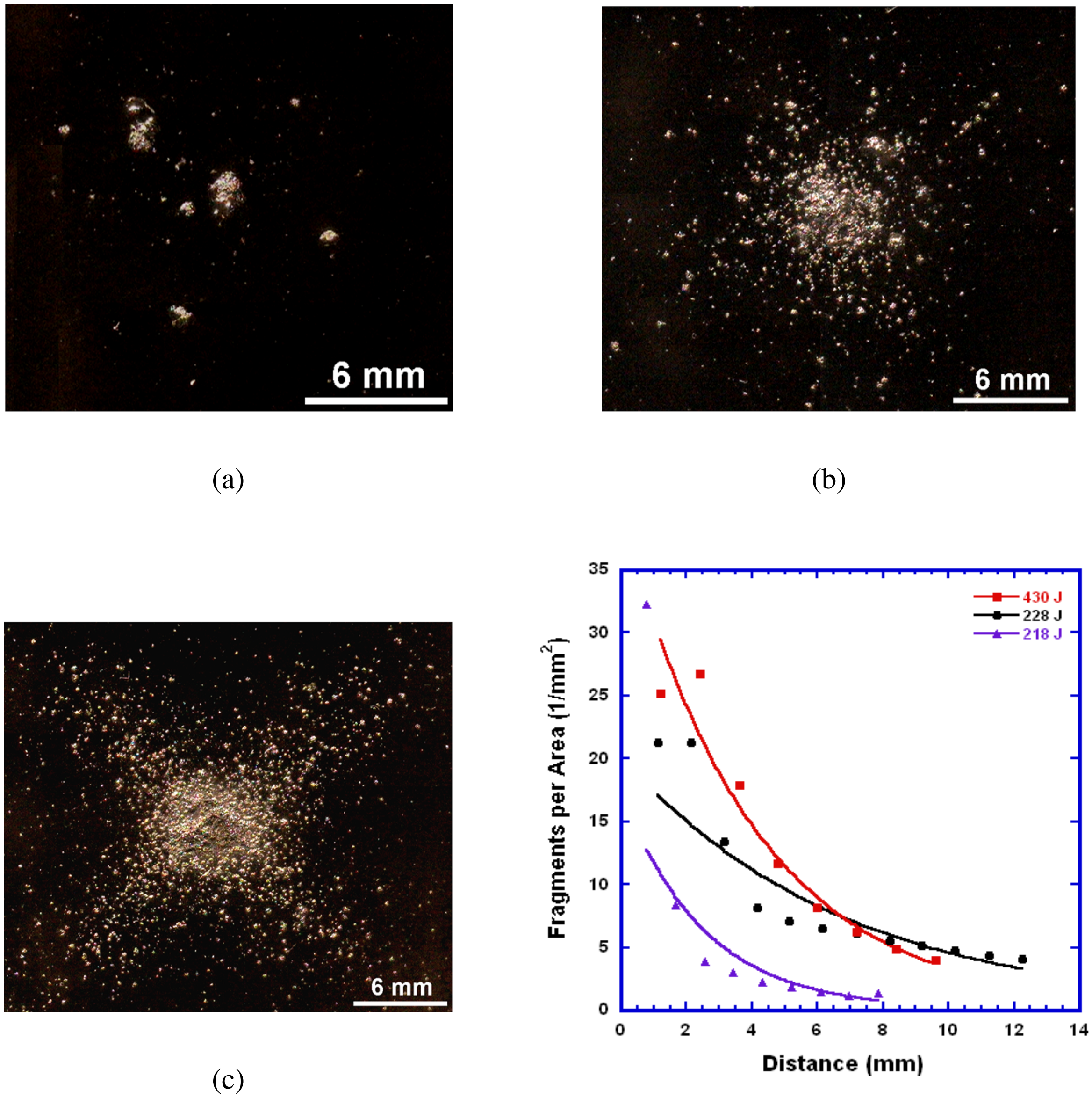

(a)

(b)

(c)

(d)

Figure 5.12: Glass shields placed behind 127 µm thick targets; (a) 218 J, 8 ns; (b) 228 J, 3 ns; (c) 430 J, 3 ns; (d) fragments per area vs. distance from central crater.

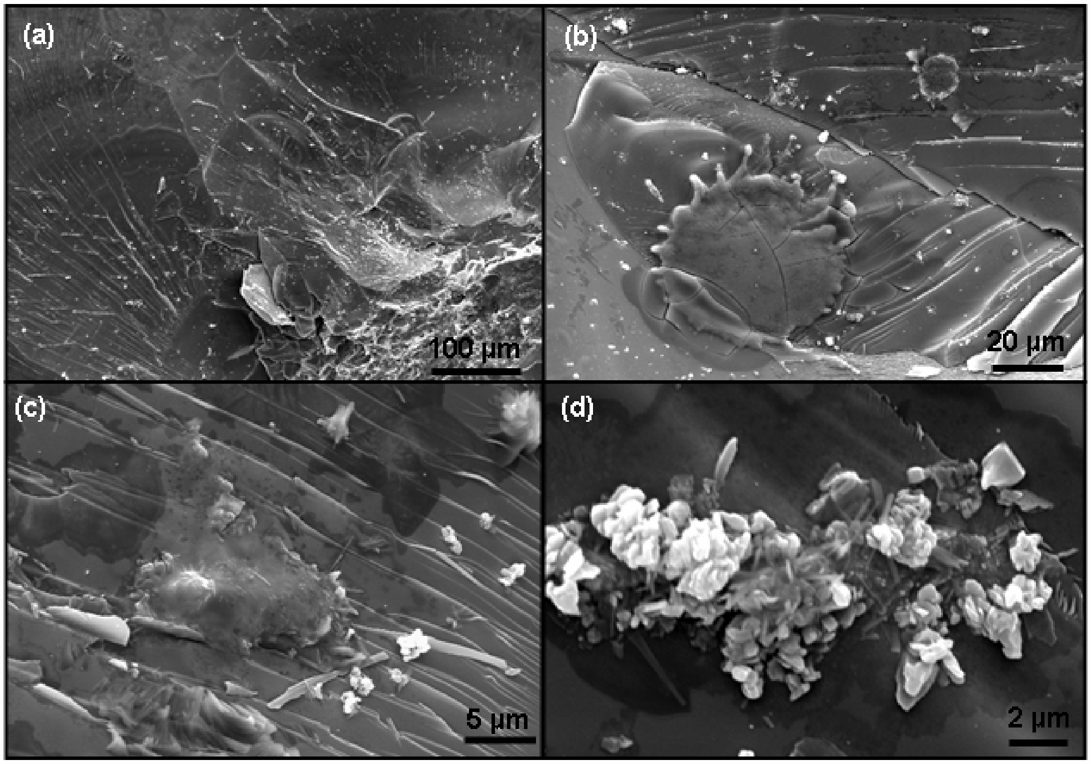

Figure 5.13: (a) SEM of glass shield behind 127 µm thick target, 218 J, 8 ns (a) damage around edges of crater; (b) splashes around central crater; (c) molten and solid vanadium particles; (c) vanadium clumps.

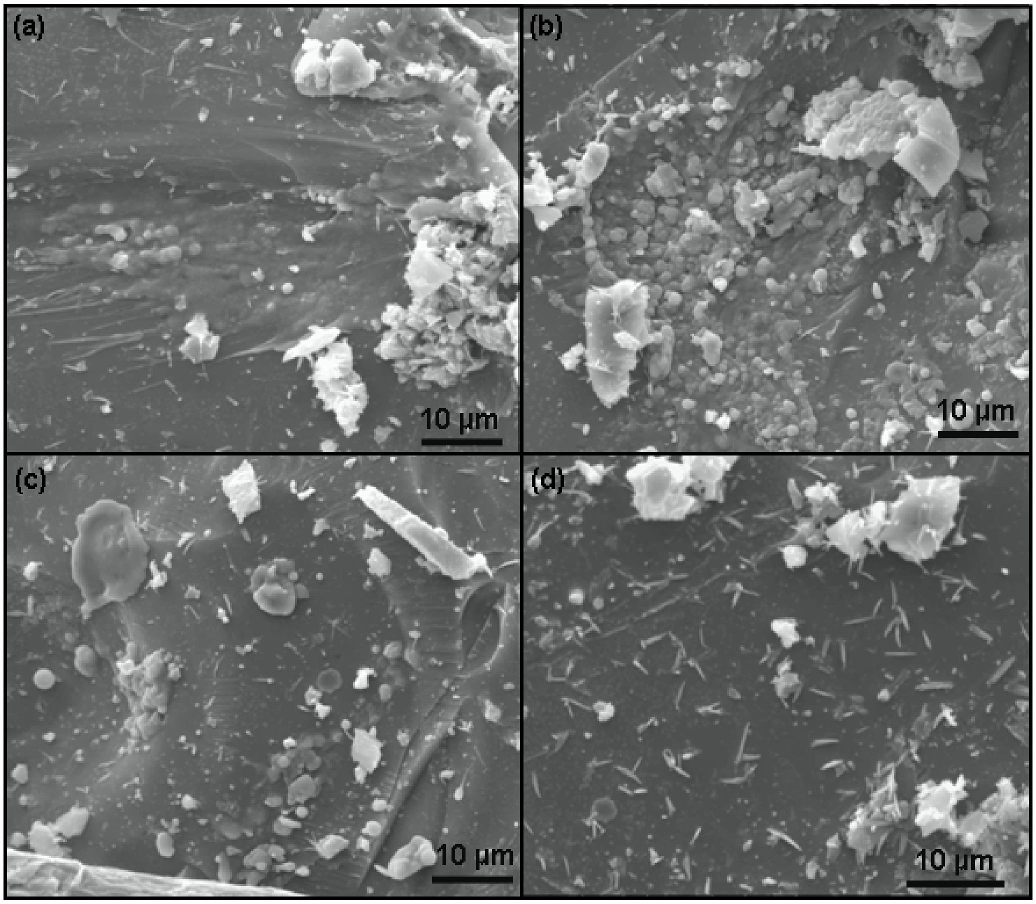

Figure 5.14: SEM of glass shield behind 127 µm thick target, 430 J, 3 ns (a) vanadium splashing around edges of central crater (b) and (c) vanadium debris, both solid and splashes; (d) vanadium whiskers.

of the spall diameter as a function of laser energy for both the 250 μm and 127 μm targets (the spalled area around the tear-off region is considered in the case of the 127 μm targets). The plot shows an increase in spall diameter (hence, spall surface area) as the energy increases. The spall diameter in the 127 μm targets is larger than that of the 250 μm. The 251 J sample was sectioned in half and mounted in order to better analyze its spall surface. Figure 5.17 shows cross-sections of the specimen. Flaking, separation along the grains, cracking, and formation of voids close to the surface are evident.

Damage in the glass shields placed behind the targets increased with laser energy, Figure 5.18, consistent with the 127 μm targets shown in Figure 5.12. It should be noted that at comparable energy levels, the damage accumulation on the glass shields decreased as the target thickness increased. For instance, the damage on the glass shield placed behind the 75 μm thick sample subjected to 167 J had much more damage than that placed behind the 250 μm sample subjected to 251 J. SEM analysis of the glass shields placed behind the 250 μm thick samples revealed much more liquification of vanadium at the higher energy level of 438 J, Figure 5.19.

5.3 Fragment Size Modeling

The fragmentation of materials under high-rate expansion has been treated extensively by Grady and co-workers [203-207]. The theoretical prediction of fragment size, S, when solid spall is dominated by the flow stress, is given by the Grady-Kipp (G-K) theory for ductile materials. This theory is based on energetic considerations where the kinetic energy of an expanding body, *T*, and the elastic energy, *U*, are equated to a

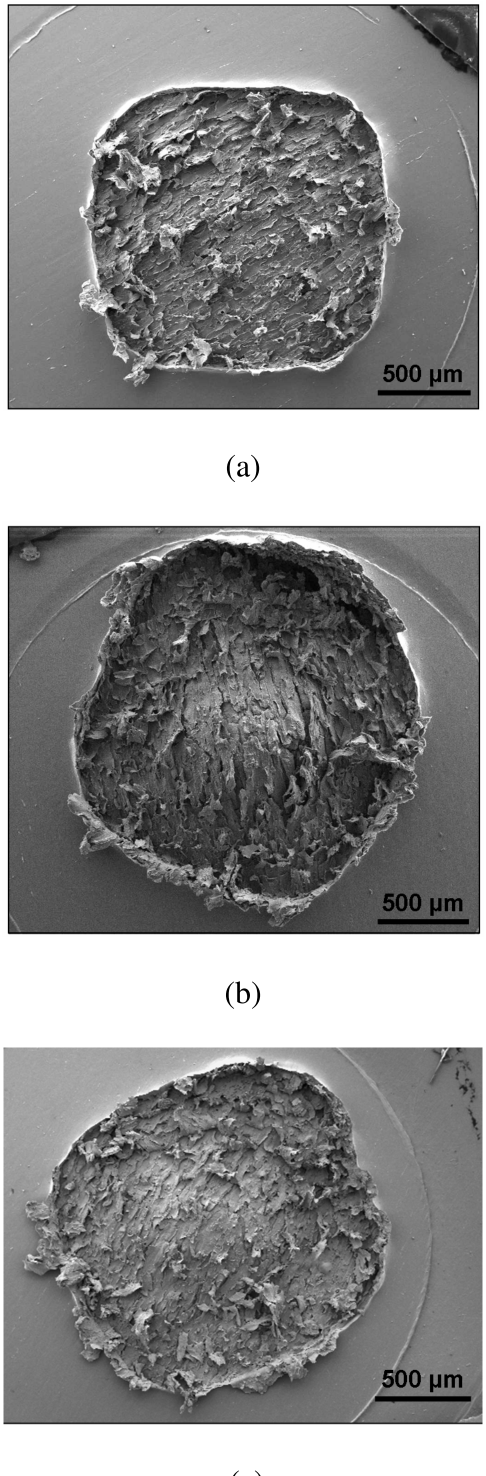

(a)

(b)

(c)

Figure 5.15: Spalling of 250 µm samples; (a) 251 J, 3 ns; (b) 438 J, 3 ns; (c) 442 J, 3ns.

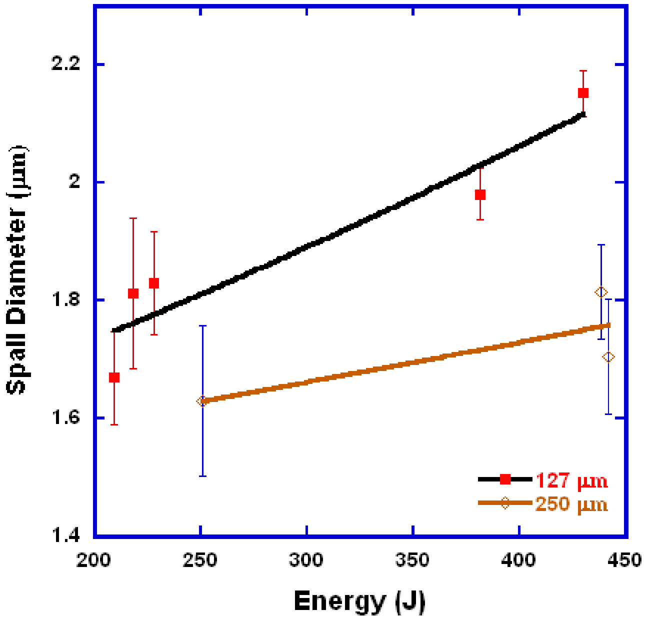

Figure 5.16: Spall diameter vs. laser energy.

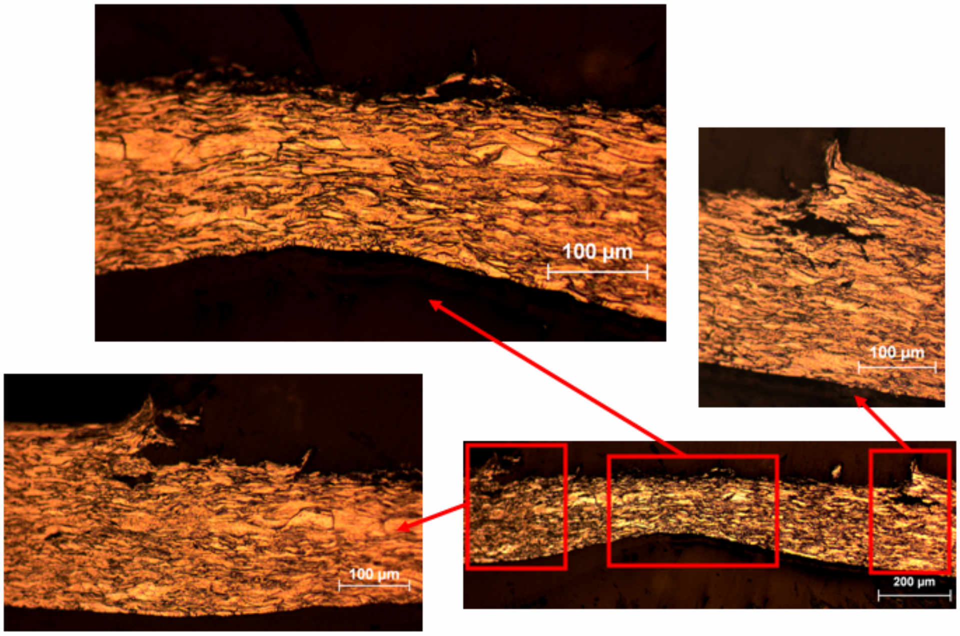

Figure 5.17: Cross-section of 250 µm, 251 J, 3ns showing the formation of incipient spall plan due to direct laser irradiation, flaking and ductile failure on spall plane, void formation and failure along grain boundaries.

ductile fracture energy, *W,* approximated as $Y\varepsilon_c$, where Y is the dynamic yield stress and ε_c is the critical strain to failure:

$$T + U \geq W \tag{4.9}$$

This leads to:

$$S = \left(\frac{6Y\varepsilon_c}{\rho \dot{\varepsilon}^2} \right)^{1/2} \tag{4.10}$$

where ρ is density and $\dot{\varepsilon}$ is the imposed strain rate. The strain rate in the current experiments can be estimated from the expansion of the spalled region as shown in the schematic of Figure 5.20 (a). We assume that the spalled portion of the target is ejected in the form of an ellipse, with major axis, a, equal to 1.25 mm (the inner radius of the washer sandwiching the target), and minor axis, b, whose critical length before failure is to be calculated. Based on tensile experiments carried out on vanadium by Yoshinaga et al. [208], it is determined that vanadium fractures at a total strain of ~ 20%. Thus, the total circumferential length of the ejected material at fracture is ~ 3mm. From the equation of the perimeter of an ellipse, $P \approx \pi\sqrt{2(a^2 + b^2)}$, one can determine the length b of the minor axis (i.e. the distance traveled by the vanadium surface before failure). The expansion velocity can be approximated as the free surface velocity, U_{fs}, which is equal to twice the particle velocity at the back surface (U_{fs}~$2U_p$). Knowing the pressure at a given distance from the front surface from Figure 5.3, U_p can be obtained from the Rankine-Hugoniot (R-H) equations. Thus, strain-rates can be obtained.

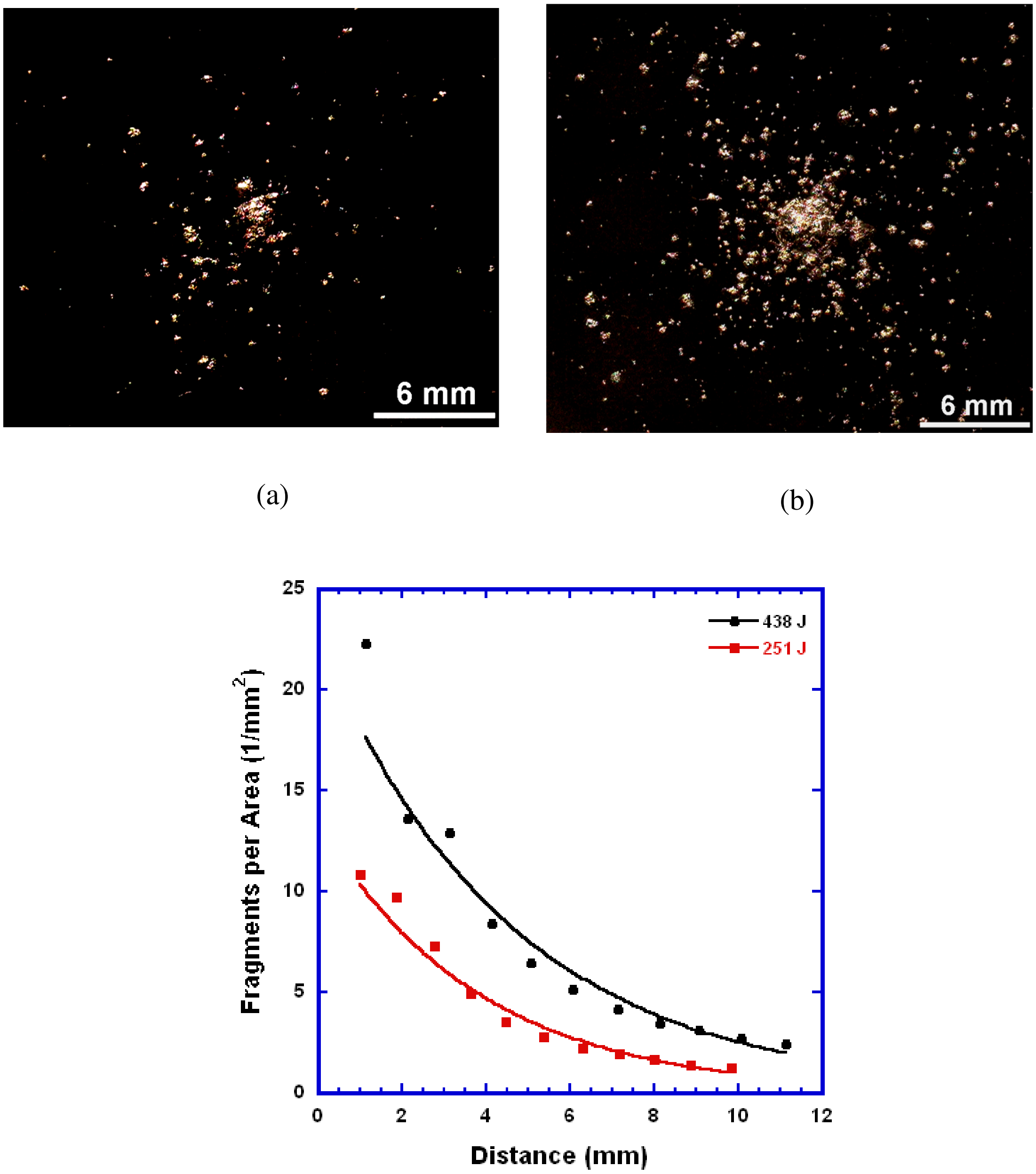

(a) (b)

(c)

Figure 5.18: Damage induced by 250 μm thick vanadium targets; (a) 251 J, 3 ns; (b) 438 J, 3 ns.

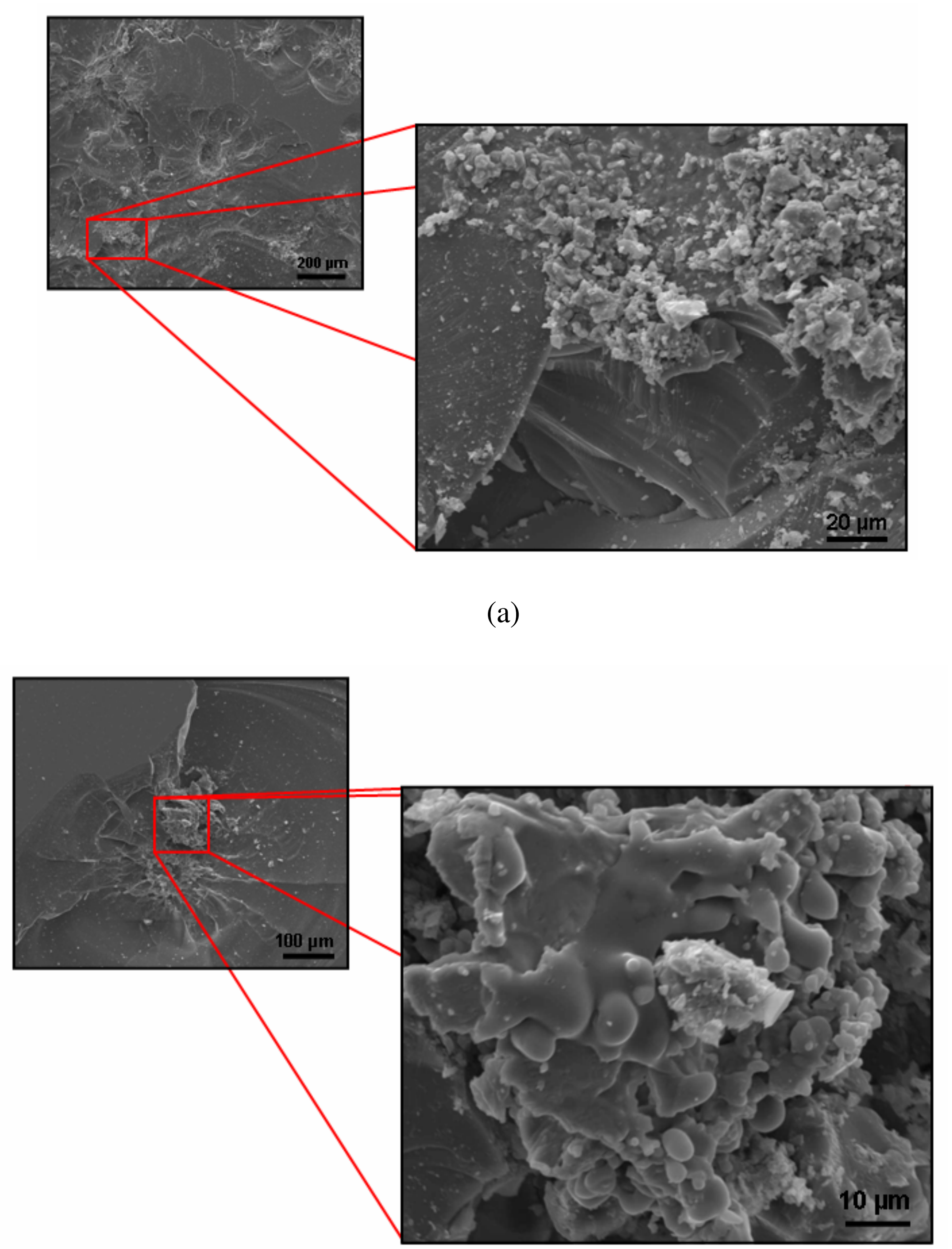

(a)

(b)

Figure 5.19: Glass shield placed behind 250 µm thick target, 438 J, 3 ns (a) debris and melting of vanadium around central crater; (b) melting on the surface of a vanadium fragment forming a subcrater away from the central crater.

Several investigators have studied the dynamic properties of vanadium under explosive loading [209], gas-gun loading [210], and split Hopkinson pressure bar deformation [211]. The dynamic yield stress was established to be ~ 480 MPa by Chabildas et al. [210], in very good agreement with work by Bat'kov et al [209]. The yield strength of vanadium does not seem to be very sensitive to strain rate. It does not vary much between strain rates of $\sim 10^4$ and 10^6 s^{-1} (the range of the current experiments). Hence, we take the dynamic yield strength, Y, of vanadium to be 480 MPa in our analysis. With all parameters determined, the fragment size, $S_{G\text{-}K}$, is plotted as a function of strain rate in Figure 5.20 (b).

We determined directly the vanadium fragment sizes based on the number of fragments collected on the glass shields. Table 5.4 shows the different experiments carried out and the total number of fragments counted on the glass shields. The total number was estimated with the aid of the imaging software, ImageJ. For simplicity, an assumption is made in all cases that the total spall area is $\frac{\pi d^2}{4}$, where d=2.5mm (the inner diameter of the washer), and the thickness of the fragments is equal to the spall thickness. Dividing the spalled area by the total number of fragments on the glass shield for all experimental cases, the area of each individual fragment can be estimated. Assuming that the fragments are geometrically square and taking the square root of this area, one obtains the fragment size, $S_{exp.}$ The experimentally determined fragment sizes are plotted as a function of strain rate in Figure 20 (b) and compared with the G-K theory.

Table 5.4: Total no. of fragments collected on the glass shields for the various experiments

Sample Thickness (µm)	**Laser Energy Level (J)**	**Total # of Fragments**
75	167	1031
75	290	2603
127	218 (8ns)	270
127	228	1150
127	430	1914
250	251	371
250	438	956

The experimentally determined fragment sizes are smaller than those obtained by the G-K model by a factor of 2-3. Considering the uncertainties in experimental measurements and simplifying assumptions in the Grady-Kipp model, the agreement is considered satisfactory. Both theory and experiment predict a decrease in fragment size with strain rate. The S_{exp} values are actually in better agreement with some fragment sizes measured from SEM micrographs of the glass shield surfaces. The sizes obtained from the G-K theory provide an overestimate. In particular, preliminary experiments (Maddox [212]) indicate that the free surface velocity is ¼ of the one calculated herein. In this case, the experimental and G-K theory would provide almost identical results. An interesting and potentially significant observation is that the 8 ns experiment provided a larger fragment size. It is possible that the thickness of the expanding layers can play a role in determining fragment size. This aspect is not incorporated into the G-K theory.

5.4 Spall Strength Determination

Values for the spall strength (σ_{spall}) of vanadium are absent in the literature, and an attempt to measure this value is made here. It is possible to determine σ_{spall} based on the experiments carried out on the 250 μm targets since a spall surface clearly developed in those experiments. We use the spall thickness measured from the optical micrographs (as in Figure 5.17) to aid in our calculations. From the micrograph, we estimate a spall thickness of ~30 μm for the 251 J experiment (and ~ 50 μm for the 438 J experiment, figure not shown here). Basic physics of waves is used to determine the tensile stress that develops at the spall plane. This tensile stress is determined by studying the pulse whose front has reached 250 μm (i.e. the back of the sample). At the spall plane, the tensile stress generated from the pulse is subtracted from the compressive stress due to the incident pulse. We estimate the spall strength to be 9 GPa for the 250 J experiment and 18 GPa for the 438 J experiment (see Figure 5.3 (b) and (c)). Clearly, a strain rate effect on the spall strength exists, as previously observed by others (e.g. work by Wang et al. [213] on laser irradiation of aluminum).

Grady [214] presents explicit expressions for the spall strength of condensed media. He derived an equation for the theoretical spall strength, which gives an upper bound value. The theoretical spall strength is derived from an analytical representation of the cold compression-tension curve based on a Morse potential and is of the form [214]:

$$P_{th} = \sqrt{\frac{U_{coh} B_o}{8 v_o}} \tag{5.11}$$

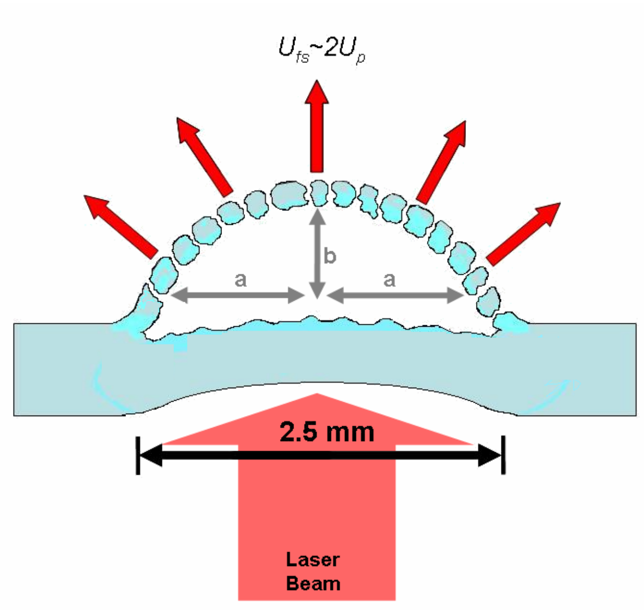

(a)

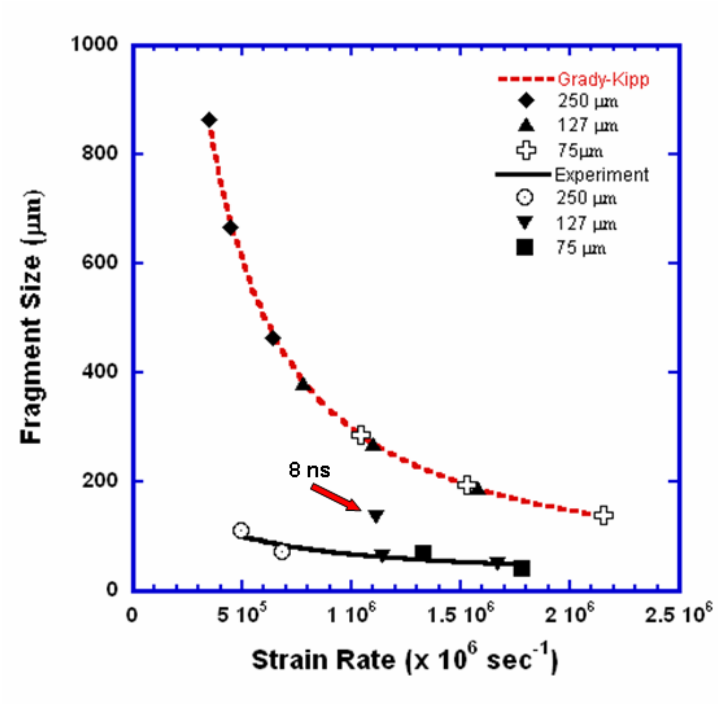

(b)

Figure 5.20: Illustration of the expansion of the spalled surface used in the Grady-Kipp analysis; (b) fragment size vs. strain rate.

where, U_{coh} is the specific cohesive energy (10.04 MJ/Kg for vanadium, calculated from data from [215] and [216]), B_o is the bulk modulus (160 GPa for vanadium), and v_o, is the specific volume at zero pressure. Equation (5.10) gives a theoretical spall strength of ~ 35 GPa. Table 5.5 presents the theoretical spall strength of various common FCC and BCC metals.

Using an energy balance analysis, Grady [214] also provides expressions for both the ductile and brittle spall strengths of condensed media, which provide values that are more consistent with experimental results. From the SEM analysis, it is safe to conclude that vanadium spalls by ductile behavior (see Figure 5.10 (c)). In other words, the spall process involves spherical cavitation (i.e. the nucleation, growth and coalescence of voids) and occurs strictly through plastic flow. Hence, we adopt the expression for ductile spall [214]:

$$P_{ds} = (2\rho\ c_o{}^2 Y \varepsilon_c)^{1/2} \tag{5.12}$$

where, ρ is density, c_o is the sound velocity at zero pressure, Y is the dynamic yield strength (480 MPa), and ε_c is the critical strain (0.2). This expression gives a spall strength of 5.5 GPa for vanadium. Figure 21 shows the theoretical ductile spall strength of Va and various other FCC and BCC metals and how they compare with experimental results obtained from [52]. These values are also tabulated in Table 5.5.

Table 5.5: Theoretical and Experimental spall strengths of various metals.

Element	Bulk Modulus (GPa)	Theoretical Spall Strength (GPa)	Theoretical Ductile Spall Strength (GPa)	Experimental Spall Strength (GPa)
Al	72.200	17.1	0.57-0.81	0.5-1.1
Cu	137.00	28.5	1	1-2.5
Va	**160.00**	**35**	**5.5**	**9-18**
Fe	168.00	35	-	1.6-4.5
Ta	200.00	42.4	6.5	4.4-6.8

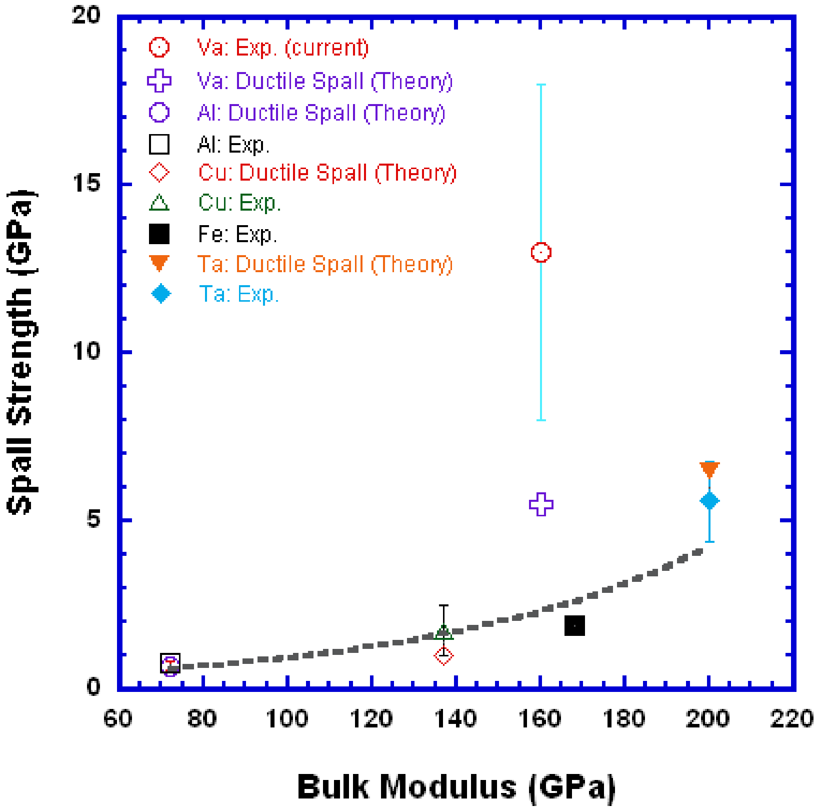

Figure 5.21: Spall strength vs. bulk modulus for various FCC and BCC metals.

Most of the theoretical ductile spall strengths of the various materials reported seem to be in the same range with that of the experimental values. The experimental values we calculated for vanadium, however, seem to be higher that the theoretical ductile spall strength by a factor of 2-3. Possible reasons for such a discrepancy maybe be due to the fact that the pulse decay profiles we based our calculations on are modeled and not actually based on VISAR data, which could introduce some error. Also, the rapid loading rates achieved in the laser experiments may have caused much higher tensile stresses to develop, producing spall strengths higher than more conventional impact situations (plate impact, explosives) and placing them closer to the theoretical spall strengths [214].

5.5 Conclusions

The following are the principal conclusions:

- Evidence of molten and resolidified fragments was observed in agreement with the solid-liquid transition induced by shock compression, which was calculated to be 150 GPa.
- The damage and fragment distribution was significantly affected by laser energy. Highest intensity experiments resulted in a high density of very small droplets distributed on the glass plate, and lowest intensity experiments resulted in a few damaged spots on the glass plates.

- Thicker foils (250 µm) showed incipient spall planes and bulk deformation by shock loading. Samples of intermediate thickness (127 µm) showed tearing away around the laser spot, and thinnest foils (75 µm) showed almost complete blow-off due to the laser interaction. At the same energy level, the damage accumulation on the glass shields decreased as the target thickness increased.
- Spalling and fragmentation were found to proceed by ductile void nucleation, growth, and coalescence. The grain boundaries were favored paths for decohesion.
- The fragmentation was quantitatively estimated as a function of laser pulse energy and duration and compared with the Grady-Kipp analysis, There is agreement within a factor of 2-3, which is considered satisfactory in view of the experimental uncertainties and theoretical assumptions.
- The spall thickness and calculated decay of the shock pulse were used to estimate the spall strength. It is found to be in the range of 9-18 GPa, and is twice the theoretical prediction from Grady [214], most likely due to the very rapid loading conditions in laser compression.

Chapter 5, in full, has been submitted for publication in Acta Materialia, 2008 (authors and co-authors: H. Jarmakani, D. Kalantar, A. Koniges, D. Eder, and M. A. Meyers).

APPENDIX A

MATLAB CODE USED FOR THE CALCULATION OF THE SLIP-TWINNING TRANSITION IN NANOCRYSTALLINE NICKEL AND NICKEL TUNGSTEN

A1. The Fundamental Code used for Cu

```
Sig_G=40*10^6;
Sig_T=300*10^6;
C2=3*10^6;
C3=2.8*10^-3;
C4=1.15*10^-4;
%T=300;
K_SG=7.8404*10^-33;
K_ICE=1.17*10^-7;
Strain_Rate_o=1;
density_o=8930;
S_Param=1.489;
Co=3940;

%Assigning pressure.
P_Shock=10^9:1000000000:120*10^9;

for i=1:120

%Temperature rise due to ICE from simulations
T_ICE(i)=318.03+2.751*10^-9*P_Shock(i);
%Temperature rise due to ICE from simulations
T_Shock(i)=1*10^-19*P_Shock(i).^2+2*10^-
9*P_Shock(i)+295.55;
%Calculating Strain_Rate from S-G equation for Shock
Strain_Rate_Shock(i)=K_SG.*P_Shock(i).^4;
%Calculating Strain_ Rate for isentropic condition
Strain_Rate_ICE(i)=K_ICE.*P_Shock(i).^(1.1);

%Calculating Strain

Vo=1/density_o;
C(i)=P_Shock(i).*Vo*S_Param^2;
D(i)=2*P_Shock(i).*Vo*S_Param-
P_Shock(i).*Vo*2*S_Param^2+Co^2;
```

```
E(i)=-(Co^2-P_Shock(i).*Vo+P_Shock(i).*Vo*2*S_Param-
P_Shock(i).*Vo*S_Param^2);
   %Solving quadratic equation
   %2 Solutions, so choose one without imaginary value
   G(i)=(-D(i)+sqrt(D(i).^2-4.*C(i).*E(i)))/(2.*C(i));
   H(i)=(-D(i)-sqrt(D(i).^2-4.*C(i).*E(i)))/(2.*C(i));

end

   %Taking log of exp(Strain)
   Sol_1=log(G);
   Strain=abs(Sol_1)
   %Strain function for [100] orientation.

for j=1:120

    Strain_func(j)=45510*Strain(j).^6-
86899*Strain(j).^5+63406*Strain(j).^4-
21834*abs(Strain(j)).^3+2901.8*Strain(j).^2+464.8*Strain(j
)-1.92;
%Z-A Equation.
%For Shock Condition
A(j)=-
C3.*T_Shock(j)+C4.*T_Shock(j).*log(Strain_Rate_Shock(j));
Sig_S(j)=Sig_G+6*(2/3)*C2.*Strain_func(j).*exp(A(j))
%For ICE Condition
A2(j)=-C3.*T_ICE(j)+C4*T_ICE(j).*log(Strain_Rate_ICE(j));
Sig_S2(j)=Sig_G+C2.*Strain_func(j).*exp(A2(j))
end
%plot
plot(P_Shock, Sig_S,'*')
hold on
plot(P_Shock, Sig_S2)
hold on
plot(P_Shock,Sig_T)
axis ([0 40*10^9 0 600*10^6])
```

A2. The Fundamental Code used for Ni:

```
Parameters
K_SG=7.8404*10^-33;
density_o=8874;
S_Param=1.46;
Co=4581;
k=0.2*10^6;
C2=160*10^6;
C2_1=2.4*10^9;
C3=0.0028;
C4=1.15*10^-4;
Sig_G=48*10^6;
%Sig_o=80*10^6;

%Twinning threshold stress
Kt=0.6*10^6;
Sig_To=600*10^6;

d1=300*10^-6;
d2=30*10^-6;
d3=3*10^-6;
d4=0.3*10^-6;
d5=0.03*10^-6;

%Assigning pressure.
P_Shock=10^9:1000000000:200*10^9;

for i=1:200

%Temperature rise due to Shock from simulations
T_Shock(i)=8*10^-20*P_Shock(i).^2+9*10^-
10*P_Shock(i)+301.5;


%Calculating Strain_Rate from S-G equation for Shock
Strain_Rate_Shock(i)=K_SG.*P_Shock(i).^4;

%Calculating Strain

Vo=1/density_o;
C(i)=P_Shock(i).*Vo*S_Param^2;
D(i)=2*P_Shock(i).*Vo*S_Param-
P_Shock(i).*Vo*2*S_Param^2+Co^2;
```

```
E(i)=-(Co^2-P_Shock(i).*Vo+P_Shock(i).*Vo*2*S_Param-
P_Shock(i).*Vo*S_Param^2);
   %Solving quadratic equation
   %2 Solutions, so choose one without imaginary value
   G(i)=(-D(i)+sqrt(D(i).^2-4.*C(i).*E(i)))/(2.*C(i));
   H(i)=(-D(i)-sqrt(D(i).^2-4.*C(i).*E(i)))/(2.*C(i));

end

   %Taking log of exp(Strain)
   Sol_1=log(G)
   Strain=abs(Sol_1)

   %Strain_func=103.66*Strain.^4+119.268*Strain.^3-
173.24*Strain.^2+66.116.*Strain+1;
   Strain_func=-269.57.*Strain.^4+398.484.*Strain.^3-
219.178.*Strain.^2+60.998.*Strain+1

%Z-A Equation.
%For Shock Condition

for j=1:200

A(j)=-
C3.*T_Shock(j)+C4.*T_Shock(j)*log(Strain_Rate_Shock(j));

Sig_o1=Sig_G+k*d1^(-.5);
%Stress1(j)=Sig_o1+C2.*(Strain_func(j)).*exp(A(j));
Stress1_1(j)=Sig_o1+C2_1.*Strain(j).^(0.53).*exp(A(j));
Sig_o2=Sig_G+k*d2^(-.5);
%Stress2(j)=Sig_o2+C2.*(Strain_func(j)).*exp(A(j));
Stress2(j)=Sig_o2+C2_1.*Strain(j).^(0.4).*exp(A(j));
Sig_o3=Sig_G+k*d3^(-.5);
%Stress3(j)=Sig_o3+C2.*(Strain_func(j)).*exp(A(j));
Stress3(j)=Sig_o3+C2_1.*Strain(j).^(0.15).*exp(A(j));
Sig_o4=Sig_G+k*d4^(-.5);
%Stress4(j)=Sig_o4+C2.*(Strain_func(j)).*exp(A(j));
Stress4(j)=Sig_o4+C2_1.*Strain(j).^(0.1).*exp(A(j));
Sig_o5=Sig_G+k*d5^(-.5);
%Stress5(j)=Sig_o5+C2.*(Strain_func(j)).*exp(A(j));
Stress5(j)=Sig_o5+C2_1.*Strain(j).^(0).*exp(A(j));
end

Sig_T1=Sig_To+Kt*d1^(-0.5);
Sig_T2=Sig_To+Kt*d2^(-0.5);
```

```
Sig_T3=Sig_To+Kt*d3^(-0.5);
Sig_T4=Sig_To+Kt*d4^(-0.5);
Sig_T5=Sig_To+Kt*d5^(-0.5);

% plot(P_Shock, Stress1)
% hold on
plot(P_Shock, Stress1_1, '--')
hold on
plot(P_Shock, Stress2)
hold on
plot(P_Shock, Stress3)
hold on
plot(P_Shock, Stress4)
hold on
plot(P_Shock, Stress5, 'r')
hold on
plot(P_Shock, Sig_T1)
hold on
plot(P_Shock, Sig_T2)
hold on
plot(P_Shock, Sig_T3)
hold on
plot(P_Shock, Sig_T4)
hold on
plot(P_Shock, Sig_T5, 'r')
axis([0 120*10^9 0 6*10^9])
```

A3. Fundamental Code Used for Ni-W:

```
% Parameters
K_SG=7.8404*10^-33;
density_o=8874;
S_Param=1.46;
Co=4581;
k=0.2*10^6;
C2=2.4*10^9;
C3=0.0028;
C4=1.15*10^-4;
Sig_G=48*10^6;
Shear_modNi=76*10^9;
Shear_mod5=82.6*10^9;
Shear_mod10=84.7*10^9;
Shear_mod13=88*10^9;
strength_factor=977*10^6;

b=0.249*10^-9;
%Sig_G=370*10^6;

%Twinning threshold stress
Kt=0.6*10^6;
Kt5=0.55*10^6;
Kt10=0.5*10^6;
Kt13=0.45*10^6;
K2=7.76*10^9;

%Stacking Fault Energy
SFE_Ni=130*10^-3;
SFE_NiW5=73.55*10^-3;
SFE_NiW10=58.3*10^-3;
SFE_NiW13=52.5*10^-3;

d1=0.2*10^-6;
d2=30*10^-6;
d3=3*10^-6;
d4=0.3*10^-6;
d5=0.03*10^-6;
d1=0.07*10^-6;
d2=0.06*10^-6;
d3=0.05^-6;
d4=0.03*10^-6;
d5=0.015*10^-6;
d6=0.009*10^-6;
```

```
%Assigning pressure.
P_Shock=10^8:100000000:80*10^9;

for i=1:800

%Temperature rise due to Shock from thermodynamic
calculations
T_Shock(i)=8*10^-20*P_Shock(i).^2+9*10^-
10*P_Shock(i)+301.5;

%Calculating Strain_Rate from S-G equation for Shock
Strain_Rate_Shock(i)=K_SG.*P_Shock(i).^4;

%Calculating Strain

Vo=1/density_o;
C(i)=P_Shock(i).*Vo*S_Param^2;
D(i)=2*P_Shock(i).*Vo*S_Param-
P_Shock(i).*Vo*2*S_Param^2+Co^2;
E(i)=-(Co^2-P_Shock(i).*Vo+P_Shock(i).*Vo*2*S_Param-
P_Shock(i).*Vo*S_Param^2);
   %Solving quadratic equation
   %2 Solutions, so choose one without imaginary value
   G(i)=(-D(i)+sqrt(D(i).^2-4.*C(i).*E(i)))/(2.*C(i));
   H(i)=(-D(i)-sqrt(D(i).^2-4.*C(i).*E(i)))/(2.*C(i));

end

   %Taking log of exp(Strain)
   Sol_1=log(G);
   Strain=abs(Sol_1);

   %Strain_func=103.66*Strain.^4+119.268*Strain.^3-
173.24*Strain.^2+66.116.*Strain+1;
   Strain_func=-269.57.*Strain.^4+398.484.*Strain.^3-
219.178.*Strain.^2+60.998.*Strain+1;

%Z-A Equation.
%For Shock Condition

for j=1:800

A(j)=-
C3.*T_Shock(j)+C4.*T_Shock(j)*log(Strain_Rate_Shock(j));
```

```
% pure Ni
Sig_oNi=Sig_G+k*d1^(-.5);
StressNi(j)=Sig_oNi+C2.*((Strain(j).^(0.3))*exp(A(j)));

% 5% W
conc5=0.05
delta_sigma5=(strength_factor^2*conc5)^(1/2);
Sig_o5=Sig_G+delta_sigma5+k*d1^(-.5);
Stress5(j)=Sig_o5+C2.*((Strain(j).^(0.3))*exp(A(j)));

% 10% W
conc10=0.1
delta_sigma10=(strength_factor^2*conc10)^(1/2);
Sig_o10=Sig_G+delta_sigma10+k*d1^(-.5) ;
Stress10(j)=Sig_o10+C2.*((Strain(j).^(0.3))*exp(A(j)));

% 13% W
conc13=0.13
delta_sigma13=(strength_factor^2*conc13)^(1/2);
Sig_o13=Sig_G+delta_sigma13+k*d1^(-.5) ;
Stress13(j)=Sig_o13+C2.*((Strain(j).^(0.3))*exp(A(j)));

end

Sig_TNi=K2*(SFE_Ni/(Shear_modNi*b))^0.5+Kt*d1^(-0.5);
Sig_T5=K2*(SFE_NiW5/(Shear_mod5*b))^0.5+Kt5*d1^(-0.5);
Sig_T10=K2*(SFE_NiW10/(Shear_mod10*b))^0.5+Kt10*d1^(-0.5);
Sig_T13=K2*(SFE_NiW13/(Shear_mod13*b))^0.5+Kt13*d1^(-0.5);


plot(P_Shock, StressNi,'r')
hold on
plot(P_Shock, Stress5, 'b')
hold on
plot(P_Shock, Stress10, 'c')
hold on
plot(P_Shock, Stress13, '--')
hold on
plot(P_Shock, Sig_TNi, 'r')
hold on
plot(P_Shock, Sig_T5, 'b')
hold on
plot(P_Shock, Sig_T10, 'c')
hold on
```

```
plot(P_Shock, Sig_T13, '--')
hold on
plot(P_Shock, Sig_T5)
hold on
plot(P_Shock, Sig_T6)
plot(P_Shock, T_Shock)
axis([0 60*10^9 0 3*10^9])
```

APPENDIX B

LAMMPS CODE USED FOR RUNNING SHOCK SIMULATIONS IN SINGLE AND NANOCRYSTALLINE NICKEL

B1. LAMMPS code used for producing a shock wave in [001] Ni:

```
units             metal
boundary          p p s
atom_style        eam

lattice           fcc 3.52
region            box block 0 50 0 50 0 200

create_box        3 box

orient            x 1 0 0
orient            y 0 1 0
orient            z 0 0 1
origin            0 0 0

create_atoms      1

pair_style        eam
pair_coeff        * *
/users/mameyers/lammps1/potentials/niyuri.pot 1 1 1

mass               1 58.693
mass               2 58.69
mass               3 58.69

neighbor         0.3 bin
neigh_modify     delay 5
region           piston block INF INF INF INF INF 3
region           bulk block INF INF INF INF 3 INF
group            piston region piston
group            bulk region bulk

set              bulk atom 1
set piston atom 2
```

```
#temperature controllers
temperature     new3d all full

#equilibrate
velocity        all create 20.0 5812775 temp new3d
fix             1 all nve


thermo          100
thermo_style    custom step temp pe ke eng press vol lx ly
lz pxx pyy pzz
thermo_modify   temp new3d norm yes

timestep        0.001
run             1000

# Shock

velocity        piston set 0 0 2.233

# run           1

fix             5 piston setforce 0.0 0.0 0.0

dump            1 all custom 250
/gpfs/mameyers/shock_release_001_40GPa.* x y z centro vx
vy vz sxx syy szz

dump_modify     1 scale no

thermo          100

thermo_style    custom step temp pe ke eng press vol lx ly
lz pxx pyy pzz

thermo_modify   temp new3d norm yes

run             10000

# To unload

velocity        piston set 0 0 0

run             12000
```

B2. LAMMPS Code used for producing a shock in nanocrystalline Ni:

```
units            metal
boundary         p p s
#atom_style       atomic
#pair_style       eam/alloy
atom_style      eam
pair_style      eam
#
read_data
/users/mameyers/lammps1/nc_work/shock_simulations/5nm/Fina
l_compress.dat
pair_coeff        * *
/users/mameyers/lammps1/potentials/niyuri.pot 1 1 1
mass              1 58.693
neighbor         2.0 bin
neigh_modify     every 1 delay 5 check yes

lattice          fcc 3.52

region           piston block INF INF INF INF INF -97
region           bulk block INF INF INF INF -97 INF
group            piston region piston
group            bulk region bulk
set              bulk atom 1
set              piston atom 2

#equilibrate
temperature     new3d all full
velocity        all create 5 5812775 temp new3d
fix             4 all nve

thermo          100
thermo_style    custom step temp pe ke eng press vol lx ly
lz pxx pyy pzz
thermo_modify   temp new3d norm yes
timestep        0.001
run             1000

#shock
velocity        piston set 0 0 1.904
fix             5 piston setforce 0.0 0.0 0.0
```

```
dump             1 all custom 1000
/gpfs/mameyers/5nm_38GPa/5nmeter_tag_38GPa.* x y z centro
vx vy vz sxx syy szz tag
thermo           100
thermo_style     custom step temp pe ke eng press vol lx
ly lz pxx pyy pzz
thermo_modify    temp new3d norm yes
#reset_timestep   0
#restart          10000
/gpfs/mameyers/5nm_38GPa/5nm_tag_38GPa_RESTART10000.*
run              10000
# To unload
velocity         piston set 0 0 0
run              12000
```

B3: LAMMPS code used for uniaxially loading and unloading 5 nm g. s. Ni sample:

```
units            metal
boundary         p p p
atom_style       atomic
pair_style       eam/alloy
#
#read_data         Nc5datNi.dat
read_restart     ../relaxation/relax.restart.10000

#pair_coeff        * *
/home/hussam/lammps/lammps/potentials/niu3
pair_coeff       * * ../niyuri.pot 1 1 1
mass             1 58.693
#
neighbor         2.0 bin
neigh_modify     every 1 delay 5 check yes

#equilibrate for 10000 steps

temperature     new3d all full
#velocity        all create 0.01 5812775 temp new3d
#fix             1 all nve
#fix             2 all temp/rescale 7 0.01 0.01 0.001 1.
#thermo          100
#thermo_modify   temp new3d norm yes
#timestep        0.0001
#run             2500

#unfix           2
#velocity        all create 300 5812775 temp new3d
#fix             3 all temp/rescale 7 300 300 0.1 1
#thermo          100
#thermo_modify   temp new3d norm yes
#timestep        0.0005
#run             2500

#unfix           3
#velocity        all create 5 5812775 temp new3d
#fix             4  all temp/rescale 7 5 5 0.1 1
#thermo          100
#thermo_modify   temp new3d norm yes
#timestep        0.001
```

```
#restart          7500 compress-00GPa
#run              2500

#unfix            4
#thermo           100
#thermo_modify    temp new3d norm yes
#dump              1 all custom 500
/gpfs/mameyers/relaxed.dump.* x y z centro type
#dump_modify       1 scale no
#dump_modify      1 format "%g %g %g %g %d" scale no

#timestep         0.001
#restart          10000 relax.restart
#run              2500

## END of RELAXATION

## Volumetric compression for 8% volume strain with strain
rate 2e10
fix              1 all nve
fix              5 all volume/rescale 1 z -76.56 76.56
thermo           100
thermo_style     custom step temp pe ke eng press vol lx ly
lz pxx pyy pzz cpu
thermo_modify    temp new3d norm yes
timestep         0.001
dump             1 all custom 500 dump.compress-expand x y
z vx vy vz centro sxx syy szz tag
restart          2000 restart.compress-expand
run              4000

## Hold at same volume
unfix            5
run              10000

## Volumetric expansion to the original volume
fix              6 all volume/rescale 1 z -88.0 88.0
run              4000

## End Simulation
```

REFERENCES

1 “**draft animal.**” Encyclopædia Britannica. 2006. Encyclopædia Britannica Online. 21 Nov. 2006, http://www.britannica.com/eb/article-9031115.

2 “**water wheel.”** About Inventors. 2006. About Inventors Online. 21 Nov. 2006, http://inventors.about.com/library/inventors/blwaterwheel.htm.

3 Energy Information Administration. Annual Energy Outlook 2001: With Projections to 2020. DOE/EIA-0383 (2001). Washington, DC: December 2000. EIA – Energy Information Administration.

4 Murray LR. Nuclear Energy: An introduction to the Concepts, Systems, and Applications of Nuclear Processes, fifth edition, Butterworth-Heinemann, Woburn, MA, 2001.

5 Heller A. “On Target Designing for Ignition,” Science and Technology Review, Lawrence Livermore National Labs, July/Aug 1999.

6 Slutz SA, Herrmann MC. Physics of Plasmas 2003;10:234.

7 Meyers MA, Mishra A, Benson DJ. Prog. Mat. Sci 2006;51:427.

8 Vogler TJ, Chhabildas LC. Int J of Impact Eng 2006;33,812.

9 Pullington M, Thompson P, Maw J. Journal of AWE 2005;5:16.

10 Heller A. How metals fail Science and Technology Review, Lawrence Livermore National Labs July/Aug 2002:13.

11 Lyzenga GA, Ahrens TJ. in Shock Waves in Condensed Matter, 1981, Eds. Nellis WJ, Seaman L, Graham RA,American Institute of Physics Conf Proceedings 1982;78;231.

12 Barker LM. Shock Waves in Condensed Matter, Eds. Asay JR, Graham RA, Straub GK, Elsevier Sci Pub, Amsterdam, 1984.

13 Mogilevskii MA, Bordzilovskii SA, Gorshkov NN. Combustion, Explosion and Shock Waves 1978;14:794.

14 Adadurov GA, Gustov VV, Zhuchenko VS, Kosygin M Yu, Yampol’skii PA. Combustion, Explosion and Shock Waves 1973;9:449.

15 Adadurov GA, Gol’danskii VI. Russian Chemical Reviews, 1981;50:948.

16 Meyers MA, Chawla KK. Mechanical Behavior of Materials, Prentice-Hall, Inc., New Jersey, 1999:236.

17 Chhabildas L C, Barker ML. in Shock Compression of Condensed Matter 1987, Eds. Schmidt SC, Holmes NC, Amsterdam: Elsevier, 1988:111-114.

18 Asay JR, Chhabildas LC, Dandekar DP. Appl Phys 1980;51:4774.

19 McQueen RG, Marsh SP, Taylor JW, Fritz JN, Carter WJ. in High Velocity Impact Phenomena, Eds. Kinslow R, Academic Press, N. 1970:293.

20 Bat’kov YV, Kanyazev VN, Novikov SA, Raevski SA, Fishman ND. J Phys IV France 2000;10:793.

21 Bat’kov YV, Kanyazev VN, Novikov SA, Raevski SA, Fishman ND. in Shock Compression of Condensed Matter 1999, Eds. Furnish MD, Chhabildas LC, Hixson RX, Melville, New York: American Institute of Physics, 2000:501.

22 Bat’kov YV, Kanyazev VN, Novikov SA, Raevski SA, Fishman, N. D., Combust. Explos. Shock Waves, 1999, Vol. 35, pp. 707-710.

23 Rosenberg Z, Bourne NK, Gray GT, Millett, JCF. In: Furnish M. D, et al., editors. Shock Compression of Condensed Matter, AIP; 2002:575-578.

24 Gray III GT, Morris CE. Journal De Phys. III, 1991;1:191.

25 Remington BA, Bazan G, Belak J, Bringa E, Caturla M, Colvin JD, Edwards MJ, Glendinning SG, Ivanov DS, Kad B, Kalantar DH, Kumar M, Lasinski BF, Lorenz KT, McNaney JM, Meyerhofer DD, Meyers MA, Pollaine SM, Rowley D, Schneider M, Stölken JS, Wark JS, Weber SV, Wolfer WG, Yaakobi B, Zhigilei LV. Metall Mater Trans 2004;35A:2587.

26 McNaney JM, Edwards MJ, Becker R, Lorenz KT, Remington BA. Metall Mater Trans 2004;35A:265.

27 Tipton R, Managan R, Amala P. Users Manual for CALE, Lawrence Livermore National Laboratory, Livermore, CA, 2002.

28 Steinberg DJ, Cochran SG, Guinan MW. J Appl Phys 1980;51:1496.

29 Hawke RS, Duerre DE, Huebel JG, Klapper H, Steinberg DJ, Keeler RN. J Appl Phys 1972;43:2734.

30 Kidder RE. in Proceedings of the Conference on Magagauss Magnetic Field Generation by Explosives and Related Experiments, Frascati, Italy, 1965;37-54.

31 Steinberg D. Lawrence Livermore Laboratory Report UCRL-14931 (Unpublished).

32 Hall CA, Phys of Plasmas 2000;7:2069.

33 Hall CA, Asay JR, Knudson MD, Stygar WA, Spielman RB, Pointon TD, Reisman DB, Toor A, Cauble RC. Rev Sci Inst 2001;71:3587.

34 Reisman DB, Toor A, Cauble RC, Hall CA, Asay JR, Knudson MD, Furnish MD. J Appl Phys 2001;89:1625.

35 Aidun JB, Gupta YM. J Appl Phys 1991;69:6998.

36 Meyers MA, Mishra A, Benson DJ. JOM 2006:41.

37 Kumar KS, Van Swygenhoven H, Suresh S. Acta Mater 2003;51:5743.

38 Meyers MA, Ashworth E. Phil Mag 1982;A46:737.

39 Fu HH, Benson DJ, Meyers MA. Acta Mat 2001;49:2567.

40 Fu HH, Benson DJ, Meyers MA. Acta Mat 2004;52:4413.

41 Chokshi RA, Karch J, Gleiter H. Scripta Metall 1989;23:1679.

42 Conrad H. Met and Mat Trans 2004;35A**:**2681**.**

43 Ashby MF, Verall RA. Acta Metall 1973;21:149

44 Weertman JR, Farkas D, Hemker K, Kung H, Mayo M, Mitra R, Van Swygenhoven H. MRS Bulletin 1999;24:44.

45 Zhu YT, Liao SG, Srinivasan SG, Zhao YH, Baskes MI, Zhou F, Lavernia EJ. Appl Phys Lett 2004;85:5049.

46 Shan Z, Stach EA, Wiezorek JM.K, Knapp JA, Follstaedt DM, Mao SX. Science 2004;305:654-657.

47 Ma E. Scripta Mater 2003;49:663.

48 Schneider MS, Kad BK, Kalantar DH, Remington BA, Meyers MA. Met Mat Trans A 2004;35A:2633.

49 Dalla Torre F, Van Swygenhoven H, Victoria M. Acta Mat 2002;50:3957.

50 Jia D, Ramesh KT, Ma E, Lu L, Lu K. Scripta Mat 2001;45:613-620.

51 Jia D, Ramesh KT, Ma E. Acta Mater 2003;51:3495.

52 Meyers MA, Aimone CT. Prog Mater Sci. 1983;28:1.

53 Davidson L, Graham RA. Phys Rep 1979;55:255.

54 Curran DR, Seaman L. Phys Rep 1987;147:253.

55 McQueen RG, Marsh SP. J Appl Phys 1962;33:654.

56 Vidal F, Johnston TW, Laville S, Barthélemy O, Chaker M, Le Drogoff B, Margot J, Sabsabi M. Phys Rev Lett 2001;86:2573.

57 Kanel GI, Fortov VE. Adv Mech 1987;10:3.

58 Rosenberg L, Luttwak G, Yeshurun Y, Partom Y. J Appl Phys 1983;54:2147.

59 Chen D, He H, Jing F. J Appl Phys 2007; 102:1.

60 Andriot P, Chapron P, Lambert V, Olive F. Shock Waves in Condensed Matter Elsevier Science, Netherlands, 1983;277.

61 Rybakov AP, Rybakov IA. Eur J Mech B Fluids 1995;14:197.

62 Zhiembetov AK, Mikhaylov, AL, Smirnov GS. AIP Conf Proc 2002;620:547.

63 Holtkamp DB, Clark DA, Garcia IA. AIP Conf Proc 2004;705:473.

64 Holtkamp DB, Clark DA, Garcia A. AIP Conf Proc 2004;705:477.

65 Fox JA, Barr DN. Appl Phys Lett 1973;22:594.

66 Cottet F, Boustie M. J Appl Phys 1989;66:4067.

67 Eliezer S, Gilath I, Bar-Noy T. J Appl Phys 1990;67:715.

68 Eliezer S, Gazit Y, Gilath I. J Appl Phys 1990;68:56.

69 Boustie M, Cottet F. J Appl Phys 1991;69:7533.

70 Lacomme M, Cazalis B, David J, Niérat G, Salères A, Sibille G. J Phys (France) IV Colloq 8 Supp J Phys (France) III 1994;4:77.

71 de Rességuier T, Cottet F. J Appl Phys 1995;77:3756.

72 Meyers MA, Gregori F, Kad BK, Schneider MS, Kalantar DH, Remington BA, Ravichandran G, Boehly T, Wark JS, Acta Mat 2003;51:1211.

73 Schneider MS, Kad BK, Kalantar DH, Remington BA, Kenik E, Jarmakani H, Meyers MA. IJIE 2005;32:473.

74 Hawreliak J, Colvin JD, Eggert JH, Kalantar DH, Lorenzana HE, Stölken JS, Davies HM, Germann TC, Holian BL, Kadau K, Lomdahl PS, Higginbotham A, Rosolankova K, Sheppard J, Wark JS. Phys Rev B 2006;74:184107.

75 Wang Y, He H, Boustie M, Sekine T. J Appl Phys 2007; 101:103528.

76 Meyers MA, Schneider MS, Jarmakani H, Kad B, Remington BA, Kalantar DH, McNaney J, Cao B, Wark J. Met Trans 2007;39A:304.

77 Cao BY, Meyers MA, Lassila DH, Schneider MS, Kad BK, Huang CX, Xu YB, Kalantar DH, Remington BA. Mat Sci Eng A 2005;409:270.

78 de Rességuier T, Signor L, Dragon A, Boustie M, Roy G, Llorca F. J Appl Phys 2007;101:013506.

79 Lubarda VA, Meyers MA, Schneider M, Remington B, Kalantar D. Acta Mat 2004;52:1397.

80 McElfresh M, Gunther J, Alford C, Fought E, Cook R, Nikroo A, Xu H, Cooley, JC, Field RD, Hackenberg RE, Nobile A. LLNL report UCRL-JRNL-215294.

81 Johari O, Thomas G. Acta Metall 1964;2:113.

82 Nguyen JH, Orlikowski D, Streitz FH, Holmes NC, Moriarty JA. Shock Compression of Condensed Matter, M. D. Furnish, L.C. Chhabildas, and R. S. Hixson, Eds., AIP Conf. Proc., Melville, New York (2004).

83 McNaney JM, Torralva B, Harper JS, Nguyen JH, Orlikowski D, Raevsky VA, Meyers MA, Kad B, Jarmakani H, Schneider MS, Bringa E, Remington BA. LLNL report UCRL-TR-218846.

84 Murr LE. In: Meyers MA, Murr LE, editors. Shock Waves and High-Strain Rate Phenomena in Metals. NY: Plenum; 1981:607-73.

85 Gray III GT. In: Meyers MA, Murr LE, Staudhammer KP, editors. Shock Wave and High Strain Rate Phenomena in Materials. NY: M. Dekker; 1992:899-911.

86 Bassim MN, Klassen RJ. MSE 1986;81:163.

87 Bassim MN, Bayoumi MR. Proceedings of the International Conference on Low-Energy Dislocation Structures", University of Virginia, 1986:317-324.

88 Bassim MN, Huang LB. MSE 1988;96:159.

89 Bassim MN, Klassesn RJ. Scr Metall 1987;21:625.

90 Sencer BH, Maloy SA, Gray III GT. Acta Mat 2005;53:3293.

91 Meyers MA, Murr LE. In: Meyers MA, Murr LE, editors. Shock Waves and High-Strain Rate Phenomena in Metals. NY: Plenum; 1981:487-530.

92 Cao BY, Lassila DH, Schneider MS, Kad BK, Huang CX, Xu YB, Kalantar DH, Remington BA, Meyers MA. MSE (A) 2005;409:270.

93 Swegle JW, Grady DE. in shock Waves in Condensed Matter-1985, eds. Y. M. Gupta, Plenum, New York, 1986:353.

94 Preston DL, Tonks DL, Wallace DC. J Appl Phys 2003;93:211.

95 Murr LE, Meyers MA, Niou CS, Chen YJ, Pappu S, Kennedy C. Acta Mat 1997;45:157.

96 Meyers MA, Vohringer O, Lubarda VA. Acta Mat 2001;49:4025.

97 Zerilli FJ, Armstrong RW. J Appl Phys 1987;61:1816.

98 Follansbee PS, Kocks UF. Acta Met 1988;36:81.

99 Steinberg DJ, Cochran SG, Guinan MW. J Appl Phys 1980;51:1496.

100 Steinberg DJ, Lund CM. J Appl Phys 1989;65:1528.

101 Thornton WG, Mitchell TE. Phil Mag 1962;7:361.

102 Diehl J. Z Metallk 1956;47:33.

103 Bringa EM, Caro A, Victoria M, Park N. JOM 2005:57.

104 Meyers MA. Mater Sci Eng 1977;30:99.

105 Meyers MA, Carvalho MS. Mater Sci Eng 1976;24:131.

106 Jones OE, Holland JR. Acta Metall 1968;16:1037.

107 Holian BL, Straub GK. Phys Rev Lett 1979; 43:1598.

108 Holian BL, Hoover WG, Moran B, Straub G K. Phys Rev A 1980;22:249

109 Holian BL. Phys Rev A 1988;37:2562.

110 Holian BL, Lomdahl PS. Science 1998;280:2085.

111 Germann TC, Holian BL, Lomdahl PS. Phys Rev Lett 2000;84:5351.

112 Tanguy D, Mareschal M, Lomdahl PS, Germann TC, Holian BL, Ravelo R. Phys Rev B 2003;68:14111

113 Germann TC, Holian BL, Lomdahl PS, Tanguy D, Mareschal M, R. Ravelo. Metall Mater Trans A 2004;35A:2609.

114 Taylor P A, Dodson BW. Phys Rev B 1990;42:1200.

115 Holian BL, Voter AF, Wagner NJ, Ravelo RJ, Chen SP, Hoover WG, Hoover CG, Hammerberg, JE, Dontje TD. Phys Rev A 1991;43:2655.

116 Ryazanov AI, Dremov VV, Kiritani M. Radiat Eff Def Solids 2002;157:209.

117 Bringa EM, Cazamias, JU, Erhart P, Stolken J, Tanushev N, Wirth BD, Rudd RE, Caturla MJ. J Appl Phys 2004;96:3793.

118 Cao B, Bringa EM, Meyers MA. Metall Mater Trans A 2007;38:1073.

119 Smith CS. Response of Metals to High Velocity Deformation, Interscience Publishers, New York, NY, pp. 483-486, 1961.

120 Meyers MA. Scripta Metall 1978;12:21.

121 Foreman AJE, English CA, Phythian W. J Philos Mag 1992;A66:655.

122 Mishin Y, Mehl MJ, Papaconstantopoulos DA, Voter AF, Kress JD. Phys Rev B 2001;63:224106.

123 Kum OJ. Appl Phys 2003;93:3239.

124 Van Swygenhoven H, Caro A. Phys Rev B 1998;58:11246.

125 Schiøtz J, Di Tolla FD, Jacobsen KW. Nature 1998;391:561.

126 Van Swygenhoven H, Spaczer M, Caro A, Farkas D, Phys Rev B 1999;60:22.

127 Yamakov V, Wolf D, Phillpot SR, Mukherjee AK, Gleiter H. Nat Mat 2002;1:45.

128 Schiøtz J, and Jacobsen KW. Science 2003;31:1357.

129 Van Swygenhoven H, Derlet PM, Frøseth AG. Nat Mater 2004;3:399.

130 Finnis M, Sinclair M. Philos Mag A 1984;50:45.

131 Jacobsen KW, Nørskov JK, Puska, MJ. Phys Rev B 1987;35:7423.

132 Jacobsen KW, Stoltze P, Nørskov JK. Surf Sci 1996;366:394.

133 Ercolessi F, Adams JB. Europhys Lett. 1994;26:583.

134 Bringa EM, Caro A, Wang Y, Victoria M, McNaney JM, Remington BA, Smith RF, Torralva BR, Van Swygenhoven H. Science;2005:309:1838.

135 Dremov V, Petrovtsev A, Sapozhnikov P, Smirnova M. Phys Rev B 2006;74: 144110.

136 Sapozhnikov FA, Dremov VV, Smirnova MS. J Phys IV France 2003;110:323.

137 Wang YM, Bringa EM, McNaney JM, Victoria M, Caro A, Hodge AM, Smith R, Torralva B, Remington BA, Schuh CA, Jarmakani H, Meyers MA. Appl Phys Lett 2006;88:061917.

138 Wang YM, Bringa EM, Victoria M, Caro A, McNaney JM, Smith R, Remington BA. J Phys IV France 2006;134:915-920.

139 Plimpton SJ. J Comput Phys 1995;117:1-19, http://lammps.sandia.gov.

140 Mishin Y, Farkas D, Mehl MJ, Papaconstantantopoulos DA. Phys Rev B 1999;59:3393.

141 Murr, LE. Interfacial Phenomena in Metals and Alloys, Addison-Wesley, Reading MA, 1975.

142 Daw MS, Baskes MI. Phys Rev Lett 1983;50:1285.

143 Daw MS, Baskes MI. Phys Rev B 1984;29:6443.

144 Rice MH, McQueen RG, Walsh JM. Solid State Phys 1958;6:1.

145 Meyers MA. Dynamic Behavior of Materials, John Wiley & Sons, Inc., New York, NY, 1994.

146 Nolder RL, Thomas G. Acta Metall 1963;11:994.

147 Greulich F, Murr LE. Mater Sci Eng 1979;39:81.

148 Esquivel EV, Murr LE, Trillo EA, Baquera MJ. Mater Sci 2003;38:2223.

149 Kelchner CL, Plimpton S, Hamilton JC. Phys Rev B 1998;58:11085.

150 Cottrell A. Dislocations and Plastic Flow in Crystals, Clarendon Press, Oxford, United Kingdom, p. 54, 1953.

151 Xu G, Argon AS. Phil Mag 2000;80:605.

152 Rice JR. J Mech Phys Sol 1992;40:256.

153 Khantha M, Vitek V. Acta Mater 1997;45:4675.

154 Meyers MA, Schneider MS, Jarmakani H, Kad B, Remington BA, Kalantar DH, McNaney J, Cao B, Wark J. Met Trans 2007;39A:304.

155 Hull D, Bacon DJ. Introduction to Dislocations, Butterworth-Heinemann, Oxford, United Kingdom, p. 147, 2001.

156 Preston DL, Wallace DC. Solid State Commun 1992;81:277.

157 Meyers MA, Jarmakani H, McNaney JM, Schneider M, Nguyen JH, Kad B. J Phys IV France 2006;13437.

158 Kadau K, Germann TC, Lomdahl PS, Holian, BL, Kadau D, Ental P, Kreth M, Westerhof F, Wolf DE. Metall Mater Trans A 2004;35A:2719.

159 Mishin Y, Mehl MJ, Papaconstantopoulos DA, Voter AF, Kress JD. Phys Rev B 2001;63:224106.

160 Odunuga S, Li Y, Krasnochtchekov P, Bellon P, Averback RS. Phys Rev Lett 2005;95:045901.

161 Vo NQ, Odunuga S, Bellon P, Averback RS, Caro A. (Submitted to Phys. Rev. B).

162 Chen M, Ma E, Hemker KJ, Sheng H, Wang Y, Cheng X. Science 2003;300:1275.

163 Schuh CA, Nieh TG, Yamasaki T. Scripta Mat 2002;46:735.

164 Schuh CA, Nieh TG, Iwasaki H. Acta Mat 2003;51:431.

165 Youssef KM, Scattergood RO, Murty KL, Horton JA, Koch CC. Appl Phys Lett 2005;87:091904.

166 Budrovic Z, Van Swygenhoven H, Derlet PM, Van Pategem S, Schmitt B. Science 2004;304:273.

167 Warner DH, Curtin WA, Qu S. Nat Mat 2007;6:876.

168 Mulford RA, Kocks UF. Acta Metall 1979:27;1125.

169 Vohringer O. Z Metall 1970;67:518.

170 Choi IS, Detor AJ, Schwaiger R, Dao M, Schuh CA, Suresh S. J Mech Phys Sol 2008;56:172.

171 Thompson AW. Acta Metall 1975;23:1337.

172 Thompson AW. Acta Metall 1977;25:83.

173 Thompson AW, Baskes MI, Flanagan WF. Acta Metall 1973;21:1017.

174 Asaro R, Suresh S. Acta Mat 2005;53:3369.

175 Andrade U. High Strain, High-Strain Rate Deformation of Copper, Doctoral Thesis, UCSD, 1993.

176 Dalla Torre F, Van Swygenhoven H, Vicoria M. Acta Mater 2002;50:3957.

177 Schwaiger R, Moser B, Dao M, Chollacoop N, Suresh S. Acta Mater 2003;51:5159.

178 Roth HA, Davis RC, Thomson RC. Met Trans A 1997;28A:1329.

179 Becker RZ. Phys 1925;26:919.

180 Seeger AZ. Naturf 1954;26:758.

181 Seeger AZ. Naturf 1954;26:818.

182 Seeger AZ, Naturf 1954;26:851.

183 Meyers MA, Vöhringer O, Lubarda VA. Acta Mater 2001;49:4025.

184 Christian JW, Mahajan S. Prog Mater Sci 1995:39.

185 Armstrong RW, Worthington PJ. in Metallurgical Effects at High Strain Rates, ed. R. W. Rhode, B. M. Butcher, J. R. Holland and C. H. Karnes. Plenum Press, New York, pp. 401-414, 1973.

186 Haasen P. Phil Mag 1958;3:384.

187 Meyers MA, Andrade UR, Chokshi AH. Metall Mater Trans 1995;26A:2881.

188 Sanchez JC, Murr LE, Staudhammer KP. Acta Mater 1997;45:3223.

189 Vohringer OZ. Metallk 1976;67:51.

190 Honeycombe RWK. The Plastic Deformation of Metals, Edward Arnold Ltd, London, pp. 163, 1984.

191 Narita N, Hatano A, Takamura J, Yoshia M, Sakamoto H. J Japan Inst Metals 1978;42:533.

192 Venables JA. Phil Mag 1961;6:379.

193 Venables JA. in Deformation Twinning, Eds. R.E. Reed-Hill, J.P. Hirth and H.C. Rogers, Gordon and Breach, New York, pp.77, 1964.

194 Vöhringer OZ. Metallk 1974;65:352.

195 Vöhringer OZ. Z Metallk 1972;11:1119.

196 Tiearney TC, Grant NJ. Met Trans A 1982;13A:1827.

197 Eder D. LLNL, unpublished work, 2007.

198 Sorkin V, Polturak E, Adler J. Phys Rev B 2003;68:174102.

199 Jephcoat AP, Besedin S. in U. S.-Japan Conference in Mineral Physics, eds. Manghnani M, Yagi T. AGU Publications, Washington, DC 1997.

200 Errandonea D, Schwager B, Ditz R, Gessmann C, Boehler R, Ross M. Phys Rev B 2001;63:132104.

201 McQueen RG, Marsh SP, Taylor JW, Fritz JN, Carter WJ. in High Velocity Impact Phenomena, ed. Kinslow R. Academic, New York, 1970.

202 Dai C, Jin X, Zhou X, Liu J, Hu J. J Phys D: Appl Phys 2001;34:3064.

203 Grady DE, Kipp ME. Int J Rock Mech Min Sci & Geomech 1979;17:147.

204 Grady DE, Kipp ME. Int J Rock Mech Min Sci & Geomech 1979;16:293.

205 Grady DE, Kipp ME. Mechs of Mats1985;4:311.

206 Kipp ME, Grady DE, Swegle JW. Int J Impact Eng 1993;14:427.

207 Grady DE, Kipp ME. Int J Impact Eng 1997;20:293.

208 Yoshinaga H, Toma K, Abe K, Morozumi S. Phil Mag 1971:23:1387.

209 Bat'kov YV, Glushak AB, Glushak BL, Novikov SA, Fishman ND. Combustion, Explosion, and Shock Waves 1995;31, No.5:605.

210 Chabildas LC, Hill CR. in Metallurgical Applications of Shock Wave and High Strain-Rate Phenomena, eds. Murr LE, Staudhammer KP, Meyers MA. Dekker New York, 1986;429-448.

211 Lennon AM, Ramesh KT. Int J Plast 1998;14, No.12:1279.

212 Maddox B. LLNL, unpublished work, 2007.

213 Wang Y, He H, Wang L, Jing, Boustie FM, Sekine T. J Appl Phys 2006;100:033511.

214 Grady DE. J Mech Phys Solids 1988;36, No.3:353.

215 Kittel, C. Introduction to Solid-State Physics, 5th edition, N. Y., Willey 1983.

216 Rose JH, Smith JR, Guinea F, Ferrante J. Phys Rev B 1984;29:2963.